Ⅰ. Introduction and Background

1.1 Introduction

Generally speaking, through the refinement of grain size from several hundreds to only a few of micrometers, or even the submicron scale [1,2], the traditional structural materials are expected to display superior mechanical properties, such as excellent superplasticity. Based on the expectancy of the material properties improvement by means of grain size refinement, continuous efforts have been made to obtain the ultrafine grained phases in recent years [3]. There have been numerous fabrication means to produce nanocrystalline materials, such as mechanical alloying and severe plastic deformation. Meanwhile, an amorphous phase can be eventually prepared by continuous processing of various methods after the acquirement of nano-grained state [4-9]. An amorphous state is metastable in terms of the thermodynamics and the atoms under an amorphous state lack crystalline long-range order. They are also called liquid metals or non-crystalline metals. It signified that the solid metals and metal alloys with liquid-like atomic arrangements are called the amorphous metallic alloys, or glassy metals alternatively.

The traditional glassy metals have been synthesized by rapid cooling from the melt at cooling rates of about 10^6 K s^{-1}. Because the high cooling rates suppress the occurrence of crystallization during the solidification process (Fig. 1.1), the amorphous alloy is a uniform material without anisotropy. Since the first discovery of amorphous metals prepared by rapid solidification of melts by Klement et al. in 1960 [10], this kind of new alloys have generated wide interest among scientists and engineers because of their unique characteristics owing to their amorphous structure. Some of the characteristics identified include high strength and toughness, good wear resistance, special soft magnetic properties, and so on. For instance, the aluminum base amorphous alloys have high tensile strength above 980 MPa [11], well above the typical strength level of 300-500 MPa for most commercial Al crystalline alloys. But the amorphous structure may be easy to transform into a more stable crystalline state when the metallic glass undergoes any heating process, and such special properties disappear. The comparisons of the properties between the traditional metals and metallic amorphous alloys are shown in Table 1.1 [12, 13].

Amorphous alloys can be prepared by several ways and these methods can be divided into five leading categories [14]: rapid quenching from the melt, vapor quenching, particle bombardment methods, solid-state reaction and casting of multi-element alloys, etc.

The amorphous alloys prepared by rapid quenching from the melt need high cooling rates (10^6 K s^{-1}or above) to avoid crystallization to occur and the shapes of these alloys are mostly ribbons, sheets or fine powders [15]. It is not very easy to achieve such a high cooling rate and the small size of the prepared alloys will limit their practical uses. In contrast, the last two methods mentioned above received increasing attention in the past decade, since these two ways make it possible to prepare nanocrystalline or amorphous phases in bulk form under lower cooling rates [16]. In 1988, the new multi-component alloy systems with much lower cooling rate have been discovered [17]. Figure 1.2 shows the relationship between the critical cooling rate, maximum sample thickness and reduced glass transition temperature (T_{rg}) for amorphous alloys reported to date [18-22]. Recent years, the lightweight glassy metals such as the Zr, Ti, Mg, Al base alloys with the aim of meliorating the specific strength were the developing emphasis. In addition, the alloys with the mixture of amorphous and nano-crystalline phases prepared from the crystallization of the amorphous alloys have also attracted attention due to the promotion of their properties [23].

In order to improve the glass forming ability (GFA) of alloys, researchers worldwide devote themselves to find out a better way to synthesize the amorphous alloys and a better arrangement of the composition in the glassy metals. These efforts increase the convenience to study the properties of nanocrystalline or amorphous alloys, and the possibility of their practical industry applications. It is generally believed that the nanocrystalline or amorphous alloys own highly developing potential in the future.

1.2 Methods to prepare the amorphous metallic alloys

There were a number of methods in synthesizing the amorphous alloys developed in past decades, and generally they can be classified into the following five types [14]:

(1) Rapid quenching from the melt,

(2) Vapor quenching,

(3) Particle bombardment methods,

(4) Solid-state reaction,

(5) Casting of multi-element alloys.

The detailed descriptions of these methods are presented below.

1.2.1 Rapid quenching from the melt

Rapid solidification is one of the traditional technologies to produce the amorphous alloys. Various ways used for rapid solidification include the melt spinning, planar flow casting, melt extraction, piston-and-anvil, free jet melt-extrusion, twin roller, in rotating-water spinning process, laser treatment, atomization and Taylor wire method. The major concepts of this technology are first melting the alloys and then quenching them onto a cool substrate with high thermal conductivity. One can get a glassy metal easily by rapid quenching because this approach can generate high cooling rates, 10^4 to 10^{12} K s^{-1}. Four of the mainline methods are shown schematically in Fig. 1.3 [14]. The shape of glassy metal prepared by rapid quenching is often obtained in the form of ribbon or sheet of 20-50 μm in thickness (or the powders with 20-100 μm in diameter), and the thickness of sample is kept small in order to speed up the heat exchange. In Fig. 1.4, for example, the glassy metals prepared by the splat quenching technology which was been develop by Duwez's research group [10] require cooling rates of about 10^6–10^8 Ks^{-1} with a thickness of about 50 μm. In addition, the cooling rate of each method was also be influenced by the experimental conditions. Such as in the method of melt spinning, the cooling rate increases with increasing wheel speed. Although there are some limitations of cooling rates and the sizes of amorphous alloys for the rapid solidification, this method can still be considered to be an efficient and commercialized way to synthesize metallic glasses.

1.2.2 Vapor quenching

The preparation of amorphous alloys may also be obtained by depositing the alloys in the vapor state onto a cool substrate. There are two methods that belong to this category: thermal evaporation and sputtering, and they can generate relatively high cooling rates over 10^8 Ks^{-1}. Figure 1.5 shows the schematic diagrams of these methods [14].

In thermal evaporation method [24], an emitting vapor of the desired contents is generated under a high vacuum chamber by heating a source alloys, then the vapor is deposited on a substrate and a thin film of amorphous phase is formed. Besides, in the sputtering method [25], a gas (generally Ar) at a low pressure is ionized under an applied voltage. The positive gas ions are being driven toward the cathode of alloy and sputter the atoms from the cathode. These atoms will deposit on the specimen forming an amorphous film. This sputtering process allows better composition control in forming thin amorphous films than the deposition process [26].

These methods can be used to condense elemental metals or alloys and may also be used to produce bulk glasses, but the devices are very expensive and need long time to deposit a bulk material.

1.2.3 Particle bombardment methods

A number of amorphous alloys have been prepared by irradiation with high-energy electrons, heavy ions such as Ni^+ or fission fragments. These methods include the neutron and ion bombardment irradiation, electron beam irradiation, ion implantation and ion beam mixing. Since the first amorphization of the compound U_6Fe by this method in 1962 [27], several compounds such as NiTi and Zr_3Al have also been studied using this technology. From their observations, an alloy could be vitrified by the aid of high doses with high dose rates under low temperature. The constraints of these methods are that the compound amorphization by this technology must be the compound with low critical defect density and low defect mobility [28], because the vitrified process is accomplished through the crystal expansion [29].

1.2.4 Solid-state reaction

Except for the amorphization under the high cooling rate, the alloys can be vitrified by interface diffusion with a special arrangement of composition. It is called a solid-state reaction. This method forces the atoms of each element to diffuse homogeneously in a solid state under low temperature in order to maintain the existence of metastable amorphous phase.

Three methods have been developed based on this concept: hydrogen-induced amorphization [30], mechanical alloying [31], and multiplayer interdiffusion.

In 1983, a new method of synthesizing metallic glasses has been found throughout the discovery that a compound (Zr_3Rh) could be vitrified by hydrogen absorption because that as the fast diffusion of hydrogen into Zr_3Rh, the free energy of crystalline Zr_3Rh must be raised above that of the amorphous phase. Hydrogenation has been found to be possible in many binary metal compounds of which one constituent is a hydride former, such as ZrAl and others. This method is called the diffusion-induced amorphization.

On the other hand, the processes of mechanical alloying and multiplayer interdiffusion belong to the mechanically aided amorphization. These methods are the low temperature processes without the limitation of cooling rates.

Mechanical alloying is a high-energy ball milling process to produce the amorphous phase by blending of elemental powders or compounds. During the process of ball milling, the amorphous phase is achieved through the repeating cold welding and fracture occurred between the powders [32]. In 1983, a $Ni_{60}Nb_{40}$ glassy metal has been prepared by this method [33]. Based on a series of research works on this amorphous alloy [34,35], one can find that the concentration of oxygen picked up during mechanical alloying is responsible for the lower glass forming ability of the sample, since the oxygen impurity may act as heterogeneous nucleants and thus hinder the glass formation. The impurity may also be introduced during the ball milling process and impede the vitrification of powders. It should also be notice that the induced contamination during ball milling process results in enhanced tendency in inducing crystalline-glassy cyclic phase transformation, as occurred in some MA alloys (such as $Zr_{50}Al_{50}$, $Zr_{67}Cu_{33}$ and $Co_{75}Ti_{25}$) [36]. Besides, the severe temperature rise during MA to even several hundreds in Celsius degrees may occur and make the recrystallization of amorphous powder.

If the above mentioned problems can be eliminated, the mechanical alloying is still an easy way to prepare the amorphous metallic alloys. But for the purpose of easy applications, the powders need to be sintered or extruded into a bulk form. It becomes very difficult to compress the amorphous metallic powders due to their high hardness [37] and the amorphous state of alloy could not be easily maintained after the sintering or extrusion process.

Another important approach in the study of amorphization was the metal-metal reactions in thin films and multiplayer interdiffusion attracted more attention in the past decade. The sample prepared for this method consisted of alternating layers of various metals with thin thickness and the amorphization occurred during the accumulative roll bonding (ARB) process. This kind of configuration provided small diffusion distances for each element. Figure 1.6 is the schematic illustration of this process [38]. For instance, Schwarz and Johnson reacted multiplayer thin foils of elemental crystalline Au and La to form an amorphous alloy in 1983 [39]. This method is also a low temperature process and cold rolling leads to a signification refinement of the microstructure. According to characterization of an ARB amorphous Zr-Al-Ni-Cu alloy [40], the diffusion of each element can be fastened by several orders of magnitude via lattice defects or interfaces introduced into the sample during heavy deformation. Besides, the applied low strain rates increase the effective reaction time during deformation. Due to the fact that lubricants or hard steel balls (as in MA) are not used during ARB, it prohibits strong contamination, and results in enhanced stability of the amorphous alloys, with less tendency in inducing crystalline-glassy cyclic phase transformation as occurred in some MA alloys. Detailed description of this technique will be discussed latter.

1.2.5 Casting of multi-element alloys

In recent years, researchers tend to pay more attention to another method called casting of multi-element alloys. The procedure of the casting process is very simple. First, the chosen pure elements with decided amount are placed in a furnace under vacuum or protective atmosphere, such as Ar, and then are repeatedly melted until they are mixed homogeneously. The attractive aspect of this method is that one can prepare the amorphous alloys in bulk form and shape them into any needed form by simple steps. The critical cooling rate increases with increasing sample size. That is the reason why the traditional casting method could not synthesize metallic glass. Now one can achieve the goal of amorphization by selecting special element systems that could show, for example, large negative heat of mixing. This kind of multi-element alloy owns great glass forming ability because it needs very low critical cooling rate, as discussed in next section. The surrounding atmosphere during casting of multi-element alloy must contain very low oxygen content to avoid crystalline phase nucleation.

1.3 The systems of glassy metal

1.3.1 The evolution of amorphous alloys component

The systems of glassy metals component can be divided into five major categories shown in Table 1.2 [14]. The binary alloy consists of metal and metalloid (such as Si, P, B….) is the most popular glassy metal before 1988, because it is the first amorphous alloy system synthesized by the rapid solidification technique. These binary alloys need very high cooling rates (10^6-10^8 K s^{-1}) to be vitrified and the production size is very small. The noble metal base amorphous alloys, such as Pd-Ni-P and Pt-Ni-P alloys with lower critical cooling rates of the order of 10^3 K s^{-1} [41] and larger size [42] have been developed in 1980. But the cost of this kind of material is too high to use. The development of amorphous alloys undergoes a major breakthrough in 1988. In that year, the Mg-Ce-Ni amorphous alloys with much lower cooling rates (below 10^3 K s^{-1}) have been found by Inoue et al [17]. This kind of glassy metal has very high tensile fracture strength and large GFA. After that the Mg-TM-Ln, Ln-Al-TM, Zr-Al-TM, Hf-Al-TM and Ti-Zr-TM amorphous alloy systems with great GFA and unique properties have been developed gradually (TM= transition metals; Ln= lanthanide metals). More recently, researchers focused in the multi-component alloy systems, especially for the Zr base alloys, because these alloy systems could be vitrified into a bulk form by casting with a very low cooling rate of about 10 K s^{-1} and their supercooled region is very wide (ΔT_x = 80-100 K) [43]. Table 1.3 [44] summarizes the typical bulk amorphous alloy systems reported up to date since 1988 and they can be divided into nonferrous (including the noble metal-base alloys) and ferrous alloy systems. The ferrous group metal base alloys are the soft ferromagnetic materials.

1.3.2 The glass forming ability

Scientists try to prepare a glassy metal with better thermal stability by changing the proportion of each element and the methods of vitrification. The thermal stability of the amorphous alloy reflects the ability to resist crystallization tendency, it is also called the glass forming ability (GFA). Initially, the glass forming ability of an alloy was determined by the critical cooling rate (R_c). The high cooling rates was used to suppress the occurrence of crystallizationn in order to obtain the amorphous alloy. However, the exact value of critical cooling rate of some vitrification methods is not easily to measure. Hence, some parameters estimated based on the DSC or DTA measurement were used to react the glass forming ability of the amorphous alloy. Most famous parameters are the reduced glass transition temperature, T_{rg} ($=T_g/T_l$, T_l is the liquidus temperature) and the supercooled liquid regime, ΔT_x. There is a clear tendency for the critical cooling rate to decrease with increasing T_{rg}, as shown in Fig. 1.2 [44]. It means that the glass forming ability of an alloy increased as the reduced glass transition temperature increasing.

Moreover, the temperature interval of a supercooled liquid ΔT_x ($=T_x-T_g$) is defined by the difference between glass transition temperature and crystallization temperature (T_x). If T_g is unchanged, the thermal stability of an amorphous alloy increased with increasing T_x. Figure 1.7 reveals that the critical cooling rate also increases with increasing supercooled liquid regime [45], so the synthesized size of glassy metal increases.

Unfortunately, the results of GFA determined by means of T_{rg} and ΔT_x can not satisfy all of the alloy systems at the same time [46-51]. Hence, a new parameter, γ ($=T_x/(T_g+T_l)$), is proposed by Lu and Liu [52]. Table 1.4 reveals T_{rg}, ΔT_x and γ for various alloy systems. The critical cooling rate, R_c (K/s) and the least dimension of the sample, Z_c (mm) can be expressed by the followed equations,

$$R_c = 5.1\text{x}10^{21}\exp(-117.19\,\gamma), \qquad (1.1)$$

$$Z_c = 2.8\text{x}10^{-7}\exp(41.7\,\gamma), \qquad (1.2)$$

These two equations reveal much better accuracy than T_{rg}, and can be successfully used in developing the bulk Fe-Nd-P alloy.

1.3.3 Three empirical rules for the synthesization of amorphous alloys

The bulk amorphous alloys have dense randomly packed atomic configurations. It indicates that if the atoms of each element are easier to pack densely, the glass forming ability of the amorphous alloys is higher. That is to say, the glass forming ability increases with increasing difficulties of nucleation and growth during the synthesizing process of glassy metals. This is because, based on the kinetic point of view, the forming of crystalline and amorphous state is a simultaneous and competing process. From the previous studies, another way to increase GFA is to choose a multi-element alloy with suitable component proportion. One can choose the alloy composition based on the following three empirical rules:

(1) The multi-component systems consist of more than three elements and it is better that the difference in atomic size ratios among the three main constituent elements exceed about 12-15%. It is called the anti-Hume-Rothery criterion and which is a reversed thinking from the Hume-Rothery criterion [53]. Based on the Hume-Rothery criterion, if one wants to prepare a crystalline alloy, the difference in atomic size ratios should be less than 15%. Therefore we know that the large difference in atomic size ratios can impede the formation of crystalline alloy.

(2) Large negative heats of mixing among the three main constituent elements are needed. The negative heat of mixing is also regarded as the ability of atomic bonding between two distinct atoms (for instance, A-B or A-C). The large negative heat of mixing refers to the fact that the bonding ability of the same atoms is very weak and they tend to break the bonds of each other in order to bind with the distinct atoms. Hence the A atoms may be surrounded by B or C atoms as far as possible. If there are three different elements mixed together and the difference in atomic size ratio is very large, it is too difficult for atoms to locate the precise position and form the stable crystalline structure during the quenching process. Therefore the atomic configuration presents a high dense but irregular packing, it is also called an amorphous structure. But the influence of this rule for the vitrification of alloys is inferior to first anti-Hume-Rothery rule.

(3) The component proportion of each element could be decided based on the equilibrium phase diagram, and the best proportion in the phase diagram was close to that of a very low melting eutectic point [54]. This is because that it avoids the possibility in precipitating the crystalline phase by a large supercooled liquid region.

From the pervious results in past decades [18-22], it has been clarified that the multi-component amorphous alloys synthesized on the base of above three rules can have the characteristics of higher degrees of dense randomly packed atomic configurations, the formation of liquid with new atomic configuration, and multi-component interactions on a short- range order. The reasons for the stabilization of supercooled liquid and the high glass forming ability for the multi-element alloys that satisfy the three empirical rules are summarized below.

(1) The solid/liquid interfacial energy of the multi-component alloy is higher than the binary alloy because the multi-component alloy consists of many kinds of element. The increase in the interfacial energy leads to the suppression of nucleation of the crystalline phase efficiently because of the decrease in the melting temperature.

(2) The atomic size ratio of the multi-element alloy is very large and it results in the increasing difficulty of atomic rearrangement, leading to a decrease of atomic diffusivity and an increase of viscosity. Thus the new liquid can have a higher T_g.

(3) The large negative heat of mixing among the three main constituent elements leads to the strong bonding energy between the distinct elements. On the other hand, the interactions of each element on a short-range order are very severe and the atomic rearrangement on a long-range scale for crystallization is insufficient, resulting in the suppression of crystalline phase growth.

Simply speaking, a multi-element alloy satisfies the three empirical rules is a material with lower melting temperature and higher glass transition temperature. That is to say, this kind of amorphous alloy possesses a high thermal stability of supercooled liquid (i.e., T_g/T_l increased, as shown in Fig. 1.2).

1.4 Characterization of amorphous alloys

The unique characteristics contributed from the amorphous structure are superior to the traditional crystalline material. The properties of bulk multi-element amorphous alloys are described below.

1.4.1 Mechanical properties

Table 1.5 [12,13] summarizes the comparison of the mechanical properties among the Zr base amorphous alloys, cast stainless steel and Ti alloys. The data in Table 1.5 and some literatures [45,55-57] demonstrates that the glassy metals own very high (i) yield strength, (ii) toughness, (iii) hardness, (iv) impact fracture energy, (v) fatigue strength, (vi) bending strength, (vii) bending deflection, and (viii) great workability. The tensile strength for most of amorphous alloys exceeded 1000 MPa [58,59], and this value is much better than that of traditional crystalline alloys. The coefficient of thermal expansion might be zero for some amorphous alloys with special composition and these alloys can be used in the high precision instruments. In addition, the bulk amorphous alloys exhibit lower Young's modulus (E) than those of any kind of crystalline metallic alloys, as shown in Fig. 1.8 [44]. Another mechanical feature of the bulk amorphous alloys is that they are strong not only in the longitudinal loading direction but also in the transverse loading direction. This is because the atoms of amorphous alloys are bonded in anisotropic type, allowing small displacements of atoms to resist deformation result from the applied stress in any direction.

Moreover, an excellent elongation of the amorphous alloy can be obtained in the supercooled region and it behaves like the ceramic glass with high forming ability at the temperature above T_g. It has been reported that the tensile elongation reaches about 15,000% [60] for the $La_{35}Al_{25}Ni_{20}$ amorphous alloy at 227℃ (T_g = 200℃) and $5x10^{-4}$ s^{-1}. The La base amorphous alloy was claimed to have the opportunity to reach about 150,000%, even approaching 10^6 %. This value is well higher than the highest superplasticity record of 8800% for all kinds of metallic or ceramic materials. If one picks up the filament near the fracture region of the La base amorphous tensile specimen and conducts the second-time tensile test, the elongation still can reach about 1000% [60]. Furthermore, the value of strain-rate sensitivity, m, of amorphous alloy for the deformation in the supercooled region reaches 1.0 [61], suggesting that the deformation obeys the Newtonian flow behavior under an appropriate strain rate condition. This situation is very different from that of the normal metallic or ceramic crystalline materials (m～0.3-0.7). But some other reports pointed out that the m value of the amorphous alloys just reaches ～0.5 and there are still arguments about the deformation mechanism [62-64]. The high strength makes the metallic glasses favorable for reinforcement additives or as face material in golf clubs. The amorphous alloys have also been used as spring, die material, cutting material, etc [4].

1.4.2 Chemical properties

The very high corrosion resistance were be observed in some amorphous alloys due to the homogeneous single phased structure, even better than that of conventional stainless steel [65]. This property is due to the lack of grain boundaries, dislocations, second phase particles and the other crystal defects in the amorphous alloys. Besides, one can improve the corrosion resistance of amorphous alloys by adding some kinds of corrosive solute. For instance, the corrosion resistance of Zr-Al-Ni-Cu amorphous alloy increases as one adds the corrosive solute, such as Nb, Ta, Ti or Cr, is added [45]. The effect of Cr addition on the improvement of corrosion resistance is inferior to that of Nb, Ta or Ti addition. The other chemical properties of the amorphous alloys are the good wear resistance and catalytic property. The glassy metals can act as good corrosion resistant reaction vessels, catalysts, gas absorbers and ion-adhesion materials [66].

1.4.3 Magnetic properties

Permeability stands for the soft magnetic property of the material. Some amorphous alloys exhibit great permeability that attracts the attention for industrial applications [67]. The metallic glasses with soft magnetic properties can be divided into two categories: TM-M and TM-TM (TM: Fe, Co, Ni, Zr, Hf, etc; M: B, C, Si, P, Ge, etc.) The major amorphous alloy systems with soft magnetic properties belong to the former group, which M can be 15-30 at% to the extent. High permeability of the amorphous alloy resulted in minimum magnetic energy loss. Hence, the application range of this kind of magnetic amorphous alloy is very wide, including the magnetic head of a recorder, high frequency transformer, wave filter, etc.

1.5 The metallic glass containing nanocrystalline second phase

Another interesting research field is the amorphous alloys with nanocrystalline second phases. It is not very easy for the alloys to maintain the amorphous phase and nanocrystalline second phase at the same time. But the variation of mechanical properties because of nanophase precipitation is worth to notice. Take the Al base amorphous alloy with nanosized Al particles for example [68,69], the tensile strength of the alloy is 1.4 times of pure amorphous alloy. The second phase particles contributed the high mechanical strength [70] to the amorphous alloy, due to the fact that (1) the nano scale Al second phase is the defect-free structure without dislocation; (2) the precipitation of nano scale Al phases filled in the vacancies of amorphous structure and reduce the interfacial energy of alloy and (3) the Al precipitation can be treated as the obstacle dispersed in the amorphous matrix during the deformation process. Therefore, the ability of an amorphous alloy to resist plastic deformation can be improved if the Al second phase particles can precipitate in the amorphous alloys with appropriate content, size and dispersing distance. Although the strength of amorphous alloys can be improved by the precipitation of second phase particles, the toughness may decrease drastically at the same time. Hence, the precipitation of nano-crystalline second phases in the amorphous alloy for the improvement of mechanical properties should be carefully controlled.

Meanwhile, the thermal stability of the amorphous alloy also can be enhanced by the nano-crystalline second phase [71]. According to the study made by Inou et al. [72], T_x increased because of the presence of ZrC second phase in the Zr base amorphous alloy. Therefore, the thermal stability of the amorphous alloy(ΔT_x) increased with increasing T_x.

1.6 The aims in this research

The synthesization of nanocrystalline and amorphous alloys have attracted great attention due to their characteristics and future potential. But according to the above descriptions, the small sizes and narrow supercooled liquid range of metallic glasses still retard the application in practice. Hence, it is necessary to synthesis new amorphous alloy systems with high glass forming ability in bulk form. Moreover, our laboratory mainly studied the mechanical and superplastic properties of lightweight base alloys over the past years and we would like to extend our experience to adopt the lightweight elements (such as Zr, Al, Mg, Ti….) as major components to synthesize amorphous alloys as much as possible. This consideration is based on not only the material cost but also the specific strength. The feasibility of application seems to increase with increasing specific strength. Once the synthesis of new lightweight amorphous alloys is achieved, characterization of their properties will be followed.

The major selected vitrification method in this study is solid-state reaction. The procedures of solid-state reaction are more complicated than that of casting, but the influence of cooling rate on amorphization process is less important in the former routine. Except for amorphization from the liquid phase using high cooling rates, numerous alloys can be vitrified by interface diffusion through solid state reactions. Solid-state reactions have been one of the methods received increasing attention in the past decade, since they make possible to prepare metallic glasses in bulk form without rapid cooling rates. Mechanical alloying (MA) [33-35] and accumulative roll bonding (ARB) [38-40,73] belong to this category. The emphasis was focused on the ARB method, but the finding in this study can compare with the results from the MA method.

The alloy prepared by ARB can be transformed into nano-grained state or eventually amorphous phase. The samples prepared for ARB consist of alternating layers of various elements with thin thickness 20-100 μm. Through the accumulative passes of cold rolling for around 40-100 cycles, significant microstructure refinement will be achieved. The layer thickness reduction and residual strain accumulation are very important for the severe plastic deformed ARB process and discussed as below.

If the layer thickness reduction is set to be 50% per F&R cycle, the thicknes after n cycles is expressed as,

$$t_n = \frac{t_0}{2^n}, \tag{1.3}$$

where t_o is the initial thickness of foil. The total thickness reduction ratio, r_l, after n cycles is expressed as,

$$r_l = 1 - \frac{t_n}{t_0} = 1 - \frac{1}{2^n}, \tag{1.4}$$

According to the von Mises yielding criterion and plain strain condition [57], the lateral extension of layer is ignorable. Therefore, the accumulated true strain after n cycles can be predicted as,

$$\varepsilon_n = \frac{2}{\sqrt{3}} \ln(t_n / t_0) = \frac{2n}{\sqrt{3}} \ln 2 \approx 0.8n, \tag{1.5}$$

Successful vitrification of multi-element alloys by ARB has been reported [40]. However, the effects from individual element have not been established. Therefore, one of the aims in this study is to examine the evolution of various coarse-grained Zr base alloy systems.

Unlike the more matured mechanical alloying (MA) process, ARB has been much less systematically studied. Mechanical alloying on the Zr alloys has been conducted from 1980's [34]. Recent MA studies by Inoue et al. [72] have shown that the starting powders tended to agglomerate and formed particles with thick multilayered structure at the early milling stage. The layer thickness decreased with increasing ball milling time and the amorphous phase formed as the layered structure disappeared. It is interesting to note that the microstructural evolution of MA powders is analogous to that occurred during ARB, both including extensive multiplayer interdiffusion during the process. In comparison with the MA method, ARB with its internal generation of large interfacial areas prohibits strong contamination of the foils, and leads to enhanced stability of the resulting amorphous alloys. Meanwhile, the amorphization process of the MA specimens occurred as the accumulated defects make the free energy of the crystalline phase higher than that of the amorphous phase [74]. It can be surmised that the vitrification mechanism of ARB and MA methods may be similar to some degrees. But the severe temperature rise occurred during MA would seriously affect its nanocrystallization and amorphization processes. In contrast, if the specimen dimension is small enough so as to easily release the heat from the rollers, and if the rolling speed is slow, the temperature rise during the ARB process could be much minor. For ARB at a rolling strain rate of 19 s^{-1}, the maximum temperature rise was estimated to be 167^{o}C [75]. If the rolling strain rate is controlled to be less than 1 s^{-1}, then the temperature rise should be less than 50^{o}C. The possible temperature increment of 10-200^{o}C may also assist to a certain degree in the interdiffusion of elements during the ARB process.

Most previous research on the nanocrystalline and amorphous alloys made by the ARB route has been focused on their unique physical or mechanical properties. The detailed characterizations on the evolution of nanocrystallization and amorphization processes by ARB have not been systematically studied. Hence, the other aim in current study is to examine the gradual microstructural evolution of nanocrystallization and amorphization mechanism of various Zr-X based binary, ternary, and pentanary alloys during ARB by means of TEM characterization; and to compare with the findings from the MA method. Besides, the influence of effective diffusion distance of atoms will also be investigated.

Due to the easily synthesization of the alloy, another selected method of amorphous alloys is the casting of multi-element alloys. Once an amorphous alloy is synthesized by the ARB method, the composition of this alloy is adopted in the casting process. The properties of the resulted specimen are compared with those of the ARB specimens too.

Ⅱ. Experimental Procedures

2.1 The amorphous alloy systems

The major adopted synthesis method for fabricating amorphous alloys in this study is the accumulative roll-bonding process. Some selective alloy systems are also synthesized by the arc melting process in order to compare with the ARB specimens. A number of the purified elemental foils (or rods) are selected for forming the binary, ternary, or pentanary alloys with nanocrystalline or amorphous phases. These elemental foils (or rods) are intended to be common and low priced materials on earth, such as Al, Cu, Ni, Ti, Zr, etc. Table 2.1 lists the related information of the elemental foils prepared for the ARB route, including the hardness, atomic radius and ΔH_m data. And Table 2.2 reveals the diameter and purity of elemental rods. The purity of all elements is above 99 at%.

It is intended to identify the alloy system and alloy content for high glass formability, and to evaluate the criteria based on three empirical rules mentioned in Chap. 1. Since the current popular bulk amorphous alloys are mostly Zr based, Zr was also chosen as the base metal in this study so as to compare with reported results. Other elements such as Al, Cu, Ni, or Ti with different proportions are included. Moreover, it is also tried to synthesize an alloy system with the equal atomic percent inspired by the study of Hsu et al. [9]. Figure 2.1 presents the available binary phase diagram for the Zr-Al, Zr-Cu, Zr-Ni, and Zr-Ti systems. The flow chart of experiment procedures is shown in Fig. 2.2.

Among the alloy systems, Zr-Ti was selected to be the focus of all fundamental studies. With the addition of the third element, the Zr-Ti-Cu and Zr-Ti-Ni ternary alloys are examined. Finally, the pentanary Zr base alloye, with the compositions close to the optimum glass forming ability or equal atomic percent, are explored.

2.2 Synthesization methods

2.2.1 The ARB method

In this method, the pure elemental foils were adopted to form the amorphous alloys. Stacking foils of different materials are repeatedly roll bonded. Detailed descriptions of the ARB process are presented below.

Firstly, the stacked foils of Zr and other metals (Al, Cu, Ni, or Ti) around 80-100 μm in thickness (thicker than the foils of 7.5~50 μm used in most previous studies [76]) were all cleaned by acetone before and after rolling, and rolled at room temperature (25^{o}C). The elemental foils were first cut into pieces measuring 20 mm in width and 120 mm in length, and stacked in order. The stacked foils were then manually folded for two or three times, resulting in an initial ARB specimen, measuring 20 mm in width, 30 mm in length and 1 mm in thickness (with around 10-13 layers of various elemental foils), ready for the ARB process. The step of manual folding plays an important role to keep the staked foils in order during ARB, especially for the first ten folding and rolling (F&R) cycles.

The major compositions in atomic percent of the binary and ternary Zr-X alloys in this study are all assigned to be 1:1, such as the $Z_{50}Al_{50}$, $Z_{50}Cu_{50}$, $Z_{50}Ni_{50}$, $Z_{50}Ti_{50}$, $Z_{34}Ti_{33}Cu_{33}$ and $Z_{34}Ti_{33}Ni_{33}$ alloys. Limit tests were conducted on the binary Zr-Ti alloy systems with proportion 3:1 and 1:3 for comparison, namely $Z_{75}Ti_{25}$ and $Z_{25}Ti_{75}$. Two pentanary alloys $Zr_{20}Ti_{20}Ni_{20}Cu_{20}Al_{20}$ and $Zr_{52}Ti_{5}Ni_{15}Cu_{18}Al_{10}$ were also characterized. The alloy systems for the ARB study are summarized in Table 2.3.

The stacked specimen was rolled by a 350-ton (HF 200×200) cold and hot rolling machine, as shown in Fig. 2.3. The roller diameter is 140 mm and the roller length is 220 mm. Four different rolling speeds (30, 25, 22.5 and 20 mm/s) were adopted for each folding and rolling cycle and the processing time for each pass is around 1-2 seconds, corresponding to a mean strain rate ($\dot{\varepsilon}$) in the range of 0.4-0.8 s^{-1}. The strain rate is calculated by $\dot{\varepsilon} = \frac{\varepsilon_n}{\Delta t}$, where Δt is the processing time. The true strain ε after 1 cycle is 0.8 (according to the Von Mises' yielding criterion and plain strain condition [57], as introduced in Sec. 1.6) and $\varepsilon_n \approx 0.8n$, where n represents the F&R cycle numbers.

The lower rolling strain rate applied was to lower the possible temperature rise and increase the effective reaction time during ARB deformation process. In-situ temperature measurements using attached thermocouples of the rolled specimens were conducted for selected cases. The maximum temperature rise from room temperature, ΔT, was only 25^{o}C, reaching a working temperature during the current ARB experiments of T~50^{o}C.

The thickness reduction for each F&R cycle was set to be 50%. As the reduction in thickness reached to 50%, the rolled specimen is folded into two halves and cleaned by acetone. After cleaning, the dried divided specimens are stacked, roll-bonded and cleaned again and again. No lubricants are used during ARB process in order to prohibit strong contamination and result in enhanced stability of the amorphous alloys. Nevertheless, some materials were lost because the sample became brittle during the ARB process. Small parts of the specimen were sampled after 40, 60, 80, 90, and 100 cycles for off line analyses. It is time-consuming to form the amorphous alloys via the ARB process, but the advantage of this process is to synthesize the metallic glass in a plate shape directly. The plate or sheet specimens are convenient for further analyses or applications after ARB. And the effect of critical cooling rate essential for the rapid solidification technique plays no role in ARB.

2.2.2 Arc melting and melt spinning methods for multi-element alloys

The minor method adopted in this study was the arc melting process for making multi-element alloys. Pure elemental rods were used in this route. The used device (in National Sun Yat-Sen University) is the Centorr Series 5 Bell Jar Single Arc Furnace, and no dropping casting or melting spinning design is included in this system. The resulted maximum operating temperature is 3500^{o}C. Figure 2.4 shows the photograph and schematic drawing of the arc melting insidedevice.

Before the starting of arc melting process, the high purity argon gas needs to be blown into the melting furnace several times to flush the oxygen away, since the crystallization during rapid solidification would also result from the oxygen impurity. Then, a number of elemental rods with chosen component proportions are placed on the Cu mold inside the furnace. Cold water is flowing through the bottom of the Cu mold. The cold water can prevent the Cu mold from damage by the arc in the melting process, and it also increases the heat exchange speed between the melted material and Cu mold. The inner environment of furnace is not under vacuum condition. Argon gas is continuously purged into the furnace and the furnace maintains a positive argon pressure in order to ensure a low oxygen vapor pressure environment inside the furnace.

Finally, a high voltage is added to the arc melting instrument and then the produced arc melts the elemental rods. This melting process should be repeated for more than five times to confirm the homogeneous mixing of composition. This method is a generally recognized convenient way to form an alloy. If the selection of compositional elements is appropriate, a bulk-form amorphous alloy can be easily synthesized by this route. The shape of alloy prepared by the arc melting step is a half ball type. It is not convenient for off line analyses, and the resulting samples need extra works (such as cutting, grinding, polishing, etc.) for the preparation of subsequent testing specimens. Since there is no rapid dropping design in this system, the cooling rate of such arc melting process is not fast enough to form an amorphous alloy with set compositions. Therefore, it needed to further conduct the drop casting or melt spinning processes for complete vitrification of the alloys. The drop casting and melt spinning experiments are conducted in Prof. Jang’s laboratory in I-Shou University. Figures 2.5 and 2.6 reveal the photograph of drop casting and melt spinning devices.

The schematic sectional drawing in Fig. 2.5 shows the drop casting instrument (Miller co. Aerowave, AC/DC, Hybird Arc Welding Power Source) in Prof. Jang’s laboratory. Its upper part is similar to the arc melting furnance in NSYSU, except for the detachable Cu mold and a wedge-shaped mold connected to the bottom of flat Cu mold. The wedge-shaped mold was designed to increase the cooling rate of alloys via the surrounding cooling water system. Before the drop casting process, the purified argon gas is blown into the melting furnace several times to make certain the low oxygen content inside furnace. Then the drop casting device is operated under an argon atmosphere and the operating voltage is 17 keV. After the gas flushing process, a previous produced sample (by the arc melting method) is cleaned by alcohol and placed in the Cu mold of furnace. Then the specimen is arc melted again, and the remelted alloy drop cast into the designed chilled mold. The half ball-shaped specimen made by arc melting process is transformed into a wedge-shaped one via the drop casting step. The cooling rate for such wedge-shaped samples is higher than that for the half-balled type. Part of specimen near the tip (with the highest cooling rate) of the wedge-shaped alloy is also gathered for analysis.

For the easy operation of rapid cooling melt spinning process, residual wedge-shaped alloy is cut into pieces and put into a quartz tube (with 8 mm in diameter and 180 mm in length). The bottom of quartz tube has a small hole and the inner surface is covered with a thin layer of BN. (The BN layer is used to avoid the interaction between alloy and tube at high temperatures.) Just like the arc melting process, several times of gas flushing step were performed before melt spinning experiment. Then the quartz tube is placed and heated in a chamber surrounded by argon atmosphere and the chamber is directly controlled by the high frequency (8 kW) melting system. When the remelting of all pieces of alloy is completed, the melted metal is sprayed onto the surface of Cu wheel through the hole in the tube bottom by high pressured (2-3 atm) argon. The wheel is rotated with high speed of 25 m/s (20 Hz) and its diameter is 400 mm. The resulting specimen is thin ribbon type with 0.5 mm in width and 100 μm in thickness. Small parts of the ribbons are sampled for latter property characterizations.

2.3 Phase identification by XRD

The nanocrystallization and vitrification degree of the resulting alloy structure were first identified by a Diano 5000 X-ray diffractometer (XRD) at room temperature after the synthesis process. Filtered Cu Kα radiation operated at 40 kV and 30 mA, and a graphite monochrometer are employed. The diffraction angle covers from $2\theta = 20^o$ to 90^o at a scanning rate of 1^o per minute. The flat rolling plane of alloys is characterized and the specimen is always sampled form the center of synthesized alloys. Before XRD analysis, the specimens needed to be cleaned by acetone. No grinding step is necessary for the ARB alloy. But a thin layer of alloys made by the arc melting or melting spinning method must be ground away before XRD identification, in order to remove the oxidized outer surface.

2.4 SEM characterizations

The elemental layer and grain size refinement of roll bonded alloys were examined by scanning electron microscopy (SEM), using mainly backscattered electron images (BEI). The edge-on cross-sectional plane is viewed in SEM/BEI analysis. The JSM 6400 SEM is employed to characterize the microstructure and multiplayer morphology. Before SEM characterizations, the cross-sectional plane of ARB specimens is mounted and ground by silicon-carbide abrasive papers (#600, #800, #1000, #1200, and #1500) with water, and then polished by solutions mixed with Al_2O_3 powders (1 μm, 0.3 μm, and 0.05 μm). If the arc melting or melting spinning alloy was also examined by SEM, specimens were etched by a H_2O + 10% HF solution after grinding.

Besides, the elemental mutual diffusion was examined using an energy dispersive spectrometry (EDS) equipped on JSM-6400 SEM or Jeol 6335 field emission gun SEM.

2.5 Microhardness testing

Microhardness testing was conducted using a SHIMADZU HMV-2000 Vicker's microhardness tester. The measurement for the ARB alloy is made on the flat rolling plane, and the specimen (subject to 40 to 100 F&R cycles) was mounted in the epoxy resin in order to avoid the effect of the induced micro-cracks during roll bonding process. The mounted sample was ground by silicon-carbide abrasive papers (#600, #800, and #1000) with water before the hardness measurement. But no mounting step is necessary for specimens made by the arc melting or melt spinning methods.

In this study, the hardness test was carried out using a load of 500-1000g with 10-15 second and the hardness value of each sample was averaged from 10 stored data. The microhardness data is used to investigate the grain size refinement of alloy, and to roughly calculate the Young's modulus at room temperature.

2.6 TEM characterizations

Both the cross-sectional and flat rolling planes of the resulting alloys are characterized by the Jeol 3010 analytical TEM (AEM) with Link eXL-II Energy Dispersive X-ray Analysis (EDS). The evolution of grain size refinement and the defect induced during ARB were carefully investigated by TEM. And the EDS system was used to identify the composition of the observed phase. Image Intensifier and CCD Camera (GARAN 622-SC) Fiber Optically coupled TV system attached on the AEM were used for the observation of interfaces between the nanocrystalline and amorphous phases by high resolution lattice images.

The operation voltage for TEM is 200 keV or 300 keV (for high resolution). TEM thin foils were first punched mechanically and then ground by silicon-carbide abrasive papers (#1200, #1500, and #2000) with water. The ARB sample is highly brittle and most of specimen could be lost during grinding. Therefore the resulted TEM foil is small and needs to be adhered to a mesh 200 Cu net (with 3 mm in diameter).

After grinding, the TEM foil is thinned by the Gatan 691 precision ion polishing system (without cooling system). Figure 2.7 presents the photograph of the Gatan 691 precision ion polishing system. The operation voltage is 4 keV and the tilting angle is in the range of 7^o-10^o. Ion gun source was produced by high purify argon gas. The precision ion polishing system is designed to produce high quality TEM specimens. The TEM foils can be speedy thinned by double ion beams, which come from both sides of specimen with positive and negative angles.

2.7 DSC thermal stability analysis

After the XRD or TEM analyses for confirming the vitrification degree, some of the amorphous alloy systems are subject to thermal analysis to examine their thermal stability.

Such investigations in terms of the microstructure, mechanical properties, and thermal properties of various alloys are integrated. The gathered information is useful for studies on forming or structural applications. Phase transformation would occur during the DSC scanning process. Therefore, the amorphization of ARB specimens subjected to different F&R cycles can also be roughly estimated from the heat capacity of DSC curves.

A Setaram 131 differential scanning calorimeter, DSC, was used to determine the T_x, T_g, and T_m. During the DSC measuring process, the sample was sealed in a crucible made by stainless steel at heating rates 10-40 ^{o}C/min within the argon atmosphere.

Ⅲ. Results

3.1 Sample preparation

3.1.1 Specimens made by ARB

In the initial attempt of this method, it was tried to synthesize a pentanary alloy system with the equal atomic percent inspired by the study of Hsu et al. [9]. Several pieces of elemental foils were prepared based on the desired composition and directly stacked without pre-bonding. The ARB process then proceeded using such loosely stacked foils. During the repeated rolling process, some of foils would be slipped out of the stacked specimen due to the lack of friction between the smooth interfaces. It brought about the considerable loss of specimen, the change of designed composition, and the hindrance of the smooth strain accumulation of roll bonding cycles. Hence, it was also tried to raise the rolling temperature for helping the accumulation of roll bonding cycles, although the original design of ARB should be performed at room temperature. The results revealed that the raise of rolling temperature was futile for the occurrence of nanocrystallization and vitrification. And it made ARB a time-consuming process. Section 3.2 concisely showed some results of above mentioned part.

Therefore, numerous subsequent efforts were made to keep the staked foils in order during the ARB process at room temperature. Firstly, it was tried to cover the stacked layers with pure Fe foil. But the difficulty of rolling increased due to the high hardness of Fe foil. Parts of Fe foil were broken into pieces and some small pieces took part in the alloying process during ARB. It also changed the designed compositions and resulted in an uncontrollable experimental factor.

After many times of experiments, it was finally found that the staked foils can keep in order during rolling process by adding a simple step before ARB. The step is outlined in Fig. 3.1. The strips of foils were stacked and then manually folded several times until the overall specimen thickness is enough for the ARB process. This step of manual folding before ARB is very important, especially for the first ten F&R cycles, because it makes the stacked foils to tie themselves down each other.

3.1.2 Specimens made by arc melting

The samples prepared by this method were used to compare with the ARB specimens. The selection of alloy component was based on the alloy systems made by ARB. Since the nanocrystalline or amorphous alloys produced by the arc melting process are still governed by the cooling rate, and the arc furnace in NSYSU has no drop casting design, the alloy synthesized by such an arc melting was only conducted for the pentanary alloy systems, namely, the $Zr_{20}Ti_{20}Ni_{20}Cu_{20}Al_{20}$ and $Zr_{52}Ti_{5}Ni_{15}Cu_{18}Al_{10}$ alloys. The gathered bulk typed samples were analyzed immediately. If there was no amorphous phase occurred, drop casting and melt spinning in ISU were followed. Except for pervious mentioned pentanary alloy systems, the drop casting and melt spinning process were also be performed for some binary systems (according to the composition of ARB method), such as $Zr_{50}Ti_{50}$, in ISU directly. The inclusion of Ti in the performed ARB alloy systems would raise the viscosity of the melt, making the dropping during drop cast or spraying onto the roller difficult. Also, the resulting ribbon became oxidized seriously. There were only a few alloys successfully produced by melt spinning, consequently.

3.2 Some results for alloys made by the preliminary try-and-error ARB methods

From SEM observations, the gradual evolution of foil thinning and alloy mixing in stacked foils with increasing ARB cycles can be easily realized. The specimens in this section were simply stacked and then directly roll bonded without the manually folded step (Fig. 3.1) before ARB. Figure 3.2 shows the backscattered electron images (BEI) for the rolling plane of the ARB $Zr_{20}Ti_{20}Ni_{20}Cu_{20}Al_{20}$ sample after 40, 60 and 80 F&R cycles at room temperature. It is obvious that the thinning and bonding of each foil indeed improve with increasing F&R cycles. With F&R up to 40 cycles, the BEI in Fig. 3.2 (a) shows the apparent inhomogeneous mixing of each element. It is a result of the large difference of initial hardness among these elements, making the mixing more difficult. But as the F&R cycle increases, the accumulated shear stress forces the harder phases to break into smaller phases and finally gets a much more homogeneous mixing structure, as shown in Figs. 3.2 (b) and (c).

As the description in pervious section 3.1.1, it was also intended to define the proper rolling temperature for enhancing the vitrification of preliminary tried pentanary alloy system, $Zr_{20}Ti_{20}Ni_{20}Cu_{20}Al_{20}$. The XRD pattern gathered from a $Zr_{20}Ti_{20}Ni_{20}Cu_{20}Al_{20}$ specimen roll bonded at 250^{o}C to 40-80 F&R cycles is shown in Fig. 3.3. At such a rolling temperature, the cracking problem at the ARB sample edge decreased greatly, but most peaks in the XRD pattern were still contributed by the pure elements. The intensity of these sharp peaks decreased with increasing ARB cycles. But the elevated rolling temperature seemed to hinder vitrification and made ARB a time-consuming process. Therefore the raise of rolling temperature is not a suitable process for amorphization.

For the above reason, the subsequent ARB works shifted back to the ambient room temperature. All stacked foils were manually folded several times before the beginning of ARB process. In order to reduce the complexity of multi-elemental alloying, the ARB experiment started from the binary alloy to clarify the role of each element.

3.3 X-ray diffraction analyses

All analyzed specimens in the sections after 3.2 were prepared by the manually pre-folded step before ARB and synthesized at room temperature.

Figure 3.4 is the XRD pattern of the $Zr_{50}Al_{50}$ specimen roll bonded at room temperature to 40-100 F&R cycles. Note that the initial hardness readings of the Zr and Al foils are distinctly different. The much softer Al (H_v ~ 22, Table 2.1) would be preferentially sheared with the harder Zr (H_v ~ 174, Table 2.1) nearly unchanged. No vitrification occurs during ARB in this alloy system. All XRD peaks were contributed from the pure elements and no evident of intermediate compound formation was traced. The intensity of Al peaks all decreased with increasing ARB cycles, but the Zr peaks, such as (0002) and $(2\bar{1}\bar{1}1)$, did not. Those strong peaks left in the 100-cycle specimen are mainly associated with Zr. Therefore, It was tried to synthesize other alloy systems with different initial conditions (such as atomic radius, hardness…etc.).

Figures 3.5 to 3.7 present the XRD patterns of $Zr_{50}Cu_{50}$ (H_v ~174 and 131 for Zr and Cu, respectively), $Zr_{50}Ni_{50}$ (H_v ~174 and 163 for Zr and Ni, respectively) and $Zr_{50}Ti_{50}$ (H_v ~174 and 183 for Zr and Ti, respectively). Apparent peak height reductions can be seen in these patterns, but the amorphization tendency can only be observed in Fig. 3.7. After 83 F&R cycles, the peaks contributed from Zr in the Zr-Ti alloy are hardly detectable in XRD patterns and the Zr-Ti alloy transformed into an amorphous state. The broad diffuse hump starts from $2\theta \sim 23^o$ and ends at $2\theta \sim 45^o$ (corresponds to a plane spacing from 2.0-4.0 Å), with its center of the diffuse peak located at $2\theta \sim 33^o$ (a plane spacing ~2.7 Å). It is not referred to any of the elemental spacing and is slightly smaller than the closest plane spacing for HCP Zr (3.17 Å) and Ti (2.89 Å). It is conceivable that the closest spacing is referred to the interspacing between Zr and Ti in the amorphous alloy.

It appears that an efficient ARB process needs to accumulate effectively the rolling shear strain for all involved elemental foils. Two kinds of elemental foils with distinctly different hardness levels would encounter problems in accumulate shear strains. The harder foils would not be deformed evenly, since the softer foils would be preferentially deformed and impose much lower pressure on the harder ones. In contract, foils with compatible hardness readings would undergo more efficient mutual deformation by the counterpart. The vitrification tendency did not seem to depend on the atomic size difference (Table 2.1) for the current binary Zr-X alloy systems subject to room temperature ARB. The first vitrified Zr-Ti alloys possess a small size difference of Δa ~ 9%, much lower than the ineffective Zr-Al (Δa ~ 12%, Table 2.1), Zr-Cu (Δa ~ 21%) alloys and Zr-Ni (Δa ~ 23%). This trend differs from the general guild line, i.e., anti-Hume-Rothery rule, followed by most cast amorphous materials.

The XRD patterns for the most efficiently vitrified alloy system via ARB, Zr-Ti, with different component proportions are shown in Figs. 3.8 and 3.9. Although the complete broadening hump was not yet accomplished at the end of current F&R cycles, both patterns exhibited more intense vitrification tendency than those gathered from other alloy systems. With non-equal portions of the Zr and Ti content, the XRD peaks left in the 90-cycle $Zr_{25}Ti_{75}$ specimens (Fig. 3.8) are mostly from Ti, and those in the $Zr_{75}Ti_{25}$ specimens (Fig. 3.9) are mostly from Zr. With equal amount of Zr and Ti, both with comparable initial hardness, the mutual deformation each other proceed most pronouncedly.

It is also worth paying attention to the step of manually folded before ARB. Figure 3.10 shows the XRD pattern of $Zr_{50}Ti_{50}$ subject to only one time of manually folded step before ARB. Hence, the resulting initial thickness and the number of interfaces for the $Zr_{50}Ti_{50}$ specimen in Fig. 3.10 are only half of those in Fig. 3.7. Insufficient thickness and interfaces delayed the occurrence of vitrification as well.

Figures 3.11 to 3.14 show the XRD patterns for the ternary and pentanary alloy systems. In Figs. 3.11 to 3.14, some strong and sharp peaks are still retained after 100 F&R cycles. With compatible hardness for Zr, Ti, and Ni (H_v ~174, 183, and 163), the vitrification degree of $Zr_{34}Ti_{33}Ni_{33}$ appears to be higher than that for $Zr_{34}Ti_{33}Cu_{33}$; the latter contains the softer Cu with H_v ~131. The pentanary $Zr_{20}Ti_{20}Ni_{20}Cu_{20}Al_{20}$ exhibited no sign of amorphization after 80 F&R cycles, presumably due to the inducing soft Al foils. Finally, the major XRD peaks for Zr are persistently retained in the pentanary $Zr_{52}Ti_5Ni_{15}Cu_{18}Al_{10}$ specimen subject to 100 F&R cycles. Combining the observations in Figs. 3.4 to 3.14, there are three notable points. Firstly, the diffraction peaks in all ternary and pentanary specimens (independent of alloy systems and F&R cycles) were still contributed by the pure elements with minimum or nil shifts in the corresponding diffraction angles for the pure elemental foils, even when the peaks become broadened due to the size and strain broadening effects. Secondly, no evidence of intermediate compound formation was found. Thirdly, with increasing F&R cycles, apparent peak height reduction can be seen, and a diffuse and broad hump located at 2θ ~33^o becomes more and more evident. These three observations suggest that the refined nanocrystalline phases are basically still pure elements in nature. But the amorphous matrix is a homogenous solid solution.

With increasing F&R cycles, the XRD peaks are not only shorted but also broadened. The XRD peak broadening can be quantitatively related to the refinement of phase size to the nano scale, as presented and discussed in Sec. 3.4. The XRD results can also be related to the SEM-BEI side-view observation presented in Sec. 3.5.

3.4 Grain size evaluations

Form the XRD patterns shown in the pervious sections, apparent peak broadening is evident in specimens subject to high F&R cycles. The grain size, d, was seen to decrease (from over 100 μm down to 20 nm or less) with increasing F&R cycles, and can be roughly estimated by the broadening of XRD peaks, *B*. *B* is the $\Delta\theta$ width at half height of peak. The simple Scherrer function [77] was first adopted for all alloy systems, namely,

$$B = \frac{k\lambda}{d_{hkl}\cos\theta}, \tag{3.1}$$

where d_{hkl} is the grain size along the [hkl] direction, θ is the Bragg angle, λ is the X-ray wavelength (1.5406 Å), and k is a constant defined in the range of 0.89 to 0.94 [78] and mostly taken as 0.9. For example, the calculated d value based on Eqn. (3.1) for $Zr_{50}Ti_{50}$ after 80 F&R cycles was in the range of 5.5 to 8.6 nm.

With the consideration of XRD peak broadening induced by residual strain η, another equation should be applied [79], i.e.

$$B\cos\theta = \frac{k\lambda}{d_{hkl}} + \eta\sin\theta. \tag{3.2}$$

Figure 3.15 shows an example for the grain size d of Zr in the $Zr_{50}Ni_{50}$ alloy estimated by Eqns. (3.1) and (3.2), along with the extracted microstrain η. The extracted microstrain η was mostly around 1-2%, except for a few cases with F&R cycles greater than 100. Table 3.1 summaries the grain size (nm) of Zr and microstrain η, estimated by Eqns. (3.1) and (3.2) for the binary, ternary and pentanery Zr-X alloy systems. The data on microstrain for various Zr-X alloys are in the reasonable range of 1% to 5%. Some extracted values in Table 3.1 are not fully rational. This is because that the accuracy of datum extraction would be strongly affected by the measurement of *B*. In some cases, peak overlapping would lead to measurement uncertainty. Figure 3.16 shows the average data on the nanocrystalline phase size estimated by Eqn. (3.2) as a function of F&R cycle for various binary, ternary and pentanary Zr-X based alloys.

The volume fraction of the amorphous phase present in various specimens can also be estimated by the relative weighting of the XRD diffuse hump. The amorphous volume fraction was found to increase with increasing ARB cycles. Table 3.2 summaries the estimated values of amorphous volume fraction, and Fig. 3.17 shows the increasing trend as a function of F&R cycle for various binary, ternary and pentanary Zr-X based alloys, based on the XRD patterns.

3.5 SEM observations

Figures 3.18 to 3.21 present the BEI side view of some typical ARB binary samples. In Fig. 3.18 for the $Zr_{50}Al_{50}$ alloy, the initial hardness values of Zr and Al vary significantly (Table 2.1); thus the softer Al carried most of the deformation. After 40 and 80 F&R cycles (Figs. 3.18 (a) and (b)), Al has been appreciably thinned, leaving the much thicker and harder Zr layers or broken pieces (the lighter phase). The initial mutual foil hardness becomes critical since the foils need to effectively deform each other to render thinning and mixing.

Figure 3.19 is the SEM-BEI side view for the $Zr_{50}Cu_{50}$ alloy. The contrast of different element under SEM/BEI observation is unclear in this alloy. This is because the initial thickness of Cu foil is only 30 μm and it can be thinned very quickly at the beginning of ARB. Therefore, the obvious layer structure of Cu is no longer reflected by BEI after 40 F&R cycles. But the Cu indeed existed in the $Zr_{50}Cu_{50}$ alloy and it can be proved by the EDS analysis in next section.

This point can be proved by the observation of SEM-BEI side views for $Zr_{50}Ni_{50}$ and $Zr_{50}Ti_{50}$ alloys, shown in Figs. 3.20 and 3.21. After 40 and 80 F&R cycles (such as Figs. 3.20 (a) and (b)), the foil thinning and mutual mixing appeared to be much more effective in the Zr-Ni and Zr-Ti systems with compatible initial hardness readings (Zr: 174, Ni: 163 and Ti: 183) and hence more severe mutual shear strain. The foils of $Zr_{50}Ti_{50}$ alloy can be thinned to submicrometer levels after 40 cycles. Based on above studies, incompatible hardness of different elemental foils would raise more difficulties to complete mixing. The foil thinning and amorphization efficiency of $Zr_{50}Al_{50}$ alloy appears to be less than $Z_{50}Ni_{50}$ and $Zr_{50}Ti_{50}$ one.

Figures 3.22 and 3.23 reveal the BEI side view of the $Zr_{25}Ti_{75}$ and $Zr_{75}Ti_{25}$ alloys. The foil thinning efficiency for these two alloys is somewhat less than $Zr_{50}Ti_{50}$ alloy, especially at the early stage of ARB. However, a uniform mixed structure of both alloys can finally observed after over 80 F&R cycles. The effect of composition proportion discrepancy for the foil thinning efficiency of the Zr-Ti alloys is noticeable.

Comparing the SEM-BEI side view of some typical ARB samples, including the above mentioned binary alloys, ternary $Z_{34}Ti_{33}Cu_{33}$ (Fig. 3.24) and $Z_{34}Ti_{33}Ni_{33}$ (Fig. 3.25), and pentanary $Zr_{20}Ti_{20}Ni_{20}Cu_{20}Al_{20}$ (Fig. 3.26) and $Zr_{52}Ti_{5}Ni_{15}Cu_{18}Al_{10}$ (Fig. 3.27) systems, it can be seen that the vitrification process is most effective in the Zr-Ti alloy systems. It appears that an efficient ARB process needs to effectively accumulate the rolling shear strain for all involved elemental foils. Since there is no external hard ball to bombard the elemental materials, as in the case of MA, the shear strain experienced by one elemental foil results from the mutual squeezing of other neighboring foils. The initial hardness of the elemental foils appeared to seriously affect the efficiency of grain size refinement and vitrification.

With the third elemental foil added in the ARB process, the efficiency of foil thinning and mixing depends on the relative hardness of each foil. The resulting $Zr_{34}Ti_{33}Cu_{33}$ specimens are presented in Figs. 3.24. The softest Cu foil would always be preferentially sheared and torn by the two other harder ones, and the two harder Zr and Ti foils would deform each other strongly after that. It means that the Cu foils to be fractured into pieces first and then the Zr and Ti foils become intact and deform each other. On the other hand, the efficiency of foil thinning shown in Fig. 3.25 for $Z_{34}Ti_{33}Ni_{33}$ with more compatible hardness of different elemental foils is obvious much better than that in Figure 3.24. The nanocrystallization and amorphization processes for $Zr_{34}Ti_{33}Ni_{33}$ appear to proceed more slowly than those for $Zr_{50}Ti_{50}$, but more rapidly than those for $Zr_{50}Ni_{50}$.

The worst situation is the pentanary $Zr_{20}Ti_{20}Ni_{20}Cu_{20}Al_{20}$ alloys with the even softer Al ($H_v \sim 22$), as shown in Figs. 3.26. The Zr layers remained to be 10-20 μm even after 80 cycles. Nevertheless, the pentanary $Zr_{52}Ti_5Ni_{15}Cu_{18}Al_{10}$ alloy behaved better, as shown in Figs. 3.27, since the abundant Zr layers themselves would shear and deform each other. Thus the initial thinning proceeds rapidly, but the later nanocrystallization and amorphization speeds slow down, as evident from Table 3.3.

Table 3.3 compares the resulting Zr foil thickness reduction with increasing cycles for the alloys studied. For the Zr-Ti system, the foils can be thinned to submicron levels after 40 cycles. For ternary and pentanary, a higher proportion of Zr and Ti (such as $Zr_{34}Ti_{33}Ni_{33}$) brought about great efficiency of foil thinning.

3.6 EDS analyses

Figure 3.28 shows the typical SEM/EDS measurement across an inter-layer boundary, showing the elemental interdiffusion at room temperature enhanced by the repeatedly heavy deformation. The EDS result for the $Zr_{50}Al_{50}$ alloy shown in Fig. 3.28(a) reveals a pronounced diffusion. However, due to the thicker Zr layer left, complete mixing was not achieved. For the $Zr_{50}Ni_{50}$ alloy, shown in Fig. 3.28(b), a homogeneous mixing state can be reached after 100 F&R cycles. However, the beam diameter of SEM/EDS is 0.1 μm and it caused the unidentified cross sectional microstructure of the $Zr_{50}Ti_{50}$ alloy subjected to 80 F&R cycles. Therefore, the EDS line scan result for the $Zr_{50}Ti_{50}$ alloy after 80 F&R cycles is meaningless. Hence, the line scan measurement for $Zr_{50}Ti_{50}$ was replaced by the multi-points

EDS analyses. The result also reveals that a homogeneous mixing state of $Zr_{50}Ti_{50}$ alloy can be reached after 80 F&R cycles. Other SEM-EDS results for the $Zr_{50}Cu_{50}$ and $Zr_{34}Ti_{33}Cu_{33}$ alloys are presented in Fig. 3.29. However, it should be noted that the SEM/EDS spatial resolution is limited, especially including the beam broadening effect [80]. The actual elemental mixing needs to be revealed by the TEM. Table 3.4 and Figure 3.30 reveal the SEM multi-points EDS analyses for the $Zr_{52}Ti_5Ni_{15}Cu_{18}Al_{10}$ alloy after different F&R cycles. In Fig. 3.30, the composition variation or the standard deviation (that represents the mixing degree) decreased with increasing roll bonding cycles.

3.7 Microhardness test

The sample hardness was measured by using the SHIMADZU HMV-2000 microhardness tester. Ten positions were chosen randomly for each sample and the average values were recorded. The applied load is 1000 g and holding time is 10 seconds. The maximum and minimum values were excluded and the remaining five values were averaged.

Microhardness results of the binary, ternary and pentanery Zr-X alloy systems are shown in Figure 3.31. Hardness of ARB specimen increases with increasing roll bonding cycles because of the extensive accumulated strain. Based on our pervious observation in binary alloy systems, the initial hardness of the elemental foils appeared to seriously affect the efficiency of grain size refinement and vitrification. The foils thinning and mixing situations of the alloys with comparable hardness were seen to be much better. The similar effect was also seen in the ternary or pentanary alloys. Throughout the study, it is consistently found that elemental foils with compatible initial hardness would be nanocrystallized or vitrified in a more effective way.

Figure 3.32 is the hardness variation of Zr-Ni [81] and Zr-Ti alloy systems with different composition combinations after 80 F&R cycles. The H_v hardness can be raised from the initial ~170 to nearly 450, an increment factor of ~2.5 due to mainly grain size refinement via the ARB process. But the composition dependence of hardness was not pronounced. Similar results were also found in other Zr-X alloys [81,82].

3.8 TEM results

The X-ray results are all referred to the averaging measurements for the bulk volume. Local variations of the nanocrystalline and amorphous phases in terms of the nanocrystalline phase size, spatial distribution of the nanocrystalline and amorphous regions cannot be traced. TEM observations provide the direct information on the spatial distribution. With increasing F&R cycles to over 40, the grain size was seen to decrease rapidly to the nano regime, and an apparent amorphous phase can also be traced by the TEM diffraction patterns.

The representative TEM micrographs and associated diffraction patterns for the $Zr_{50}Cu_{50}$ alloy after 80 F&R cycles are shown in Fig. 3.33. With the F&R cycles up to 80, the average size of the nanocrystalline phase is ~10 nm, and the amorphous volume fraction is estimated to be around 50%. The results are in fair agreement with the pervious XRD estimation.

According to the results in pervious sections, the nanocrystallization and amorphization seems to proceed most efficiently for the Zr-Ti system with compatible hardness readings for Zr and Ti. Therefore, systematic TEM studies on the $Zr_{50}Ti_{50}$ alloy after various ARB cycles are made and the results are shown in Figs. 3.34-3.37.

Figure 3.34 presents the TEM micrographs of the $Zr_{50}Ti_{50}$ alloy after 40 cycles. The Zr and Ti elemental grains have been effectively refined to 20-100 nm, with an average phase size of 50 nm. This average size is larger than that estimated by XRD using Eqn. (3.2) (12.6nm, Table 3.1). The reflection spots in the associated diffraction patterns, after one-to-one indexing, are all referred to hexagonal pure Zr or Ti. There are very limited amounts of the amorphous phase (less than 20% in volume fraction), as judged from the bright and dark field images as well as diffraction patterns. Meanwhile, the TEM dark field image reveals apparent dislocation activity in the nanocrystalline grains larger than 20 nm (Fig. 3.35); and hardly any defect contrast can be seen in the Zr or Ti nanocrystalline phase smaller than 15 nm. There is no intermetallic compound induced in any of the Zr-X systems, dislike the MA case with appreciable adiabatic heating [83].

With the F&R cycles increased to 60 for the $Zr_{50}Ti_{50}$ alloy, the phase sizes are suddenly refined to around 10 nm, varying from 5-20 nm, as shown in Fig. 3.36 (a). The background in Fig. 3.36 (a) shows the presence of limited amorphous phases. The diffraction spots and rings in the inserted diffraction pattern are still originated from pure Zr and Ti, meaning that the nanocrystalline phases are those unmixed hard particles left from the previous severe deformation and diffusion processes. Appreciable amounts of the amorphous regions are found (~40% in volume fraction), as illustrated in Fig. 3.36 (c).

After F&R cycles of 80 for the $Zr_{50}Ti_{50}$ alloy, most regions are either complete vitrified or contain a few fine nanocrystalline phases around 3-5 nm in size in the amorphous matrix, as shown in Fig. 3.37. The estimated amorphous volume fraction is around 80%. The residual nanocrystalline size in $Zr_{50}Cu_{50}$ alloy after 80 ARB cycles is larger than that of $Zr_{50}Ti_{50}$ alloy, and the observed amorphous volume fraction for $Zr_{50}Cu_{50}$ alloy is smaller than the one for $Zr_{50}Ti_{50}$ alloy. It means that the $Zr_{50}Cu_{50}$ alloy with distinct initial hardness values reveal the similar nanocrystallization or amorphization trend, but the evolution pace is somehow slower. After further rolling to 83 cycles, nearly complete vitrification was observed in the $Zr_{50}Ti_{50}$ specimen.

Meanwhile, the diffuse intensity halo in the diffraction pattern of Fig. 3.37(f) is seen to extend from the beam center outward to g-vector~0.48 $Å^{-1}$ (or d~2.1 Å), which is the resolution limit of the TEM. And the other continuous broad peak located at g~0.348 $Å^{-1}$ (or d~2.87 Å, similar to the XRD results). These may correspond to the range for the first and second nearest neighbor distances of the $Zr_{50}Ti_{50}$ amorphous phase. The evolution trend of the nanocrystalline phase size and amorphous volume fraction as a function of F&R cycle based on TEM characterizations is presented in Table 3.5 and Fig. 3.38 to 3.39. The data in Fig. 3.38 to 3.39 are slightly different from those in Figs. 3.16 to 3.17 obtained from the XRD analyses.

Figures 3.40 and 3.41 reveal TEM observations for $Zr_{25}Ti_{75}$ and $Zr_{75}Ti_{25}$ alloys after 90 F&R cycles. The residual nanocrystalline phases are originated from pure Zr and Ti, and the phase size is in the range of 3-20 nm for both alloys. The observed amorphous volume fraction is around 60%. The resulted grain size refinement and amorphous volume fraction of $Zr_{25}Ti_{75}$ and $Zr_{75}Ti_{25}$ alloys after 90 F&R cycles is similar to that of the $Zr_{50}Ti_{50}$ alloy after 60 F&R cycles. It implied that the composition discrepancy also affects the amorphization efficiency of an alloy with comparable initial hardness.

As for the ternary $Zr_{34}Ti_{33}Cu_{33}$ and $Zr_{34}Ti_{33}Ni_{33}$ alloys, the spatial distribution of the nanocrystalline and amorphous phases was seen to be more scattered. Figure 3.42 shows the apparent different microstructures in $Zr_{34}Ti_{33}Cu_{33}$ alloy after an even higher F&R cycle of 100, one with nanocrystalline grains of ~20 nm and minimum amorphous phases (Fig. 3.42(a)), and the other with finer nanocrystalline grains of ~5 nm in the amorphous matrix (Fig. 3.42(c)). In some other large region, complete amorphous phase is observed, as presented in Fig. 3.42(e). The nanocrystallization evolution trend of this alloy is also compared in Fig. 3.38. Besides, the TEM bright field images and their associated diffraction patterns for the $Zr_{34}Ti_{33}Ni_{33}$ alloy after 100 F&R cycles were shown in Figure 3.43. The nanocrystalline grains are in the range of 10 nm to 3 nm. The grain size variation of the $Zr_{34}Ti_{33}Ni_{33}$ specimen after 100 F&R cycles is less than that of $Zr_{34}Ti_{33}Cu_{33}$. The higher degree of structure in-homogeneity in this $Zr_{34}Ti_{33}Ni_{33}$ alloy is a result of compatible hardness of Ni with respect to Zr and Ti.

The pentanary alloys show even more sluggish and more inhomogeneous structure evolution at later stages. Figure 3.44 is an example for the $Zr_{52}Ti_5Ni_{15}Cu_{18}Al_{10}$ alloy after 100 F&R cycles, showing the still rather large nanocrystalline phase of pure Zr measuring ~60-100 nm in Fig. 3.44(a), fine nanocrystalline phases ~5 nm in size within the amorphous matrix in Fig. 3.44(c), and finally a complete vitrified region in Fig. 3.44(e). The occasionally large nanocrystalline phases greater than 50 nm in size were not observed in the binary and ternary alloys after 100 F&R cycles. The evolution trend of the pentanary alloys is also included in Fig. 3.38.

The transformation from the nanocrystalline to amorphous state is also of concern. The smallest grain size observed in the TEM bright or dark field image, as well as the estimated grain size based on the Scherrer equation for XRD broadening peaks, is around 3 nm. Figures 3.45 to 3.46 show the interface region between the nanocrystalline and amorphous phases. The TEM/EDS measurements of nanocrystalline and amorphous phases for the $Zr_{50}Ti_{50}$ alloy after 60 F&R cycles and the $Zr_{25}Ti_{75}$ alloy after 90 F&R cycles reveal in Figs. 3.47 and 3.48, respectively. In both figures, the compositions of nanocrystalline and amorphous phases are nearly the same.

In summary of the TEM observations, the spatial distribution of the nanocrystalline and amorphous phases is usually inhomogeneous. The extracted nanocrystalline phase size or amorphous volume fraction based on the peak broadening is only an average datum. TEM bright or dark field images reveal apparent difference in local regions. The inhomogeneous distribution of the nanocrystalline and amorphous phases differs in nature from the finding of homogeneously crystallized nanocrystalline phases in a complete amorphous alloy during well controlled annealing [84]. In the latter case, the nanocrystalline phase is in similar size and is uniformly dispersed within the amorphous matrix. The inhomogeneous microstructure of the current ARB materials would affect their mechanical or functional properties.

3.9 Thermal analyses

The DSC measurement on the ARB amorphous $Zr_{50}Ti_{50}$ alloys was shown in Fig. 3.49. This figure indicated a glass transition T_g temperature of ~390°C and the temperature interval of a supercooled liquid region ΔT_x ~60°C; both are in the similar range as those obtained in amorphous Zr alloys prepared by other routes [44]. The thermal stability properties of the ARB specimens, compared with those processed by other means, will be presented in section 4.5.

3.10 Analyses on the specimens prepared by arc melting and melt spinning

The arc melting method is a very convenient way to synthesize alloys. The original intention of adopting this method is to synthesize a well known Zr based amorphous alloy with large supercooled liquid region firstly, and then to compare the alloy characteristics with those exhibited from the ARB specimens. Figure 3.50 shows two XRD patterns of the arc melted and $Zr_{52}Ti_5Ni_{15}Cu_{18}Al_{10}$ sample, and a density ~6.8 g/cm^3. The size of wedge-shaped specimen made by drop casting route is shown in Fig. 3.51. The scanned position of arc melted sample is the bottom surface which contacts the Cu mold. The XRD peak intensities and shapes for the scanned surface with or without grinding are very different. This is because that the bottom surface is the place of a highest cooling rate but also the place with a highest possibility of heterogeneous nucleation and inhomogeneous composition. After grinding and polishing the bottom surface, the exposed region exhibit much broadened and shortened XRD peaks. There is no vitrification tendency appeared in this pattern. Hence, the subsequent melt spinning process was followed and a ribbon specimen was gathered. Figure 3.52 is the XRD pattern of the $Zr_{52}Ti_5Ni_{15}Cu_{18}Al_{10}$ ribbon specimen. Much more obvious broadening hump can be observed now. By the same way, it was also tried to synthesize the amorphous ribbons for the $Zr_{50}Ti_{50}$ and $Zr_{20}Ti_{20}Ni_{20}Cu_{20}Al_{20}$ alloy systems via melt spinning. But the ingredients of Ti in these systems are too high (50 and 20 at%) to proceed the melt spinning process due to the viscosity and oxidization effects induced by Ti. Only the $Zr_{52}Ti_5Ni_{15}Cu_{18}Al_{10}$ alloy was successfully produced.

Figure 3.53 shows the SEI of arc melted $Zr_{52}Ti_5Ni_{15}Cu_{18}Al_{10}$ sample. There appeared some large regions, similar to grains, measuring from 5 to 10 μm. Such large region size may not be the grain size since the actual grain size seems to be in the nano scale based on the XRD peak broadening effect. The region boundaries might be related to the solute inhomogeneity. In Fig. 3.53(b), there are some small cracks inside the grains, presumably due to the thermal stress induced during rapid solification. In addition, there are also some layer-like structures which might be a result of inhomogeneous mixing of the multiple elements.

Table 3.5 presents microhardness data on the pentanery Zr-X alloy systems made by arc melting, drop casting and melt spinning process. The hardness H_v value of arc melted $Zr_{20}Ti_{20}Ni_{20}Cu_{20}Al_{20}$ alloy is near ~ 800. This value is higher than that of ARB samples (H_v ~ 300-400) made only by the pure elements, because the arc melted alloy contains both multiple pure elements and some intermetallic compounds. The hardness of $Zr_{52}Ti_5Ni_{15}Cu_{18}Al_{10}$ samples made by arc melting and melt spinning methods also revealed in Table 3.5. The H_v hardness of nearly completely vitrified $Zr_{52}Ti_5Ni_{15}Cu_{18}Al_{10}$ sample made by the melt spinning method is~ 750. This value is comparable with that of vitrified ZrAlCuNiB alloy (H_v ~ 720) made by the team members of Prof. Jang's laboratory in ISU

[85].

The TEM micrographs and associated diffraction patterns for the melt spun $Zr_{52}Ti_5Ni_{15}Cu_{18}Al_{10}$ alloy are shown in Fig. 3.54. Most of the observed regions are constituted by amorphous phase (~90% in volume fraction). But there are still some residual nanocrystalline phases, and the phase sizes varied from 3-15 nm. The diffraction spots and rings in the inserted diffraction pattern are not originated from pure Zr and Ti anymore. Meanwhile, the TEM dark field image of the interface region between the nanocrystalline and amorphous phases of the melt spun $Zr_{52}Ti_5Ni_{15}Cu_{18}Al_{10}$ alloy was shown in Fig. 3.55. Unlike the grain size evolution revealed in Fig. 3.45 or Fig. 3.46, large and small nanocrystalline phases of the melt spun $Zr_{52}Ti_5Ni_{15}Cu_{18}Al_{10}$ alloy randomly dispersed in the amorphous matrix. The result of DSC measurement for the melt spun $Zr_{52}Ti_5Ni_{15}Cu_{18}Al_{10}$ alloy is shown in Fig. 3.56. The glass transition temperature T_g is not very clearly, but it still can be roughly extracted from the DSC curve. The glass transition temperature of this melt spun $Zr_{52}Ti_5Ni_{15}Cu_{18}Al_{10}$ alloy is ~430^oC and the temperature interval of a supercooled liquid region ΔT_x is ~60^oC. This value is quite consistent with those obtained in various amorphous Zr alloys made by the other method [52].

Ⅳ. Discussions

4.1 Evolution of nanocrystallization and amorphization in ARB specimen

4.1.1 Strain accumulation

The thickness reduction of specimen is set to be 50% per F&R cycle and the residual strain could be accumulated continuously. Therefore considering the von Mises yielding criterion and plain strain condition [57] (as introduced in Sec. 1.6), the thickness and true strain after n cycles can be predicted as,

$$t_n = \frac{t_0}{2^n}, \tag{1.3}$$

$$\varepsilon_n = \frac{2}{\sqrt{3}} \ln(t_n / t_0) = \frac{2n}{\sqrt{3}} \ln 2 \approx 0.8n, \tag{1.5}$$

where t_o is the initial thickness of foil. Table 4.1 shows the theoretical thickness and the true strain ε_n of each elemental foil after different F&R cycles. The thickness of Zr or other foils after 40 F&R cycles will be around $1\text{x}10^{-10}$ μm, and the accumulative true strain will be 32. But according to the SEM observation in the previous chapter, the foil thickness instead reaches around 0.5-40 μm (Table 3.3) depending on the hardness of the foil. This is because the large difference in foil hardness readings among the adopted elemental foils, rendering non-uniform deformation of the thin foils. A misaligned factor, k, has been suggested to insert into the thickness estimation expression [86], as

$$t_n = t_0 \left[\frac{(1+k)}{2} \right]^n . \tag{4.1}$$

The factor k is a result from the fact that the softer foils would be preferentially thinned;

leaving the harder foils retained as thicker layers or forced to be fractured into pieces.

Thus the actual accumulated true strain will be

$$\varepsilon_n = \frac{2}{\sqrt{3}}\ln(t_n / t_0) = \frac{2n}{\sqrt{3}}\ln(\frac{1+k}{2}). \tag{4.2}$$

The *k* value can be extracted by fitting the experimentally measured data in Table 3.3. Table 4.2 reveals the estimated *k* values and the accumulated true strain ε_n. The accumulated strain increased with increasing F&R cycles, but the efficiency was not as good as the theoretical value. For example, true strain of ZrTi alloy increased from 5.7 (40x F&R cycles) to 7.7 (80x F&R cycles).

For most cases, the *k* and ε_n values would gradually reach around 0.85 and 7.1 after 80 F&R cycles, instead of the theoretical value of 64 given by Eqn. (1.5). The significant discrepancy between the theoretically predicted and experimentally measured strain values is due to the low efficiency of strain accumulation, particular at the later ARB stage. The stacked foils would sometimes slide with each other or fracture into piece instead of being deformed or sheared. The former processes (sliding or fracture) would not cause effective foil thinning and strain accumulation.

Note that ε_n for $Zr_{50}Al_{50}$ and $Zr_{20}Ti_{20}Ni_{20}Cu_{20}Al_{20}$ is lower than other cases (such as $Zr_{50}Ti_{50}$ and $Zr_{50}Ni_{50}$), reflecting the accumulation of true strain was impeded by the larger hardness difference between Zr and Al or Cu. The actual ε_n level of ~7.2 is compatible to those experienced during MA or equal channel angular pressing (ECAP), but the actual temperatures of the latter two are usually higher due to the appreciable temperature rise. It can be regarded that the current high level of accumulated strain during ARB at room temperature would assist effectively in grain size refinement and alloy vitrification, similar to the recent work of cryogenic MA [86,88]. Figure 4.1 shows the average data on the nanocrystalline phase size of Zr estimated by Eqn. (3.2) as a function of accumulated true stain for various alloys.

4.1.2 Grain size refinement

The import of heavy plastic deformation during synthesized process can effectively refine the grain size of alloy. For example, the grain size of alloys made by ECAP method can be refined to 100-200 nm, with strain in the range of 4-8. Therefore, the grain size refinement of alloy through ARB route was expected.

The ARB method is a room temperature process without any tempering treatment. The repeated cold rolling process leads to a signification thinning of microstructure through the induced high strain. And this process also suppresses the grain recrystallization, due to the fact that a low temperature process can not supply enough activation energy. Hence, this section should be discussed with the accumulated strain in section 4.1.

Both data in Table 3.3 and 4.2 display that the efficiency of foil thinning and strain accumulation of Zr-Ti and ternary alloy systems is better than others. It can be easily understood that the foil thickness reduction was seriously affected by the initial hardness of element, because the strain accumulated by one elemental foil results from the mutual squeezing of other neighboring foils. Therefore, foil thickness reduction in $Zr_{50}Al_{50}$ alloy with lower relative hardness is worse than other alloys. Besides, the high ductility of Al foils would retard the stain accumulation of Zr.

Meanwhile, the alloy systems with more compatible hardness of selected elements can accumulate more strain during the ARB process. The high level of accumulated strain signified that great quantity of defects are induced during ARB. And the formation of subgrains and grains increased with increasing F&R cycles. The initial grain is divided. The grain size evolution of various alloy systems estimated based on XRD results is shown in

Table 3.1. Grain size variation tendency in this Table is similar to the estimated stain accumulation in Table 4.2.

The foil thinning of $Zr_{50}Cu_{50}$ alloy is not shown in Table 3.3, because of the unapparent layer structure in SEM/BEI cross sectional images. However, the grain size variations of $Zr_{50}Cu_{50}$ alloy can still be evaluated by the XRD patterns and are also shown in Table 3.1. It is noted that the compatibility of initial hardness for Zr-Cu is less than Zr-Ni. But the grain refinement of $Zr_{50}Cu_{50}$ is similar to or even better than that of $Zr_{50}Ni_{50}$. The explanation can be traced back to the initial thickness of Cu and Ni. The initial thickness of Ni (91 μm, Table 2.1) is triple of Cu (30 μm, Table 2.1). For that reason, the rate of progress for the elemental mixing in $Zr_{50}Cu_{50}$ alloy is comparable to that in $Zr_{50}Ni_{50}$, although the initial hardness of Cu is less than Ni.

Meanwhile, the XRD peak broadening was not only contributed from the increment of nanocrystalline, but also the existence of microstrain. Consequently, the volume fraction of the diffuse hump in XRD patterns in Table 3.2 can also be used to understand the degree of grain size refinement during ARB process. Table 3.2 reveals that the volume fraction of amorphous phase increases with increasing roll bonding cycles. And for most cases subjected to 80 F&R cycles, the estimated volume fraction exceeded to the value of 50%. This result is not very corresponding with former discussion and may arise from the microstrain during ARB. According to the estimation in section 3.4, the extracted microstrain is in the range of 1% to 5%. The microstrain also varied with roll bonding cycles and composition. Figure 4.2 reveals the microstrain variation for various alloy systems. It seems that the microstrain increased with increasing F&R cycles and the number of adopted elements in an alloy. When the microstrain level is appreciable, the effect of microstrain may not be casually ignored. Take $Zr_{34}Ti_{33}Cu_{33}$ alloy for example, the evaluated volume fraction of the broadening peaks in XRD pattern is rather large and does not agree with the TEM observation in Fig. 3.39. It may caused by the high value of microstain in the XRD pattern of this ternary alloy. Therefore, the estimated amorphous volume fraction of $Zr_{34}Ti_{33}Cu_{33}$ alloy based on XRD pattern (in Table 3.2) may be regarded as an overestimated value. If the effect of microstrain can took off, Table 3.2 may show a trend similar with Table 3.1, and the grain size refinement of an alloy can also be roughly realized through the variation of amorphous volume fraction during ARB.

4.1.3 Diffusion during ARB

Due to the special configuration of ARB, the elemental foils would undergo diffusion under the compression and shear stresses, resulting in physical bonding. Interdiffusion of various atoms becomes progressively effective with increasing cycles, particularly with the abundant lattice defects induced.

Table 4.3 reveals the lattice and grain boundary diffusivity (D_L and δD_B) for various elements. For instance, the lattice and grain boundary diffusivity, D_L and δD_B, for Al at room temperature are 2.18×10^{-29} m^2/s and 9.43×10^{-29} m^3/s, where δ is the grain boundary width. Assuming the processing time for each rolling pass is 2 s and δ is 1 nm, the calculated diffusion distances, X, via lattice diffusion and grain boundary diffusion per cycles are 2.64×10^{-5} nm and 1.74 nm, respectively, based on the relationship $X \approx 4\sqrt{Dt}$ [89]. Similar calculations for other elements were done, as shown in Table 4.4. Such diffusion distance at room temperature seems to be negligible. However, several effects would enhance the interdiffusion.

Firstly, the heavy rolling applied during ARB would cause severe plastic deformation plus pronounced friction (since no lubrication was used in prevention from contamination); both would raise the specimen temperature. A moderate temperature rise of ~25^{o}C from the room temperature of 25^{o}C to ~50^{o}C, as directly measured by inserted thermocouples, was found to be induced as the specimen just passed through the rollers. The temperature increment would directly lead to enhancement in effective diffusion distance, as compared in Table 4.4.

The current rolling strain rate was around 10^{-1} s^{-1}. The temperature increment could be affected by the specimen dimension and rolling speed, as mentioned above. For example, the temperature increase for 1100 Al sheets, measuring 1 mm in thickness, 40 mm in width and 300 mm in length, was reported to be ~167^{o}C at an ARB rolling strain rate of 19 s^{-1} [75]. The lower temperature rise of the current ARB experiment is a result of smaller specimen size and lower rolling speed. Using the thermal trapping models proposed by Grady and Asay [90] or Kato [91], the temperature increment during the current ARB should be at most 30^{o}C, consistent with the direct temperature measurement.

It is conceivable that even a minor temperature rise would also affect the nanocrystallization and amorphization processes via the enhancement in the elemental interdiffusion. Table 4.4 presents the relationship between diffusion distance and temperature increment. The diffusion distance during each F&R cycle at 50^{o}C would increase by one to two orders of magnitude, as compared with that at room temperature or 25^{o}C.

Secondly, with the continuous reduction in foil thickness down to 1 μm or less, as well as grain size down to 30 nm or below, significant increment of interfacial and grain boundary diffusion would occur. As the grain size decreases to 10 nm, the grain boundary region will occupy more than 25% of the specimen volume. Thus the grain boundary diffusion would overwhelm the interdiffusion process. Even the lattice diffusion would also increase several orders of magnitude with the help of deformation induced lattice defects. Estimation of the diffusivity D can be made using the Grube method [92], in which D can be extracted by solving the error function if the composition profile is known. The EDS line scan can provide various composition variation plots as a function spatial position across the elemental foils after 40-80 cycles. One example is shown in Fig. 3.28(a). The diffusivity for Al is thus calculated to be of the order of 10^{-15} m^2/s, significantly higher than the values of D_L and δD_B for Al at 25 or 50°C, consistent with the increment of 7-9 orders of magnitude of Cr diffusion in nanocrystalline Fe [93].

In short summary, the interdiffusion between neighboring elemental foils would be most greatly enhanced by the involvement of interfacial and grain boundary diffusions as the microstructures are refined down to the nanocrystalline regime. Diffusion enhanced by the deformation induced lattice defects would be secondly important. Finally, the minor temperature rise would also raise the diffusion rate by one to two orders of magnitude.

Throughout the study, it is consistent to find that the XRD or TEM diffraction peaks are originated from pure elements. There is no detectable shift of the peak position (or the corresponding d spacing). If there have been pronounced interdiffusions making the nanocrystalline phases to be a solid solution, the d spacing values should be notably altered. It raises the question why the nanocrystalline phases remain to be pure elements, but the amorphous phases are all solid solution with a local composition near bulk average, i.e., $Zr_{50}Ti_{50}$.

It appears that interdiffusion continuously proceeds most effectively in regions near the interfaces between the nanocrystalline and amorphous phases. The outer mantle of the nanocrystalline phase undergoes the effective interdiffusion with the help from the abundant interfacial area and/or the high dislocation density inside the nanocrystalline phase. Once the interdiffusion changes the mantle region of the pure-element phase into a solid solution, the mantle layer becomes amorphous, leaving the core as the elemental phase. This procedure continuously proceeds, resulting in a continuous decreasing the nanocrystalline phase size and the continuous increase in the amorphous volume fraction.

4.2 Evolution of hardness and modulus

4.2.1 Hardness effect

The hardness readings of the ARB specimens follow basically an increasing and then saturated trend with increasing F&R cycles for all alloys examined, but the increment degree differs slightly, as shown in Fig. 4.3. The increment factor of H_v hardness by 2-3 times is mainly due to grain size refinement. At the later ARB stage, the volume fraction of the amorphous phase increases, and the hardness ceases to climb up. Instead, a saturated plateau appears, implying that the amorphous phase might be softer than the nanocrystalline phases. Meanwhile, the composition dependence was not pronounced for Zr-Ti alloys with different composition combinations after 80 F&R cycles, as shown in Fig. 3.32. Similar results were also found in other Zr-X alloys (as in Fig. 4.3(b)).

On the other hand, the incompatible hardness of different elemental foils would raise more difficulties to complete mixing (according to the studies in chapter 3). In order to completely understand the hardness effect for amorphization in the same alloy system with different hardness value, a pre-hardening step was applied for a soft elemental foil before ARB process. In this study, the selected element is Cu. After the pre-hardening step by prior rolling, the hardness of Cu increased from the initial value, H_v ~ 45, to H_v ~131. The thickness also decreased from 102 to 30 μm. Then, two $Zr_{50}Cu_{50}$ alloys with different initial hardness of Cu foils were be synthesized by ARB method. The SEM and XRD results display some clues to the hardness effect on amorphization during ARB.

Figure 4.4 shows the SEM micrographs of the $Zr_{50}Cu_{50}$ alloys with and without the pre-hardening step for the Cu foils. The foils thinning and mixing situations of the alloy with the pre-hardened Cu foils were seen to be much better. Also, the XRD peak broadening was more apparent in the pre-hardening specimens, as compared in Fig. 4.5.

The similar hardness effect was also seen in the ternary or pentanary alloys. Throughout the study, it is consistently found that elemental foils with compatible initial hardness would be nanocrystallized in a more effective way. A pre-hardening step applied before ARB profited the vitrification process.

It has been repeatedly mentioned that the current ARB process operated at near room temperature does not follow the three prerequisites such as large size difference, low eutectic temperature, and negative mixing enthalpy. Therefore, ARB can be applied for alloy systems that do not comply with the above prerequisites. For example, the Zr-Ti system has the small size difference and positive mixing heat, and is among the low glass forming ability alloys. However, the ARB can render the $Zr_{50}Ti_{50}$, $Zr_{25}Ti_{75}$, and $Zr_{75}Ti_{25}$ to fully or nearly fully amorphous state.

The simple criterion for ARB is to possess the compatible initial hardness among the elemental foils. If one or more of the elemental foils are much softer than the rest, then the prehardening step is inevitable. This is the case of the current Zr-Cu system. The initial hardness of the Cu foils is only 45. After sufficient prehardening, the foil hardness becomes 131. Nevertheless, such hardening may not be applicable for all systems. For instance, the Al foils also have the low hardness of 22, but severe prehardening can only raise the hardness to around 80. The much lower recovery and recrystalization temperatures for severe deformed pure Al foils would stimulate static or dynamic annealing even at room temperature (25^{o}C) or 50^{o}C. Thus the hardness would not continuously increase to a level close to Zr (or Ti, Ni, or Cu), i.e., H_v~ 130-180. It follows that room temperature ARB still encounters the difficulty in synthesizing nanocrystalline or amorphous alloys with one or two elements which are particularly soft in nature.

4.2.2 Hall-Petch plot of vitrified $Zr_{50}Ti_{50}$ alloy

According to the microhardness measurement data in Fig 3.31, the Hall-Petch relationship for the hardness and grain size of $Zr_{50}Al_{50}$, $Zr_{50}Ni_{50}$ and $Zr_{50}Ti_{50}$ alloys is plot in Fig.4.6. Figure 4.7 is the Hall-Petch plot for $Zr_{50}Cu_{50}$ and $Zr_{34}Ti_{33}Cu_{33}$ alloys. The hardness of alloy increased with decreasing grain size at the early stage. But the hardness of the $Zr_{50}Ti_{50}$ alloy decreased as the grain size fell below 20 nm. The phenomenon of Hall-Petch breakdown was observed in $Zr_{50}Ti_{50}$ alloys. In the previous studies of metallic TiNi multilayers by cold rolling process [94], the similar result was reported. The hardness decreased presumably due to the formation of amorphous bands or the activation of grain boundary mutual sliding in these extra-fine nano-scaled materials. Moreover, a similar phenomenon was also observed in nanocrystalline nickel prepared by Schuh et al. [95]. Meanwhile, it is worthy to mention that the critical grain size responsible to the occurrence of inverse Hall-Petch plot is also varied with alloy composition.

4.2.3 Modulus evolution

By varying the applied load of the microhardness indenter within the elastic regime and measuring the indention area, the variation of the elastic modulus of the ARB alloys as a function of F&R cycle can be established, using the relationship [96,97],

$$E = \frac{dP}{dh}\frac{1}{2}\sqrt{\frac{\pi}{A}}, \tag{4.3}$$

where P is the applied load, h is the indention depth (or the displacement), A is expressed by

$$A = 24.5{h_p}^2, \tag{4.4}$$

where h_p is the permanent depth of penetration after the indenter is fully unloaded. It has been proposed that h_p can be given by

$$h_p = h_m - \left[\frac{2(\pi - 2)}{\pi}\right]\frac{P_t}{dP/dh}, \tag{4.5}$$

where h_m is the maximum displacement during loading. Figure 4.8(a) shows the elastic modulus data on the $Zr_{50}Ti_{50}$ alloy subject to different F&R cycles. The directly extracted elastic modulus of $Zr_{50}Ti_{50}$ subject to 40 F&R cycles is around 30 GPa, and this value is not rational for such an alloy. The underestimation of elastic modulus may be caused by the unsuitable usage of above mentioned equations. The adopted equations in this paragraph usually applied to the measurement of nanoindentation, but the hardness testing in this study was conducted using the microhardness indenter. The scale of measurement for the nanoindentation and microhardness indenter is very different. The applied 50mg load might lead to extra indentation displacement in the elastic regimes, causing the much lower E. Therefore, a calibration coefficient should be induced to Eqn. (4.3), to approach a more reasonable elastic modulus in this study. Take an AZ31 magnesium alloy (without any annealing treatment) to execute a similar microhardness testing, and the directly extracted elastic modulus based on Eqn. (4.3) is about 7 GPa. But according to the study by Inoue [21], the elastic modulus for Mg alloy is about 45 GPa. The discrepancy factor of the actual and extracted elastic modulus for Mg is ~ 6.4. Hence, a calibration coefficient of 6.4 is introduced to Eqn. (4.3) and the calibrated elastic modulus for the $Zr_{50}Ti_{50}$ alloy is also shown in Fig. 4.8(a).

Figure 4.8(b) reveals the representative calibrated elastic modulus data for Zr-Ti alloys subjected to various F&R cycles. The elastic modulus increases from the initial values for the pure elements (Zr: 82 and Ti: 110) to near ~ 200 GPa after 40 F&R cycles, and then declines as the amorphous phase gradually evolves. It is apparent that the modulus of the fully amorphous phase is again lower than the alloys containing predominantly the nanocrystalline phases. This is presumably due to the free volume present in the amorphous phase. An alloy with the nanocrystalline phases uniformly dispersed in the amorphous matrix would exhibit the highest hardness and modulus. This has also been reported that the hardness would increase in the partially recrystallized bulk amorphous Zr based alloy fabricated via the drop casting route [73,98]. Both the H_v hardness and calibrated elastic modulus data on the current ARB Zr-X alloys are in agreement with the bulk amorphous Zr based alloys fabricated via the drop casting route.

4.3 Composition effect

4.3.1 Zr-Ti alloy systems (1:3/1:1/3:1)

Series studies for the Zr-Ti alloy systems with different composition, namely $Zr_{25}Ti_{75}$, $Zr_{50}Ti_{50}$ and $Zr_{75}Ti_{25}$, were made and the results are shown in pervious chapters. Combining the XRD, SEM and TEM results for these three Zr-Ti alloys, it was found that the compatible initial hardness of foils is not the only factor for effective vitrificaiton during ARB. A diffuse hump appeared in the XRD pattern for $Zr_{25}Ti_{75}$ alloy, but some sharp peaks contributed from pure Zr and Ti still remained even after 90 times of roll bonding cycles. In comparison, all the residual sharp peaks in the XRD pattern of $Zr_{75}Ti_{25}$ alloy are originated from pure Zr only. Foil thinning situation for these three alloys also reveals that the thickness reduction is most effective in $Zr_{50}Ti_{50}$. Hence, it can be inferred that the elemental foils, with compatible hardness and composition proportion at the same time, is most effective for amorphization. This viewpoint can be explained as followed. For the vitrification of an alloy made by ARB method, the homogeneous mixing of selected elements should achieve and then the interdiffusion of various atoms could proceed with further rolling cycles. And the mixing of elemental foils was made by the applied plastic deformation through repeated roll bonding process. Therefore the stacking of elemental foils would also affect the mixing to some degrees. As the two element composition proportion is distinct, such as $Zr_{25}Ti_{75}$, the stacking of elemental foils would not be as uniform. Parts of region in this alloy are stacked with the same elemental foils. In these regions, the strain accumulation of one elemental foil resulted from the mutual squeezing of the neighboring foils with the same composition and the foil thinning still proceeded smoothly due to the very high hardness of Zr or Ti. But the minor elemental foils can not readily disperse in the major elemental layers evenly. Therefore, the diversity of the used quantity of elements will increase the difficulty of homogeneous mixing. The amorphization process for $Zr_{25}Ti_{75}$ and $Zr_{75}Ti_{25}$ alloys could still proceed by increasing roll bonding cycles, although the efficiency was retarded by the proportion discrepancy.

4.3.2 Ternary alloy systems

In order to realize the effect of the third added element for the amorphization in Zr-Ti alloys, two elements were added. According to the vitrification experiences gained from the binary Zr-Ti alloys, two ternary alloy systems with equal compositions, $Zr_{34}Ti_{33}Cu_{33}$ and $Zr_{34}Ti_{33}Ni_{33}$, were synthesized by ARB. The difference between Cu and Ni is the initial hardness (Cu~ H_v=131 and Ni~ H_v =163, Table 2.1). The XRD pattern for $Zr_{34}Ti_{33}Cu_{33}$ alloy reveals that the Cu peaks disappeared after 100 times of roll bonding cycles and all of the residual peaks were contributed by pure Zr and Ti. The SEM cross-sectional observation for $Zr_{34}Ti_{33}Cu_{33}$ alloy reveals that the thicker layer structure left after 80 times of roll bonding cycles belongs to the harder phase of Zr and/or Ti. Both results referred that the accumulated strain during ARB was used to refine the grain size of softer phase, Cu, in advance. The refined Cu foils became surrounded the Zr and Ti layers and hindered the inter-shearing and inter-cutting between the Zr and Ti layers during ARB.

On the other hand, the XRD pattern for $Zr_{34}Ti_{33}Ni_{33}$ alloy shows that the peak intensity of the added third element Ni did not decrease with increasing roll bonding cycle, especially for the Ni (111) plane. But the SEM side view observation for $Zr_{34}Ti_{33}Ni_{33}$ alloy reveals an effective foil thinning situation with the increasing of roll bonding cycles. It implied that the three adopted elements in $Zr_{34}Ti_{33}Ni_{33}$ alloy can be well mixed by the effect of compatible initial hardness (compared with the other ternary alloy in this study). Nevertheless, the texture of Ni (111) plane is the advantageous orientation for the rolling direction and can not be destroyed through repeated roll bonding process. Hence, the addition of Ni in Zr-Ti did not seem to be benefited for the amorphization process.

4.4 Nanocrystallization and amorphization mechanism

4.4.1 TEM evolution of $Zr_{50}Ti_{50}$ after various ARB cycles

Serial TEM studies of $Zr_{50}Ti_{50}$ subjected to 40, 60, 80 and 83 F&R cycles are conducted in order to conceive the nanocrystallization and amorphization process during ARB and the results are shown in Figs. 3.34-3.37.

With increasing F&R to over 20 cycles, the grain size was seen to rapidly decrease to nano regime, and an apparent amorphous phase can be traced by the XRD and TEM diffraction. Figure 4.9 combines the extracted grain size variation and amorphous volume fraction for the $Zr_{50}Ti_{50}$ alloy, based on XRD estimation and TEM observation. The evolution trend of the nanocrystalline phase size and amorphous volume fraction based on TEM is roughly consistent with the estimation according to XRD pattern. But the extracted Zr grain size value from XRD for the 40-cycles specimen with the accumulated true strain ~ 5.7, is quite different from that obtained from the TEM observation. Hence, the procedure of double check for the vitrification evolution by TEM observation is very important. The result in Fig 4.9(a) inferred that the estimation of nanocrystalline phase size based on XRD pattern may affected by the induced strain at the early stage of ARB. It can be confirmed by the TEM dark field image in Fig. 3.35(a). The image in this figure reveals a residual large grain with dimension near 100 nm, filled up with dislocation and strain field. Meanwhile, the accumulated true strain (based on Eqn. (4.4)) of $Zr_{50}Ti_{50}$ alloy subjected to 40 F&R cycles is 5.7 (Table 4.2(a)) and this value is comparable with that experienced during ECAP. From the viewpoint of strain accumulation, it was concluded that the grain size can be refined to less than 200 nm after 40 F&R cycles, and the effect of grain size refinement of an alloy subjected to 40 F&R cycles is similar to or even better than that via ECAP.

The gain size decreased step by step through the induced dislocation during repeated roll bonding process. The partial amorphous phase always appeared near the region with grain size less than 3 nm. Figure 3.45 (a) shows the TEM bright field images of the region possessed nanocrystalline and amorphous phases at the same time. Some nanocrystalline phase with size near 3 nm dispersed in the amorphous phase region. The composition of observed nanocrystalline phases in the TEM images were identified through the carefully indexing of diffraction pattern and double checked by the EDS system attached to TEM. The results of diffraction pattern index reveal that the residual grains are pure Zr or Ti and no intermetallic compound was found due to the fact that the ARB is a process operated at low temperature. Meanwhile, the composition of amorphous phase identified by TEM/EDS system was a fully mixed phase (50 at% of Zr and 50 at% of Ti). A similar identified result also gathered in the nanocrystalline phase. But the EDS result in the nanocrystalline phase represents only the average composition of the observed region, and this region may contain the nanocrystalline Zr and nanocrystalline Ti phases dispersed in the amorphous matrix phase. The nanocrystalline grain with size less than 5 nm can not individually identified by the TEM/EDS system due to the restriction of beam size. However, the results of diffraction pattern indexing reveal that the observed nanocrystalline phase was still constituted by pure elements. Therefore, it can be reasoned that the grain size refinement might increase the

Gibbs free energy of nanocrystalline phase. As the energy of nanocrystalline phase exceeded that of amorphous phase, the nanocrystalline was replaced by the amorphous phase. Then the atoms of refined grain mixed with the surrounded heterogeneous atoms, and an atomic configuration of new amorphous structure with a high dense but irregular packing appeared. Therefore, a completely vitrification of $Zr_{50}Ti_{50}$ alloy after 80 F&R cycles can be speedily achieved via the further addition of a few ARB cycles, because only a few fine nanocrystalline phases around 3-5 nm remained in the alloys after 80 F&R cycles.

The gradual refinement of microstructure with increasing F&R cycles is evident. It is interesting to figure out the evolution sequences and the major mechanisms. Based on the previous experiences on the severe deformation in pure metals or alloys, it is conceivable that the near 80-100 μm grain size in the initial pure element foils would undergo dislocation accumulations, dislocation cell arrangement, and (sub)grain formation, making the structure more and more refined and partitioned. The grain size would be around 0.1-0.5 μm (100-500 nm), similar to the deformation processes such as equal channel angular pressing or cyclic extrusion. The proposed refinement mechanism evolution depicted in Fig. 4.10. With increasing F&R cycles to over 40, and thus true strain above 4.0, the subsequent deformation trends to undertake through microband and shear band propagation across the matrix. This would result in rapid subdivision of the microstructure into a checkerboard form with a grain (or phase) size down to around 50 nm.

As the substructure is refined to 50 nm, the interfacial interdiffusion becomes highly effective. The amorphization process starts to occur when two or more pure elements are mixed together, forming numerous nanocrystalline phases dispersed in an amorphous matrix. The amorphous volume fraction at this stage is only about 10-20%. Subsequent interdiffusion continuously proceeded at the interfacial and mantle regions between the nanocrystalline phase and amorphous matrix. With more mantle regions become solid solution and amorphous, the core size in shrunk toward a size near 3-10 nm (Fig. 3.45), and the nanocrystalline phase is refined to a critical size around 3 nm, sudden transformation into amorphous occurs, as further ed in Sec. 4.4.3.

4.4.2 Atomic spacing of nearest neighbors

All of the diffraction maxima or rings in the XRD and TEM diffraction patterns for those nanocrystalline phases are originated from pure elements such as Zr or Ti, meaning that the nanocrystalline phases are those unmixed hard particles left from the previous severe deformation and diffusion processes. Atomic diffusion or mixing near the interface between the nanocrystalline and amorphous phases has not rendered these nanocrystalline core phases into an alloy or compound with the composition of, for example, $Zr_{50}Ti_{50}$. On the other hand, the amorphous region was found to be a fully mixed phase, as evident from the TEM/EDS measurement from the amorphous matrix. Once the interdiffusion is completed near the interface, the mantle region becomes amorphous, and the nanocrystalline phase becomes smaller, leaving the core part as elemental phases. With progressing F&R cycles and interdiffusion, the nanocrystalline phases are refined accordingly. The intensity distributions of the maxima and minima of the halo in the TEM diffraction patterns are carefully extracted from the (000) center beam outward to the high g values (where g is the reciprocal of the atomic plane d-spacing). Some of the representative plots for the binary, ternary, and pentanary Zr-X alloys are presented in Fig. 4.11. There are usually two clearer maxima; one locating at g_1 ~ 0.34-0.42 $Å^{-1}$ and the other at g_2 ~0.5-0.7 $Å^{-1}$, depending on the alloy systems. Both the g_1 and g_2 data are of concern. Nevertheless, the g_2 values of 0.5-0.7 $Å^{-1}$, or corresponding to d~1.4-2.0 Å, is already close to or below the resolution limit of the current TEM. The contrast transfer function would be oscillatory near the latter g-vector ranges [99].

Thus the maxima or minima over these regions might not reflect the actual plane spacing. Therefore, only the g_1 data are discussed here.

Table 4.5 lists the measured g_1 maxima and the transformed d-spacing values for the various Zr-X alloys. The average *d*-spacing for the nearest neighbors was found to be highest for $Z_{50}Ti_{50}$, followed in sequence by $Zr_{52}Ti_5Ni_{15}Cu_{18}Al_{10}$, $Z_{34}Ti_{33}Cu_{33}$, and $Z_{50}Cu_{50}$. This sequence is in fact consistent with the atomic size of the corresponding elements. It is conceivable that the atomic spacing for the first nearest neighbor in the amorphous phase is about the sum of the atomic radius, r_i, of these two atoms, or $d\sim r_1+r_2$. It is further assumed that the average atomic spacing is determined by the atomic molar fraction, m_i, as

$$d_{ave} = 2\left(\frac{r_1 m_1 + r_2 m_2 + \ldots r_n m_n}{n}\right). \tag{4.6}$$

Table 4.5 also includes the calculated d_{ave} for the various alloys. The sequence is consistent with the extracted *g* and *d* values. With the larger Ti atoms or smaller Cu atoms, the binary $Z_{50}Ti_{50}$ and $Z_{50}Cu_{50}$ amorphous alloys exhibit the largest or smallest atomic d-spacing for their first nearest neighbors, respectively. Nevertheless, the mean *d*-spacing values measured from TEM are all smaller than the sum of the two radii ($r_{Zr}+r_{Ti}$ or $r_{Zr}+r_{Cu}$). The same was also found in our early XRD results for amorphous $Z_{50}Ti_{50}$ where the center of the diffuse peak located at ~33^o corresponds to a plane spacing of ~2.7 Å, smaller than the closest plane spacing for HCP Zr (3.17 Å) and Ti (2.89 Å), as well as smaller than the sum of $r_{Zr}+r_{Ti}$ (3.08 Å). Similar trends can also be seen from the ternary and pentanary alloys.

It appears that the average atomic pairing between neighboring atoms in the amorphous phase is not as simple as one would expect from the sum of the two radii. There seems to be a group of atoms forming a new arrangement with tight packing. The average atom spacing within the group is low due to mutual attraction and full package. It is postulated that, beyond such an atom group, the packing density would be lower, resulting in more free volumes.

4.4.3 Transition between nanocrystalline and amorphous phase

Over the systematic TEM characterizations on the ARB specimens subject to high F&R cycles, it is sometimes observed the transition region between the nanocrystalline and amorphous regions, as shown in Figs. 3.45 and 3.46. The nanocrystalline size in the matrix was seen to decrease gradually from ~10 nm down to ~3 nm in regions close to the transition boundary. The smallest nanocrystalline size observed near the boundary is consistently around 3 nm. This size is also about the smallest grain size estimated based on the modified Scherrer equation for XRD broadening peaks. As the grain size is further refined to below 3 nm, the nanocrystalline phase seems to become unstable.

The Gibbs free energy for the nanocrystalline and amorphous phases can be separately calculated based on their enthalpy and entropy terms for the mixed and unmixed atoms of all elements involved. The enthalpy energy term would include the chemical, elastic, structural contributions [100]. Another two factors that should be considered are the strain energy and the interfacial energy when the refined crystalline phases are reduced to the nanocrystalline regime. The obtained strain energy is about 1 kJ/mole and it did not change the driving force of the transition between nanocrystalline and amorphous phases significantly [101]. Meanwhile, there is no dislocation or fault left in all nanocrystalline phases smaller than 15 nm in this study. Hence, the plastic strain field might not be very important, especially in the latter stage of ARB process. Thereby the increment of Gibbs free energy of the nanocrystalline phases should be solely a result of the interfacial energy term with no contribution from the defect strain energy. Residual elastic strain energy accumulated during ARB might exist, as evident from the extracted residual strain of ~1% when using the modified Scherrer equation for XRD broadening peaks. It is assumed that the small elastic strain would not raise the Gibbs free energy much.

On the other hand, the interfacial energy for the nanocrystalline phases cannot be ignored. It can be easily calculated that the atoms associated with the interface in a sphere of ~3 nm in size would be around 60% of the total atoms. Since there are about 500-700 atoms inside the nanocrystalline phase of ~3 nm in size, there would be around 300-400 atoms located near the interface. The total interfacial energy increment can be evaluated by

$$\Delta H_i = \sum_i I_i S_i \gamma_i \ , \qquad (4.7)$$

where I_i is the fraction of atom i locating at interface, S_i is the interfacial area, and γ_t is the interfacial energy. For ARB of multiple elements, the interfacial energy terms for each neighboring elemental nanocrystalline phases need to be separately calculated and then summationed. It was estimated that the surface energy per mole for the pure metallic elements would be raised from ~10^2 J/mol for coarse grained materials to ~10^4 J/mol for fine grains measuring 3 nm [101], or an increment of ~100 times. The increase of interfacial energy term would raise the system Gibbs free energy to a level greater than that for the metastable amorphous state. Simultaneous transformation from the nanocrystalline phase into the amorphous state would occur. Figure 4.12 is a simplified schematical illustration of the Gibbs free energy for the bulk crystalline, nanocrystalline and amorphous phases, as proposed by Chen and Liu [103]. With gradual refinement of the nanocrystalline phases, *G* for the bulk crystalline phases would be raised up to those for the nanocrystalline phases. At the critical nanocrystalline size, the energy become higher than that for the amorphous phase, and simultaneous transformation from the nanocrystalline phase into the amorphous state would occur.

As for the kinetic aspect, the rapid increase in interfacial area for the 3 nm nanocrystalline phases would result in significant increment of interfacial diffusion by several orders of magnitude. Note that the nanocrystalline phases remain basically their pure element nature in both composition and crystal structure. The drastically enhanced interdiffusion would render suddenly complete atom mixing, forming a metastable amorphous phase with the average alloy composition and amorphous atomic packing in order to lower the Gibbs free energy.

The critical size of ~3 nm appears to be a lower bound for the stability of the nanocrystalline grains in these systems. The 500-700 atoms inside the nanocrystalline phase of ~3 nm would suddenly lose their stability in form of crystalline phase. The long-range-order crystalline structure is broken down into an amorphous structure with only short range ordering. This phenomenon should be aware of when the nanocrystalline materials are applied for structural or functional applications. The unique characteristics of nano phases might be lost upon transformation to amorphous phases. Furthermore, the amorphous phase could also transform back to the nanocrystalline state at the critical size of ~3 nm, exhibiting cyclic transformation near this critical size regime. This has been observed in a number of systems subject to mechanical alloying or severe deformation [104-108]. This was because that the Gibbs free energies of the amorphous and nanocrystalline phases near such a critical size are marginally close.

4.5 Amorphization of pentanary alloy systems

4.5.1 Content of softer Al or Cu phase for the pentanary alloys made by ARB

In previous studies, the adopted elemental foils in a binary or ternary alloy system possessed compatible initial hardness and proportion is more beneficial for the vitrification during the ARB process. But for the pentanary alloy systems without any pre-hardening treatment, such as $Zr_{20}Ti_{20}Ni_{20}Cu_{20}Al_{20}$ and $Zr_{52}Ti_5Ni_{15}Cu_{18}Al_{10}$, the amorphization of $Zr_{20}Ti_{20}Ni_{20}Cu_{20}Al_{20}$ with equal proportion of selected elements is worse than that of $Zr_{52}Ti_5Ni_{15}Cu_{18}Al_{10}$. The difference of initial hardness among the elemental foils increased with increasing the adopted kinds of elements. Hence, the content of softer phases, such as Al and Cu, in two pentanary $Zr_{20}Ti_{20}Ni_{20}Cu_{20}Al_{20}$ and $Zr_{52}Ti_{5}Ni_{15}Cu_{18}Al_{10}$ alloys needed to be discussed too. Figures 3.26 and 3.27 show the SEM micrographs of the $Zr_{20}Ti_{20}Ni_{20}Cu_{20}Al_{20}$ and $Zr_{52}Ti_{5}Ni_{15}Cu_{18}Al_{10}$ alloys, respectively. The phenomena of harder phase (such as Zr and Ti) necking during ARB process can be observed in both figures. Abundant softer phases are dispersed in the $Zr_{20}Ti_{20}Ni_{20}Cu_{20}Al_{20}$ alloy, making the non-uniform foil thinning of the harder phases. Many microcracks are left between the interface of two harder phases and the necking tail even after 80 F&R cycles. Residual cracks in alloy brought about the difficulty in microhardness measurements. However, the foil thickness reduction of $Zr_{52}Ti_{5}Ni_{15}Cu_{18}Al_{10}$ in Fig. 3.27 is quite different from that of $Zr_{20}Ti_{20}Ni_{20}Cu_{20}Al_{20}$. The homogeneous foil thinning state of the $Zr_{52}Ti_{5}Ni_{15}Cu_{18}Al_{10}$ alloy can be reached at the early stage of ARB due to the scattered distribution of softer phase. Therefore, it can be inferred that the content of softer phases in a complex alloy system indeed affects the foil thinning and grain size refinement.

The estimated volume fractions of the amorphous phase based the XRD patterns of the $Zr_{20}Ti_{20}Ni_{20}Cu_{20}Al_{20}$ and $Zr_{52}Ti_{5}Ni_{15}Cu_{18}Al_{10}$ alloys are shown in Table 3.2, and the diversity of the increment of amorphous volume fraction from 40 to 100 cycles is relatively small It may also be caused by the content of softer phase. In Fig. 3.26 (b), some regions in the $Zr_{20}Ti_{20}Ni_{20}Cu_{20}Al_{20}$ alloy are constituted by several thin foils with thickness less than 0.1 μm. The composition of the regions with several thin films in Fig. 3.26 (b), is Ni, Cu and Al with different proportion (through SEM/EDS analysis). This result corresponds to the observation of XRD pattern in Fig. 3.13. It means that the grain size of the softer phases was preferentially refined, and this result was included in the XRD pattern and therefore affected the estimation of amorphous volume fraction in the $Zr_{20}Ti_{20}Ni_{20}Cu_{20}Al_{20}$ alloy. Hence, the estimated amorphous volume fraction of the $Zr_{20}Ti_{20}Ni_{20}Cu_{20}Al_{20}$ alloy is overestimated because of the abundant content of softer phases.

4.5.2 Comparison of $Zr_{52}Ti_5Ni_{15}Cu_{18}Al_{10}$ alloys made by different routes

The characterization of $Zr_{52}Ti_5Ni_{15}Cu_{18}Al_{10}$ alloys made by different methods is discussed in this section. The major synthesis method in this study is the ARB process and the alloy prepared by the melt spinning method was only used to compare with the ARB specimen. Hence, the selection of alloy component for melt spinning was based on the alloy systems made by ARB.

Based on the analysis results for the ARB $Zr_{52}Ti_5Ni_{15}Cu_{18}Al_{10}$ alloys in chapter 3, it was found that the grain size gradually decreased and the volume fraction of amorphous phases gradually increased with increasing ARB cycles. The grain size decreased from 100 μm to nanometers scale and the amorphous volume fraction reached the value of 50% after 100 F&R cycles, without any intermetallic compound produced during ARB. However, the XRD pattern for the arc melted $Zr_{52}Ti_5Ni_{15}Cu_{18}Al_{10}$ alloy reveals no obvious vitrification, and the peaks are no longer contributed by pure elements due to the nucleation of compounds upon contact with the water-cooled Cu mold [109]. Hence, the melt spinning process was followed and a nearly complete vitrification was observed in the XRD pattern of melt spun $Zr_{52}Ti_5Ni_{15}Cu_{18}Al_{10}$ alloy, where the center of the diffuse peak located at ~37^{o}. Meanwhile, the hardness values for the alloys made by arc melting, drop casting and melt spinning methods are higher than that for ARB alloys, because the latter may possess cracks inside the specimen. Besides, the hardness data in Table 3.6 show that the hardness of the arc melted, drop cast and melt spun specimens increased with increasing cooling rate, because the grain size of the alloys decreased with increasing cooling rate. But the Hall-Petch breakdown was not observed here. It may result from the alloying effect mentioned in section 4.2.2.

According to the thermal analyses data in section 3.10, the glass transition temperature of the melt spun $Zr_{52}Ti_5Ni_{15}Cu_{18}Al_{10}$ alloy is ~430^oC and the temperature interval of a supercooled liquid region ΔT_x is ~60^oC. The extracted values of the reduced glass transition temperature (T_{rg}) and γ are 0.59 and 0.41, respectively. These values are rational compared with those obtained in various bulk amorphous Zr base alloys [52]. The ARB $Zr_{52}Ti_5Ni_{15}Cu_{18}Al_{10}$ alloy is not fully vitrified after 100 F&R cycles. Hence, there are no meaningful thermal analysis results for the roll bonded $Zr_{52}Ti_5Ni_{15}Cu_{18}Al_{10}$ alloy. But the DSC measurement for the nearly completely amorphous $Zr_{50}Ti_{50}$ alloy made by ARB reveals that the temperature interval of a supercooled liquid region of this alloy is also ~60^oC.

Moreover, the TEM results of the melt spun $Zr_{52}Ti_5Ni_{15}Cu_{18}Al_{10}$ alloy reveal that there are some residual nanocrystalline phases (with size in the range of 3-15 nm), although the volume fraction of the observed amorphous phase is ~90%. The residual nanocrystalline phases can not be further eliminated unless the specimen remelts again and the cooling rate of melt spinning process increases. On the contrary, the grain size of nanocrystalline phases in ARB specimen gradually decreased with increasing ARB cycles and the amorphous volume fraction indeed increased with it. If the ARB process is continuous proceeded, a fully amorphous state can finally obtain.

It was inferred that the alloys made by ARB route possessed of similar thermal properties compared with the melt spun alloys. The resulted specimen size of the ARB alloy is larger than the melt spun sample, but the hardness of the dense specimen made by melt spinning is higher. Consequently, the synthesis method for fabricating a nanocrystalline or amorphous alloy should be selected according to the actual needs.

Ⅴ. Summary

The study of amorphous alloys can trace back to 40 years ago. But this kind of alloys received increasing attention over the past 10 years, especially for the glassy metals made by solid-state reaction and casting of multi-element alloy systems. Hence, the major adopted vitrification methods in this study are the accumulation roll bonding (ARB) process and the casting method of multi-elements. One of the famous applications of amorphous alloys is the utilization in golf industry, the Liquidmetal Golf. But the alloy ($Zr_{62}Ti_{12}Cu_{12}Ni_{11}Be_3$) they used contains beryllium and must be handled properly to avoid the health risks associated with this known carcinogen. Therefore, other trials to synthesis alloys with more common compositions were developed at Caltech, $Zr_{52}Ti_5Ni_{15}Cu_{18}Al_{10}$, by the arc-melting and ARB methods. In the initial attempts of this study, many problems, such as the loss of specimen and the change of designed composition, encountered during ARB. Therefore, numerous efforts were made to develop a stable and repeatable ARB process. It was finally found that a manually folded step before ARB is helpful to proceed the roll bonding cycles. This finding resulted in the smooth acquirement of the desired ARB alloy systems.

According to the results and discussions in previous chapters, this study can be concluded as follow:

1. Most of the peaks in XRD scan profiles for the ARB samples were contributed by the pure elements. It means that ARB is useful to avoid the contamination during roll bonding process. Hence, the ARB process is a valuable synthesis method if the purity of the alloy is an important concern.

2. The alloy systems synthesized via ARB are flat pieces with high hardness and minimum

contamination or intermetallic compound. The initial hardness of the elemental foils affects the efficiency of grain size refinement and vitrification. For softer foils, it is necessary to pre-harden before ARB. The pre-hardening step is useful to enhance the efficiency of strain accumulation, nanocrystallization, and amorphization. Elemental foils of compatible hardness would accumulate the shear strain in a more effective way. The average ARB true strain reaches ~7.5 (instead of the theoretical value of 64) after 80 F&R cycles, and such a strain level is compatible to those experienced during MA or ECAP. A large difference in hardness among elemental foils will limit the accumulation of true strain during ARB.

3. Based on the EDS analyses of the ARB alloys, the interdiffusion of various atoms becomes progressively effective with increasing cycles. Apparent enhancement of diffusion is evident during ARB via grain boundary and lattice diffusion with the help of high grain boundary area and induced lattice defects. Meanwhile, the minor temperature rise of ~25^{o}C due to the severe plastic deformation and pronounced friction during ARB, would also raise the interdiffusion of elements slightly.

4. The hardness of the ARB specimens increased with increasing F&R cycles and the increment factor of hardness by 2-3 times is due to grain size refinement. The inverse Hall-Petch behavior occurred in some alloy systems as the grain size falls below 20 nm, should be noticed. However, the inflection grain size slightly decreases as the complexity of alloy composition increasing, suggesting that alloying has slowed down the Hall-Petch breakdown. The roughly estimated elastic modulus of the $Zr_{50}Ti_{50}$ alloy, based on the hardness measurement, is near 200 GPa after 40 F&R cycles and then declines as the amorphous phase gradually evolves. The elastic modulus for the nearly completely amorphous $Zr_{50}Ti_{50}$ alloy made by ARB process is ~65 GPa.

5. The composition dependence of measured hardness was not pronounced for Zr-Ti alloy

systems with different composition combinations. But the effect of the third added element, Cu or Ni, for the amorphization in Zr-Ti alloys is different. In the XRD pattern of $Zr_{34}Ti_{33}Ni_{33}$ alloy, the texture of Ni (111) plane can not be destroyed with increasing ARB cycles because it is the advantageous orientation for the rolling direction. But no similar phenomenon was observed in the $Zr_{34}Ti_{33}Ni_{33}$ XRD pattern. Hence, the addition of Ni foils with higher initial hardness is not necessarily benefited for the amorphization process.

6. The gradual evolution of nanocrystallization and vitrification as a function of F&R cycles is established. After 40 and 80 cycles, the grain size can be refined to 30±20 and 10±5 nm, and the amorphous volume fraction reaches 40±10% and 70±20%, respectively, depending on the relative hardness. The local variation of the resulting grain size and amorphous regions in alloys after the ARB process increases with increasing number of compositional elements. It means that a more inhomogeneous structure would be obtained for alloys with more complicated compositions, even after high F&R cycles.

7. The critical size of ~3 nm appears to be a lower bound for the stability of nanocrystalline phases in the current systems. Further refinement would result in sudden transformation to the amorphous state. Cyclic transformation between the nanocrystalline and amorphous phases near this critical size would occur.

8. The compatible initial foil hardness would be most beneficial to the nanocrystallization and amorphization processes; the influence would overwhelm the atomic size effect. The prerequisites such as the large atomic size difference (the anti-Hume-Rothery rule) or the low eutectic temperature in the corresponding thermodynamic diagram imposed for the most bulk amorphous alloys are not necessarily essential.

9. The nearest neighbor distances and thermal properties of the amorphous alloys produced

by ARB are similar to those obtained by other processing routes, such as melt spinning method. The temperature interval of a supercooled liquid region, for the nearly completely amorphous $Zr_{50}Ti_{50}$ alloy made by ARB, is ~60°C. This value is in the reasonable range of those obtained in various bulk amorphous Zr base alloys [52].

10. The hardness of the ARB specimen is lower than the melt spun one, due to the loose structure resulted from the great quantity of induced interface during repeated roll bonding process. But it seems that the composition limitation of ARB is less than the casting method. Coupled with the conclusion in point 9, the selection of synthesis methods for producing nanocrystalline or amorphous alloys should be based on the actual needs in application.

References

1. E. O. Hall, Pro. Phys., Soc. London, B64, 1951, p. 747.
2. N. J. Petch, Iron and Steel Inst., 174,1953, p. 25.
3. L. L. Shaw, J. Met., 52, 2001, p. 41.
4. H. J. Guntherodt and H. Beck (ed.): Glassy Metals Ⅰ, Springer-Verlag, Berlin Heidelberg, Germany, 1981.
5. H. Beck and H. J. Guntherodt (ed.): Glassy Metals Ⅱ, Springer-Verlag, Berlin Heidelberg, Germany, 1983.
6. R.W. Cahn, P. Hassen and E. J. Kramer (ed.): Materials Science and Technology, Volume 9, VCH, New York, USA, 1991.
7. M. Atzmon: A Study of Bulk Amorphous Alloys Formed by Solid-State Reaction in Elemental Composites, Ph. D. Thesis, California Institute of Technology, California, USA, 1985.
8. C. K. Lin: The Amorphization of TM-Si (TM: transition metal) Alloy Powders by Mechanical Alloying, Master Thesis, Tatung Institute of Technology, Taiwan, 1991.
9. Y. H. Hsu: A Study on the Multicomponent Alloy Systems with Equal-Mole FCC or BCC Elements, Master Thesis, National Tsing Hua University, Taiwan, 2000.

10. W. Klement, Jr., R. H. Willens and P. Duwez, Nature, 187, 1960, p. 869.

11. A. Inoue, K. Ohtera, A. P. Tsai and T. Masumoto, Japan. J. Appl. Phys., 27, 1988, L479.

12. F. E. Luborsky (ed.): Amorphous Metallic Alloys, Butterworths, London, U.K., 1983.

13. J. J. Gilman and H. J. Leamy (ed.): Metallic Glasses, ASM, 1979.

14. R.W. Cahn, P. Hassen and E. J. Kramer (ed.): Materials Science and Technology, Volume 9, VCH, New York, USA, 1991.

15. R. W. Cahn and H. H. Liebermann, Rapidly Solidified Alloys, New York: Marcel Dekker Inc, 1993.

16. A. Sagel, N. Wanderka, R. K. Wunderlich, P. Schubert-Bischoff and H. J. Fecht, Scripta Mater., 38, 1998, p. 163.

17. A. Inoue, K. Ohtera, K. Kita and T. Masumoto, Japan. J. Appl. Phys., 27, 1988, L2248.

18. A. Inoue, Mater. Trans. Japan. Inst. Metals, 36, 1995, p. 866.

19. A. Inoue, Mater. Sci. Engng., A226-228, 1997, p. 357.

20. A. Inoue, T. Zhang and A.Takeuchi, Mater. Sci., Forum, 269-272, 1998, p. 855.

21. A. Inoue, A. Takeuchi and T. Zhang, Metall. Mater. Trans., 29A, 1998, p. 1779.

22. A. Inoue: Bulk Amorphous Alloys,Trans. Tech. Publications, Zurich, 1998.

23. Y. H. Kim, A. Inoue and T. Masumoto, Mater. Trans. JIM., 31, 1990, p. 747.

24. L. B. Davies and P. J. Grundy, J. Non-Cryst. Solids, 11, 1972, p. 179.

25. L. Holland: Vacuum Deposition of Thin Films, Chapman, London, U.K., 1966.

26. P. Chardhari, J.J. Cuomo and R.J. Gambino, IBN J. Res. Dev., 17,1973, p. 66.

27. J. Bloch, J. Nucl. Mater., 6, 1962, p. 203.

28. J. L. Brimhall and E. P. Simonen, Nuc. Inst. Meth. Phys. Res., B, 16, 1986, p. 187.

29. S. Veprek, Z. Iqbal and F. -A. Sarott, Phil. Mag., B45, 1982, p. 137.

30. X. L. Yeh, K. Samwer and W. L. Johnson, Appl. Phys. Lett., 42, 1983, p. 242.

31. Z. P. Xing, S. B. Kang, and H. W. Kim, Metall. Mater. Trans., A33, 2002, p. 1521.

32. J. Lee, F. Zhou, K. H. Chung, N. J. Kim, and E. J. Lavernia, Metall. Mater. Trans., A32, 2001, p. 3109.

33. C. C. Koch, O. B. Cavin, C.G. Mckamey and J. O. Scarbrough, Appl. Phys. Lett., 43, 1983, p. 1017.

34. L. Schultz, Mater. Sci. Eng., 97, 1988, p. 15.

35. J. Eckert, Mater. Sci. Eng., A226-A228, 1997, p. 364.

36. M. Sherif El-Eskandarany, A. Inoue, Metall. Mater. Trans., A33, 2002, p. 135.

37. R. M. German: Powder Metallurgy Science, Metal Powder Industries Federation, New Jersey, USA, 1994.

38. Y. Saito, N. Tsuji, H. Utsunomiya, T. Sakai and R. G. Hong, Scripta Mater., 39, 1998, p. 1221.

39. R. B. Schwarz and W. L. Johnson, Phys. Rev. Lett., 51, 1983, p. 415.

40. A. Sagel, H. Sieber, H. J. Fecht and J. H. Perepzko, Acta Mater., 46, 1998, p. 4233.
41. H. S. Chen, Rep. Prog. Phys., 43, 1980, p. 353.
42. H. W. Kui, A. L. Greer and D. Turnbull, Appl. Phys. Lett., 45, 1984, p. 615.
43. A. Peker and W. L. Johnson, Appl. Phys. Lett., 63, 1993, p. 25.
44. A. Inoue, Acta Mater., 48, 2000, p. 279.
45. T. G. Park, S. Yi and D.H. Kim, Scripta Mater., 43, 2000, p. 109.
46. T. A. Waniuk, J. Schroers and W. L. Johnson, Appl. Phys. Lett., 78, 2001, p. 1213.
47. A. Inoue, W. Zhang, T. Zhang and K. Kurosaka, Acta Mater., 29, 2001, p. 2645.
48. A. Inoue, W. Zhang, T. Zhang and K. Kurosaka, J. Mater. Res., 16, 2001, p.2836.
49. T. D. Shen and R. B. Schwarz, J. Mater. Res., 14, 1999, p. 2107.
50. T. D. Shen and R. B. Schwarz, Appl. Phys. Lett., 75, 1999, p. 49.
51. B. S. Murty and K. Hono, Mater. Trans., JIM 41, 2000, p. 1538.
52. Z. P. Lu and C. T. Liu, Acta Mater, 50, 2002, p. 3501.
53. R. E. Reed- Hill: Physical Metallurgy Principles, PWS, Boston, USA, 1994.
54. M. H. Cohen and D. Turnbull, Nature, 189, 1961, p. 131.
55. 吳學陞，工業材料,149 期,1999, p. 154.
56. A. Inoue, T. Zhang and T. Masumoto, Mater. Trans. Japan. Inst. Metals, 36, 1995, p. 391.
57. Y. Saito, H. Utsunomiya, N. Tsuji and T. Saka, Acta Mater., 47, 1999, p. 579.

58. 鄭振東, 非晶質金屬漫談, 建宏出版社, 1990, p. 69.

59. D. H. Bae, H. K. Lim, S. H. Kim, D. H. Kim and W. T. Kim, Acta Mater., 50, 2002, p. 1749.

60. T. Zhang, A. P. Tasi, A. Inoue and T. Masumoto, Boundary, 7, 1991, p. 39.

61. A. Inoue, Mater. Sci. Eng., A 267, 1999, p. 171.

62. Y. Kawamura, H. Kato, A. Inoue and T. Masumoto, Scripta Mater., 39, 1998, p. 301.

63. A. Inoue, Y. H. Kim and T. Masumoto, Trans. JIM, 33, 1992, p. 487.

64. T. G. Nieh, T. Mukai, C. T. Liu and J. Wadsworth, Scripta Mater., 40, 1999, p. 487.

65. R. Hasegawa (ed.): Glassy Metal: Magnetic, Chemical and Structure Properties, CRC press, Boca Raton, Florida,1983.

66. 莊裕仁: 機械月刊, 四月號, 2000, p. 357.

67. C. Suryanarayana, A. Inoue and T. Masumoto, J. Mater. Sci., 15, 1980, p. 1993.

68. G. S. Choi, Y. H. Kim, H. K. Cho, A. Inoue and T. Masumoto, Scripta Mater., 33, 1995, p. 1301.

69. A. Inoue, K. Nakazato, Y. Kawamura, A. P. Tsai and T. Msumoto, Mater. Trans. JIM, 35, 1994, p. 95.

70. N. Tsuji, Y. Saito, H. Utsunomiya and S. Tanigawa, Scripta Mater., 40, 1999, p. 795.

71. W. H. Wang, Q. Wei and H. Y. Bai, Appl. Phys. Lett., 71, 1997, p. 58.

72. M. Sherif El-Eskandarany and A. Inoue, Mater. Trans., A33, 2002, p. 2145.

73. G. Wilde, H. Sieber and J. H. Perepzko, Scripta Mater., 40, 1999, p. 779.

74. C. Suryanarayana, Progress in Mater. Sci., 46, 2001, p. 1.

75. N. Tsuji, T. Toyoda, Y. Minamino, Y. Koizumi, T. Yamane, M. Komatsu and M. Kiritani, Mater. Sci. Eng., A350, 2003, p. 108.

76. H. Sieber, J. S. Park, J. Weissmuller and J. H. Perepezko, Acta Mater, 49, 2001, p. 1139.

77. B. E. Warren, X-Ray Diffraction. Addison-Wesley Pub. Inc., London. 1969.

78. B. D. Cullity (ed), Elements of X-ray Diffraaction, 2nd ed. Addison-Wesley Pub. Inc., Indiana. 1978.

79. C. Suryanaraya, M. Norton, X-ray Diffraction, a Practical Approach. Plenum Press, New York. 1998.

80. M. H. Loretto: Electron Beam Analysis of Materials, 2nd ed., Chapman & Hall Pub, 1994.

81. 洪英博，以累積滾壓加工製做奈米或非晶質合金之研究，國立中山大學材料科學研究所碩士論文, 2002.

82. 邱薰毅，以累積滾壓及熔液噴旋法開發奈米或非晶質輕量 Zr-Cu 基合金，國立中山大學材料科學研究所碩士論文, 2003.

83. P. Y. Lee, J. Jang and C. C. Koch, J. Less-Common Metals., 140, 1988, p. 73.

84. T. H. Hung, J. S. C. Jang and J. C. Huang, unpublished research, National Sun Yat-Sen University, Kaohsiung, Taiwan, 2004.

85. 張量然, 添加硼對 ZrAlCuNi 塊狀非晶質合金結晶行為的影響, 義守大學材料科學與工程學系碩士論文, 2003.

86. M. Atzmon, J. D. Verhoeven, E. D. Gibson and W. L. Johnson, Appl. Phys. Lett., 45, 1984, p. 1052.

87. F. Zhou, S. R. Nutt, C. C. Bampton and E. J. Lavernia, Metall. Mater. Trans., A34, 2003, p. 1985.

88. F. Zhou, X. Z. Liao, Y. T. Zhu, S. Dallek and E. J. Lavernia, Acta Mater., 51, 2003, p. 2777.

89. P. G. Shewmon: Diffusion in Solids, McGraw-Hill Book Co., NY, 1973.

90. D. E. Grady and J. R. Asay, J. Appl. Phys., 53, 1982, p. 7350.

91. K. Kato: Metal Plastic Working, Maruzen, Tokyo, Japan, 1970, p. 161.

92. R. E. Reed-Hill and R. Abbaschian: Physical Metallurgy Principles, 3rd ed, PWS Pub. Co., Boston, 1992, p. 373.

93. Z. B. Wang, N. R. Tao, W. P. Tong, J. Lu and K. Lu, Acta Mater., 51, 2003, p. 4319.

94. K. Tsuchiya, H. Nakayama, Z. G. Liu, M. Umemoto, K. Morii and T, Shiizu, Mater. Trans. JIM, 42, 2001, p. 1987.

95. C. A. Schuh, T. G. Nieh and T. Yamasaki, Scripta Mater., 46, 2002, p. 735.

96. W. C. Oliver and G. M. Pharr, J. Mater. Res., 7, 1992, p. 1564.

97. G. M. Pharr, W. C. Oliver and F. R. Brotzen, J. Mater. Res., 7, 1992, p. 613.

98. J. Eckert, A. Reger-Leonhard, B. Weiβ and M. Heilmaier, Mater. Sci. and Eng., A301, 2001, p. 1.

99. J. C. H. Spence: Experimental High-Resolution Electron Microscopy, 2nd ed, Oxford University Press, NY, 1988.

100. A. W. Weeber, J. Phys., F17, 1987, p. 809.

101. M. Atzmon, K. M. Unruh and W. L. Johnson, J. Appl. Phys. 58, 1985, p. 3865.

102. M. S. Tsao, C. B. Guang, G. C. Hsu, T. F. Gin, T. G. Wang and G. S. Gi: Nano Mater., HIT Press, Harbin, China, 2001, p. 13.

103. Y. G. Chen and B. X. Liu, Acta Mater., 47, 1999, p. 1389.

104. M. Sherif El-Eskandarany, K. Aoki, K. Sumiyama and K. Suzuki, Scripta Mater., 36, 1997, p. 1001.

105. B. S. Murty and S. Ranganathan, Int. Mater. Rev., 43, 1998, p. 101.

106. J. S. C. Jang and C. C. Koch, J. Mater. Res., 5, 1989, p. 124.

107. S. Veprek, Z. Iqbal and F. A. Sarott, Phil. Mag. B, 45, 1982, p. 137.

108. J. S. C. Jang and H. P. Shih, Mater. Chem. Phys., 70, 2001, p. 217.

109. Y. Yokohama, K. Fukaura and A. Inoue, Intermetallics, 10, 2002, 1113.

Table 1.1 Comparison of the characteristics of traditional metals and metallic glasses [12,13].

Property	Traditional metals	Metallic amorphous alloys
Structure	crystalline	amorphous
Bonding	metallic	metallic
Yield strength	non- ideal	almost ideal
Workability	ductile	ductile
Hardness	low to high	very high
UTS	low to high	very, very high
Thermal conductivity	good	good
Electric resistance	very low	very low
Corrosion resistance	poor to good	very good
Magnetic properties	various	various

Table 1.2 The classification of amorphous alloy systems [14].

Categories	Representative alloy systems	Major content variation range
1. T^2 or noble metal＋metalloid	Au-Si, Pd-Si, Co-P, Fe-B, Fe-P-C, Fe-Ni-P-B, Mo-Ru-Si, Ni-B-Si	15-25at% metalloid
2. T^1 metal＋T^2 (or Cu)	Zr-Cu, Zr-Ni, Y-Cu, Ti-Ni, Nb-Ni, Ta-Ni, Ta-Ir	35-65at% Cu or T^2
3. A metal＋B metal	Mg-Zn, Ca-Mg, Mg-Ga	various
4. T^1 metal＋A metal	(Ti, Zr)-Be, Al-Y-Ni	20-60at%Be, 10at%Y-5at%Ni
5. Radioelement＋T^1	U-V, U-Cr	20-40at% T^1

※ A metal: Li, Mg group; B metal: Cu, Zn, Al group.

※ T^1 metal: Sc, Ti, V group; T^2 metal: Mn, Fe, Co, Ni group.

Table 1.3 Bulk amorphous alloy systems and calendar years when details about each alloy system were first published [44].

I. Nonferrous metal base	Year
Mg-Ln-M (Ln= lanthanide metal; M= Ni, Cu or Zn)	1988
Ln-Al-TM (TM= VI-VIII group transition metals)	1989
Ln-Ga-TM	1989
Zr-Al-TM	1990
Zr-Ti-Al-TM	1990
Ti-Zr-TM	1993
Zr-Ti-TM-Be	1993
Zr-(Nb, Pd)-Al-TM	1995
Pd-Cu-Ni-P	1996
Pd-Ni-Fe-P	1996
Pd-Cu-B-Si	1997
Ti-Ni-Cu-Sn	1998
II. Ferrous metal base	Year
Fe-(Al, Ga)-(P, C, B, Si, Ge)	1995
Fe-(Nb, Mo)-(Al, Ga)-(P, B, Si)	1995
Co-(Al, Ga)-(P, B, Si)	1996
Fe-(Zr, Hf, Nb)-B	1996
Co-Fe-(Zr, Hf, Nb)-B	1996
Ni-(Zr, Hf, Nb)-(Cr, Mo)-B	1996
Fe-Co-Ln-B	1998
Fe-(Nb, Cr, Mo)-(P, C, B)	1999
Ni-(Nb, Cr, Mo)-(P, B)	1999

Table 1.4 Summary of ΔT_x, T_{rg} , γ , critical cooling rate R_c and critical section thickness Z_c for typical bulk amorphous alloys [52].

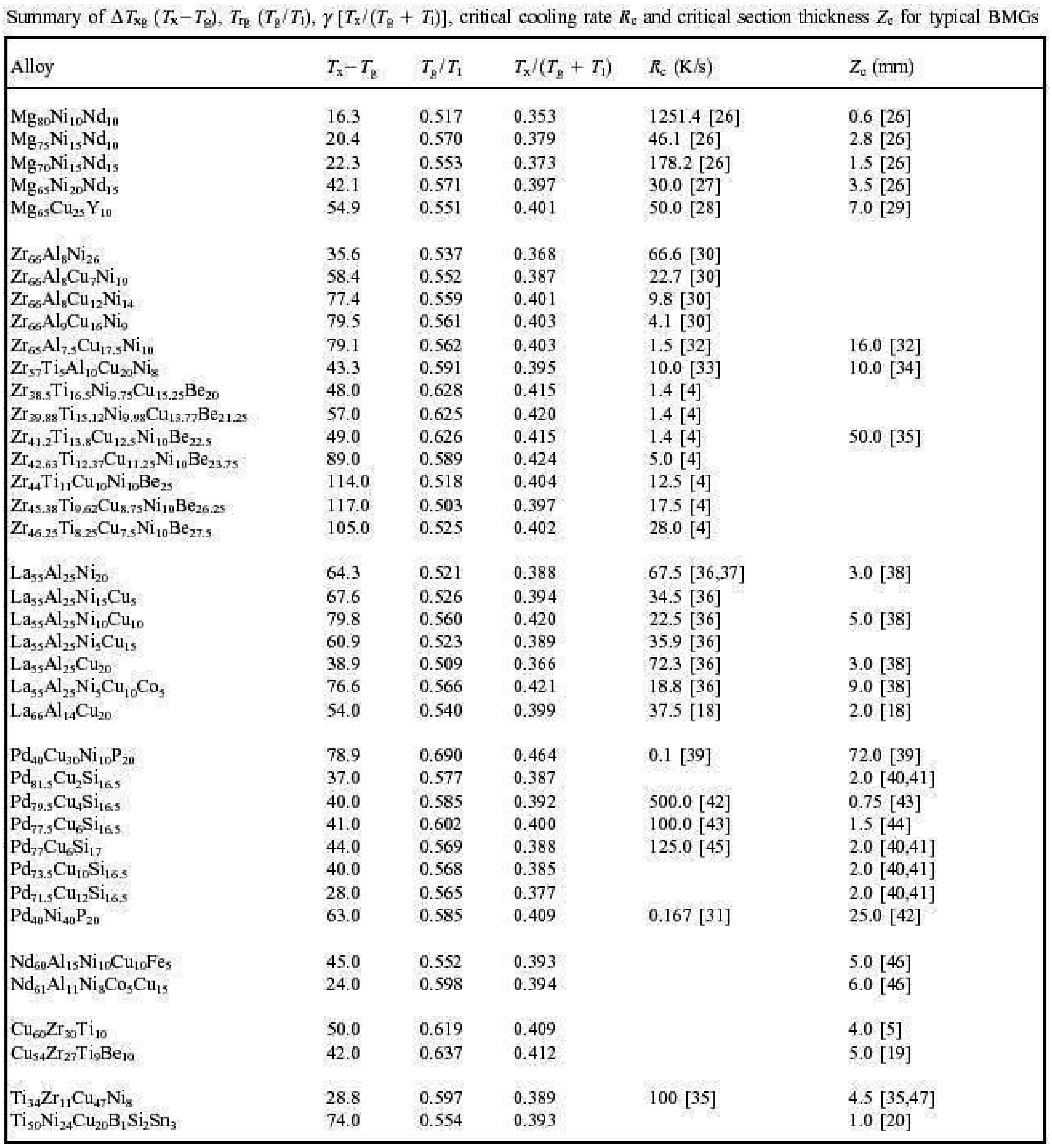

Summary of ΔT_{xg} ($T_x - T_g$), T_{rg} (T_g/T_l), γ [$T_x/(T_g + T_l)$], critical cooling rate R_c and critical section thickness Z_c for typical BMGs

Alloy	$T_x - T_g$	T_g/T_l	$T_x/(T_g + T_l)$	R_c (K/s)	Z_c (mm)
$Mg_{80}Ni_{10}Nd_{10}$	16.3	0.517	0.353	1251.4 [26]	0.6 [26]
$Mg_{75}Ni_{15}Nd_{10}$	20.4	0.570	0.379	46.1 [26]	2.8 [26]
$Mg_{70}Ni_{15}Nd_{15}$	22.3	0.553	0.373	178.2 [26]	1.5 [26]
$Mg_{65}Ni_{20}Nd_{15}$	42.1	0.571	0.397	30.0 [27]	3.5 [26]
$Mg_{65}Cu_{25}Y_{10}$	54.9	0.551	0.401	50.0 [28]	7.0 [29]
$Zr_{66}Al_8Ni_{26}$	35.6	0.537	0.368	66.6 [30]	
$Zr_{66}Al_8Cu_7Ni_{19}$	58.4	0.552	0.387	22.7 [30]	
$Zr_{66}Al_8Cu_{12}Ni_{14}$	77.4	0.559	0.401	9.8 [30]	
$Zr_{66}Al_9Cu_{16}Ni_9$	79.5	0.561	0.403	4.1 [30]	
$Zr_{65}Al_{7.5}Cu_{17.5}Ni_{10}$	79.1	0.562	0.403	1.5 [32]	16.0 [32]
$Zr_{57}Ti_5Al_{10}Cu_{20}Ni_8$	43.3	0.591	0.395	10.0 [33]	10.0 [34]
$Zr_{38.5}Ti_{16.5}Ni_{9.75}Cu_{15.25}Be_{20}$	48.0	0.628	0.415	1.4 [4]	
$Zr_{39.88}Ti_{15.12}Ni_{9.98}Cu_{13.77}Be_{21.25}$	57.0	0.625	0.420	1.4 [4]	
$Zr_{41.2}Ti_{13.8}Cu_{12.5}Ni_{10}Be_{22.5}$	49.0	0.626	0.415	1.4 [4]	50.0 [35]
$Zr_{42.63}Ti_{12.37}Cu_{11.25}Ni_{10}Be_{23.75}$	89.0	0.589	0.424	5.0 [4]	
$Zr_{44}Ti_{11}Cu_{10}Ni_{10}Be_{25}$	114.0	0.518	0.404	12.5 [4]	
$Zr_{45.38}Ti_{9.62}Cu_{8.75}Ni_{10}Be_{26.25}$	117.0	0.503	0.397	17.5 [4]	
$Zr_{46.25}Ti_{8.25}Cu_{7.5}Ni_{10}Be_{27.5}$	105.0	0.525	0.402	28.0 [4]	
$La_{55}Al_{25}Ni_{20}$	64.3	0.521	0.388	67.5 [36,37]	3.0 [38]
$La_{55}Al_{25}Ni_{15}Cu_5$	67.6	0.526	0.394	34.5 [36]	
$La_{55}Al_{25}Ni_{10}Cu_{10}$	79.8	0.560	0.420	22.5 [36]	5.0 [38]
$La_{55}Al_{25}Ni_5Cu_{15}$	60.9	0.523	0.389	35.9 [36]	
$La_{55}Al_{25}Cu_{20}$	38.9	0.509	0.366	72.3 [36]	3.0 [38]
$La_{55}Al_{25}Ni_5Cu_{10}Co_5$	76.6	0.566	0.421	18.8 [36]	9.0 [38]
$La_{66}Al_{14}Cu_{20}$	54.0	0.540	0.399	37.5 [18]	2.0 [18]
$Pd_{40}Cu_{30}Ni_{10}P_{20}$	78.9	0.690	0.464	0.1 [39]	72.0 [39]
$Pd_{81.5}Cu_2Si_{16.5}$	37.0	0.577	0.387		2.0 [40,41]
$Pd_{79.5}Cu_4Si_{16.5}$	40.0	0.585	0.392	500.0 [42]	0.75 [43]
$Pd_{77.5}Cu_6Si_{16.5}$	41.0	0.602	0.400	100.0 [43]	1.5 [44]
$Pd_{77}Cu_6Si_{17}$	44.0	0.569	0.388	125.0 [45]	2.0 [40,41]
$Pd_{73.5}Cu_{10}Si_{16.5}$	40.0	0.568	0.385		2.0 [40,41]
$Pd_{71.5}Cu_{12}Si_{16.5}$	28.0	0.565	0.377		2.0 [40,41]
$Pd_{40}Ni_{40}P_{20}$	63.0	0.585	0.409	0.167 [31]	25.0 [42]
$Nd_{60}Al_{15}Ni_{10}Cu_{10}Fe_5$	45.0	0.552	0.393		5.0 [46]
$Nd_{61}Al_{11}Ni_8Co_5Cu_{15}$	24.0	0.598	0.394		6.0 [46]
$Cu_{60}Zr_{30}Ti_{10}$	50.0	0.619	0.409		4.0 [5]
$Cu_{54}Zr_{27}Ti_9Be_{10}$	42.0	0.637	0.412		5.0 [19]
$Ti_{34}Zr_{11}Cu_{47}Ni_8$	28.8	0.597	0.389	100 [35]	4.5 [35,47]
$Ti_{50}Ni_{24}Cu_{20}B_1Si_2Sn_3$	74.0	0.554	0.393		1.0 [20]

Table 1.5 Comparison of the mechanical properties for the amorphous alloy, Ti-alloy and cast stainless steel [12,13].

Alloys	YS (MPa)	Density (g/cm^3)	Hardness (HRC)
Zr-12Cu-12Ti-11Ni-3Be	1900	6.1	50
Ti-6Al-4V	800	4.5	30
Cast stainless steel	850	7.8	30

Table 2.1 Initial thickness (t_o), purity, hardness (H_v), atomic radius, atomic radius difference and heat of mixing (ΔH_m) with respect to Zr for the elemental foils applied.

	Zr	Al	Cu	Ni	Ti
t_o, μm	76	102	30	91	102
Purity, at%	99.8%	99%	99.9%	99%	99.6%
H_v	174	22	131	163	183
r, Å	1.62	1.43	1.28	1.25	1.48
Δr	--	-12%	-21%	-23%	-9%
ΔH_m, kJ/mole	--	-44	-23	-49	~0

Table 2.2 The diameter and purity of the elemental rods applied.

	Zr	Al	Cu	Ni	Ti
Diameter, mm	6.2	6.35	6.35	6.35	6.4
Purity, at%	99%	99%	99.9%	99.5%	99.7%

Table 2.3 The alloy systems selected in the ARB study.

The number of alloy elements	Composition (at%)
2	$Zr_{50}Al_{50}$, $Zr_{50}Cu_{50}$, $Zr_{50}Ni_{50}$ (1:1)
2	$Zr_{75}Ti_{25}$, $Zr_{50}Ti_{50}$, $Zr_{25}Ti_{75}$ (3:1, 1:1, 1:3)
3	$Z_{34}Ti_{33}Cu_{33}$, $Z_{34}Ti_{33}Ni_{33}$ (1:1:1)
5	$Zr_{20}Ti_{20}Ni_{20}Cu_{20}Al_{20}$ (1:1:1:1:1) $Zr_{52}Ti_{5}Ni_{15}Cu_{18}Al_{10}$

Table 3.1 The grain size (in unit of nm) of Zr and microstrain (η, %) estimated by Eqns. (3.1) and (3.2) for (a) binary and (b) ternary and pentanary Zr-X alloy systems. The values shown in parentheses () are estimated by Eqn. (3.1); and the values shown in square brackets [] are estimated by Eqn. (3.2).

(a)	$Zr_{50}Al_{50}$	$Zr_{50}Cu_{50}$	$Zr_{50}Ni_{50}$	$Zr_{50}Ti_{50}$	$Zr_{25}Ti_{75}$	$Zr_{75}Ti_{25}$
40	(19.9) [32.5] 0.64%	(12.4) [34.2] 2.31%	(15.7) [33.9] 1.06%	(10.1) [12.6] 0.58%	(6.5) [10.6] 2.69%	(8.9) [14.6] 1.25%
60	(18.09) [30.2] 1.21%	(6.6) [20.9] 4.85%	(12.9) [19.9] 1.53%	(7.7) [10.5] 1.61%	(6.1) [5.1] 1.57%	(7.5) [10.5] 1.52%
80	(15.16) [16.3] 0.66%	(5.4) [10.9] 3.23%	(10.9) [15.4] 1.65%	(4.4) [5.3] 2.14%	(6.4) [4.2] -1.01%	(5.9) [4.1] -2.17%

(b)	$Zr_{34}Ti_{33}Cu_{33}$	$Zr_{34}Ti_{33}Ni_{33}$	$Zr_{20}Ti_{20}Ni_{20}Cu_{20}Al_{20}$	$Zr_{52}Ti_{5}Ni_{15}Cu_{18}Al_{10}$
40	(8.9) [29.1] 3.77%	(10.3) [25.3] 2.52%	(13.7) [44.4] 2.28%	(13.8) [34.9] 1.96%
60	(8.3) [22.3] 3.52%	(8.4) [17.8] 2.78%	(11.3) [40.8] 2.93%	(6.9) [20.9] 4.07%
80	(6.2) [16.2] 4.72%	(5.8) [6.1] 1.27%	(13.8) [32.5] 1.97%	(6.9) [17.2] 3.58%

Table 3.2 The volume fraction (%) of the amorphous phase estimated by the XRD patterns for (a) binary and (b) ternary and pentanary Zr-X alloy systems.

(a)	$Zr_{50}Al_{50}$	$Zr_{50}Cu_{50}$	$Zr_{50}Ni_{50}$	$Zr_{50}Ti_{50}$	$Zr_{25}Ti_{75}$	$Zr_{75}Ti_{25}$
40	<1	45	7	30	49	36
60	5	52	27	56	56	39
80	15	54	42	71	63	46
100	18	64	55	100	65	54

(b)	$Zr_{34}Ti_{33}Cu_{33}$	$Zr_{34}Ti_{33}Ni_{33}$	$Zr_{20}Ti_{20}Ni_{20}Cu_{20}Al_{20}$	$Zr_{52}Ti_5Ni_{15}Cu_{18}Al_{10}$
40	45	42	20	22
60	47	55	38	42
80	60	64	44	61
100	63	74	55	69

Table 3.3 Representative data on the final thickness (in unit of μm) of the Zr foils after different F&R cycles for (a) binary and (b) ternary and pentanary Zr-X alloy systems.

(a)	$Zr_{50}Al_{50}$	$Zr_{50}Ni_{50}$	$Zr_{50}Ti_{50}$	$Zr_{25}Ti_{75}$	$Zr_{75}Ti_{25}$
40	34.1	1.6	0.6	0.7	0.7
60	2.2	0.8	0.3	0.4	0.5
80	1.4	0.6	<0.1	<0.1	<0.1

(b)	$Zr_{34}Ti_{33}Cu_{33}$	$Zr_{34}Ti_{33}Ni_{33}$	$Zr_{20}Ti_{20}Ni_{20}Cu_{20}Al_{20}$	$Zr_{52}Ti_{5}Ni_{15}Cu_{18}Al_{10}$
40	0.5	0.4	21.9	0.8
60	0.4	0.3	19.9	0.4
80	0.2	0.2	15.4	0.3

Table 3.4 The SEM/EDS results illustrating the composition variation for the $Zr_{52}Ti_5Ni_{15}Cu_{18}Al_{10}$ alloy after different F&R cycles.

	Zr	Ti	Ni	Cu	Al
40	56.3±5.5	4.7±4.4	15.9±10.1	17.7±4.1	7.3±2.1
60	60.9±5.8	4.8±3.6	12.8±2.9	16.1±3.4	5.7±2.1
80	54.5±1.5	5.6±1.9	15.1±1.6	18.3±1.8	7.3±0.9

Table 3.5 The volume fraction (%) of the amorphous phase and the nanocrystalline size (nm) evaluated from TEM observations for some Zr-X alloy systems. The values shown in parentheses () are referred to the volume fraction.

	$Zr_{50}Cu_{50}$	$Zr_{50}Ti_{50}$	$Zr_{34}Ti_{33}Cu_{33}$	$Zr_{34}Ti_{33}Ni_{33}$	$Zr_{52}Ti_5Ni_{15}Cu_{18}Al_{10}$
40	--	(20%) 20-100	--	--	--
60	--	(40%) 5-20	--	--	--
80	(50%) 5-15	(80%) 2.5-5	--	--	--
90	(60%) 3-10	(100%) --	(40%) 10-50	(50%) 6-20	(30%) 20-150
100	(70%) 2.5-7.5	--	(50%) 5-20	(70%) 3-10	(50%) 10-100

Table 3.6 Microhardness data on the pentanary Zr-X alloy systems made by arc melting, drop casting and melt spinning processes.

Composition	$Zr_{20}Ti_{20}Ni_{20}Cu_{20}Al_{20}$	$Zr_{52}Ti_{5}Ni_{15}Cu_{18}Al_{10}$		
Hardness (H_v)	Arc melting	Arc melting	Drop casting	Melt spinning
	816	593	634	750

Table 4.1 Theoretical thickness (t_n, in unit of μm) and true strain ε_n of each elemental foil after different F&R cycles.

	40x F&R	60x F&R	80x F&R	100x F&R
t_n (Zr)	$6.9\text{x}10^{-11}$	$6.6\text{x}10^{-17}$	$6.3\text{x}10^{-23}$	$5.9\text{x}10^{-29}$
t_n (Al)	$9.3\text{x}10^{-11}$	$8.8\text{x}10^{-17}$	$8.4\text{x}10^{-23}$	$8.1\text{x}10^{-29}$
t_n (Cu)	$9.3\text{x}10^{-11}$	$8.8\text{x}10^{-17}$	$8.4\text{x}10^{-23}$	$8.1\text{x}10^{-29}$
t_n (Ni)	$8.3\text{x}10^{-11}$	$7.89\text{x}10^{-17}$	$7.5\text{x}10^{-23}$	$7.2\text{x}10^{-29}$
t_n (Ti)	$9.3\text{x}10^{-11}$	$8.8\text{x}10^{-17}$	$8.4\text{x}10^{-23}$	$8.1\text{x}10^{-29}$
ε_n	32	48	64	80

Table 4.2 Representative data on the estimated k values and the accumulated true strain ε_n after different F&R cycles for (a) binary and (b) ternary and pentanary Zr-X alloy systems.

(a)	$Zr_{50}Al_{50}$		$Zr_{50}Ni_{50}$		$Zr_{50}Ti_{50}$		$Zr_{25}Ti_{75}$		$Zr_{75}Ti_{25}$	
	k	ε_n	k	ε_n	k	ε_n	k	ε_n	k	ε_n
40	0.96	0.93	0.82	4.36	0.77	5.64	0.78	5.38	0.78	5.35
60	0.88	4.28	0.86	5.03	0.82	6.53	0.83	6.15	0.83	6.15
80	0.90	4.74	0.88	5.72	0.84	7.71	0.84	7.71	0.84	7.71

(b)	$Zr_{34}Ti_{33}Cu_{33}$		$Zr_{34}Ti_{33}Ni_{33}$		$Zr_{20}Ti_{20}Ni_{20}Cu_{20}Al_{20}$		$Zr_{52}Ti_{5}Ni_{15}Cu_{18}Al_{10}$	
	k	ε_n	k	ε_n	k	ε_n	k	ε_n
40	0.76	5.91	0.76	5.91	0.94	1.45	0.78	5.38
60	0.83	6.15	0.82	6.53	0.95	1.55	0.83	6.15
80	0.86	6.71	0.86	6.71	0.96	1.87	0.86	6.71

Table 4.3 Lattice and grain boundary diffusivity (D_L and δD_B) of each element at RT (25°C) and 50°C.

	Zr	Al	Cu	Ni	Ti
D_L at RT, m^2/s	1.48×10^{-38}	2.18×10^{-29}	5.87×10^{-40}	3.13×10^{-54}	4.37×10^{-36}
δD_B at RT, m^3/s	1.47×10^{-35}	9.43×10^{-29}	2.94×10^{-33}	2.43×10^{-35}	3.57×10^{-33}
D_L at 50°C, m^2/s	5.62×10^{-36}	1.84×10^{-27}	2.76×10^{-37}	2.24×10^{-50}	4.47×10^{-34}
δD_B at 50°C, m^3/s	7.07×10^{-34}	1.30×10^{-27}	7.58×10^{-32}	8.83×10^{-34}	7.39×10^{-32}

Table 4.4 Diffusion distances via lattice and grain boundary diffusion (X_L and X_{GB}, in unit of nm) per F&R cycle at RT (25°C) and 50°C.

	Zr	Al	Cu	Ni	Ti
X_L, at RT	6.89×10^{-10}	2.64×10^{-5}	1.37×10^{-10}	1.00×10^{-17}	1.18×10^{-8}
X_{GB}, at RT	6.86×10^{-4}	1.74	9.70×10^{-3}	8.82×10^{-4}	1.07×10^{-2}
X_L, at 50°C	1.34×10^{-8}	2.43×10^{-4}	2.97×10^{-9}	8.46×10^{-16}	1.23×10^{-7}
X_{GB}, at 50°C	4.75×10^{-3}	6.45	4.92×10^{-2}	5.32×10^{-3}	4.87×10^{-2}

Table 4.5 Comparison with the experimentally extracted (from TEM diffraction patterns) and theoretically calculated *d*-spacing values.

	$Zr_{50}Ti_{50}$	$Zr_{50}Cu_{50}$	$Zr_{34}Ti_{33}Cu_{33}$	$Zr_{52}Ti_5Cu_{18}Ni_{15}Al_{10}$
g (TEM)	0.348 Å^{-1}	0.415 Å^{-1}	0.398 Å^{-1}	0.373 Å^{-1}
d (TEM)	2.87 Å	2.41 Å	2.51 Å	2.68 Å
d (cal)	3.08 Å	2.88 Å	2.91 Å	2.93 Å

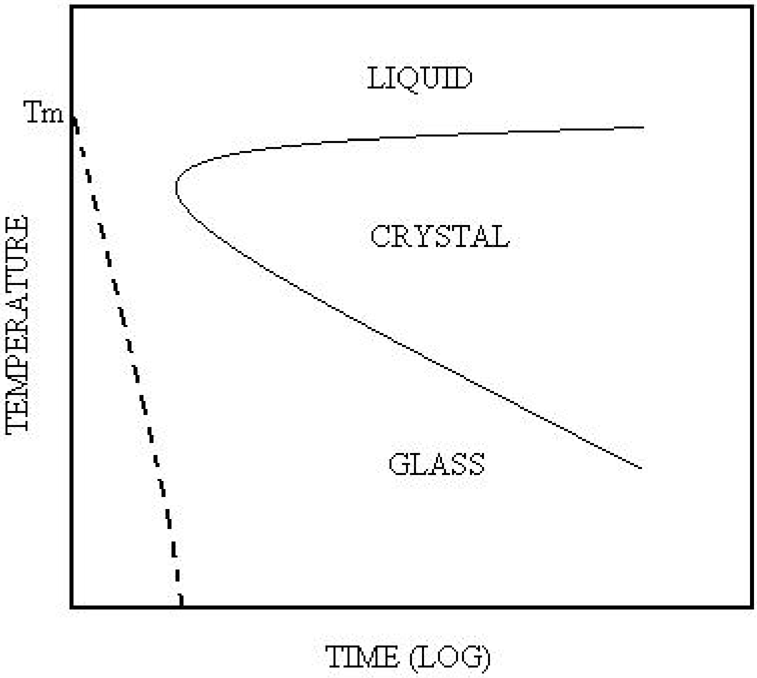

Figure 1.1 Schematic TTT diagram for crystal growth in an undercooled melt.

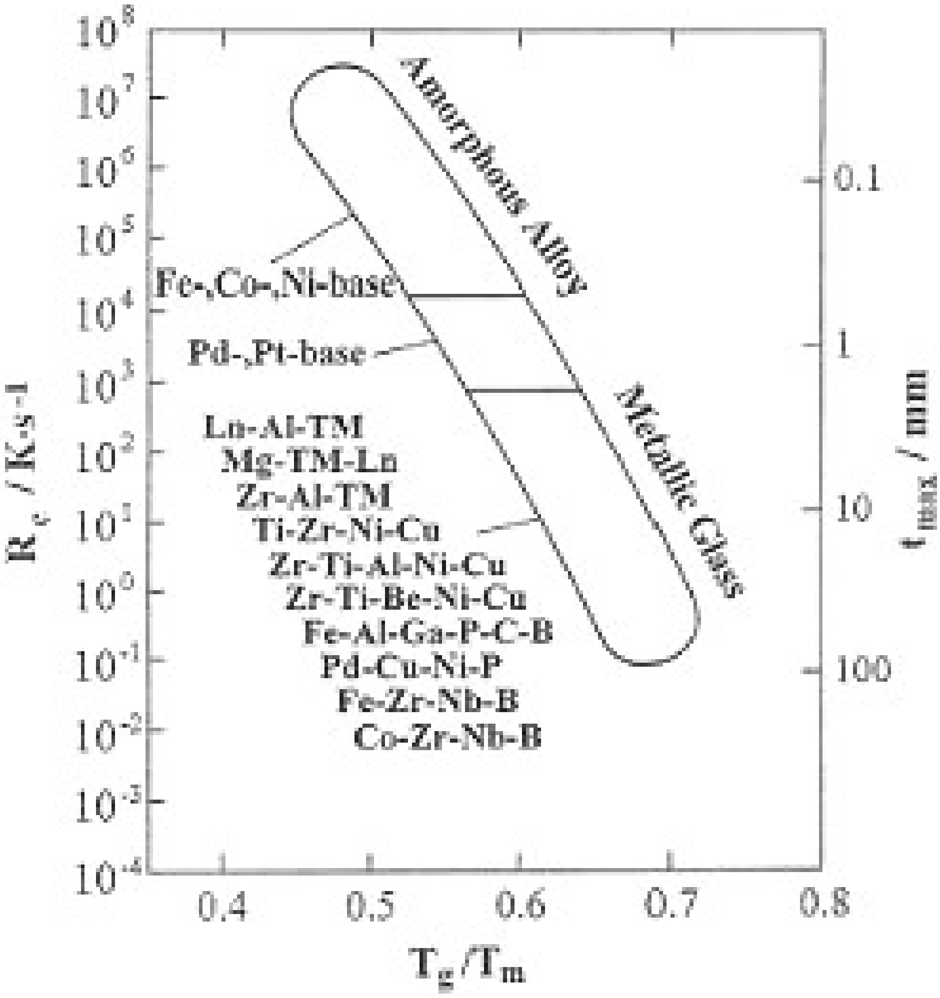

Figure 1.2 Relationship between the critical cooling rate (R_c), maximum sample thickness (t_{max}) and reduced glass transition temperature (T_g/T_m) for bulk amorphous alloys.

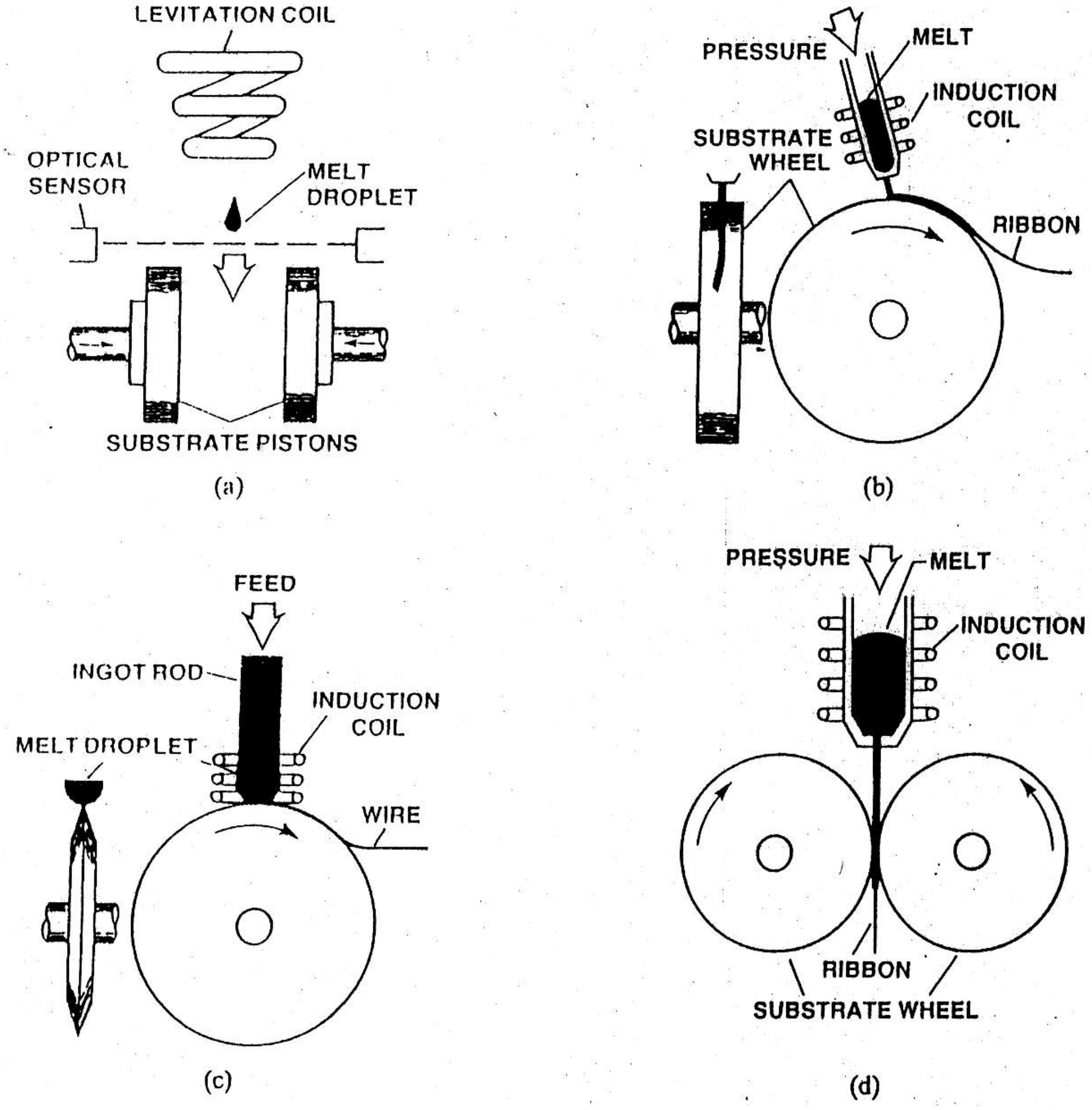

Figure 1.3 Schematic drawings of four quenching methods from the melt: (a) piston and anvil, (b) melt spinning, (c) melt extraction, and (d) twin roller quenching.

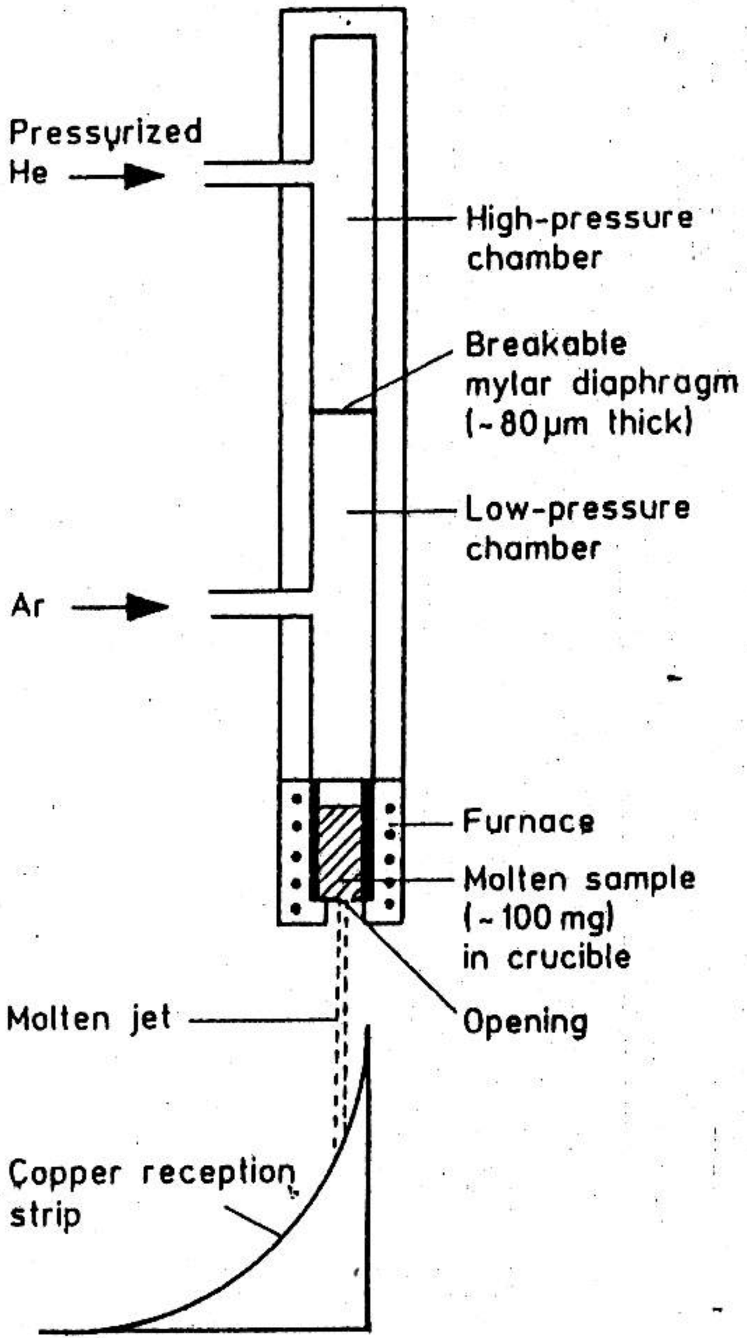

Figure 1.4 Schematic drawing of the splat quenching method.

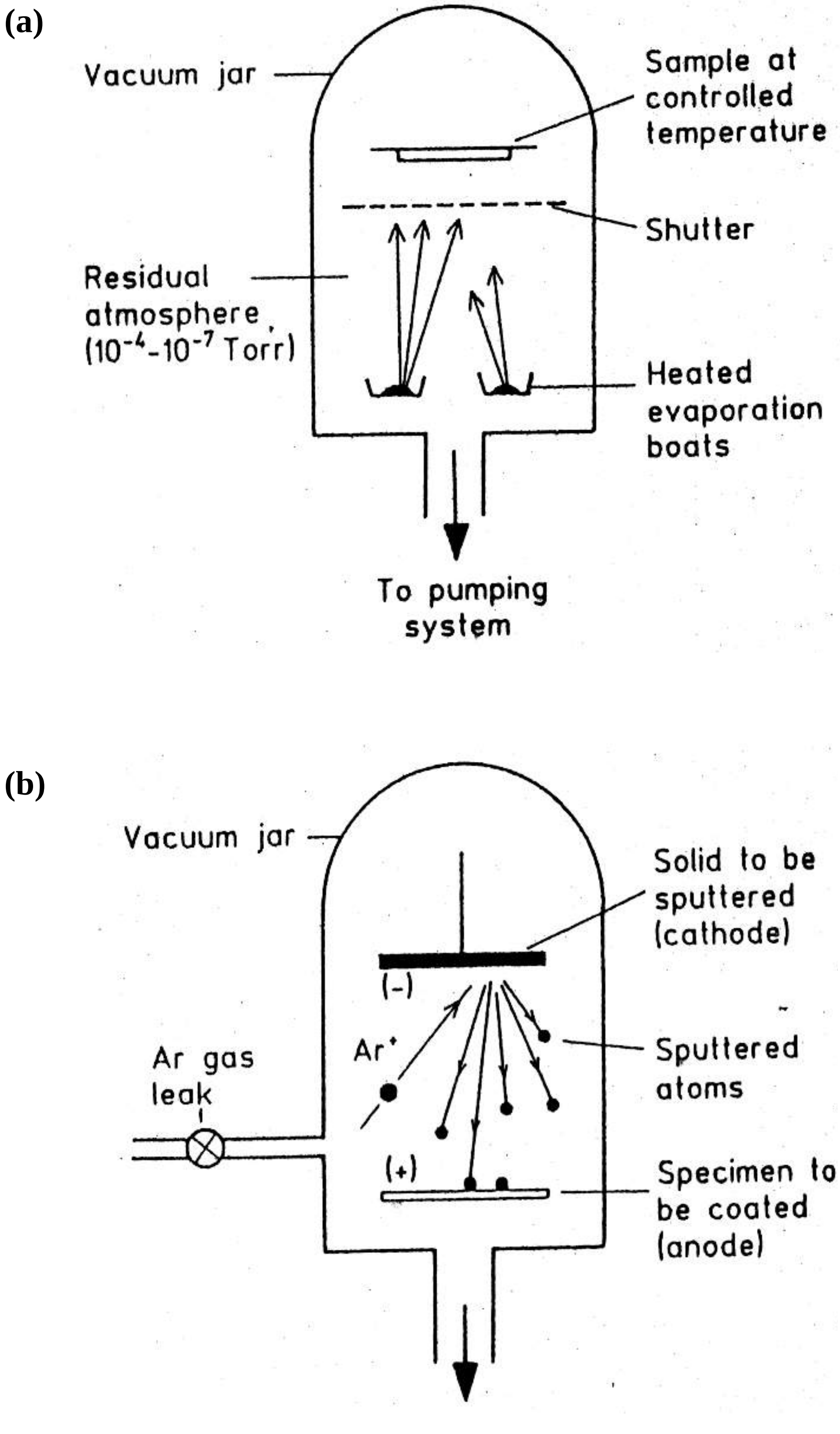

Figure 1.5 Schematic illustration showing the vapor quenching methods: (a) thermal evaporation, and (b) sputtering method.

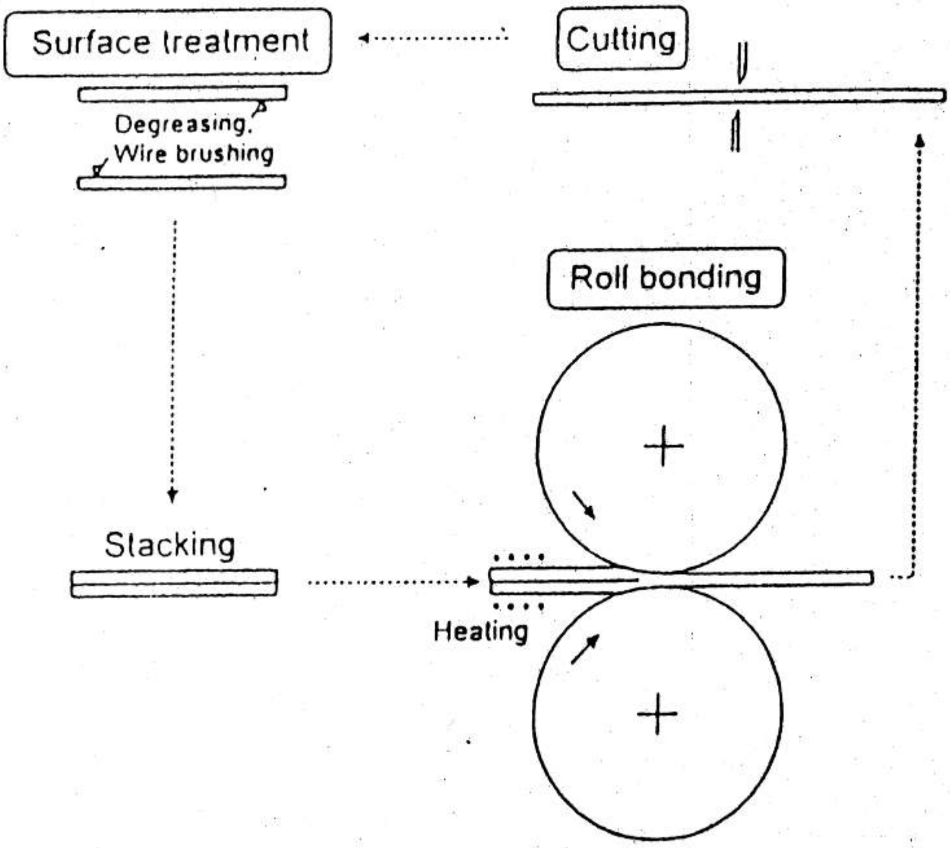

Figure 1.6 Schematic drawing of the accumulative roll-bonding (ARB) process.

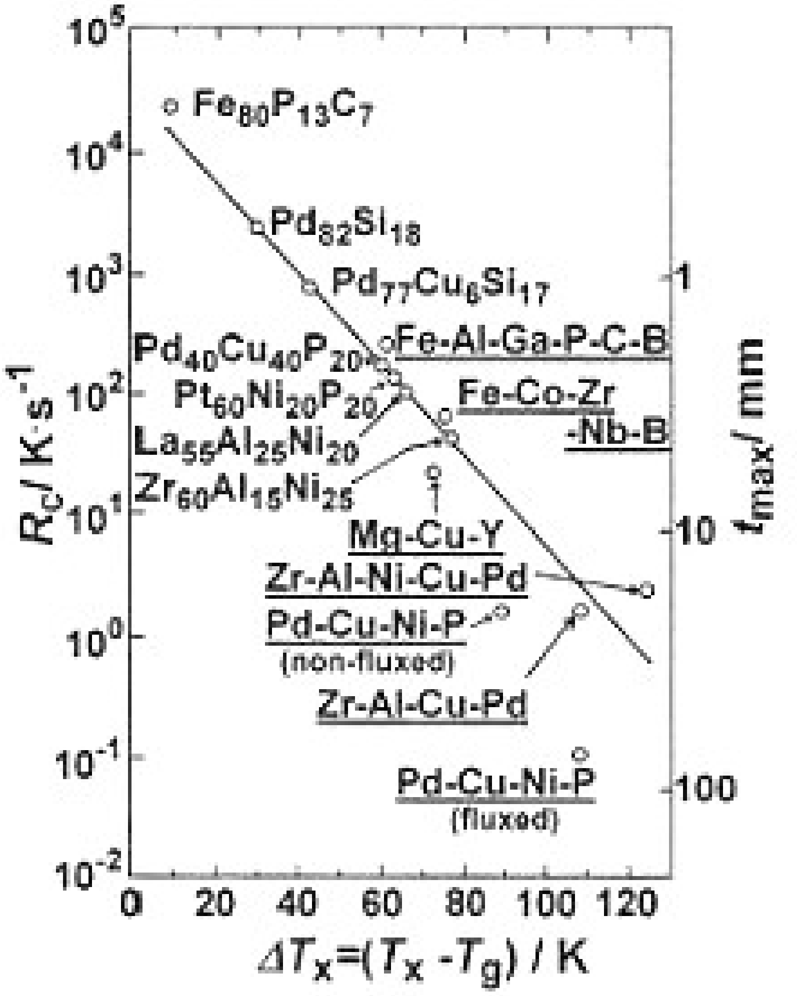

Figure 1.7 Relationship between the critical cooling rate (R_c), maximum sample thickness (t_{max}) and normalized ΔT_x for various metallic amorphous alloy systems.

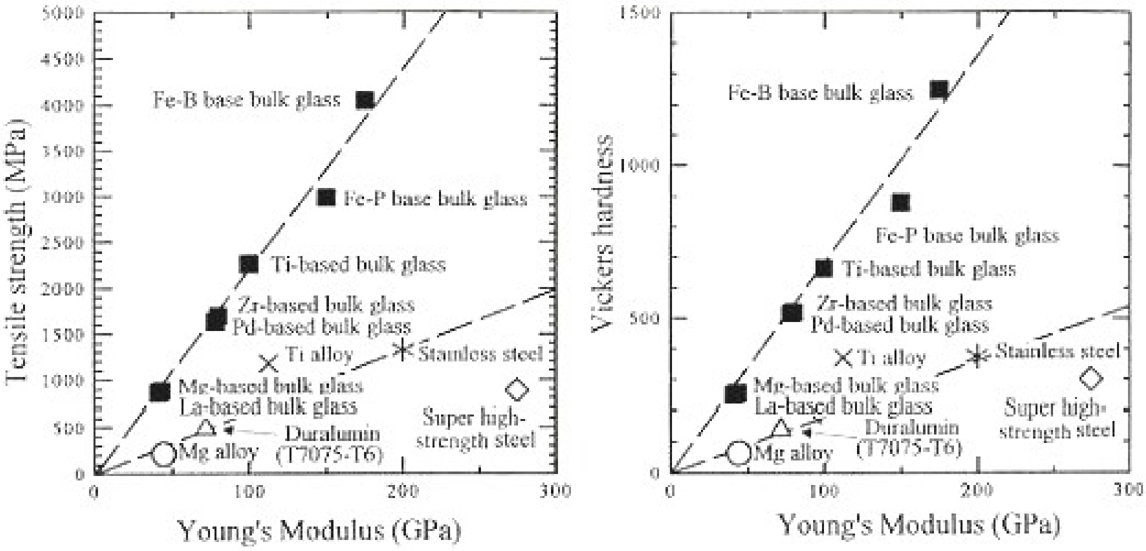

Figure 1.8 Relationship between the Young’s modulus, tensile strength and hardness for various metallic amorphous alloy systems.

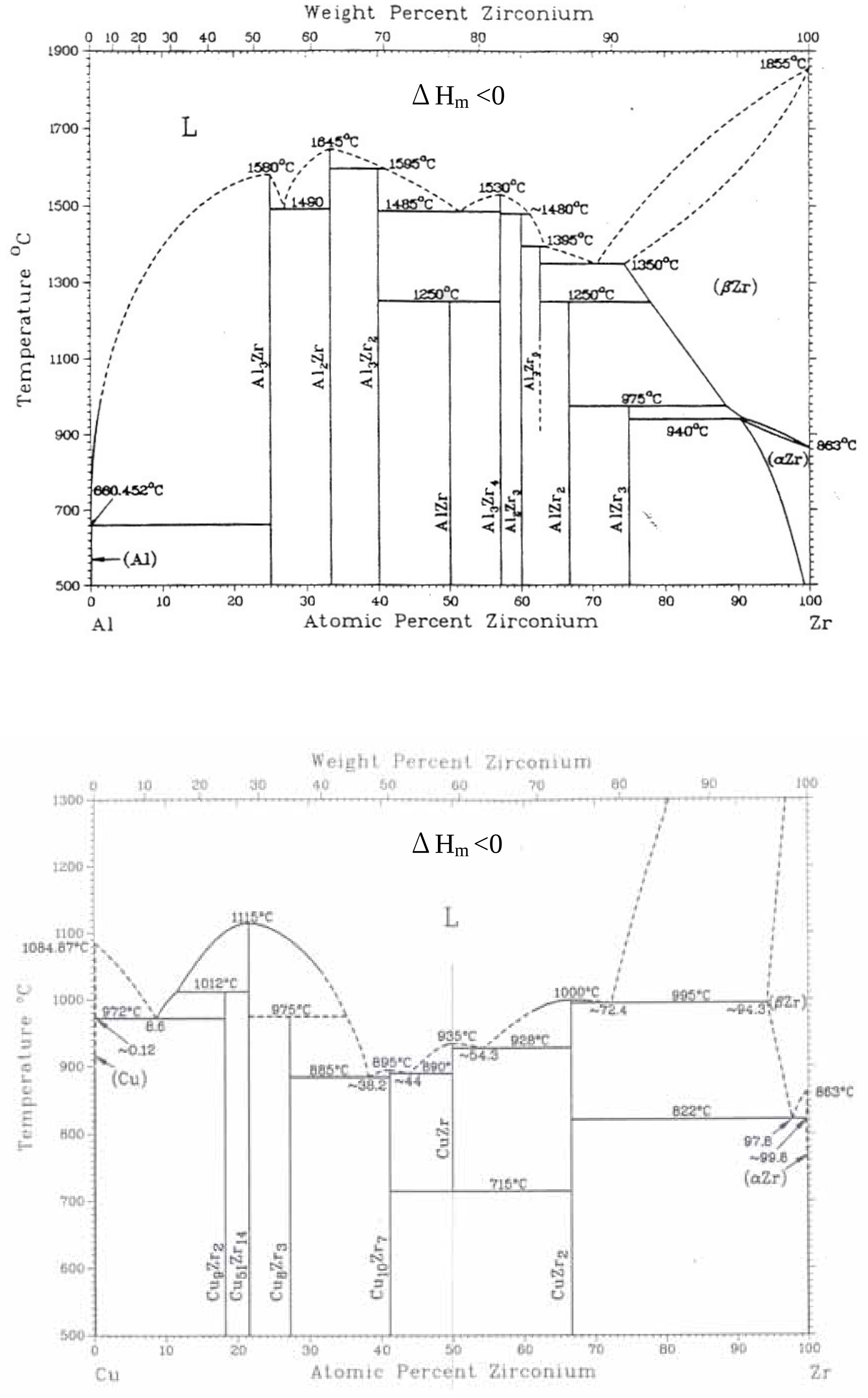

Figure 2.1 Binary phase diagrams for the Zr-Al, Zr-Cu, Zr-Ni, and Zr-Ti systems.

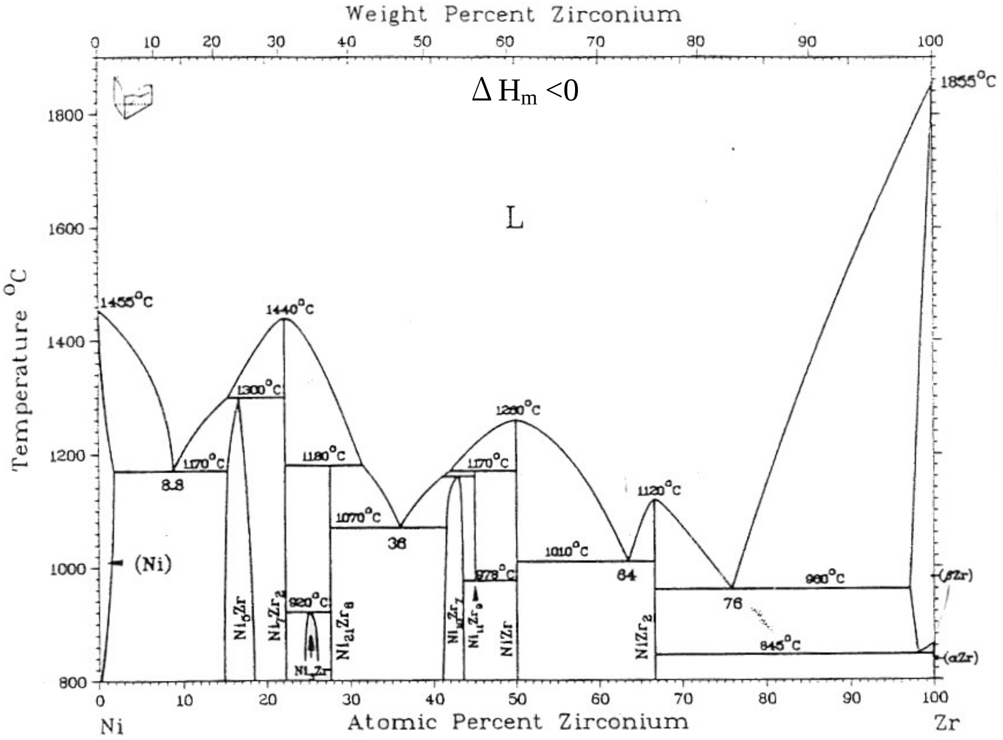
Weight Percent Zirconium
Δ H$_m$ <0
L
1855°C
1455°C
1440°C
1300°C
1260°C
1170°C
1180°C
1170°C
1120°C
1070°C
1010°C
978°C
960°C
920°C
845°C
8.8
36
64
76
(Ni)
Ni$_5$Zr
Ni$_7$Zr$_2$
Ni$_3$Zr
Ni$_{21}$Zr$_8$
Ni$_{10}$Zr$_7$
Ni$_{11}$Zr$_9$
NiZr
NiZr$_2$
(βZr)
(αZr)
Temperature °C
Atomic Percent Zirconium
Ni
Zr

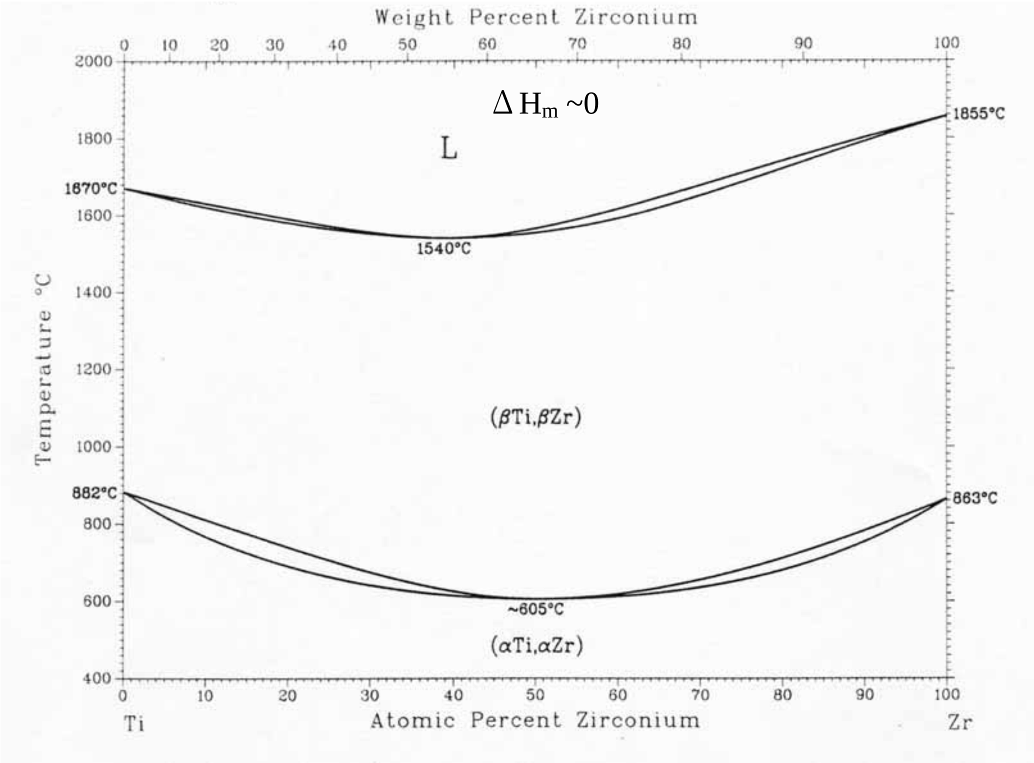
Weight Percent Zirconium
Δ H$_m$ ~0
L
1855°C
1670°C
1540°C
(βTi,βZr)
882°C
863°C
~605°C
(αTi,αZr)
Temperature °C
Atomic Percent Zirconium
Ti
Zr

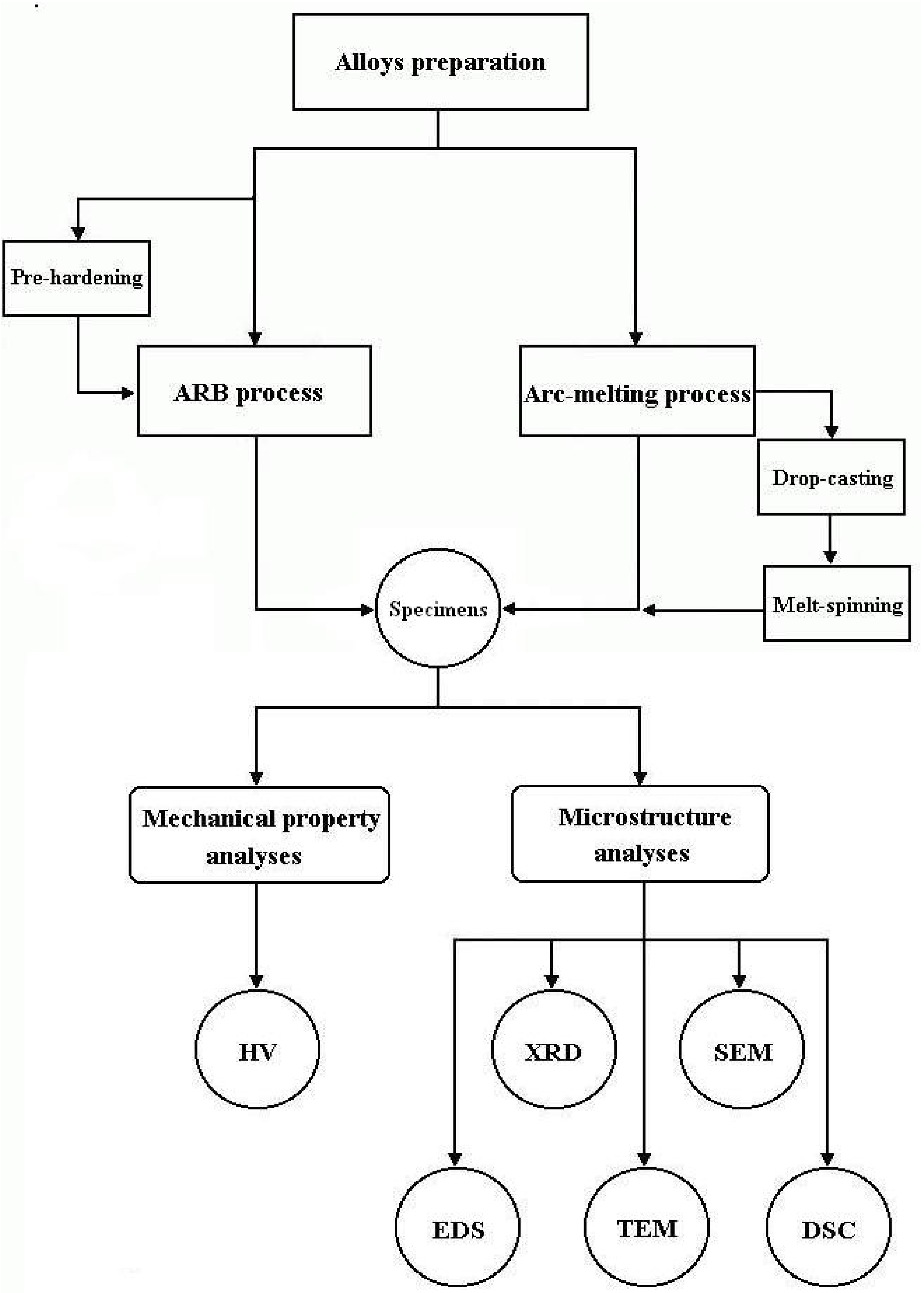

Figure 2.2 Flow chart showing the experiment procedures. The pre-hardening step was applied on the Cu foils, rendering the initial Cu foils of t_o= 102 μm and H_v= 46 to the foils applied for ARB with t_f= 30 μm and H_v= 131.

Figure 2.3 Photograph of the HF 200×200 cold and hot rolling machine.

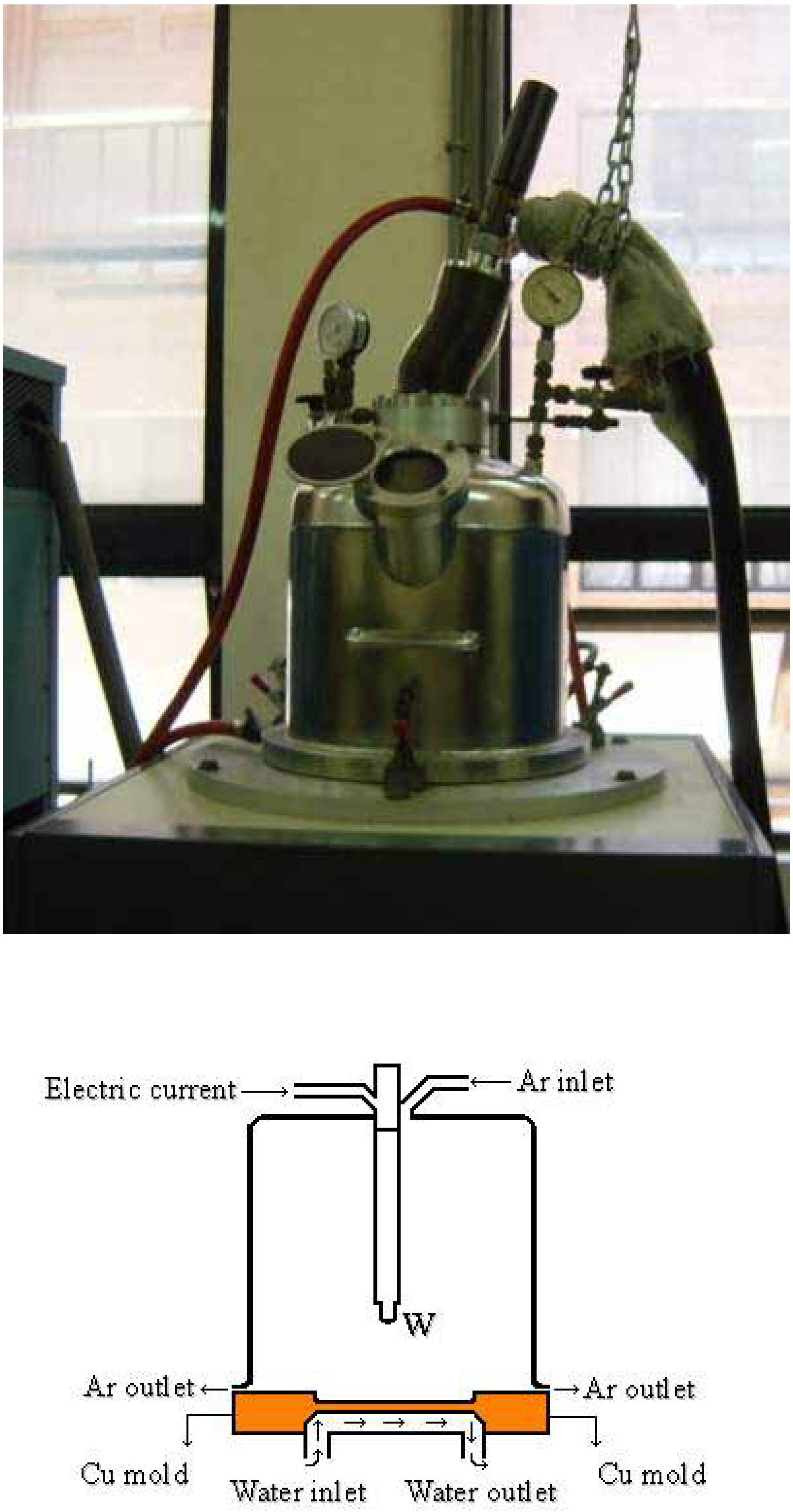

Figure 2.4 Photograph and schematic drawing of the arc melting device.

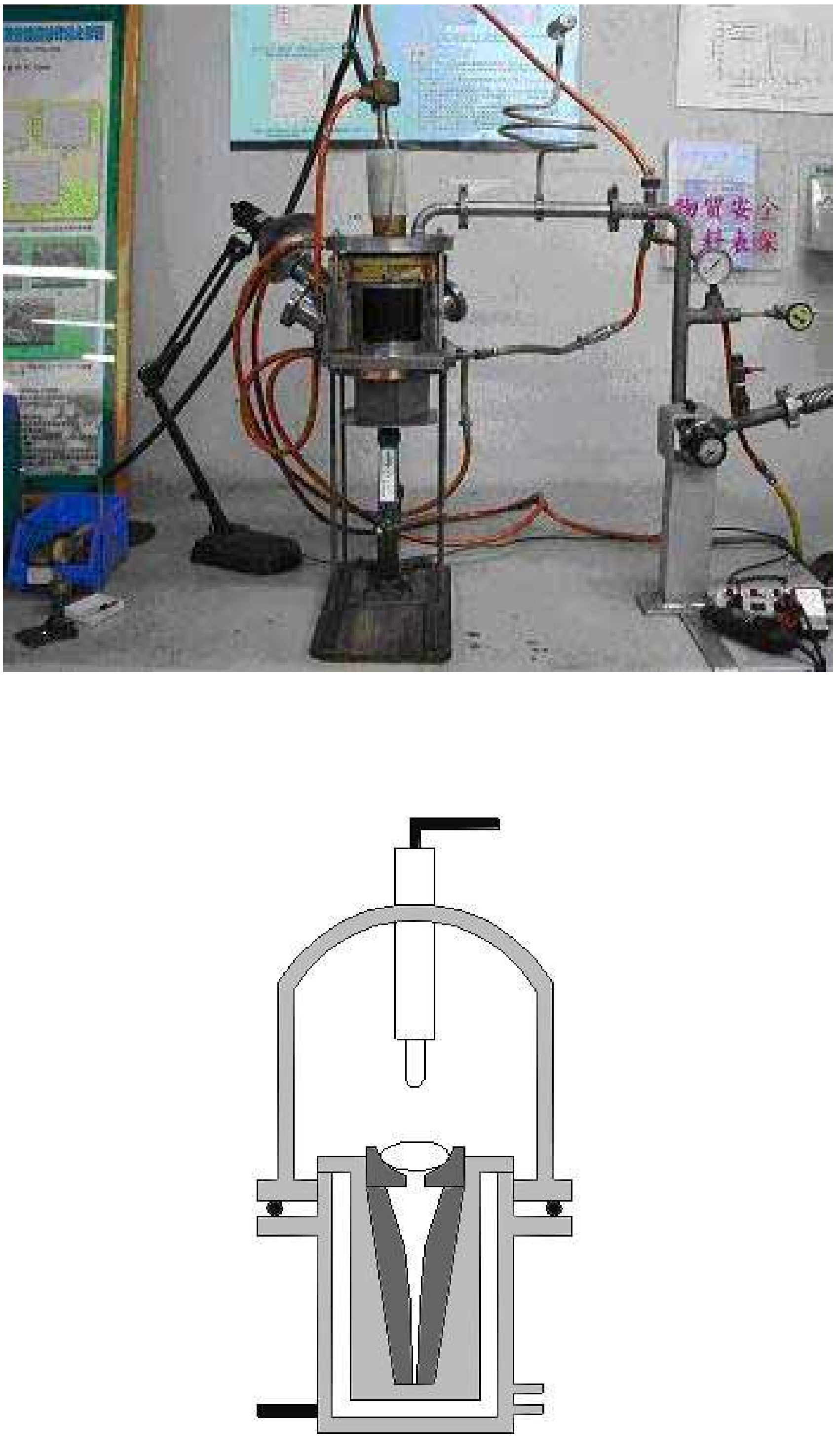

Figure 2.5 Photograph and schematic drawing of the drop casting instrument.

Figure 2.6 Photograph of the melt spinning devices.

Figure 2.7 Photograph of the Gatan 691 precision ion polishing system.

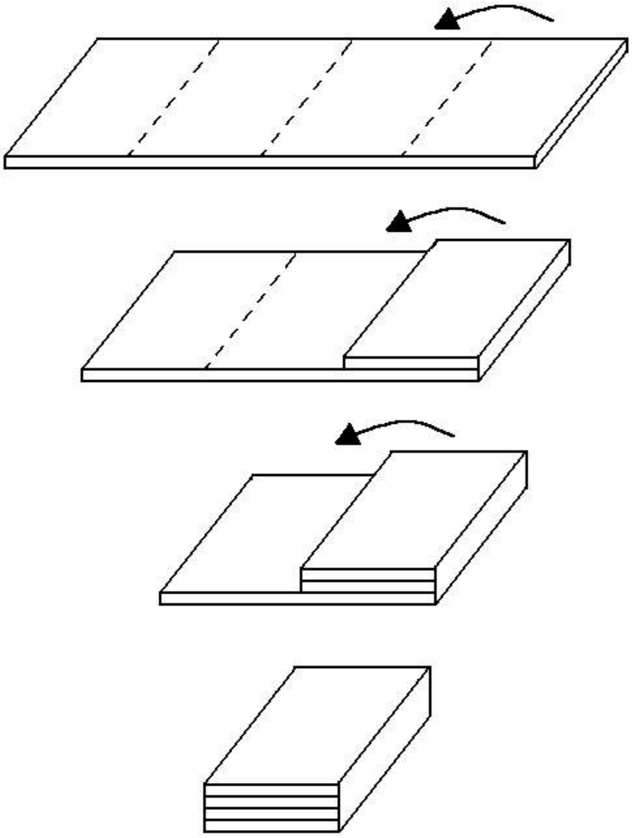

Figure 3.1 Brief draft revealing the step of manual folding before ARB.

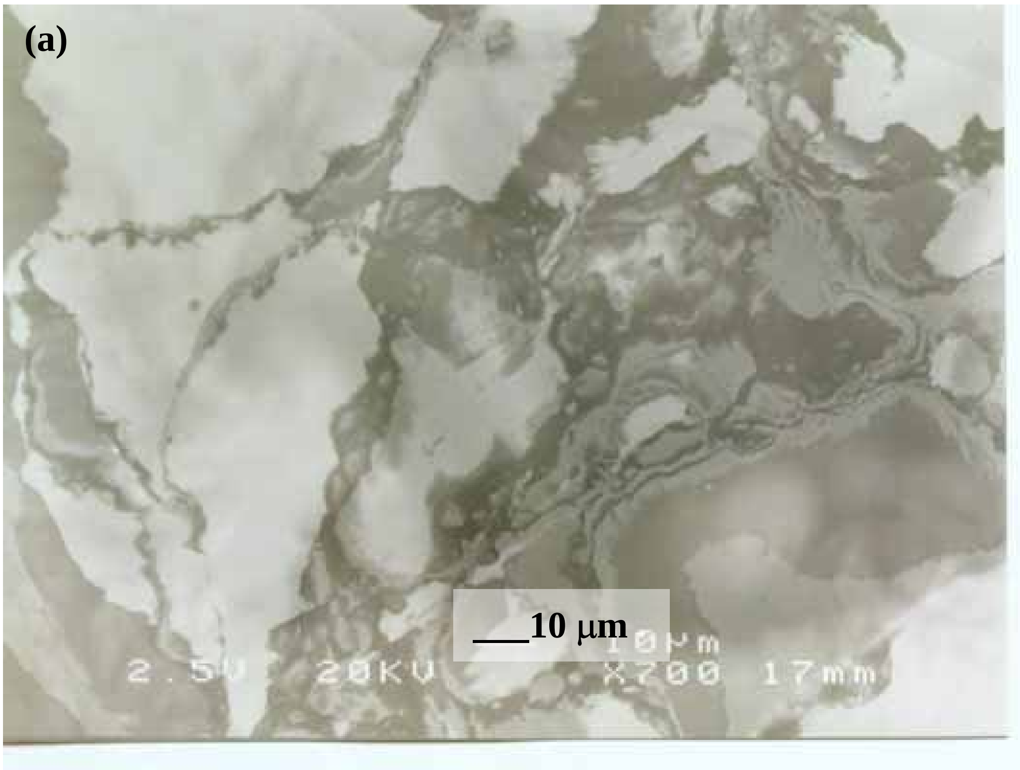

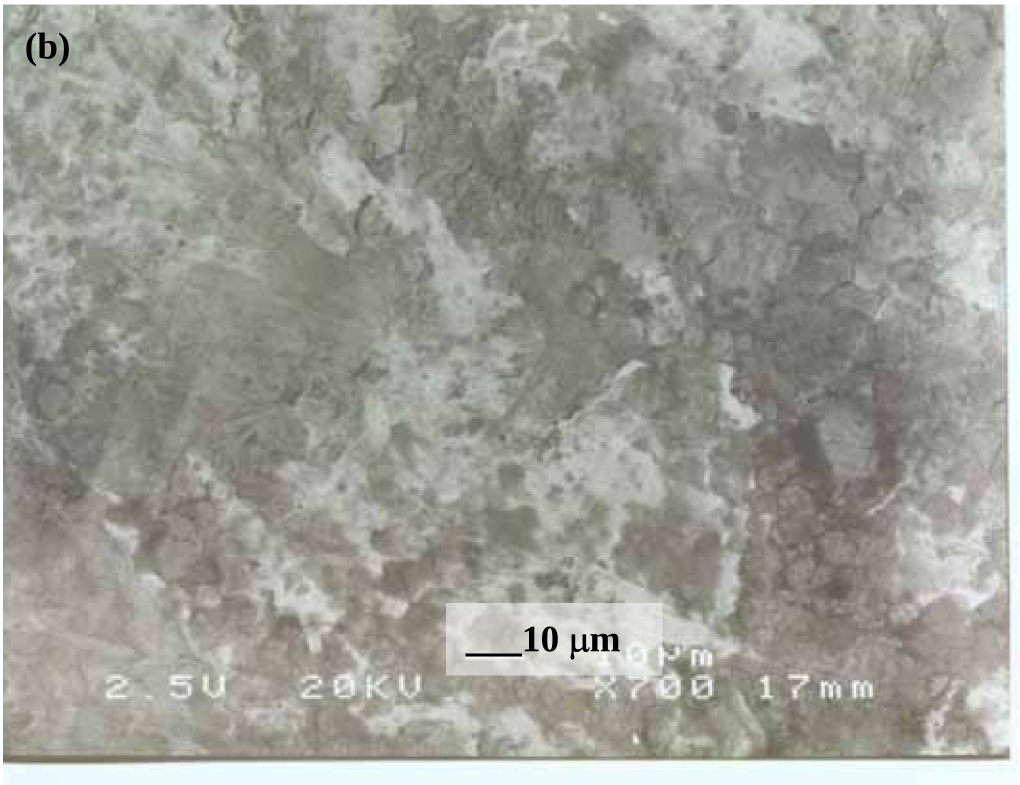

Figure 3.2 SEM/BEI of the ARB samples ($Zr_{20}Ti_{20}Ni_{20}Cu_{20}Al_{20}$) after different roll bonding cycles at room temperature: (a) 40 cycles, (b) 60 cycles, (c) 80 cycles.

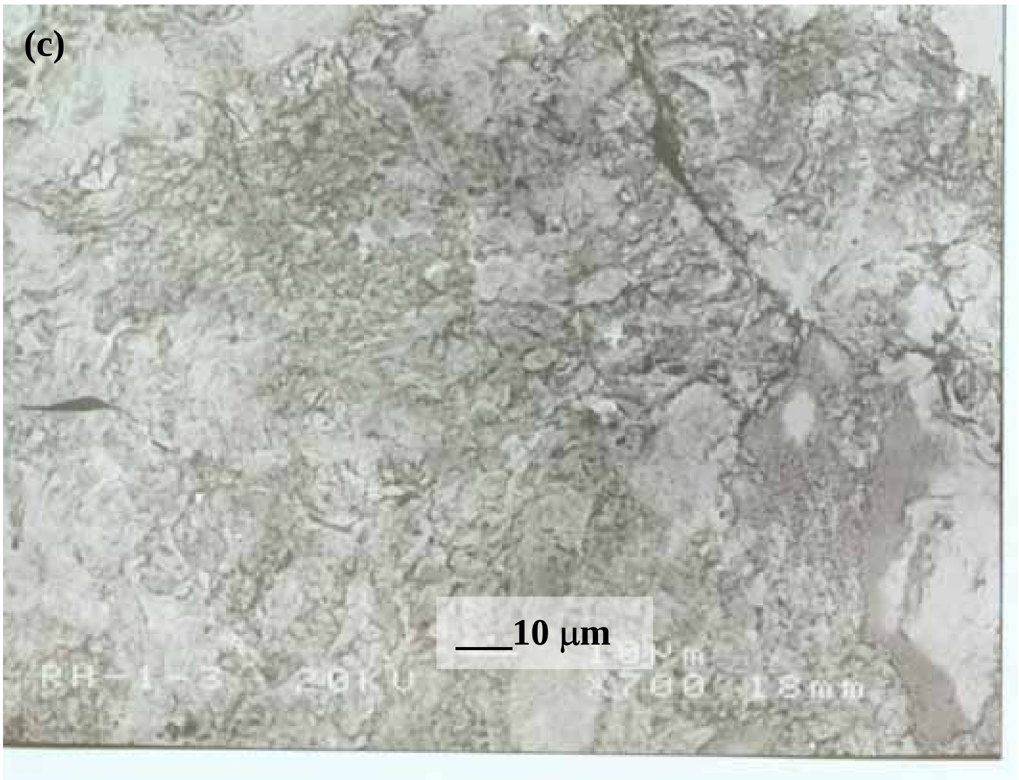
(c)
___10 μm
RA-1-3 20KU 10μm X700 18mm

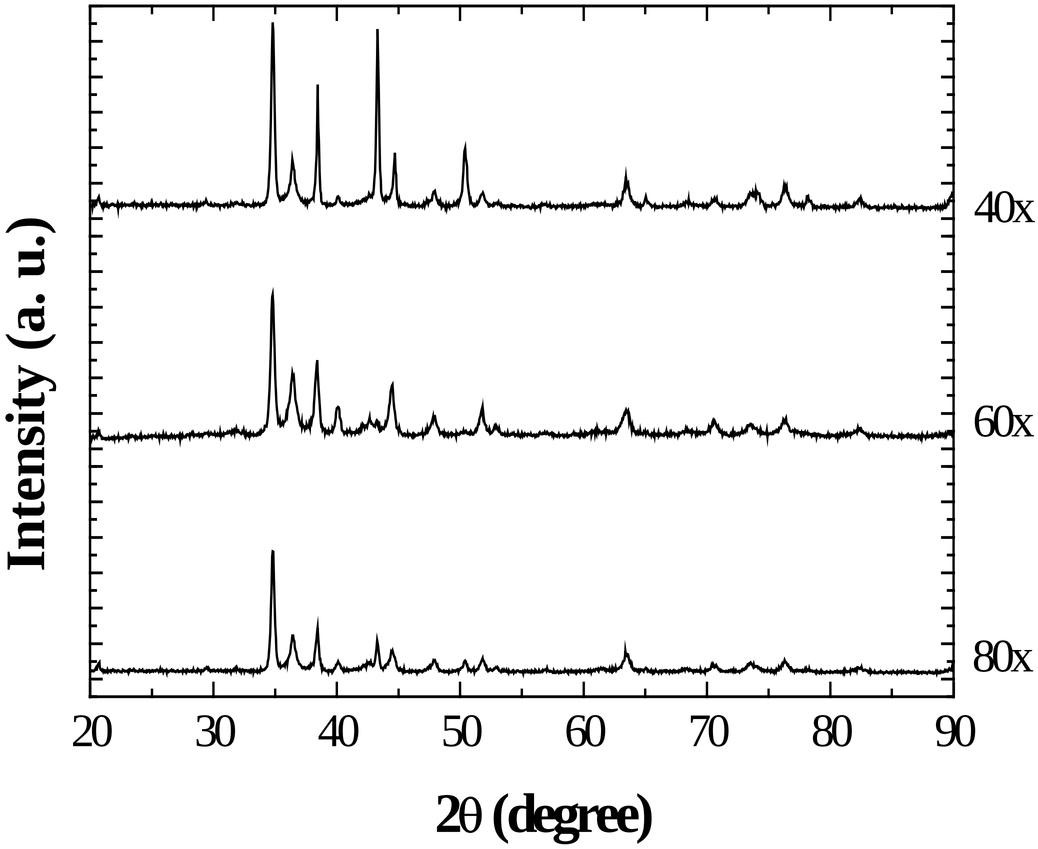

Figure 3.3 XRD patterns of the ARB samples ($Zr_{20}Ti_{20}Al_{20}Cu_{20}Ni_{20}$) after different roll bonding cycles at 250 ^{o}C.

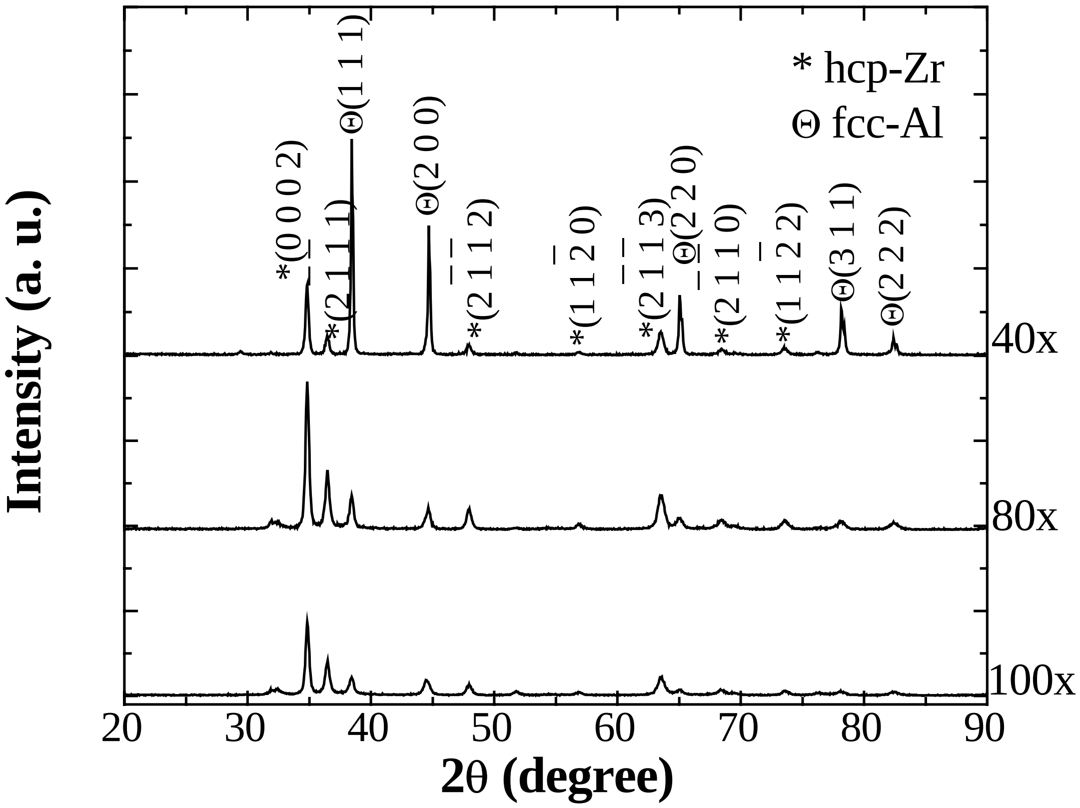

Figure 3.4 XRD patterns of the $Zr_{50}Al_{50}$ specimen after different roll bonding cycles at room temperature.

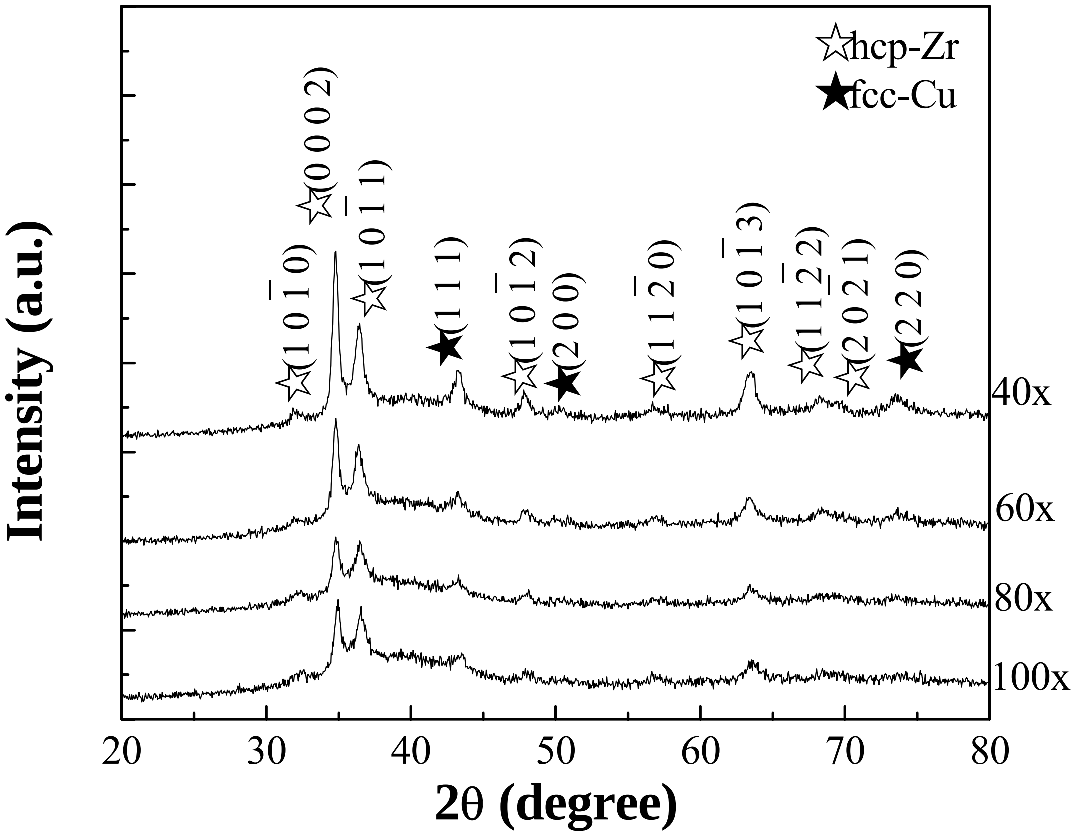

Figure 3.5 XRD patterns of the $Zr_{50}Cu_{50}$ specimen after different roll bonding cycles at room temperature.

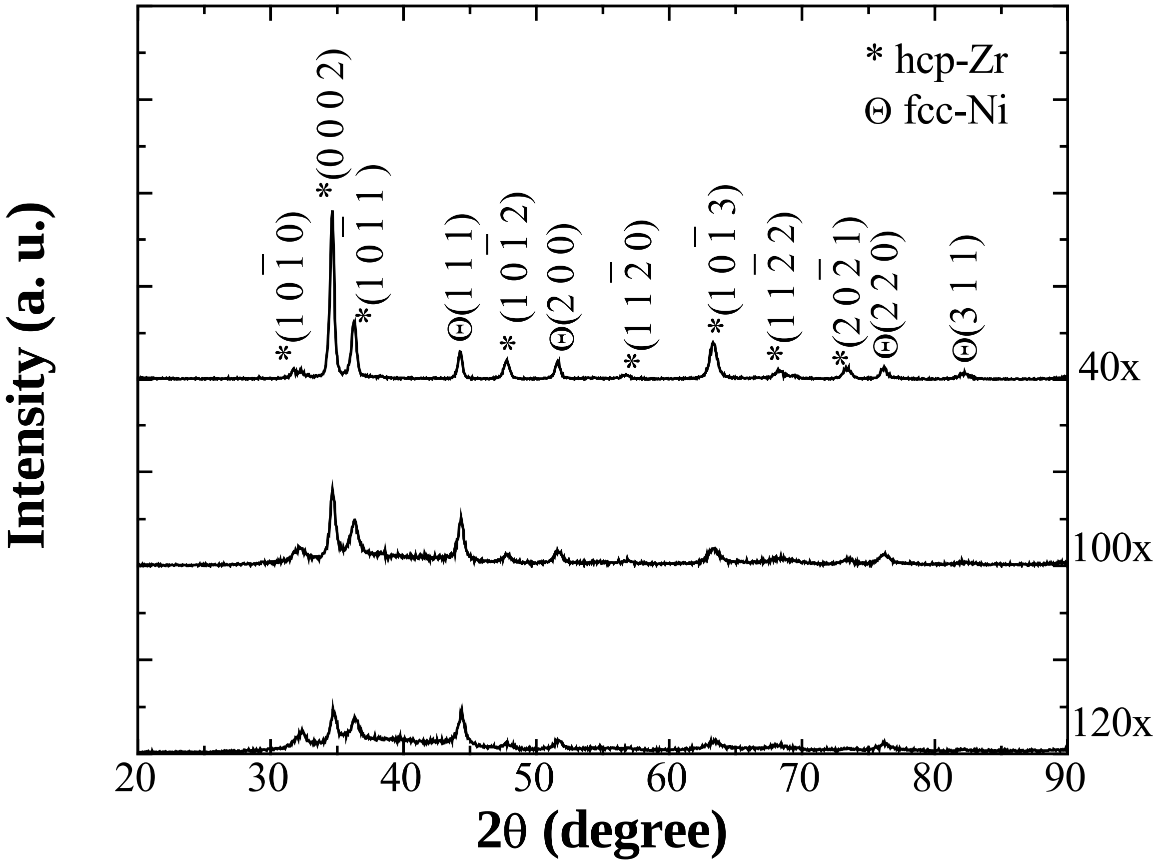

Figure 3.6 XRD patterns of the $Zr_{50}Ni_{50}$ specimen after different roll bonding cycles at room temperature.

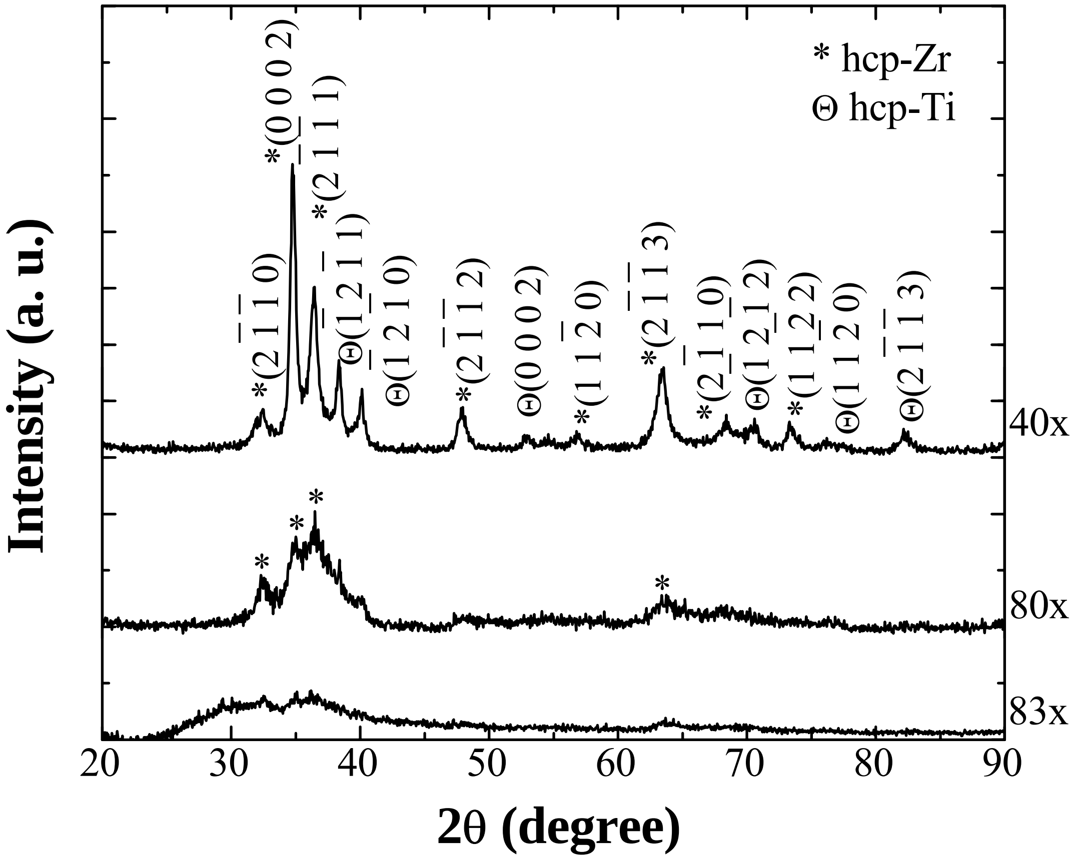

Figure 3.7 XRD patterns of the $Zr_{50}Ti_{50}$ specimen after different roll bonding cycles at room temperature.

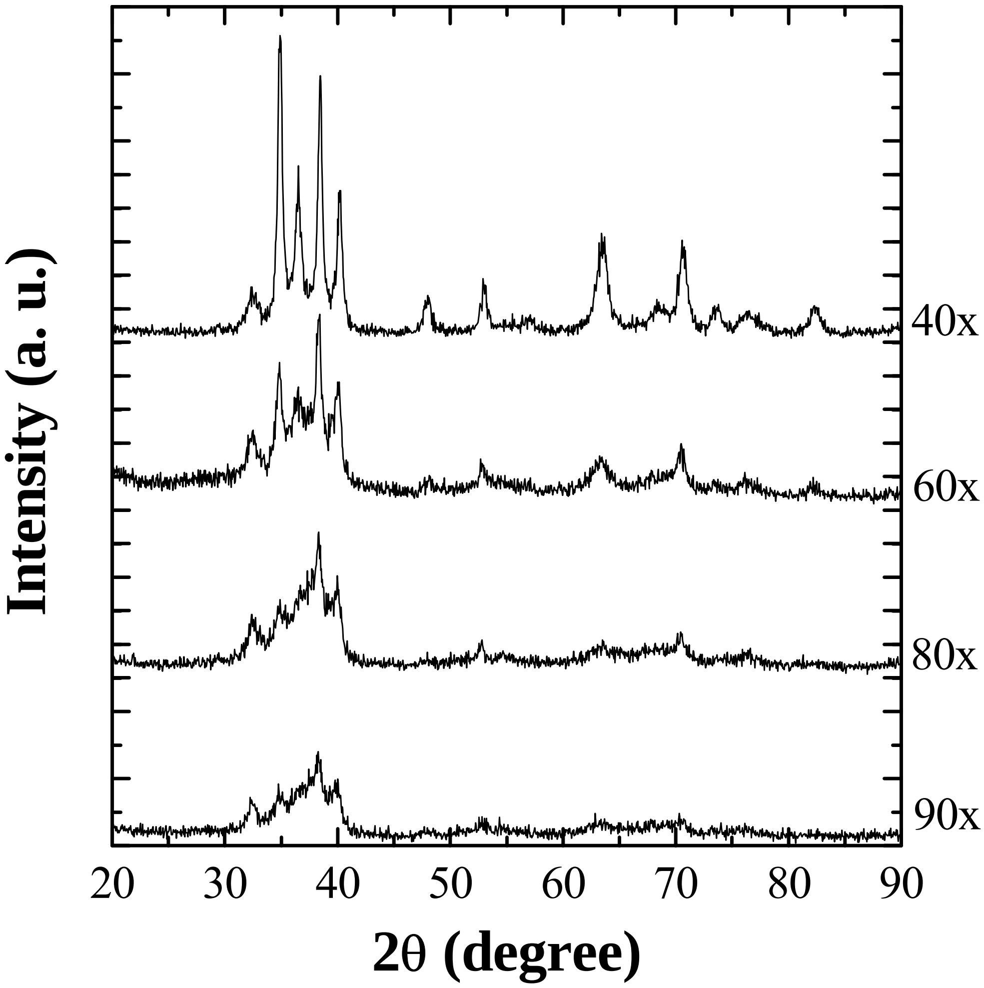

Figure 3.8 XRD patterns of the $Zr_{25}Ti_{75}$ specimen after different roll bonding cycles at room temperature.

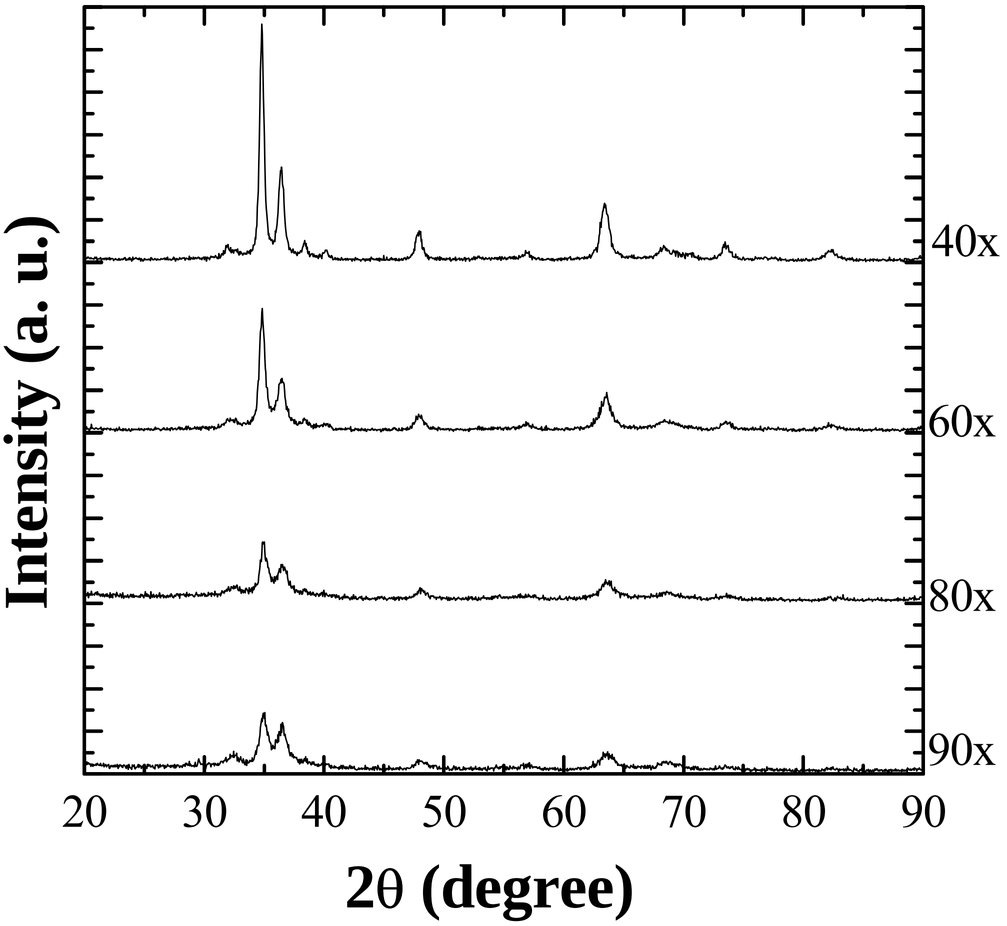

Figure 3.9 XRD patterns of the $Zr_{75}Ti_{25}$ specimen after different roll bonding cycles at room temperature.

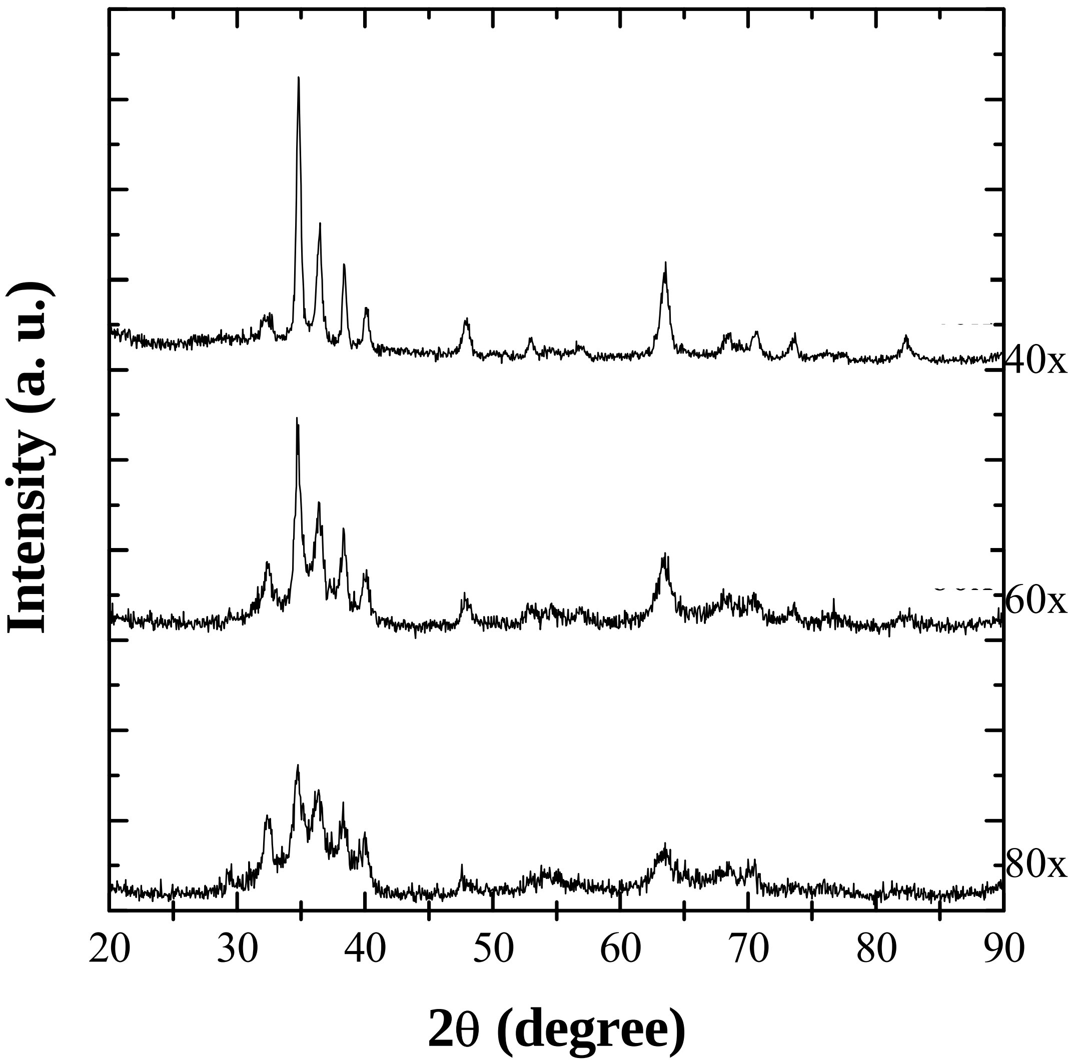

Figure 3.10 XRD patterns of the $Zr_{50}Ti_{50}$ specimen subjected to only one time of manually folded step before ARB.

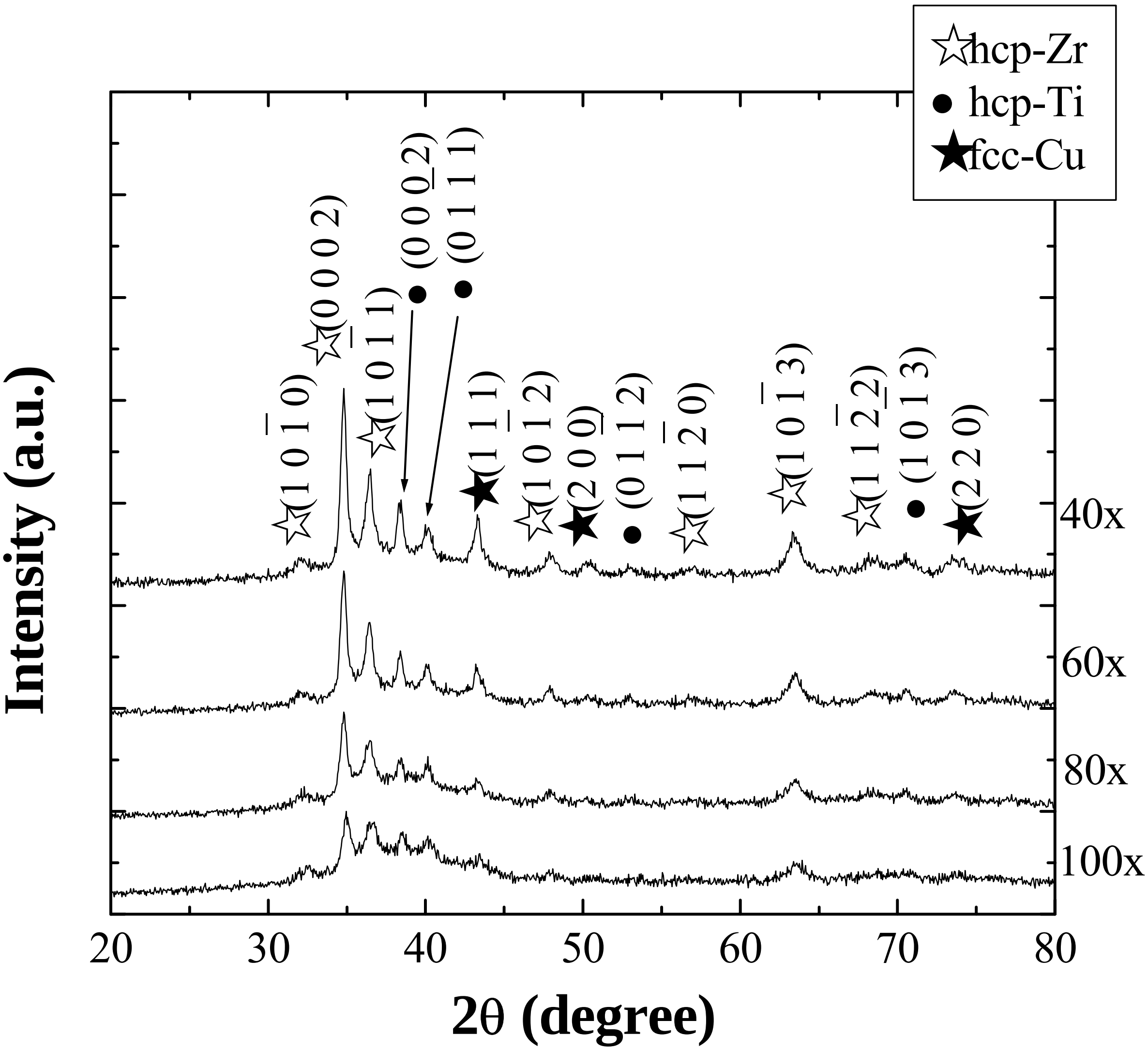

Figure 3.11 XRD patterns of the $Z_{34}Ti_{33}Cu_{33}$ specimen after different roll bonding cycles at room temperature.

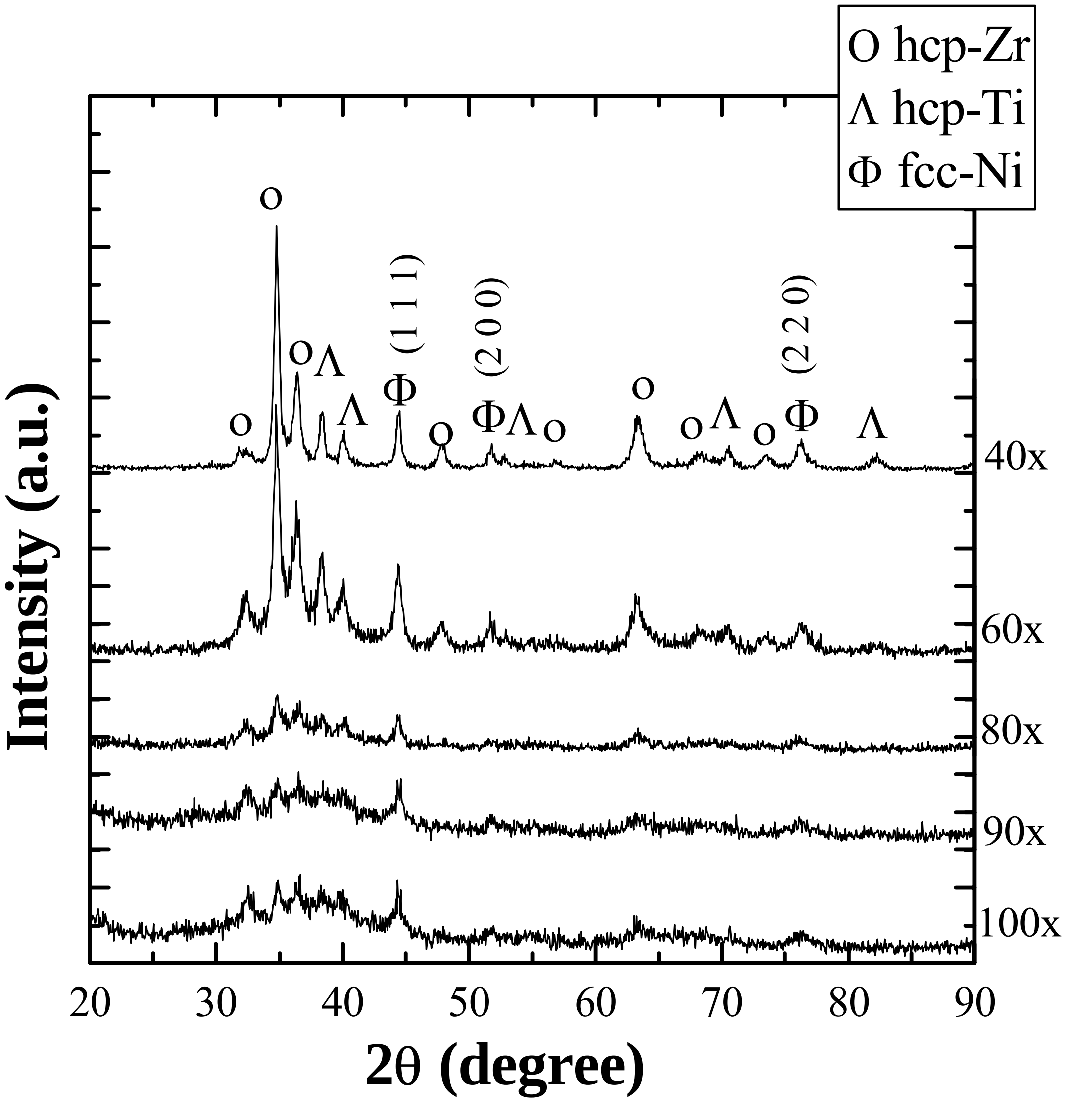

Figure 3.12 XRD patterns of the $Z_{34}Ti_{33}Ni_{33}$ specimen after different roll bonding cycles at room temperature.

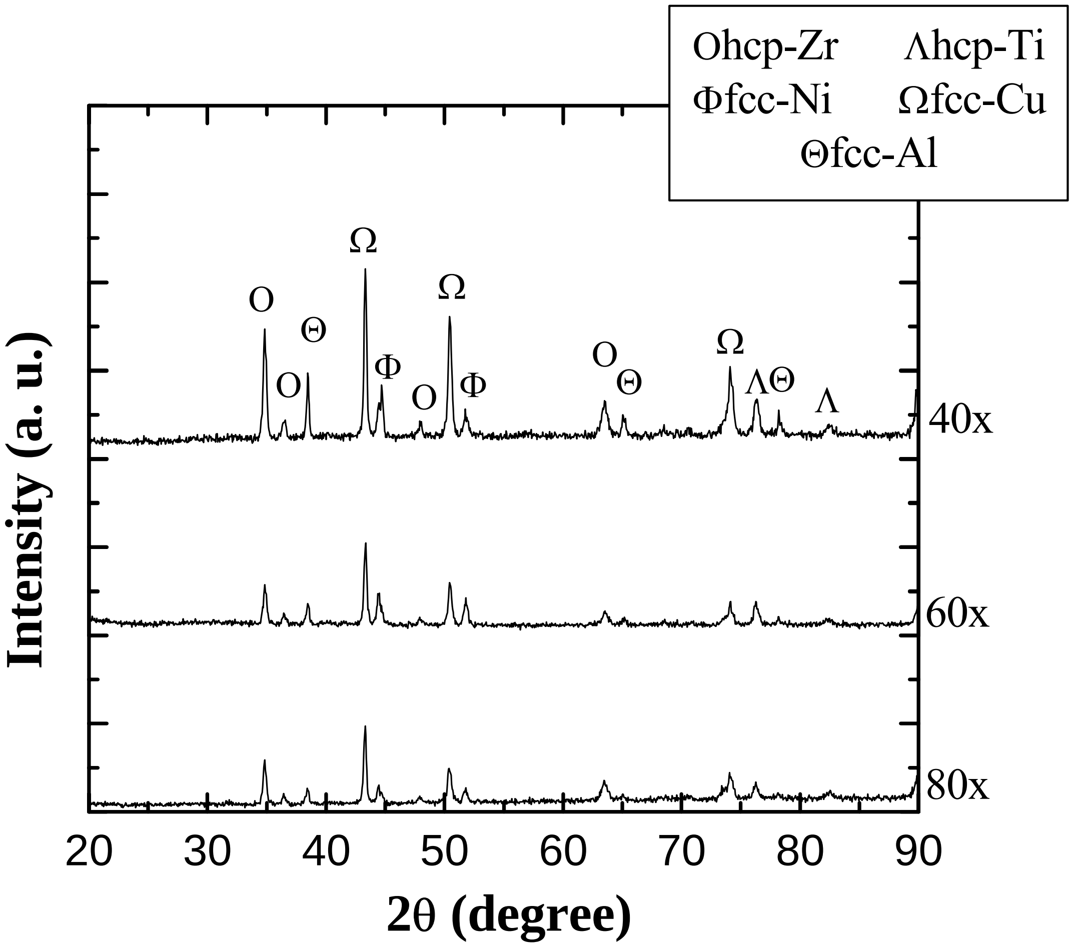

Figure 3.13 XRD patterns of the $Zr_{20}Ti_{20}Ni_{20}Cu_{20}Al_{20}$ specimen after different roll bonding cycles at room temperature.

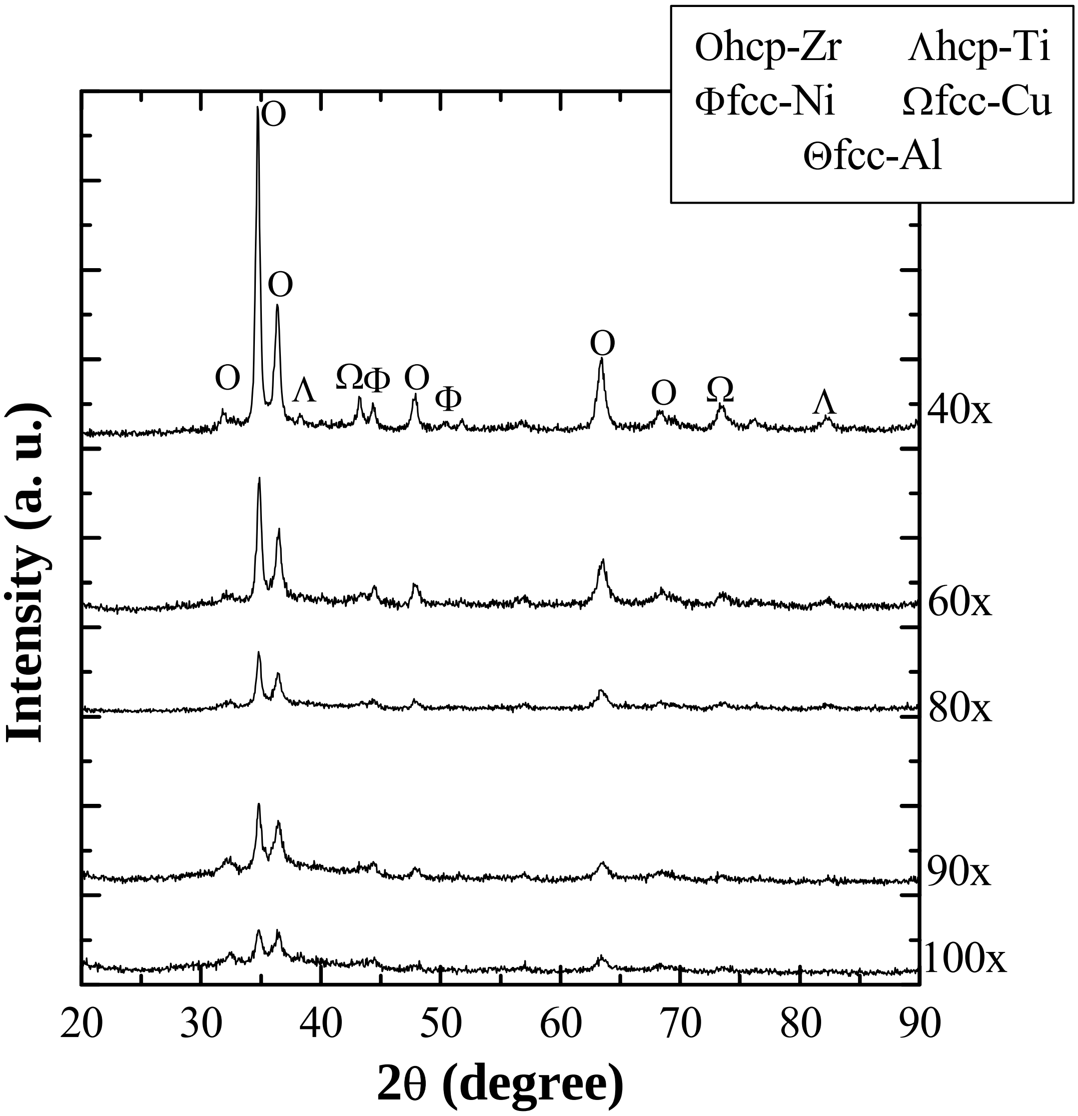

Figure 3.14 XRD patterns of the $Zr_{52}Ti_5Ni_{15}Cu_{18}Al_{10}$ specimen after different roll bonding cycles at room temperature.

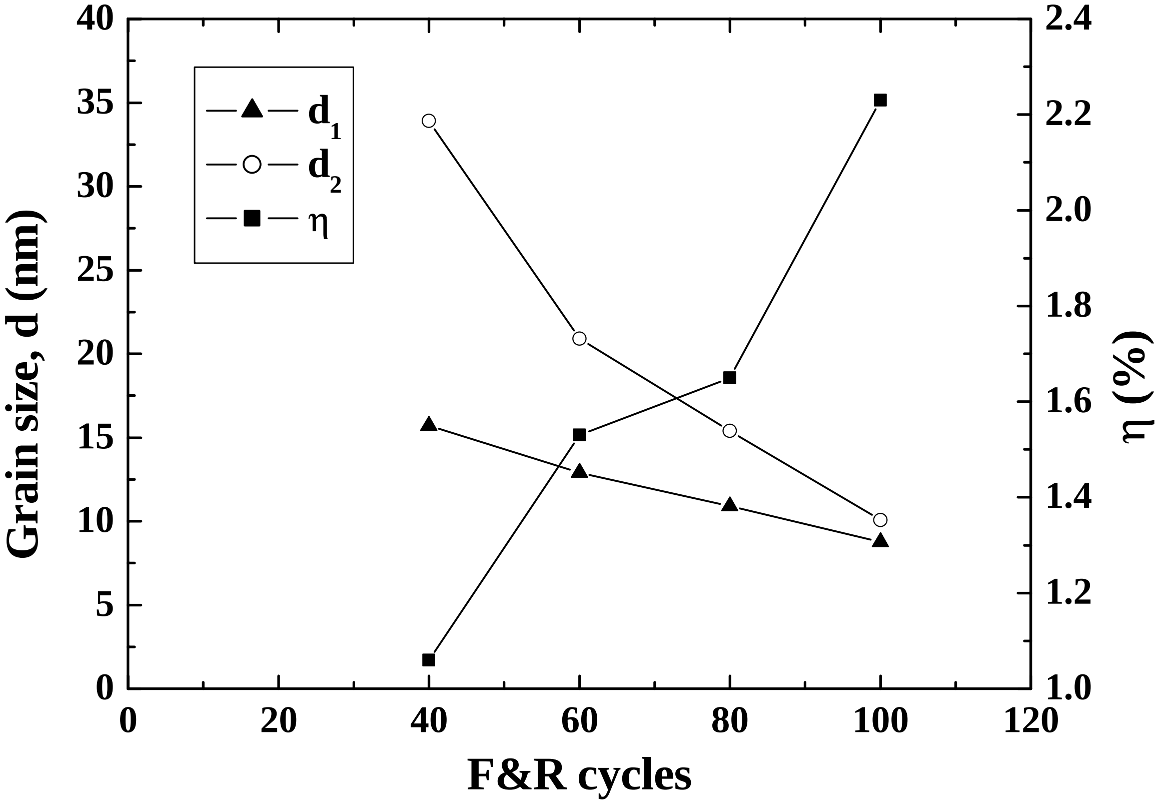

Figure 3.15 The variation of the extracted Zr grain sizes by Eqns. (3.1) and (3.2), d_1 and d_2, together with the microstrain η as a function of rolling cycles, determined from XRD peak broadening analysis for $Zr_{50}Ni_{50}$.

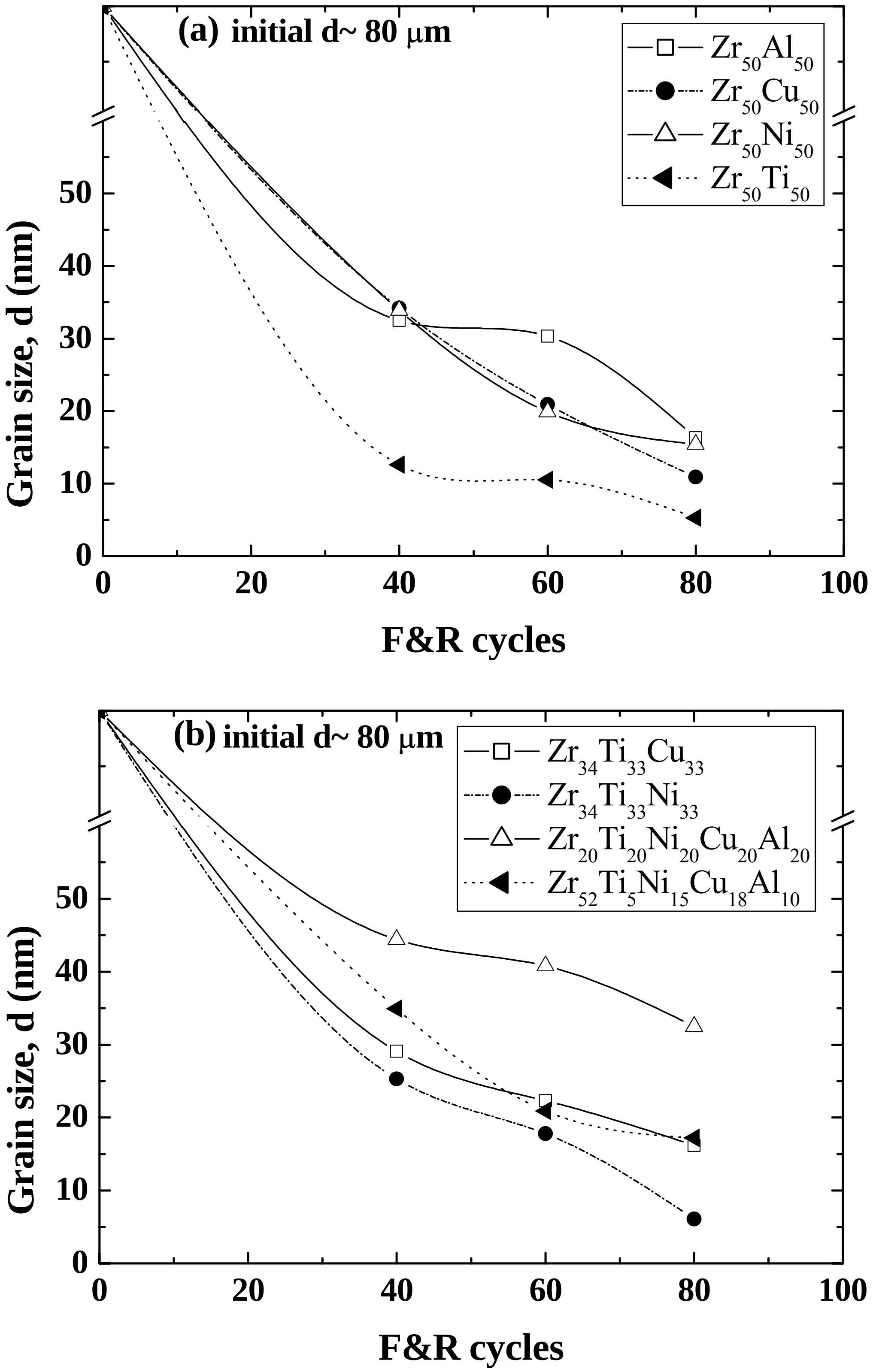

Figure 3.16 The variations of the nanocrystalline grain size of Zr estimated by Eqn. (3.2) for (a) binary and (b) ternary and pantanary alloys as a function of F&R cycles, based on the XRD results.

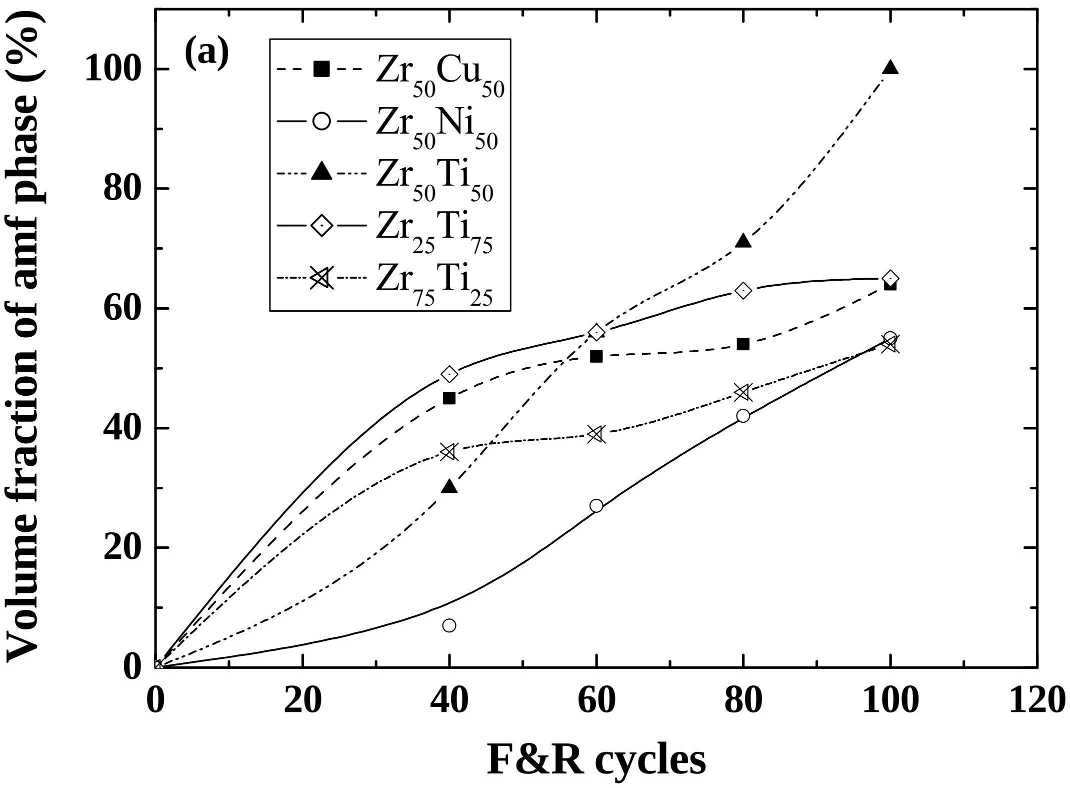

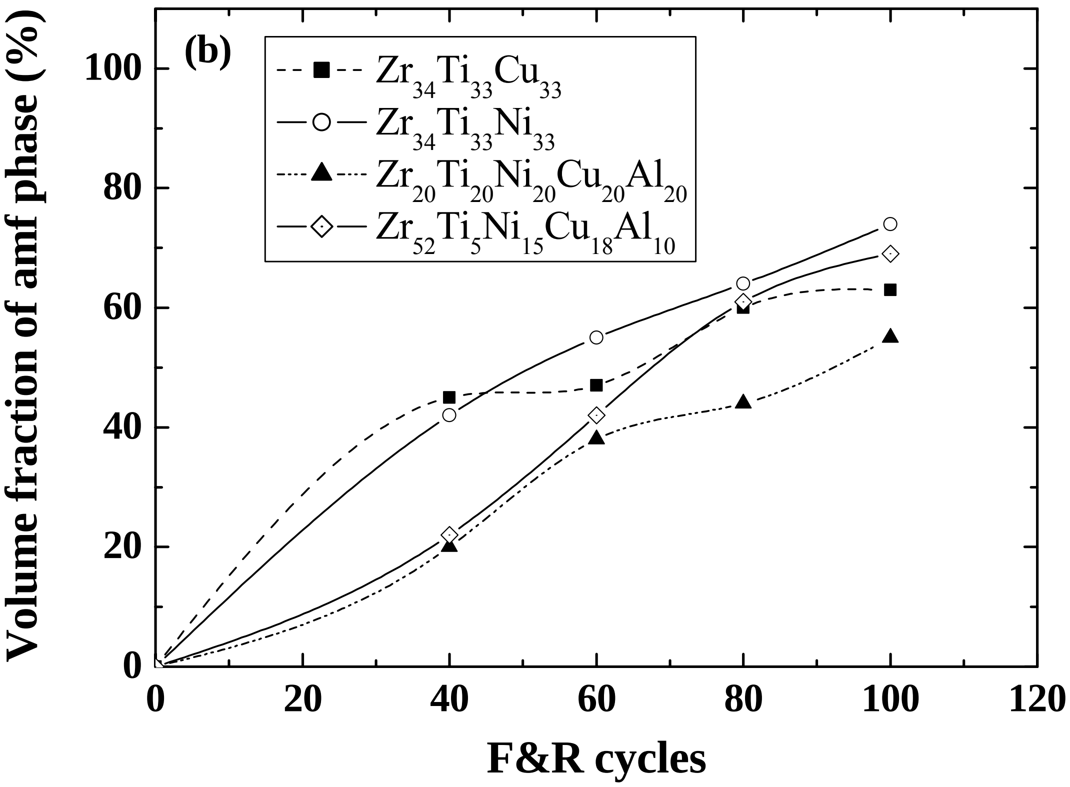

Figure 3.17 The amorphous volume fraction estimated from the XRD results for (a) binary and (b) ternary and pantanary alloys as a function of F&R cycles.

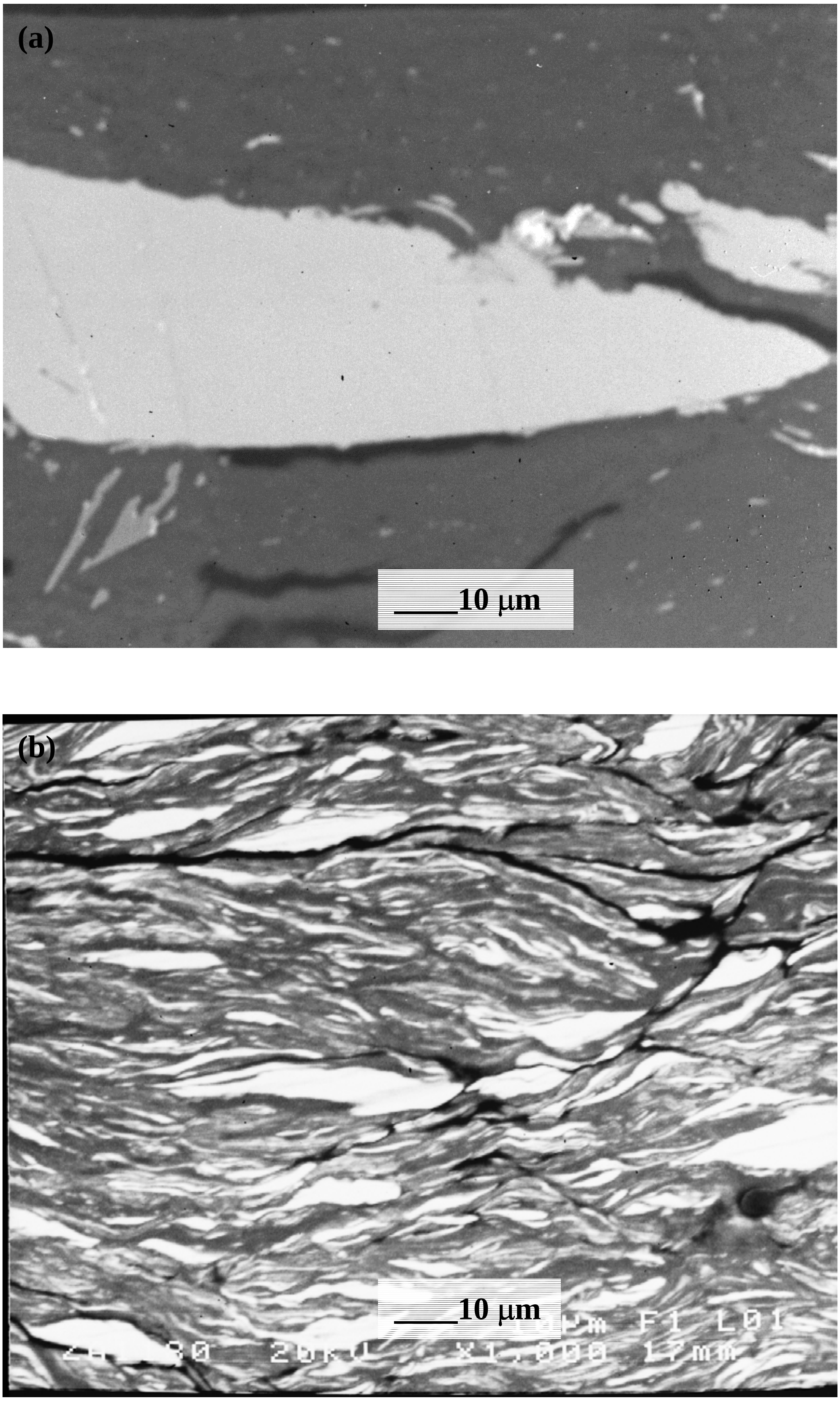

Figure 3.18 SEM/BEI side view of the $Zr_{50}Al_{50}$ alloy after different roll bonding cycles: (a) 40 cycles and (b) 80 cycles.

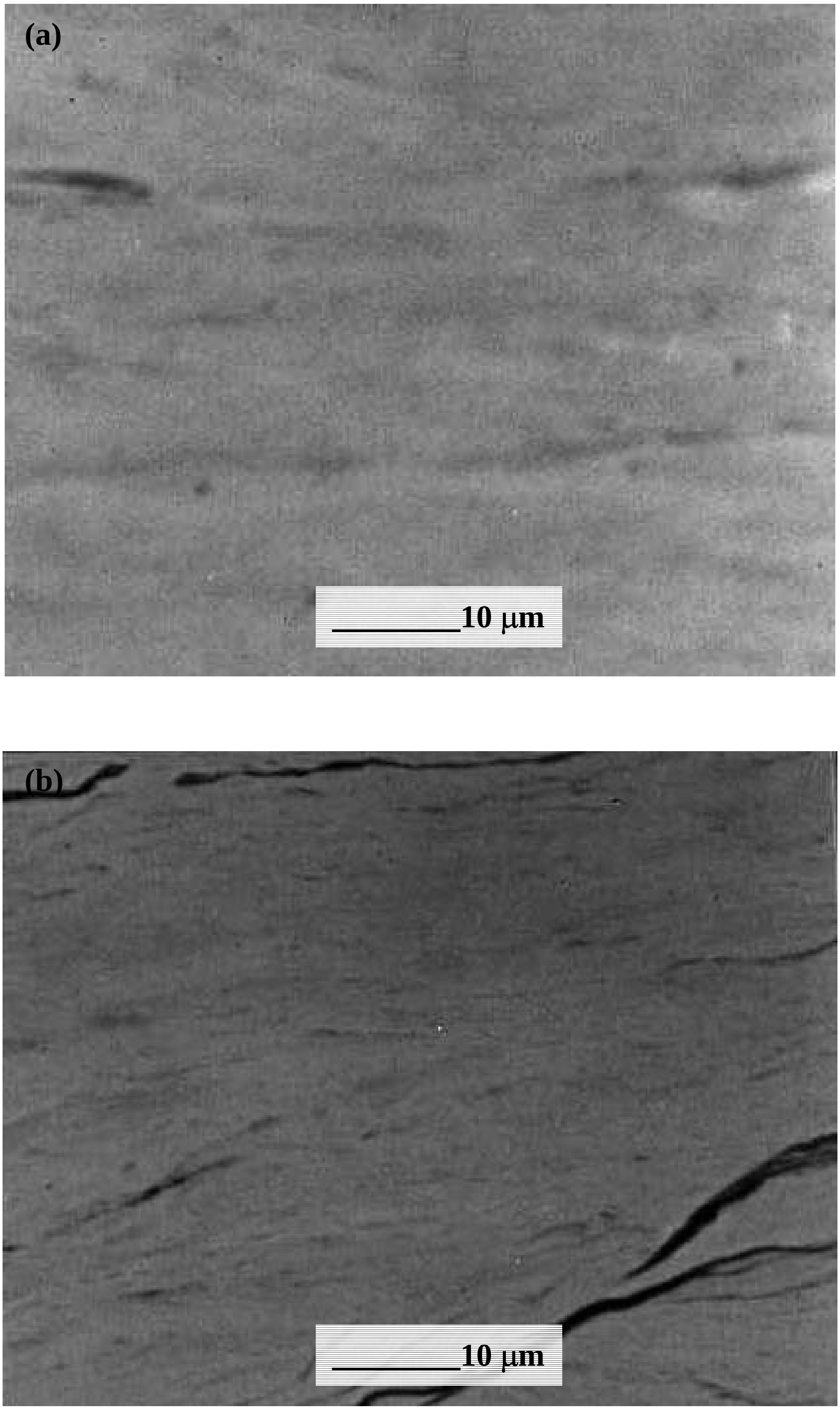

Figure 3.19 SEM/BEI side view of the $Zr_{50}Cu_{50}$ alloy after different roll bonding cycles: (a) 40 cycles and (b) 80 cycles (Note that the Cu foils have been rolled to 30 µm and prehardened to H_v= 131, thereby the layer contrast becomes weaker).

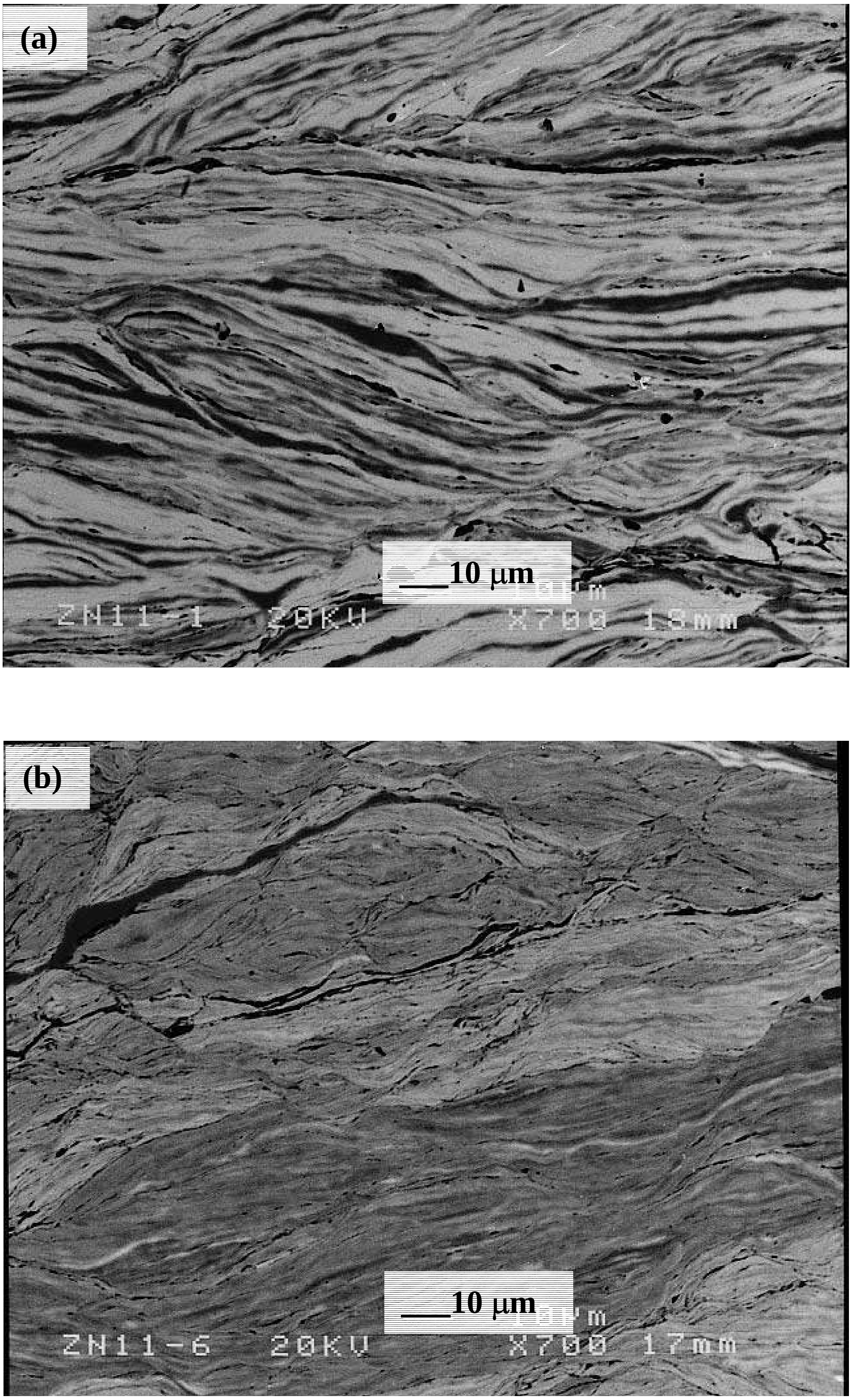

Figure 3.20 SEM/BEI side view of the $Zr_{50}Ni_{50}$ alloy after different roll bonding cycles: (a) 40 cycles and (b) 80 cycles.

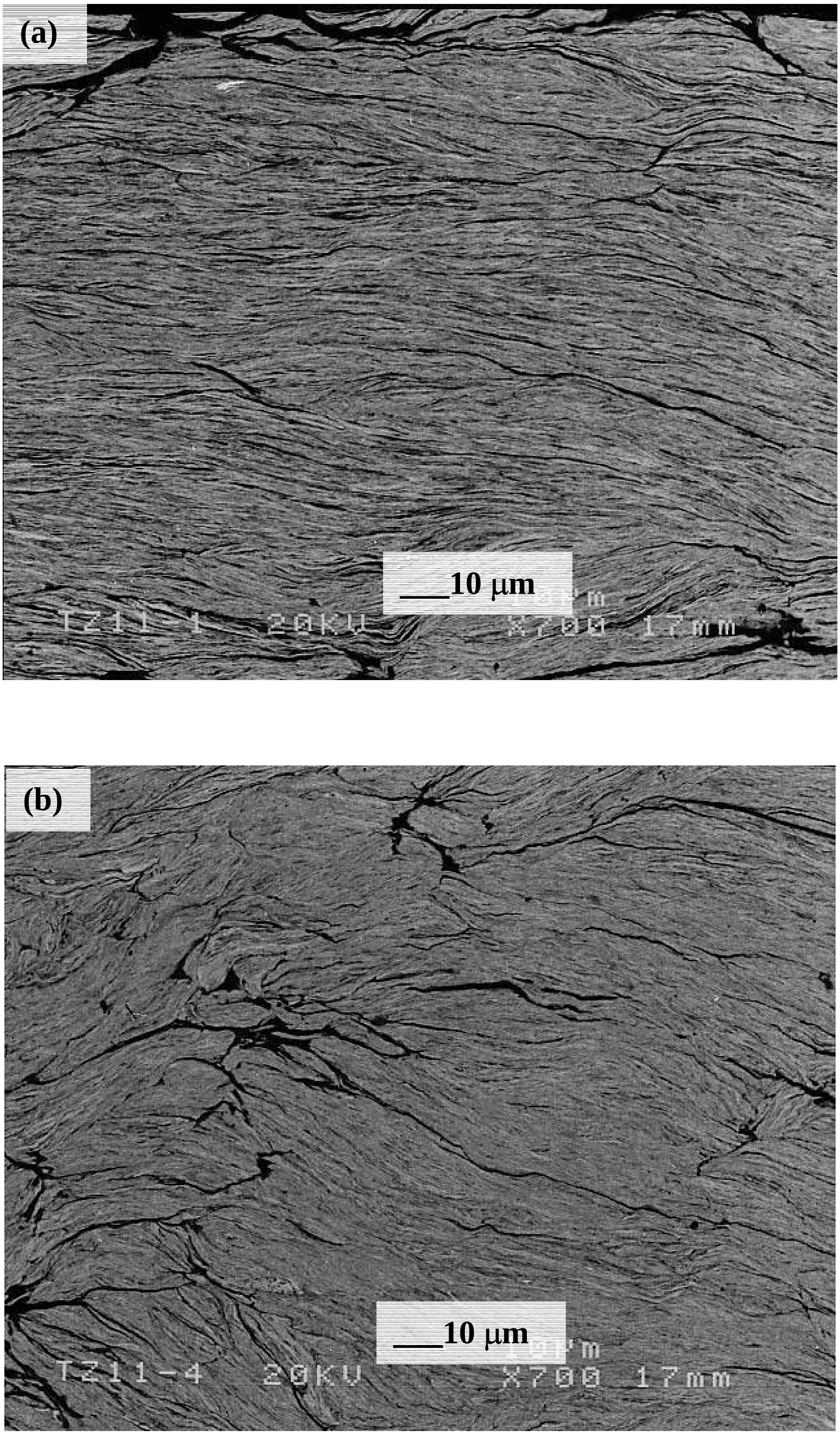

Figure 3.21 SEM/BEI side view of the $Zr_{50}Ti_{50}$ alloy after different roll bonding cycles: (a) 40 cycles, (b) 60 cycles, (c) 80 cycles and (d) 83 cycles.

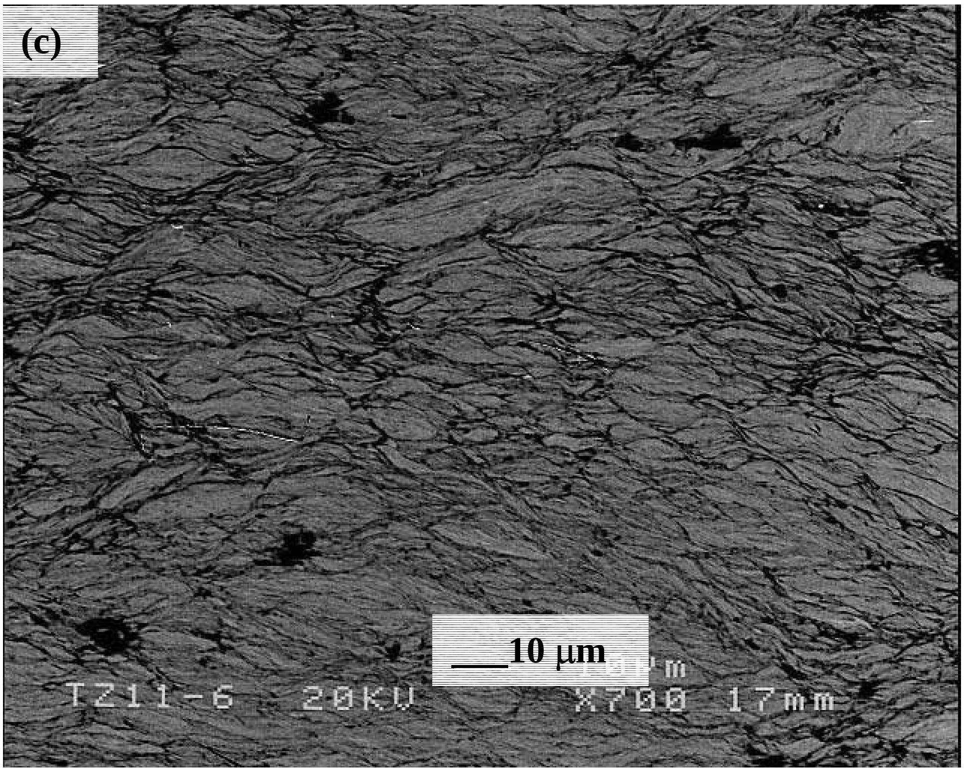
(c)
10 µm
TZ11-6 20KV X700 17mm

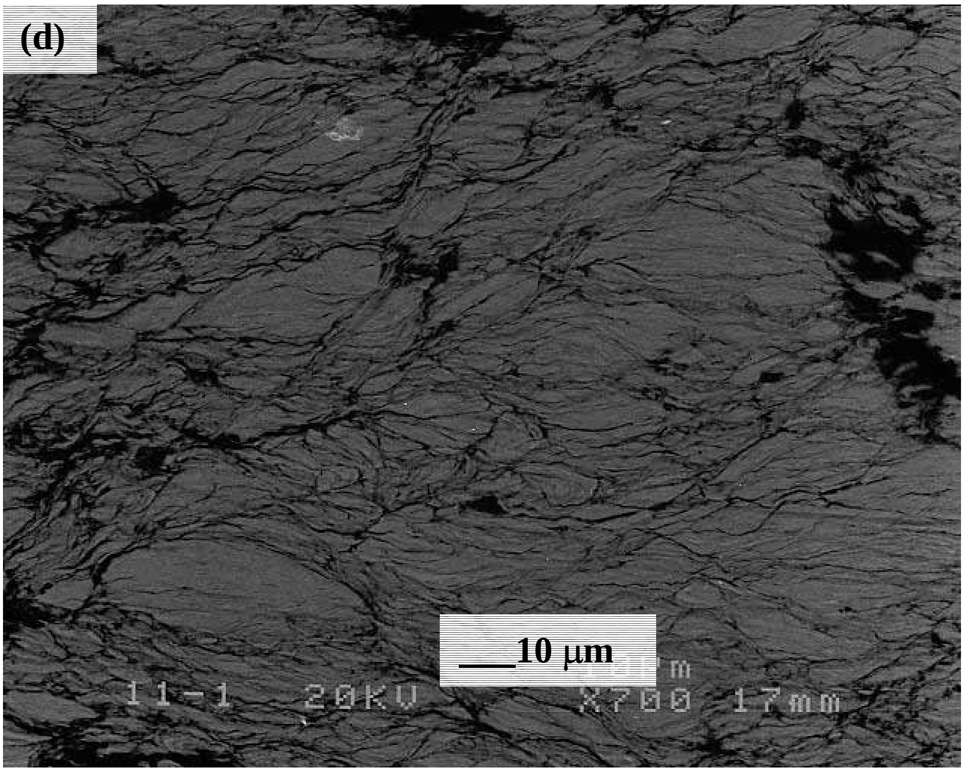
(d)
10 µm
11-1 20KV X700 17mm

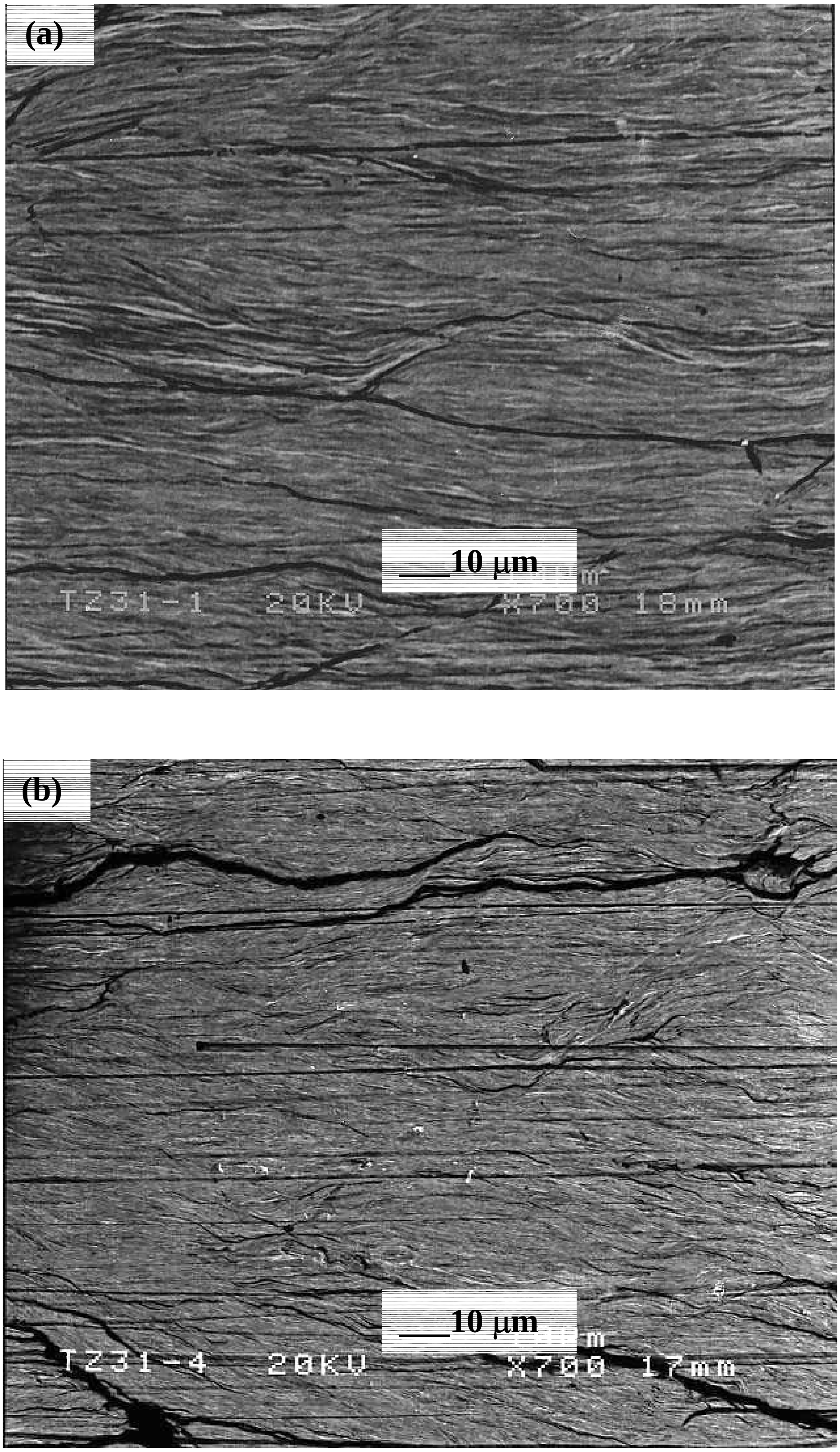

Figure 3.22 SEM/BEI side view of the $Zr_{25}Ti_{75}$ alloy after different roll bonding cycles: (a) 40 cycles, (b) 60 cycles, (c) 80 cycles and (d) 90 cycles.

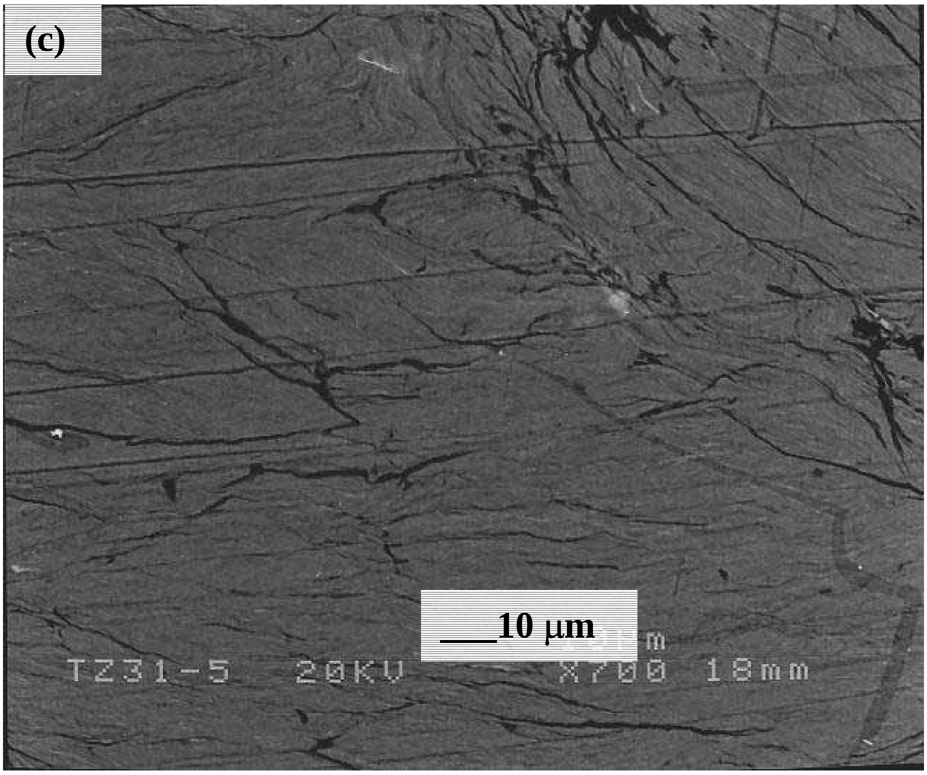
(c)
10 μm
TZ31-5 20KV X700 18mm

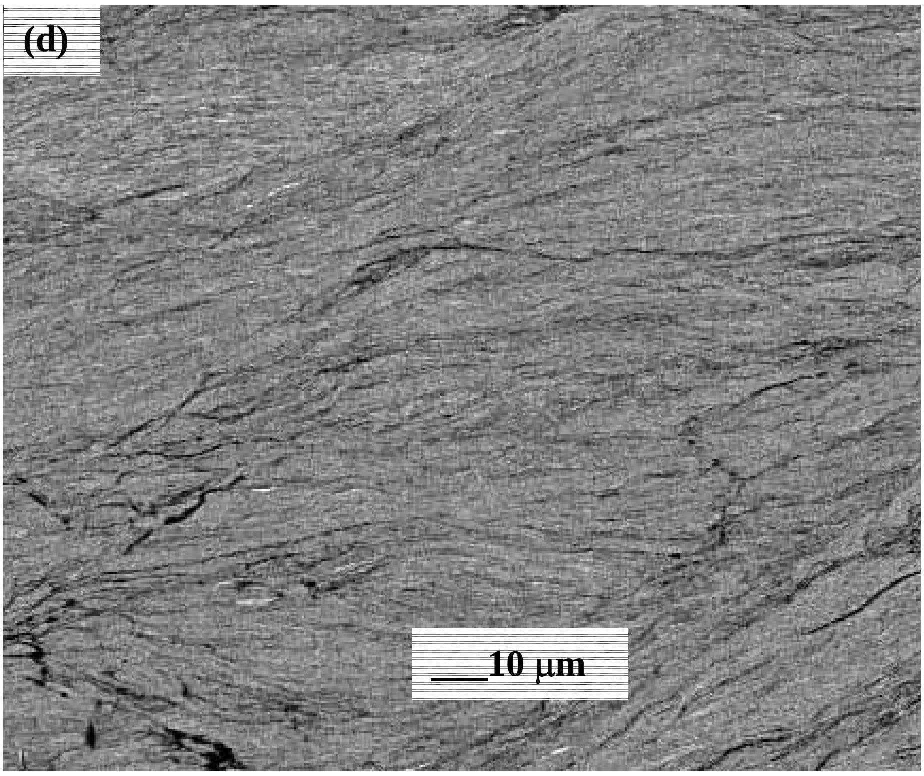
(d)
10 μm

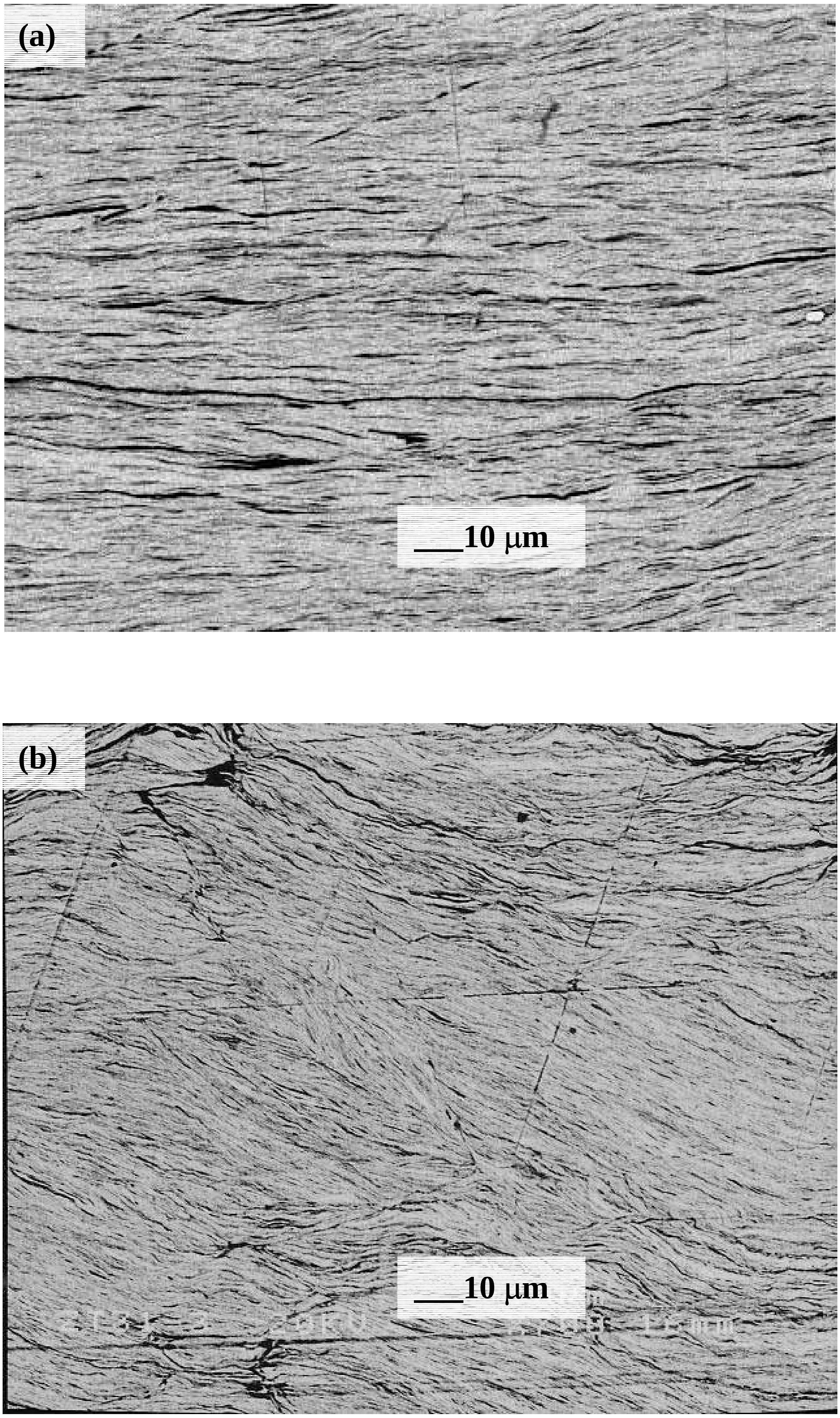

Figure 3.23 SEM/BEI side view of the $Zr_{75}Ti_{25}$ alloy after different roll bonding cycles: (a) 40 cycles, (b) 60 cycles (c) 80 cycles and (d) 90 cycles.

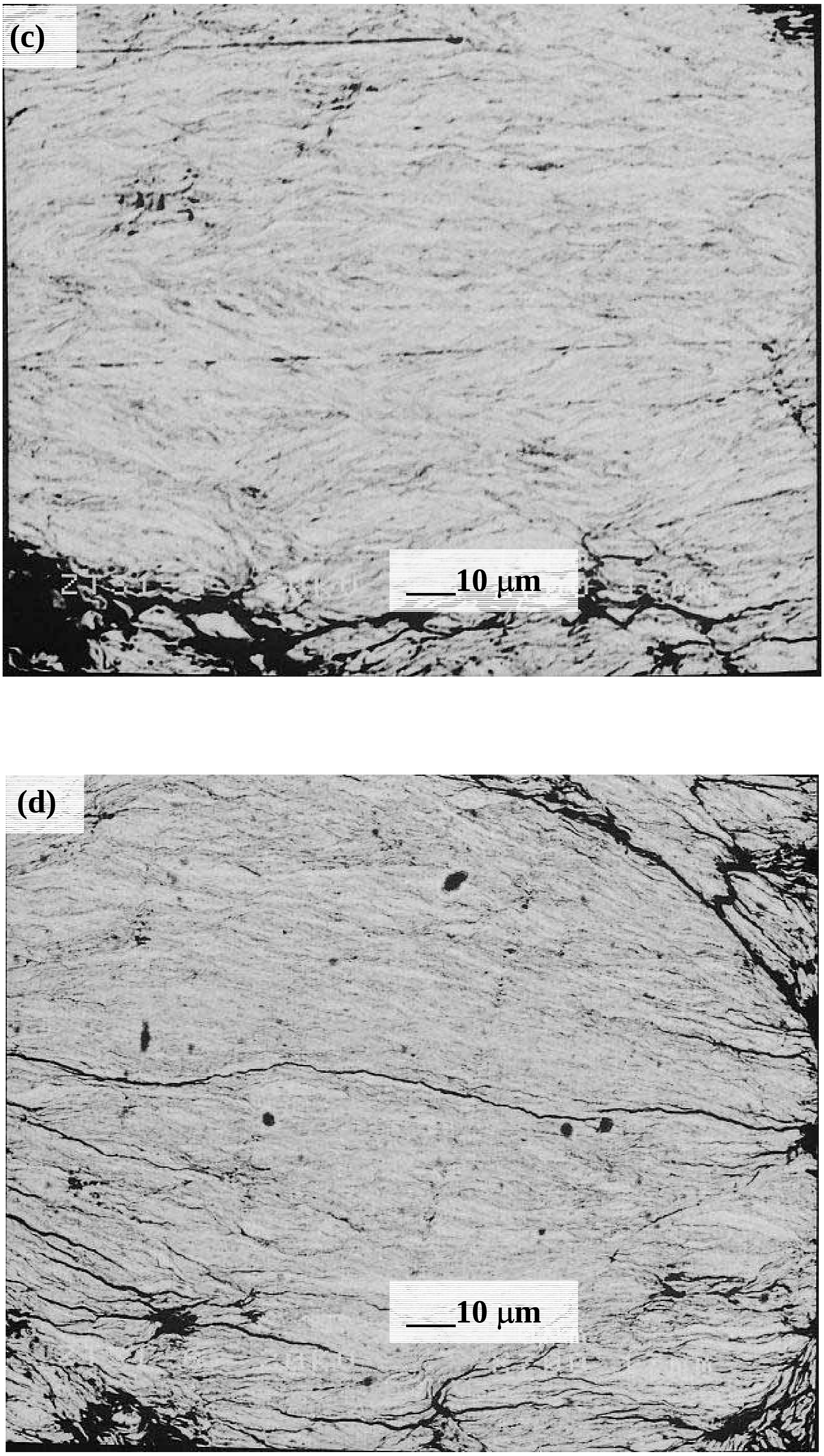
(c)
10 µm
(d)
10 µm

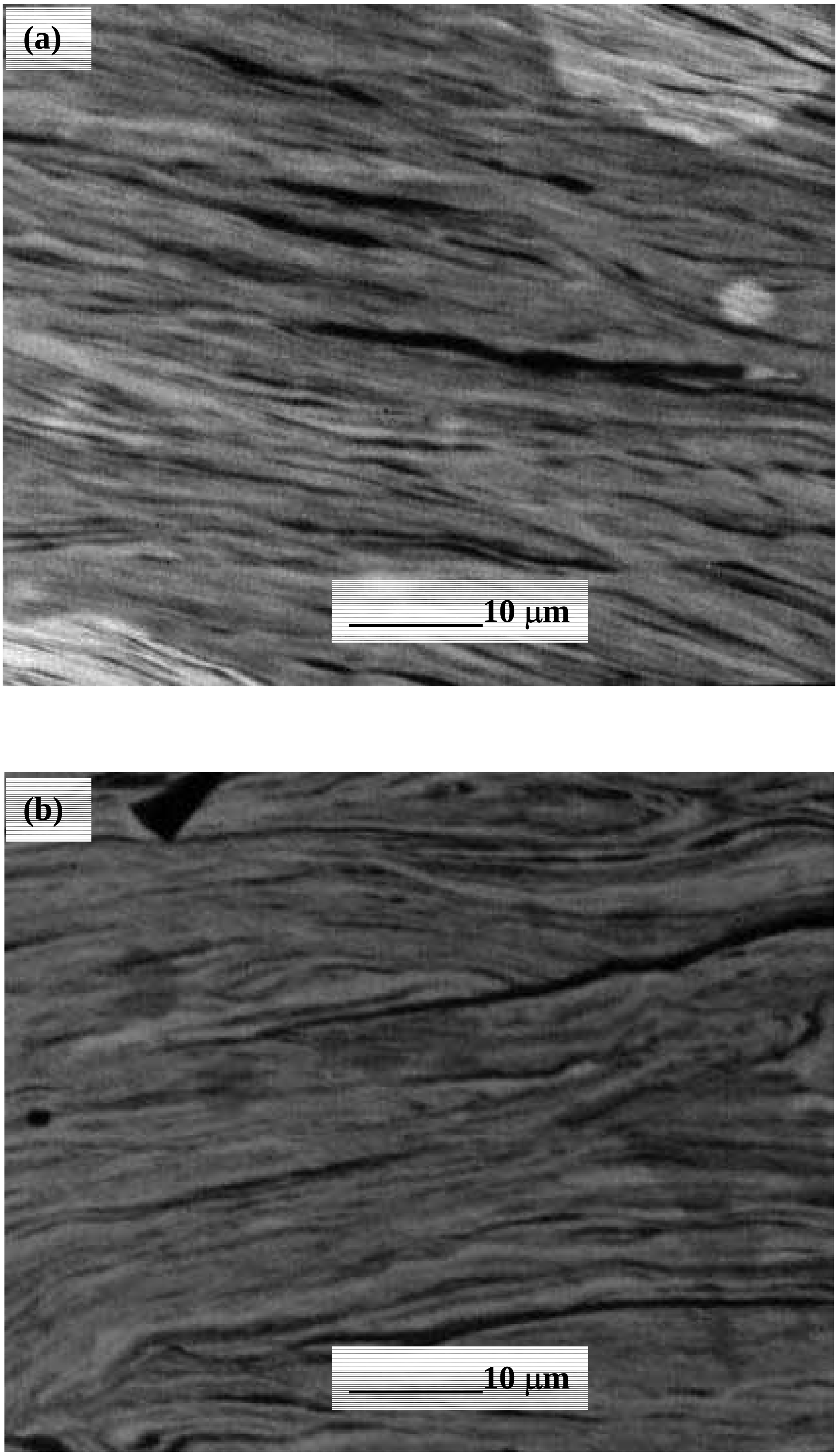

Figure 3.24 SEM/BEI side view of the $Z_{34}Ti_{33}Cu_{33}$ alloy after different roll bonding cycles: (a) 40 cycles, (b) 60 cycles, (c) 80 cycles and (d) 100 cycles.

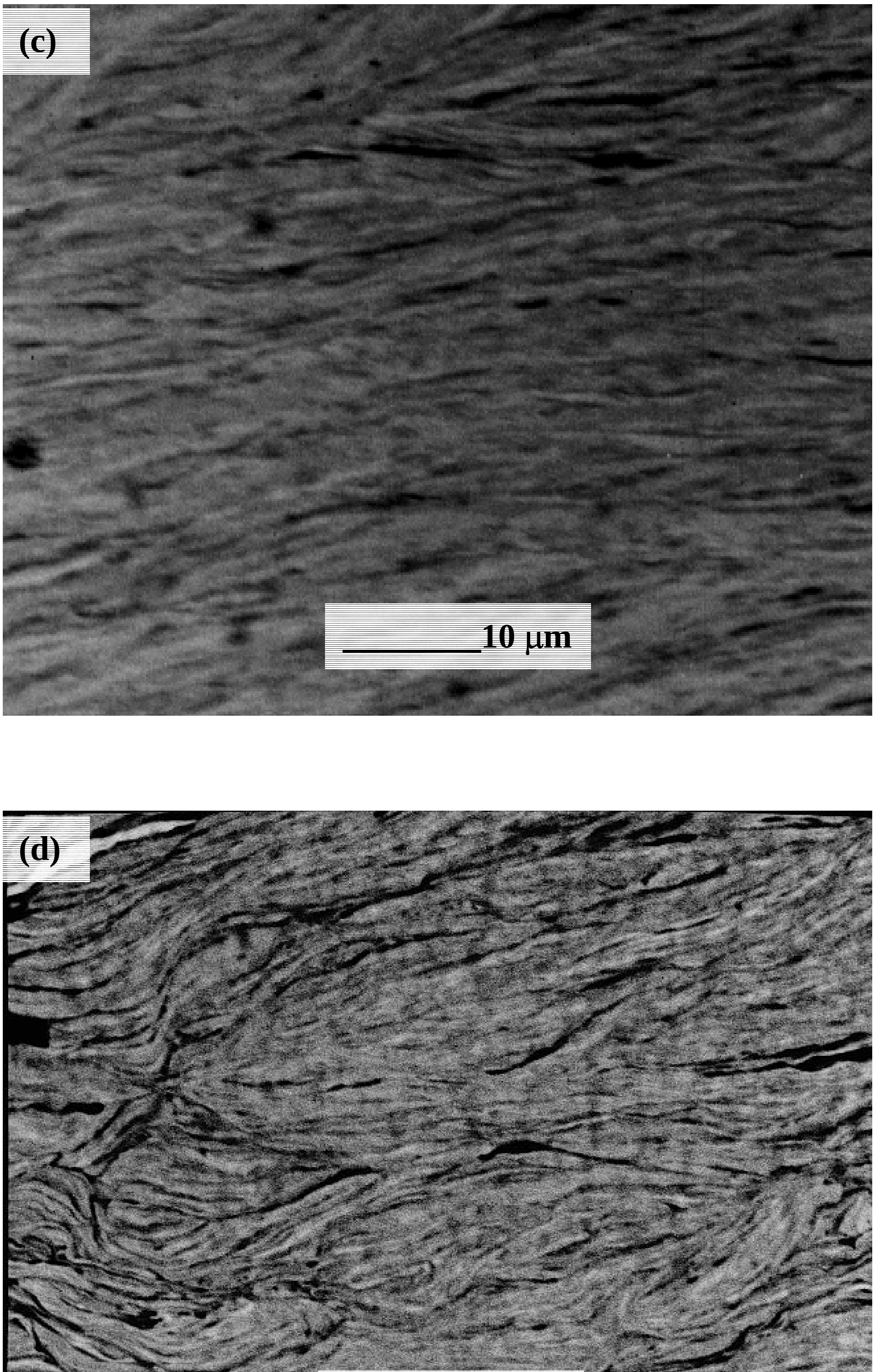
(c)
10 μm
(d)
10 μm
21C101 20KV X2,000 10mm

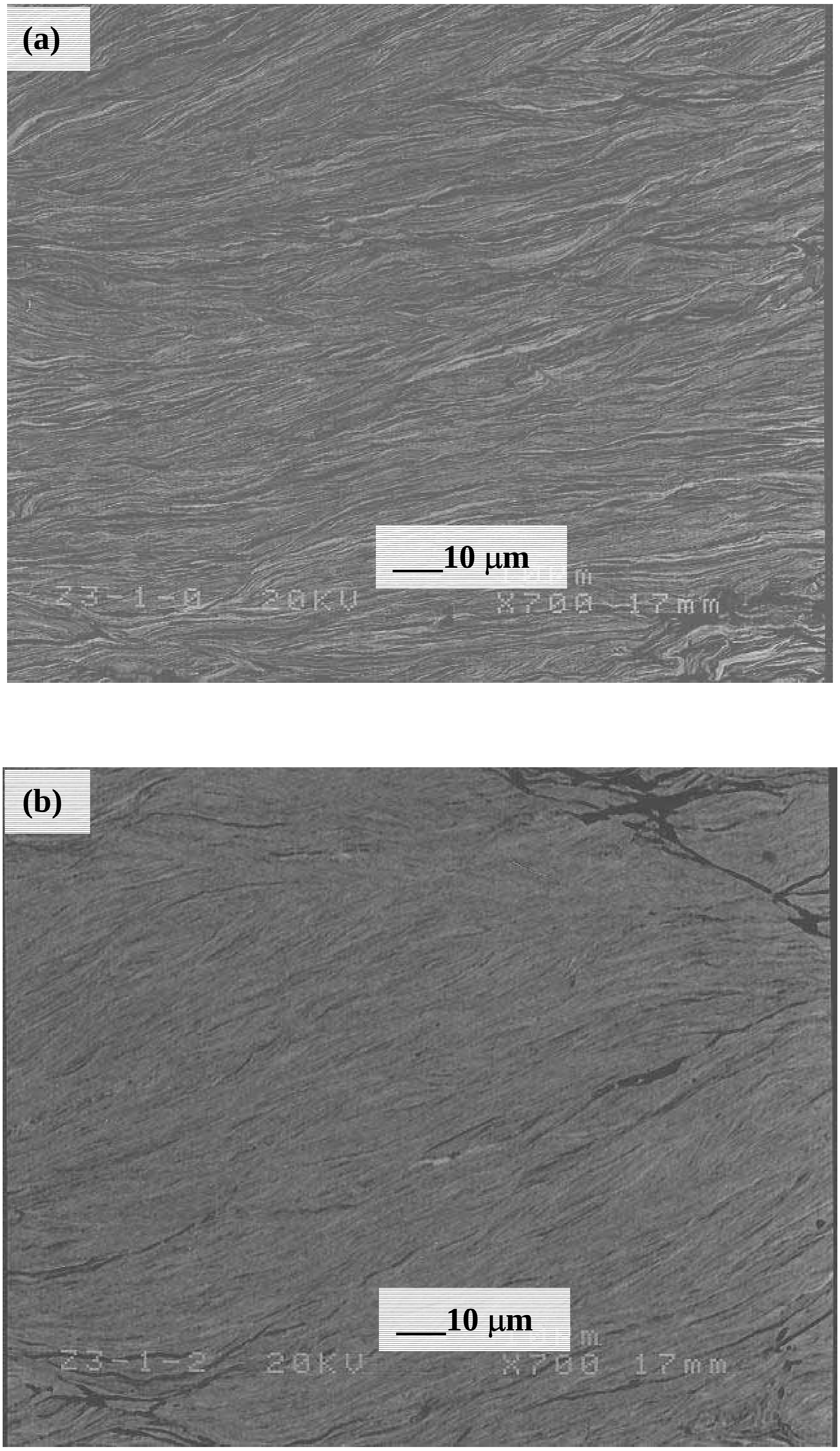

Figure 3.25 SEM/BEI side view of the $Z_{34}Ti_{33}Ni_{33}$ alloy after different roll bonding cycles: (a) 40 cycles, (b) 60 cycles (c)80 cycles and (d) 100 cycles.

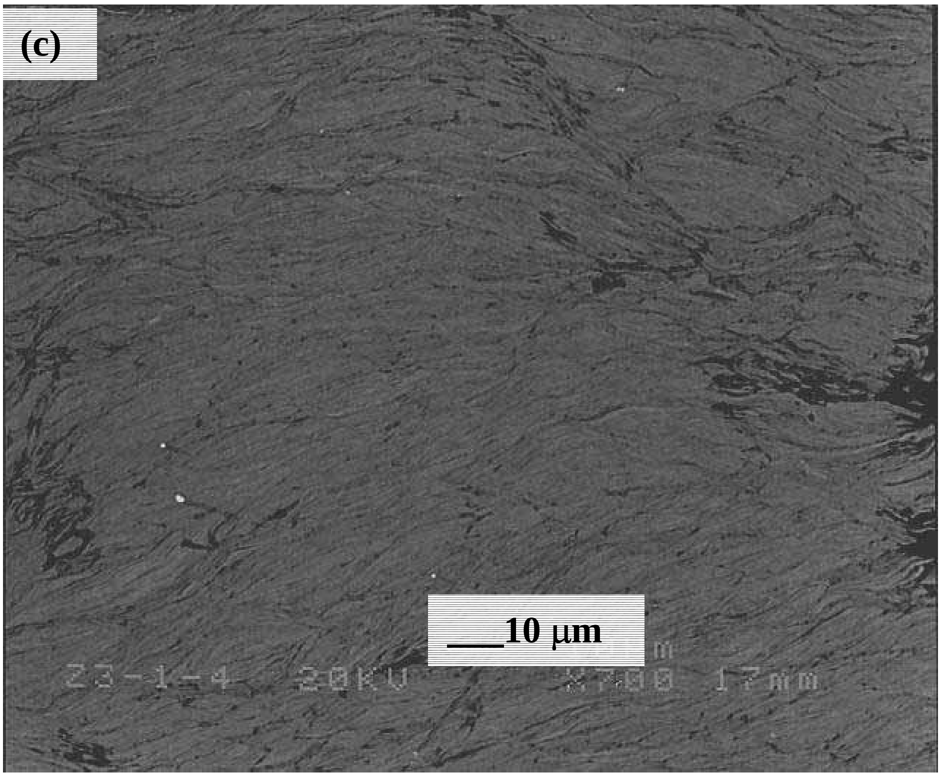
(c)
10 μm
23-1-4 20KV X700 17mm

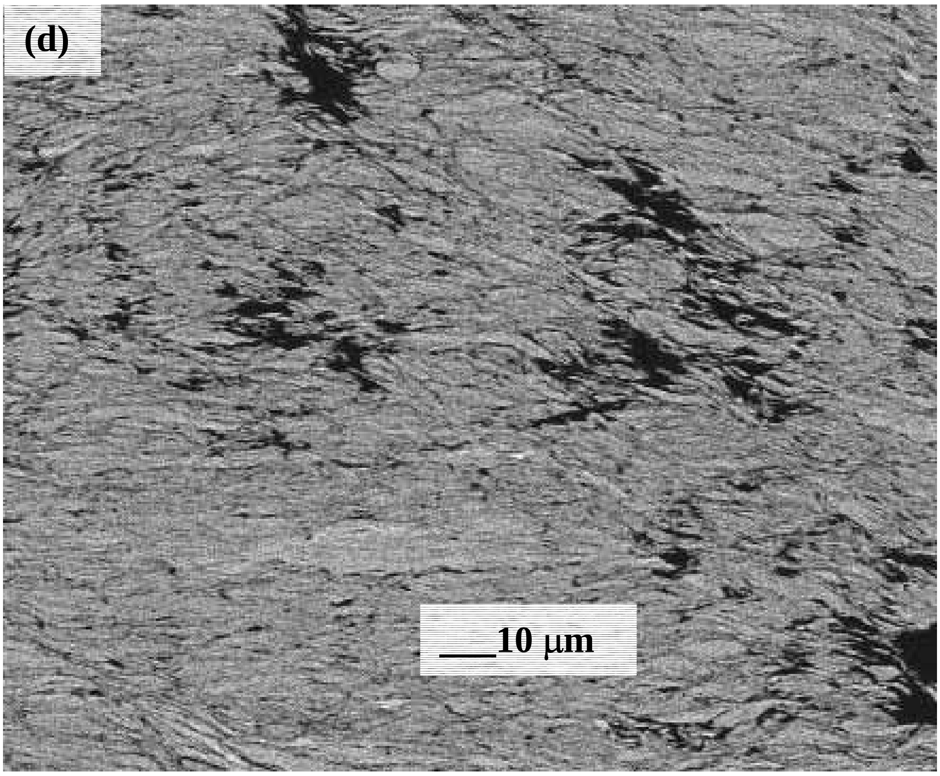
(d)
10 μm

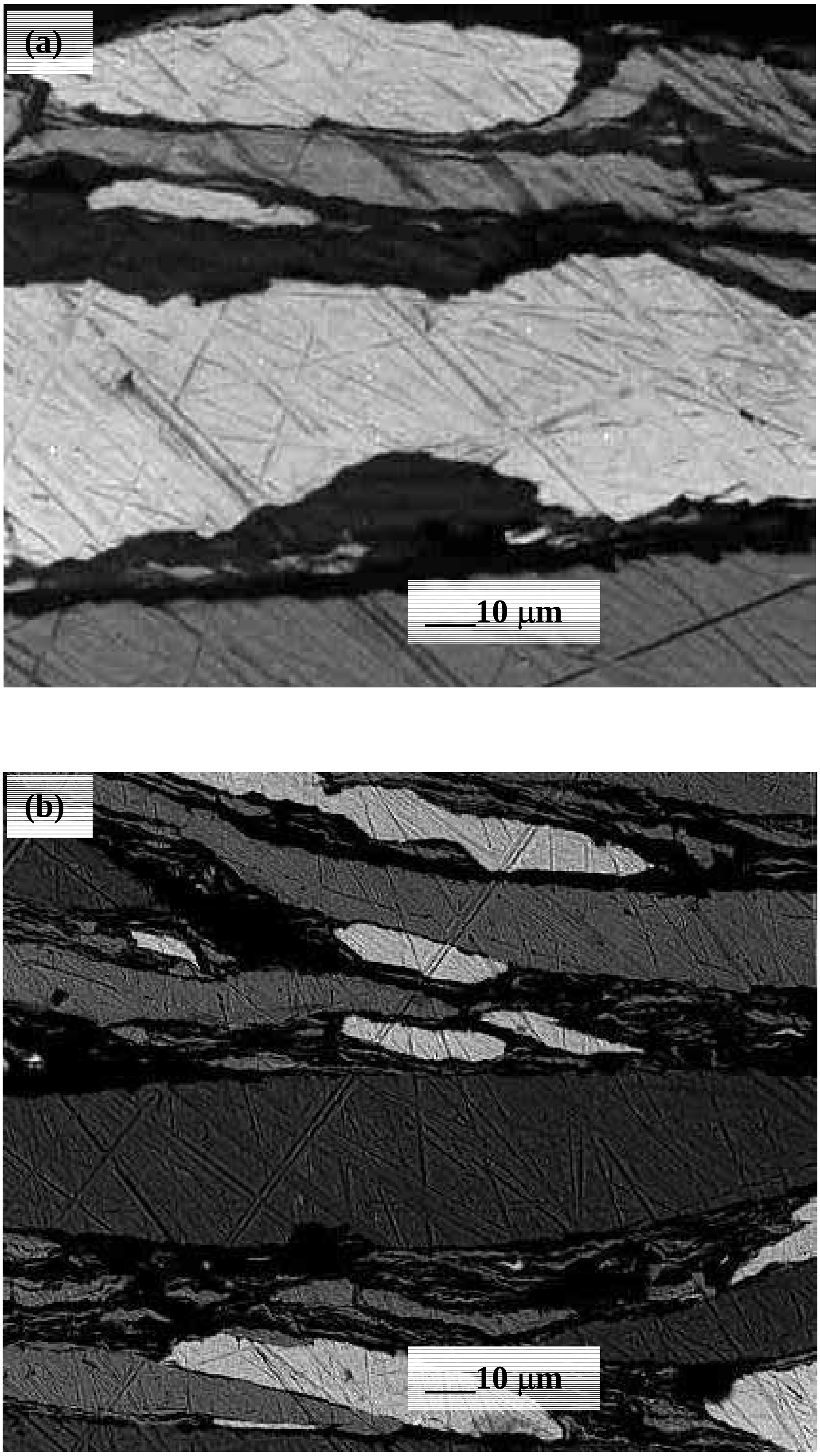

Figure 3.26 SEM/BEI side view of the $Zr_{20}Ti_{20}Ni_{20}Cu_{20}Al_{20}$ alloy after different roll bonding cycles: (a) 40 cycles and (b) 80 cycles.

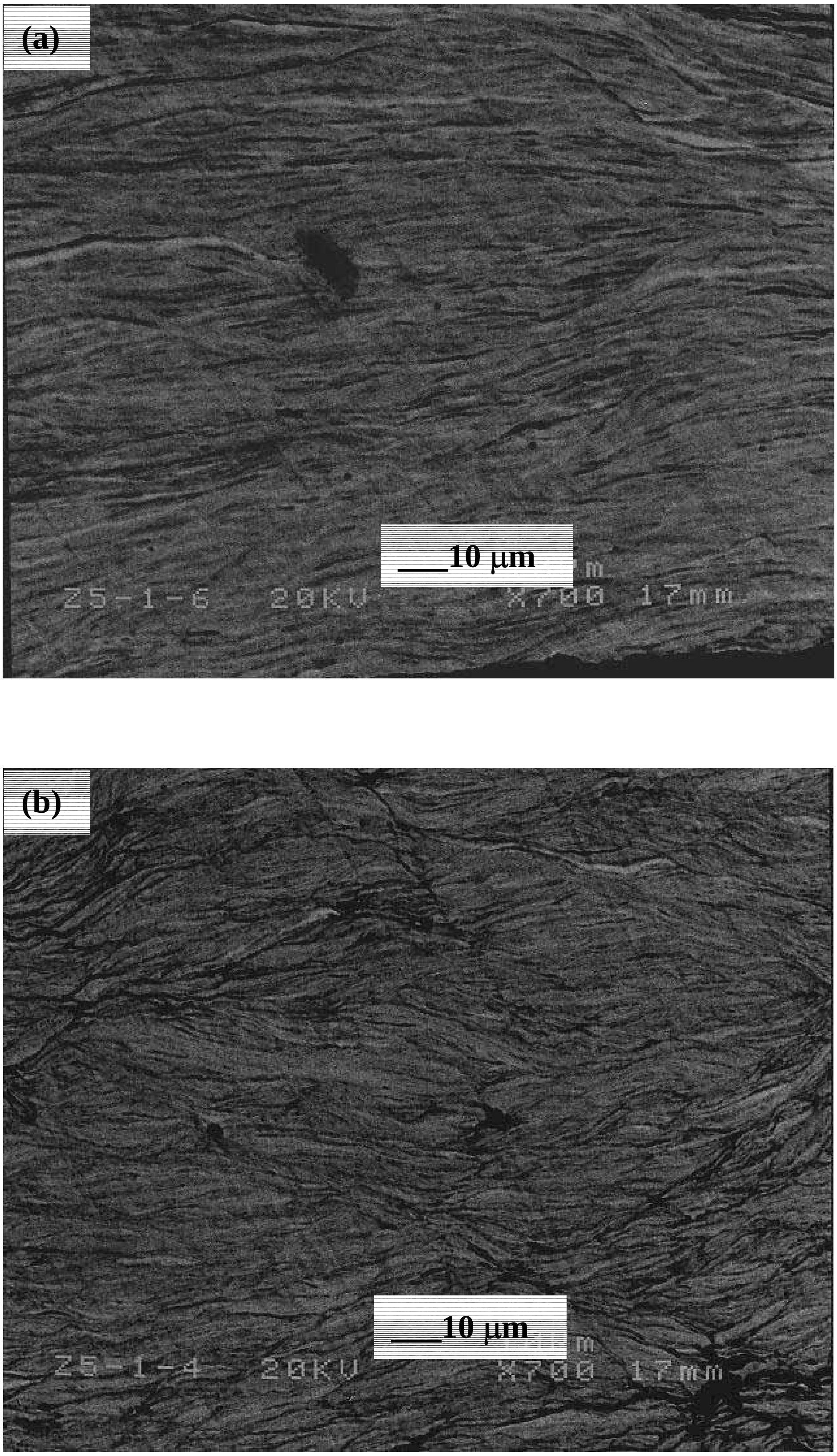

Figure 3.27 SEM/BEI side view of the $Zr_{52}Ti_5Ni_{15}Cu_{18}Al_{10}$ alloy after different roll bonding cycles: (a) 40 cycles, (b) 60 cycles, (c) 80 cycles and (d) 90 cycles.

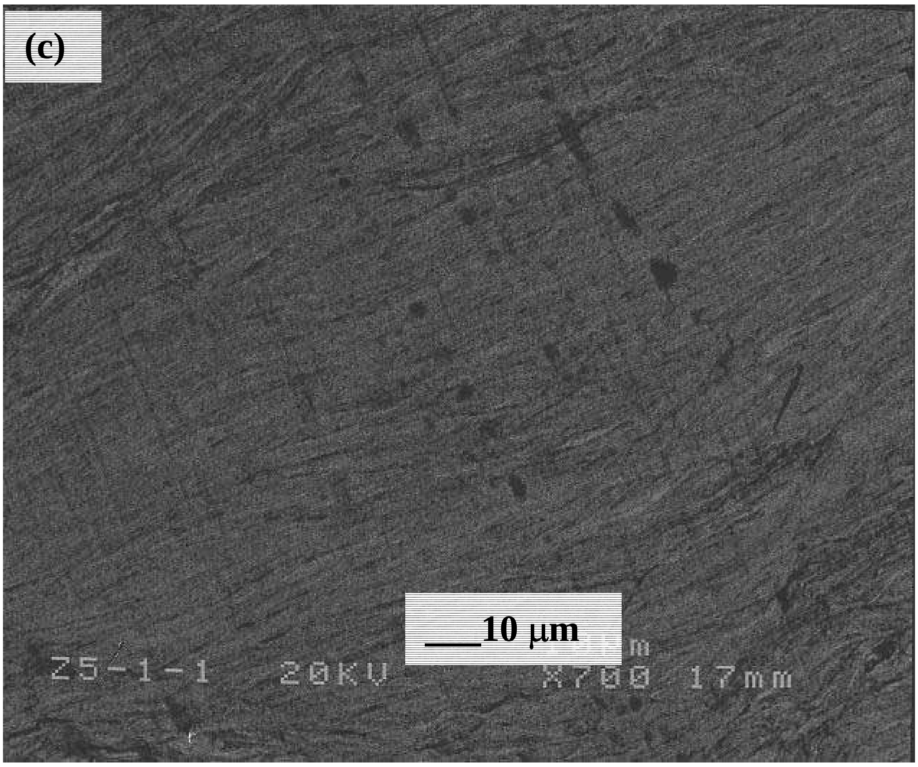
(c)
10 μm
Z5-1-1 20KV X700 17mm

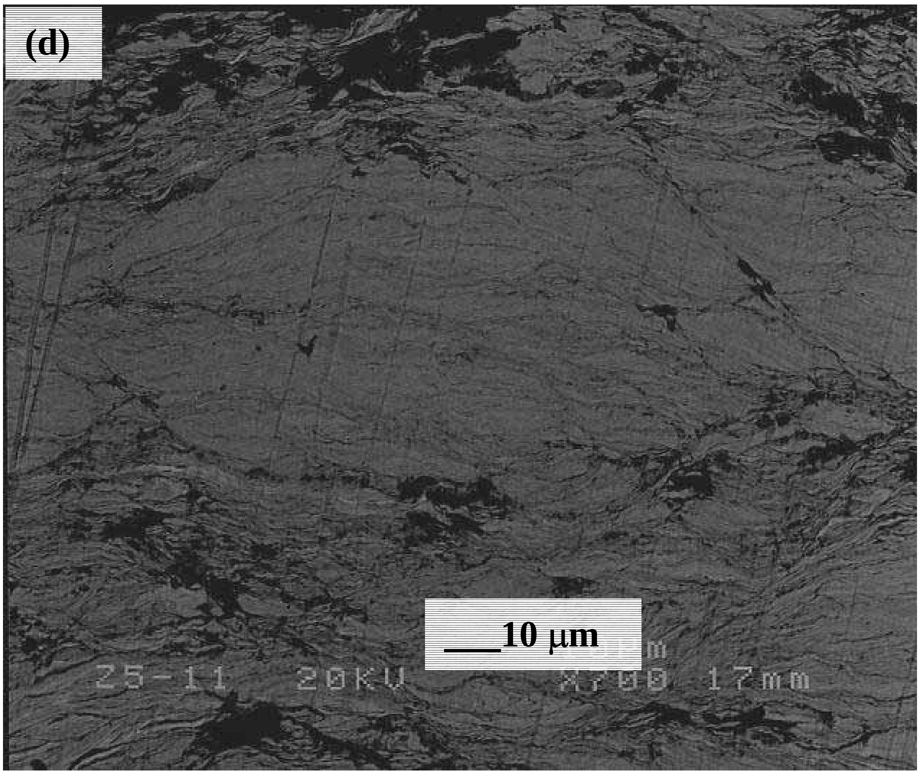
(d)
10 μm
Z5-11 20KV X700 17mm

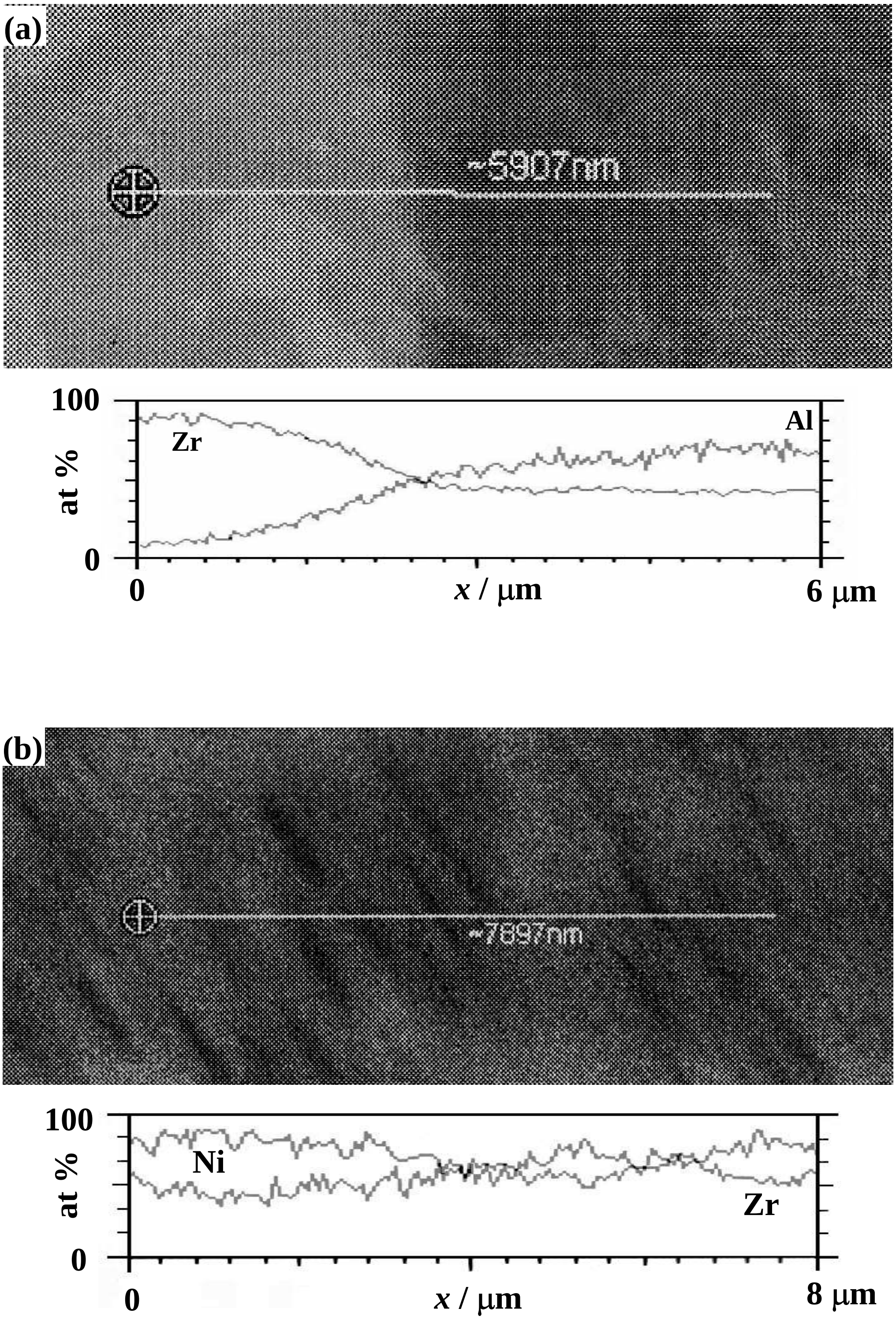

Figure 3.28 The SEM/EDS line scan measurement in (a) $Zr_{50}Al_{50}$ and (b) $Zr_{50}Ni_{50}$ alloy after 100 F&R cycles.

(a) Zr-Cu, 40 cycles

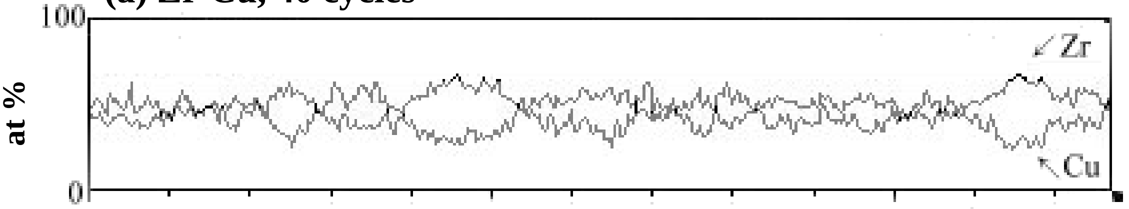

(b) Zu-Cu, 80 cycles

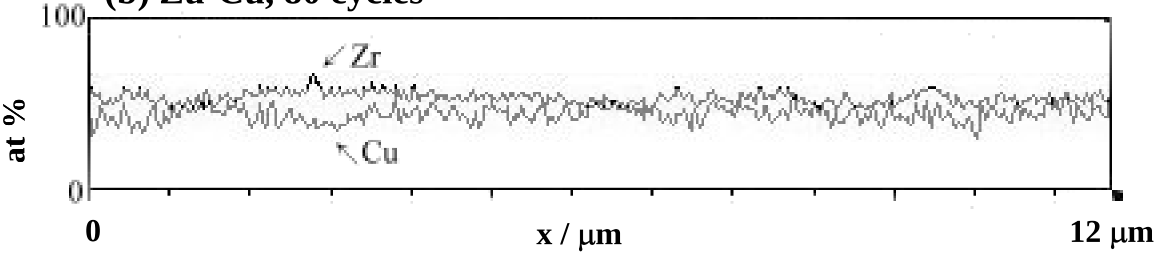

(c) Zr-Ti-Cu, 40 cycles

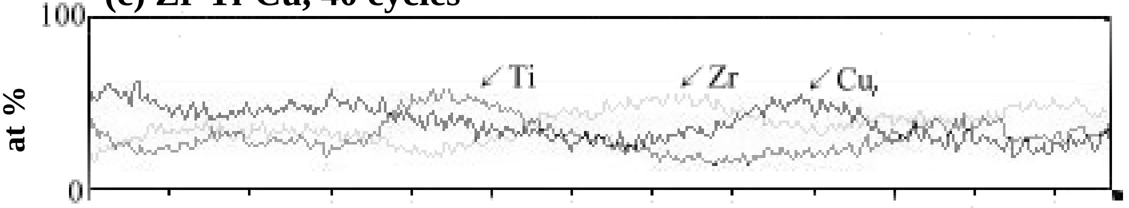

(d) Zr-Ti-Cu, 80 cycles

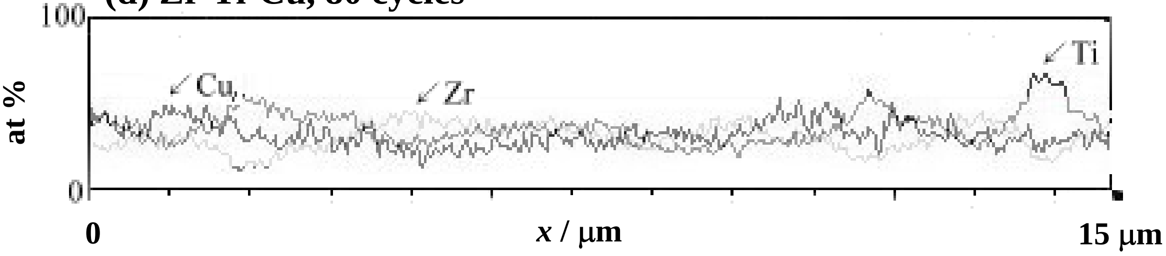

Figure 3.29 The SEM/EDS line scan measurement for (a)(b) $Zr_{50}Cu_{50}$ and (c)(d) $Zr_{34}Ti_{33}Cu_{33}$ alloys after 40 and 80 F&R cycles.

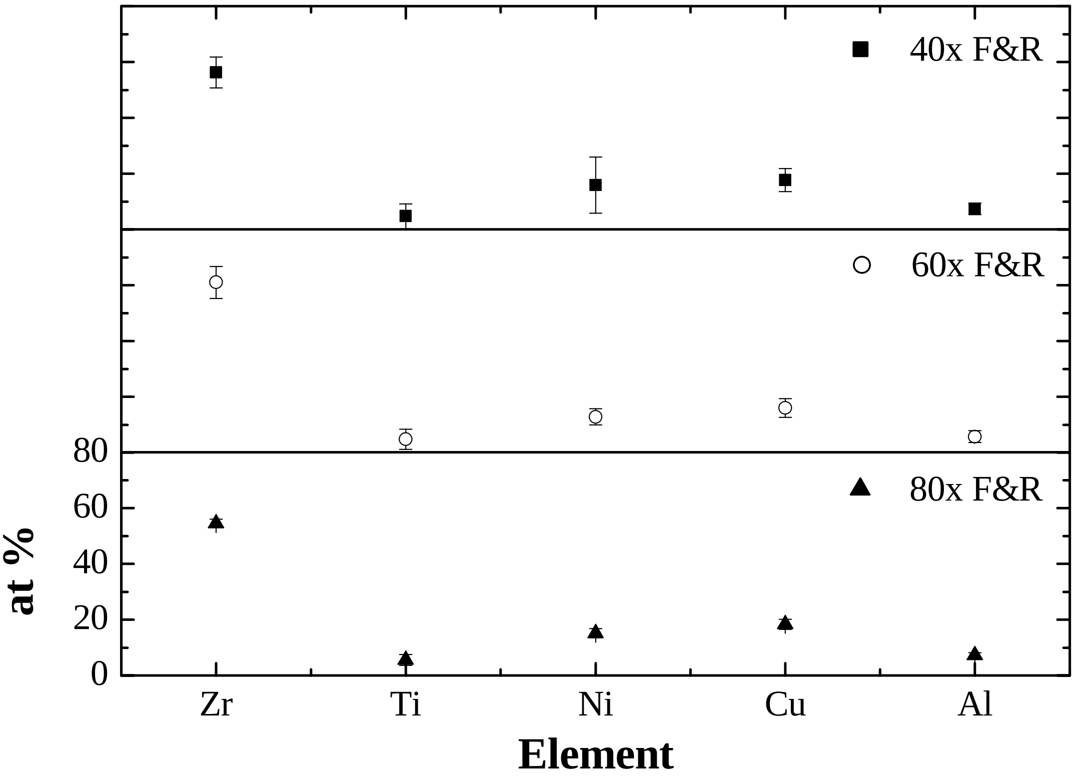

Figure 3.30 The SEM/EDS results illustrating the composition variation via scattering bars for the $Zr_{52}Ti_5Ni_{15}Cu_{18}Al_{10}$ alloy after different F&R cycles.

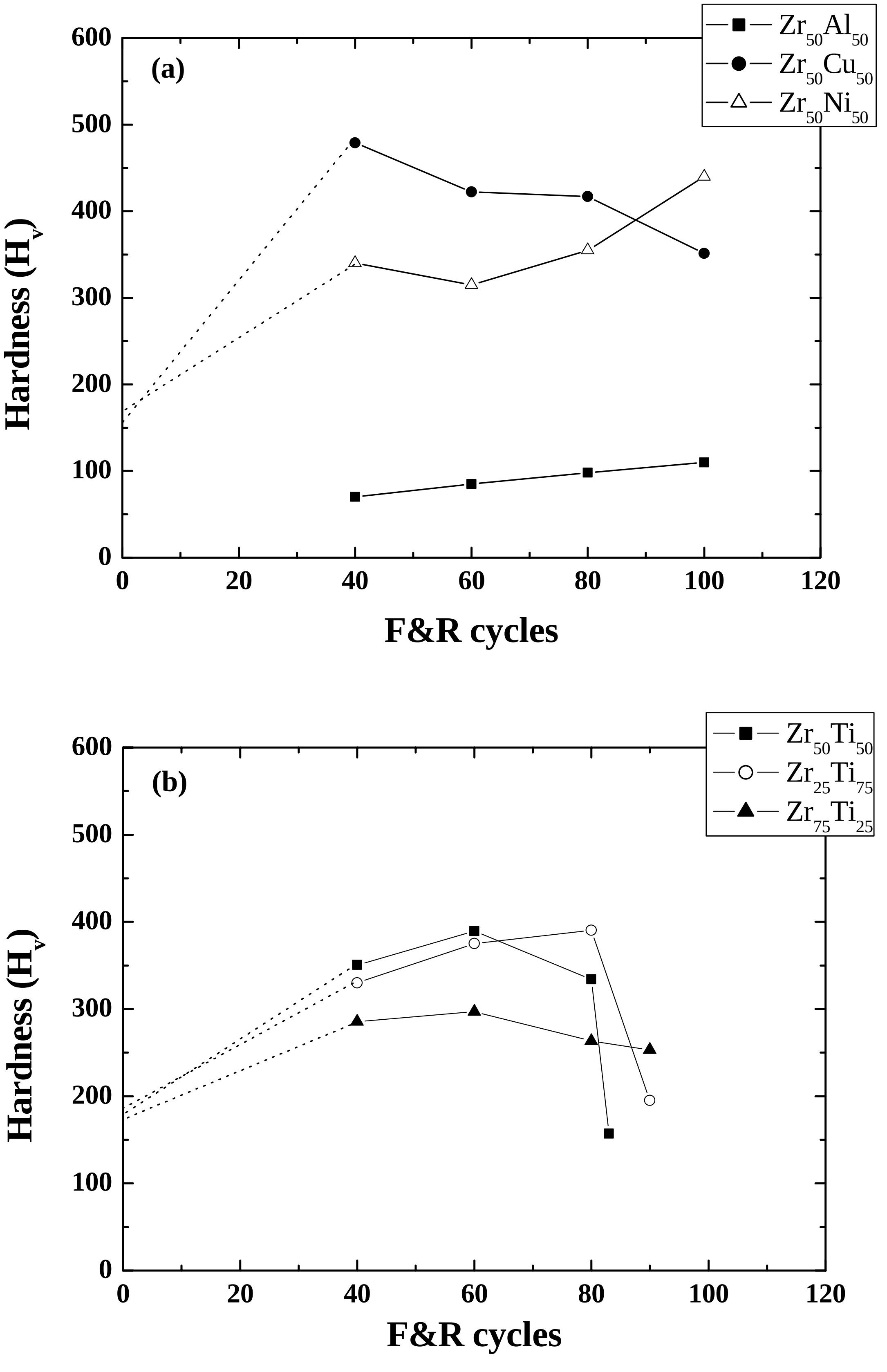

Figure 3.31 Relationship between the microhardness measurements and roll bonding cycles for various Zr-X systems: (a) (b) binary and (c) ternary and pentanary alloys.

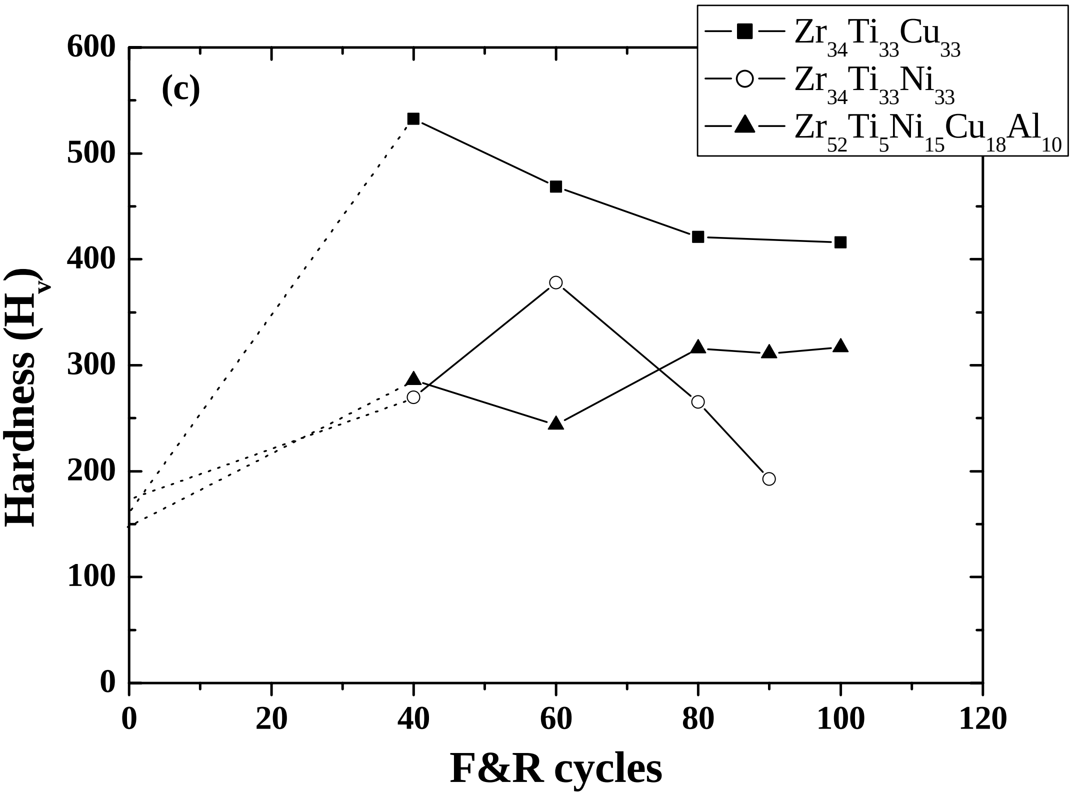
(c)
Hardness (H_v)
F&R cycles
0
100
200
300
400
500
600
0
20
40
60
80
100
120
$Zr_{34}Ti_{33}Cu_{33}$
$Zr_{34}Ti_{33}Ni_{33}$
$Zr_{52}Ti_5Ni_{15}Cu_{18}Al_{10}$

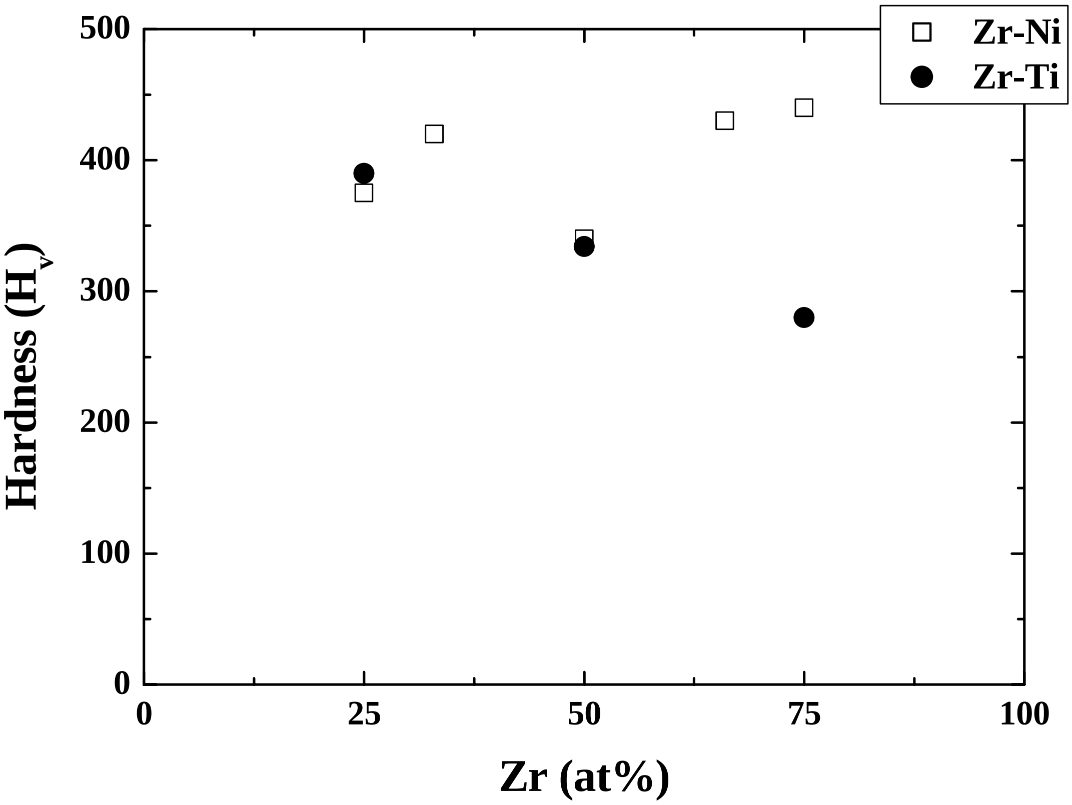

Figure 3.32 The variation of the microhardness readings for the Zr-Ni [81] and Zr-Ti systems with different composition combinations after 80 F&R cycles.

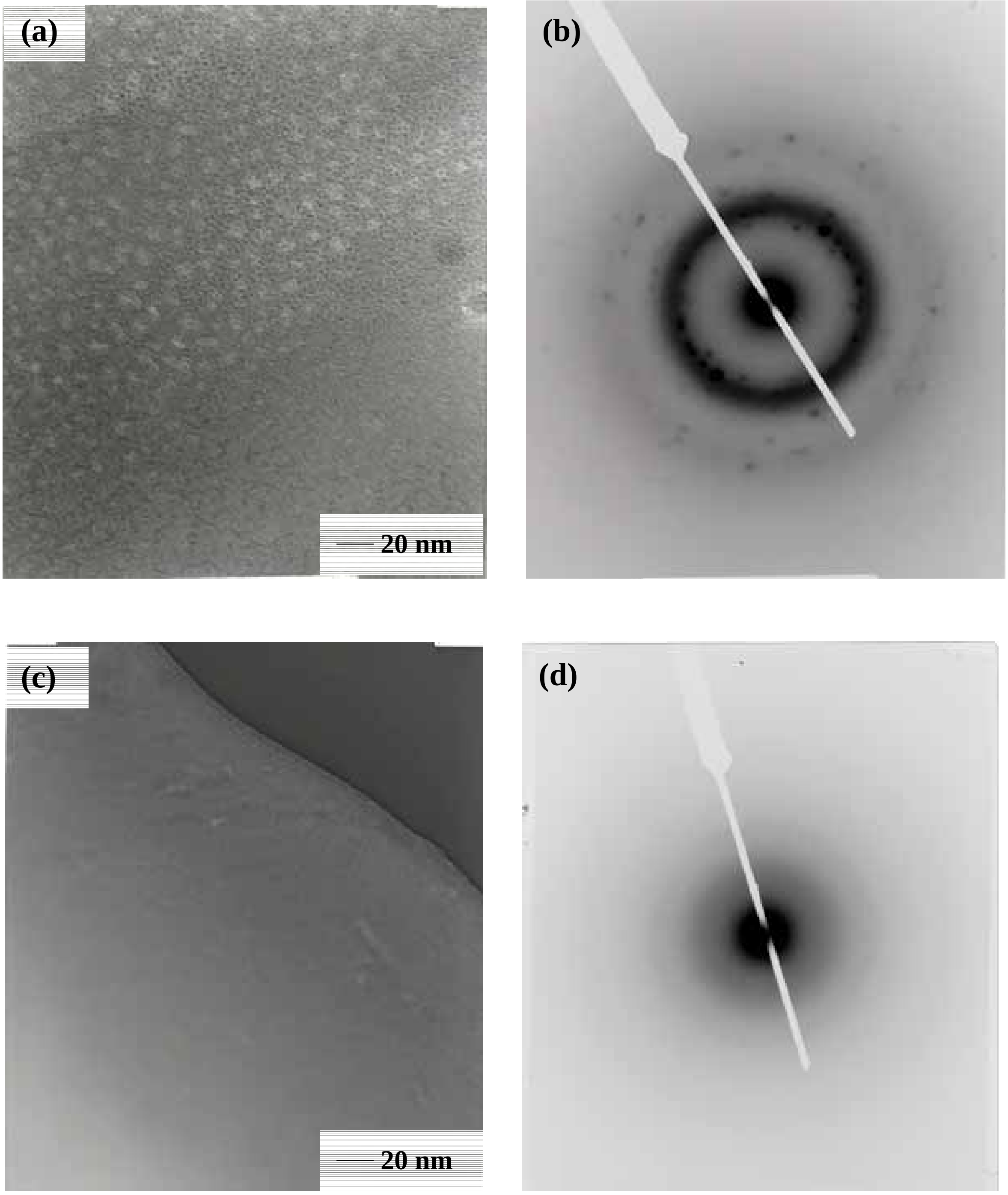

Figure 3.33 TEM bright field images and their associated diffraction patterns for the $Zr_{50}Cu_{50}$ alloy after 80 F&R cycles: (a)(b) showing the nanocrystalline region, and (c)(d) showing the amorphous regime.

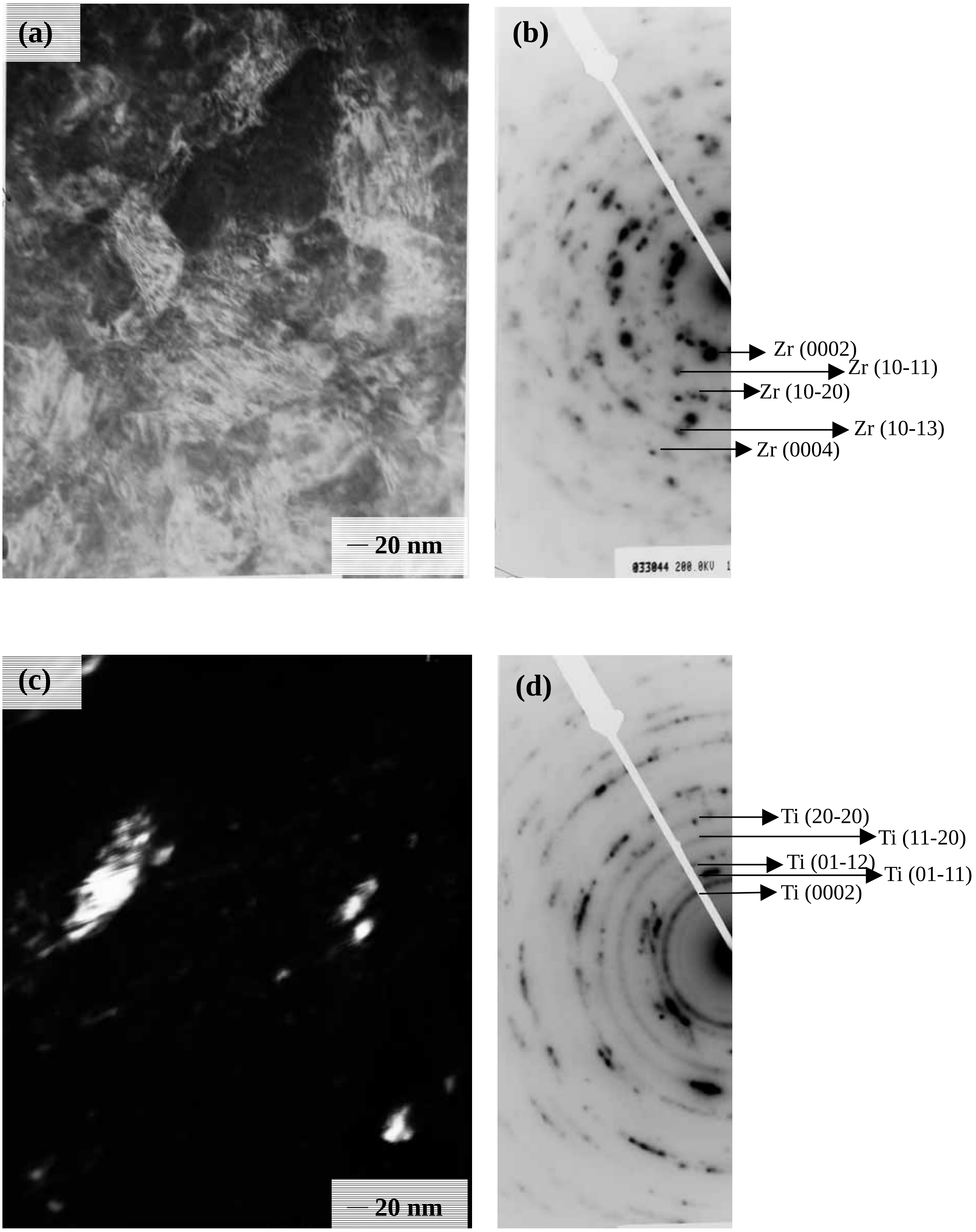

Figure 3.34 TEM (a) bright field image, (c) dark field image, and (b)(d) associated diffraction patterns for the $Zr_{50}Ti_{50}$ alloy after 40 F&R cycles.

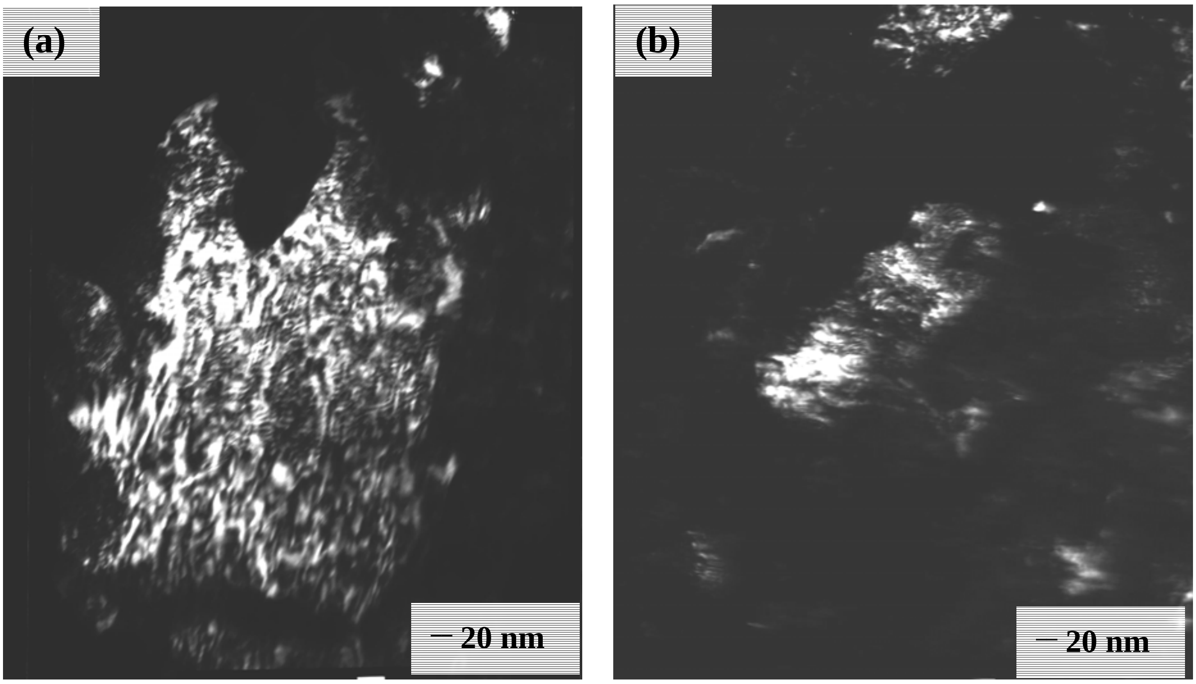

Figure 3.35 TEM dark field images of the $Zr_{50}Ti_{50}$ alloy after 40 F&R cycles, showing (a) the intense dislocation strain contrast in larger grains, and (b) much less defect activities with decreasing nanocrystalline size.

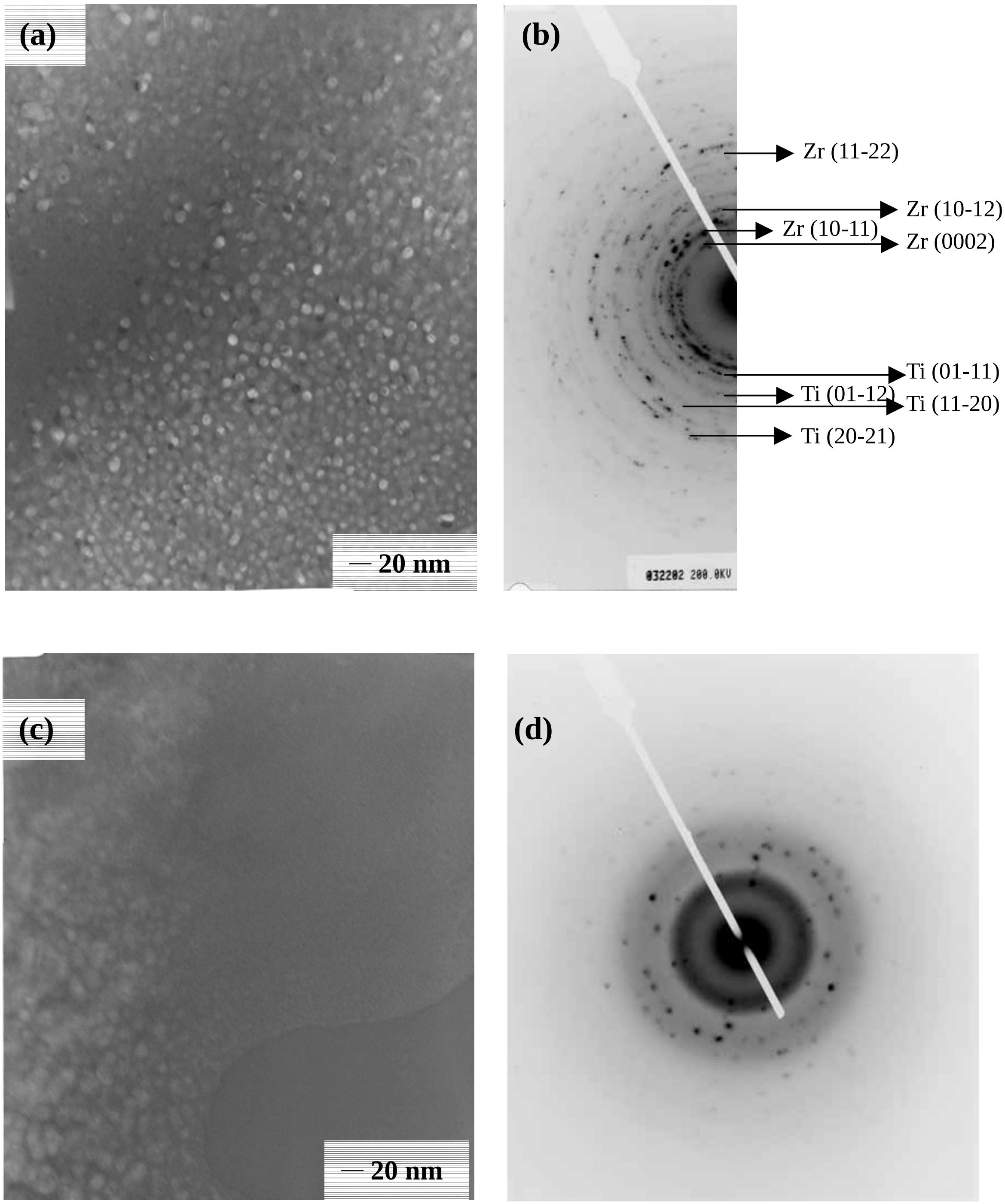

Figure 3.36 TEM bright field images and their associated diffraction patterns for the $Zr_{50}Ti_{50}$ alloy after 60 F&R cycles: (a)(b) showing the nanocrstalline region, and (c)(d) showing the partial amorphous regime.

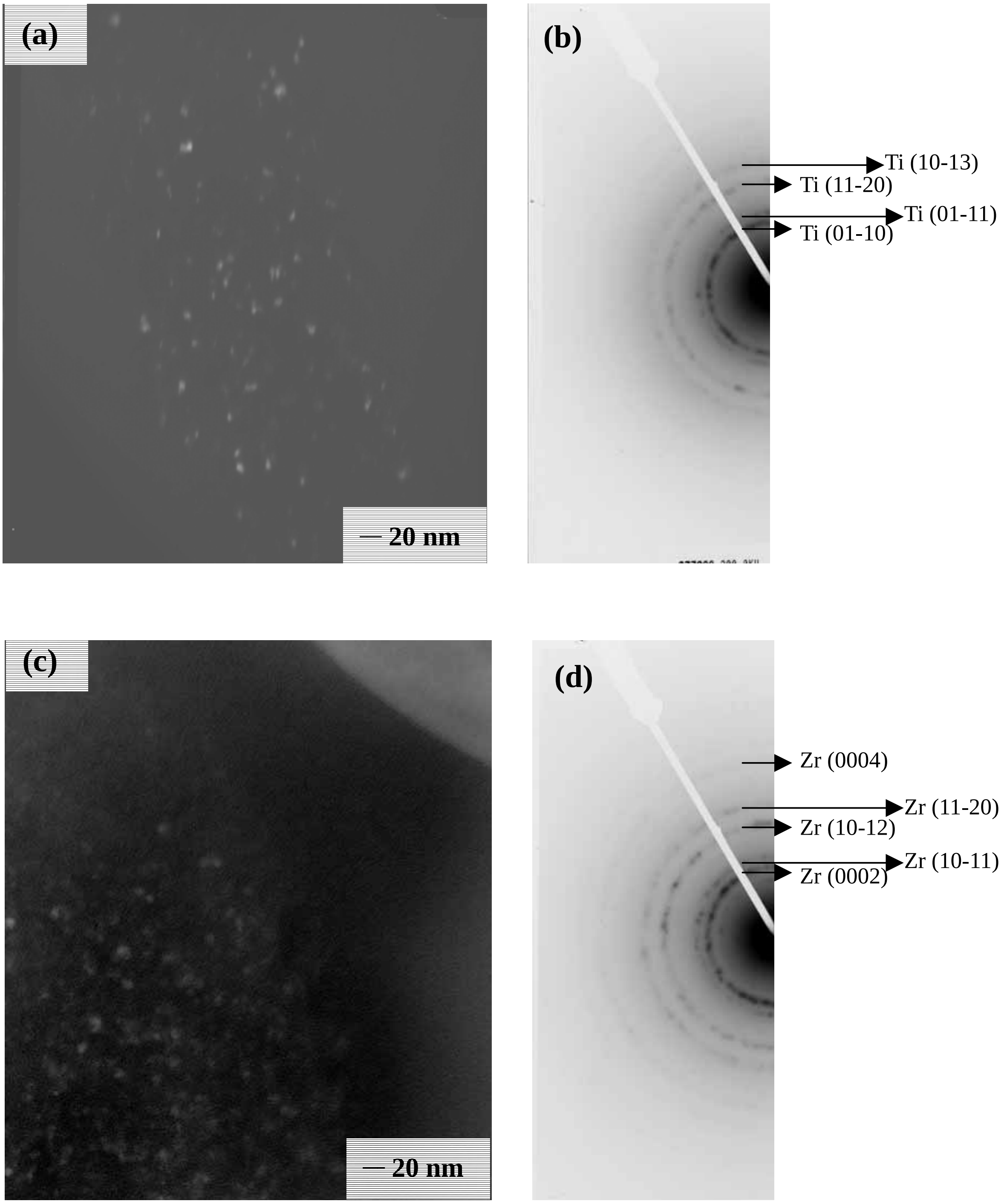

Figure 3.37 TEM bright field images and their associated diffraction patterns for the $Zr_{50}Ti_{50}$ alloy after 80 F&R cycles: (a)-(d) showing the nanocrystalline phases in the amorphous matrix, and (e)(f) showing the amorphous regime.

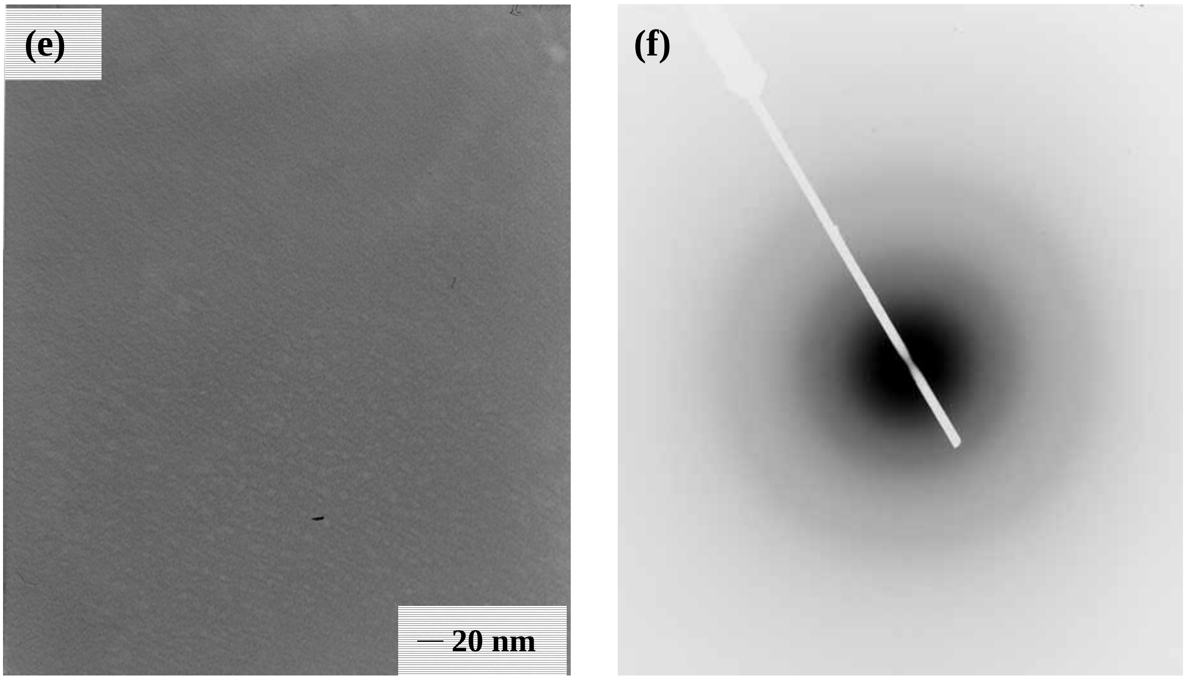
(e)
20 nm
(f)

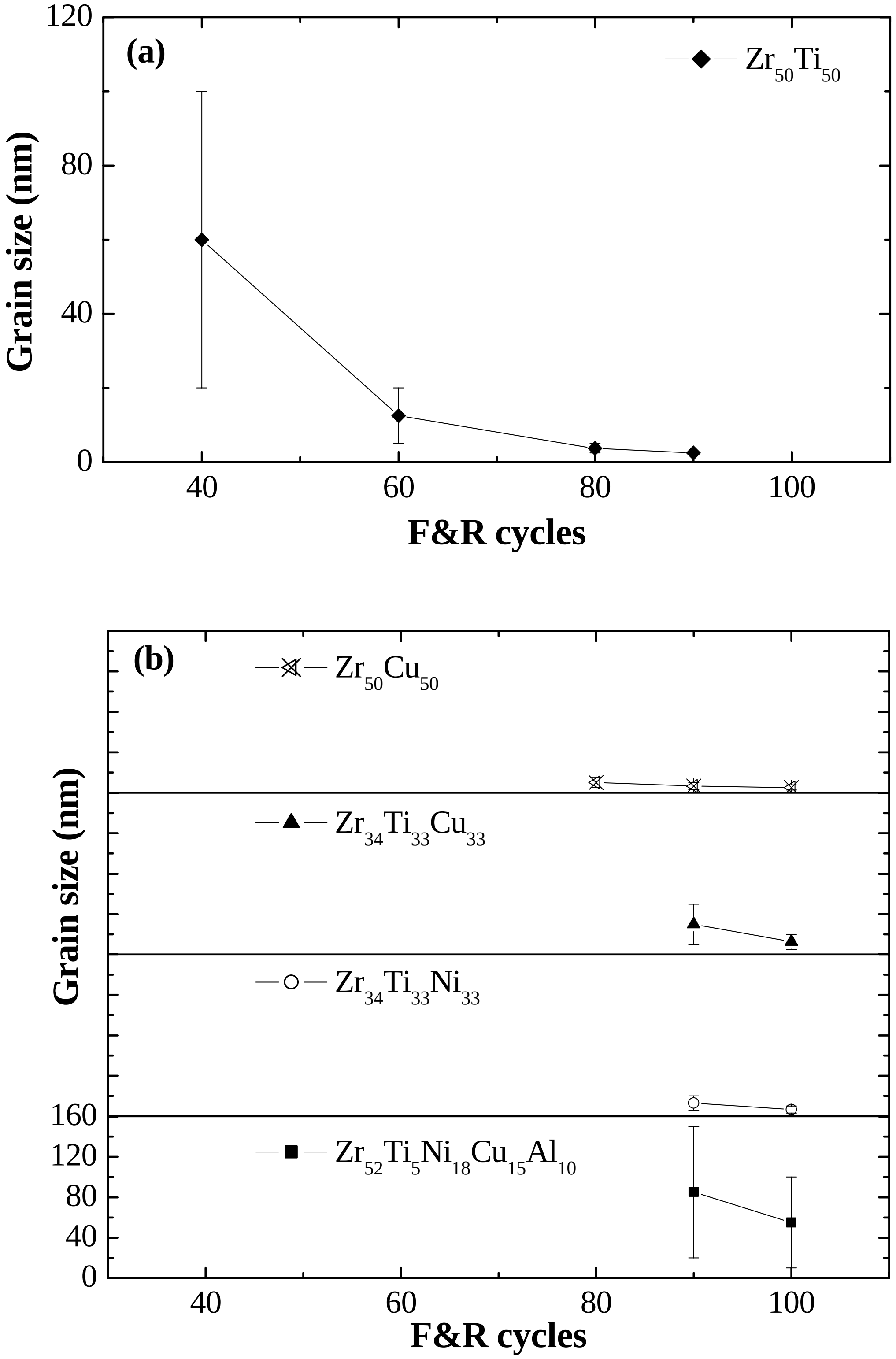

Figure 3.38 The variations of nanocrystalline grain size for (a) $Zr_{50}Ti_{50}$, and other (b) binary, ternary and pantanary alloys as a function of F&R cycles, based on the TEM observations. The data in (b) are presented separately since the scattering bars would overlap each other.

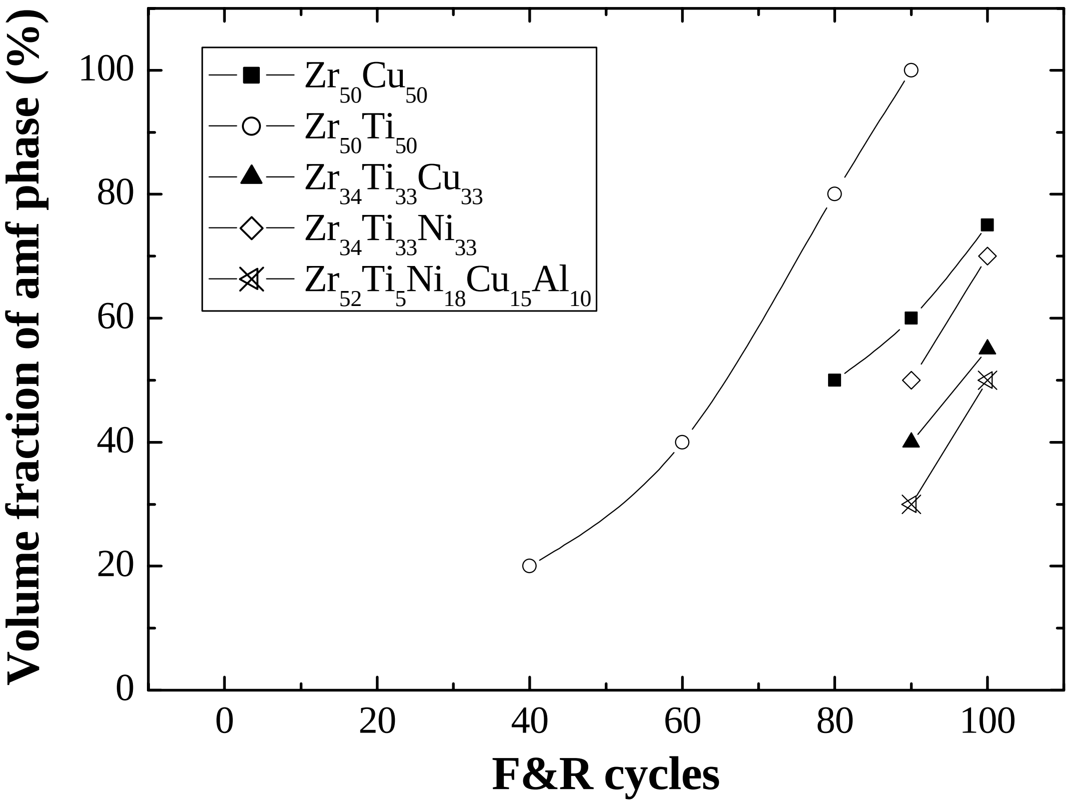

Figure 3.39 The variations of the amorphous volume fraction in various Zr-X alloys as a function of F&R cycles, based on the TEM observations.

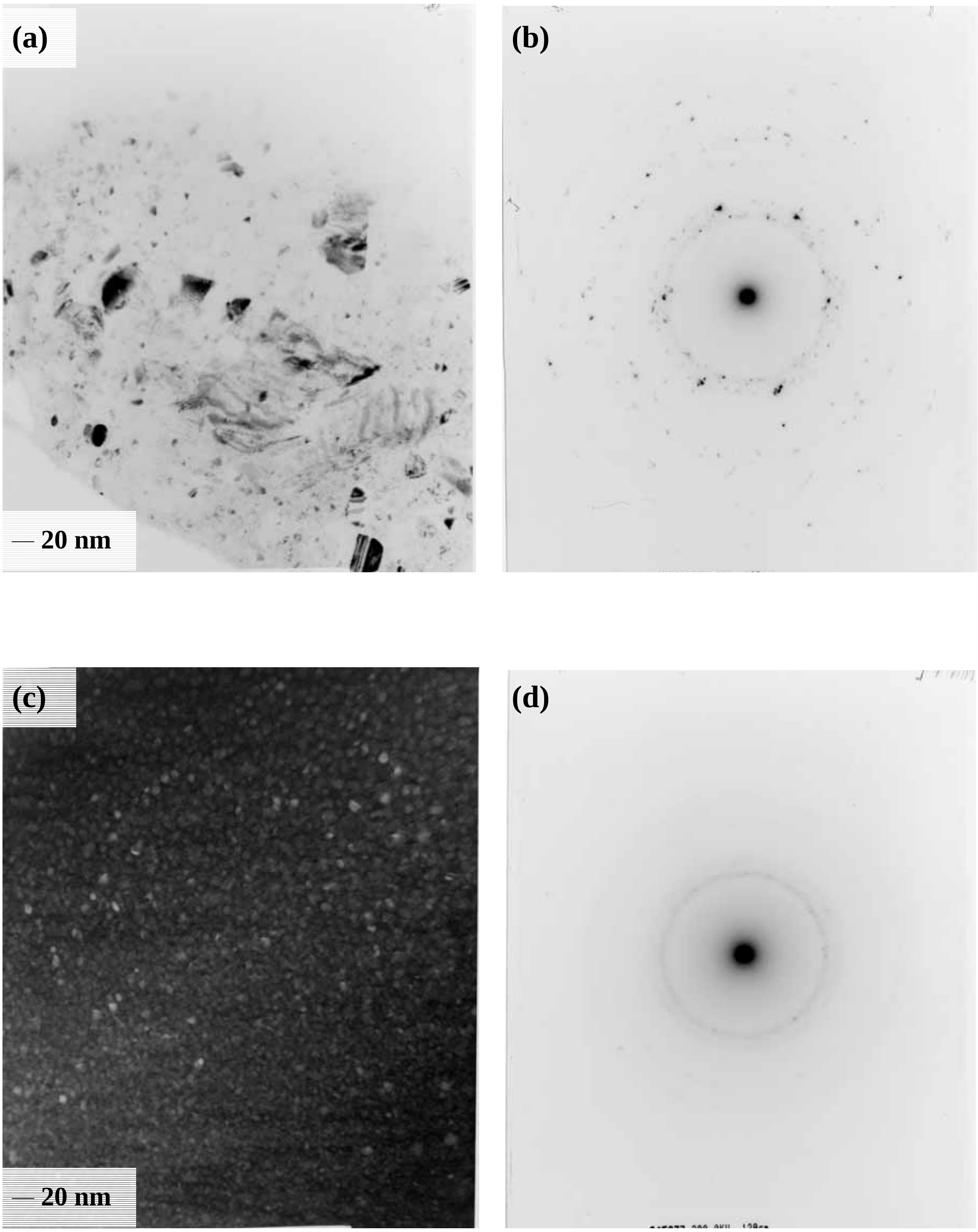

Figure 3.40 TEM bright field and dark field images and their associated diffraction patterns for the $Zr_{25}Ti_{75}$ alloy after 90 F&R cycles: (a)(b)(c)(d) showing the nanocrystalline region, and (e)(f) showing the partial amorphous regime.

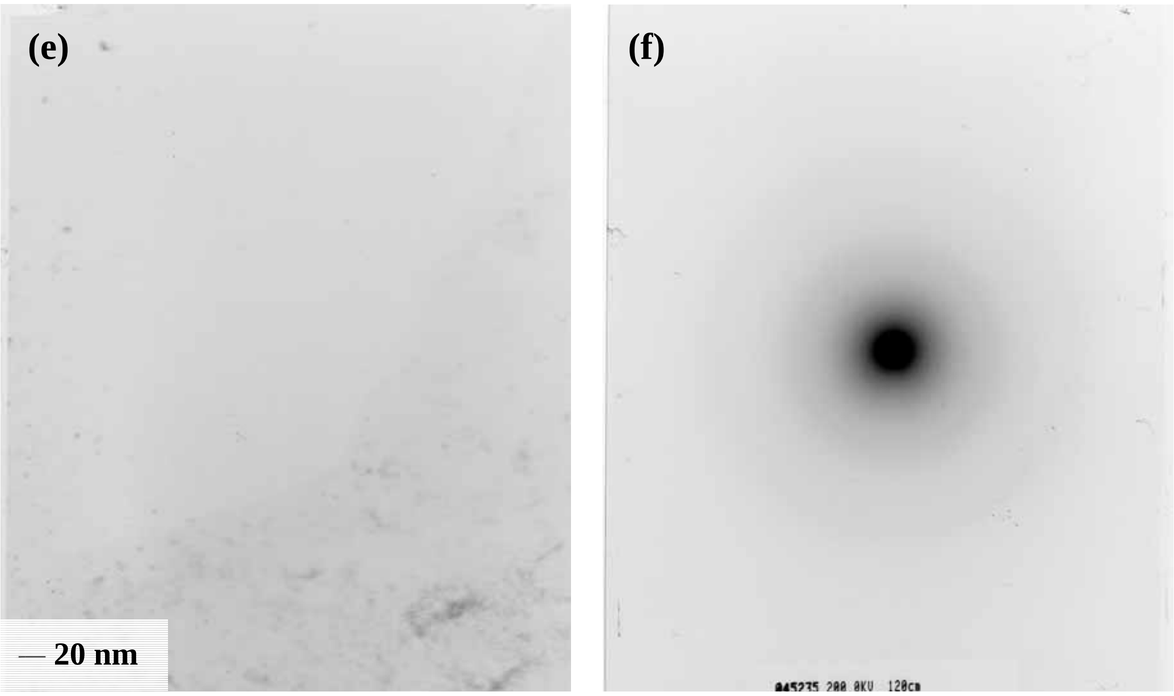
(e)
— 20 nm
(f)
045235 200.0KV 120cm

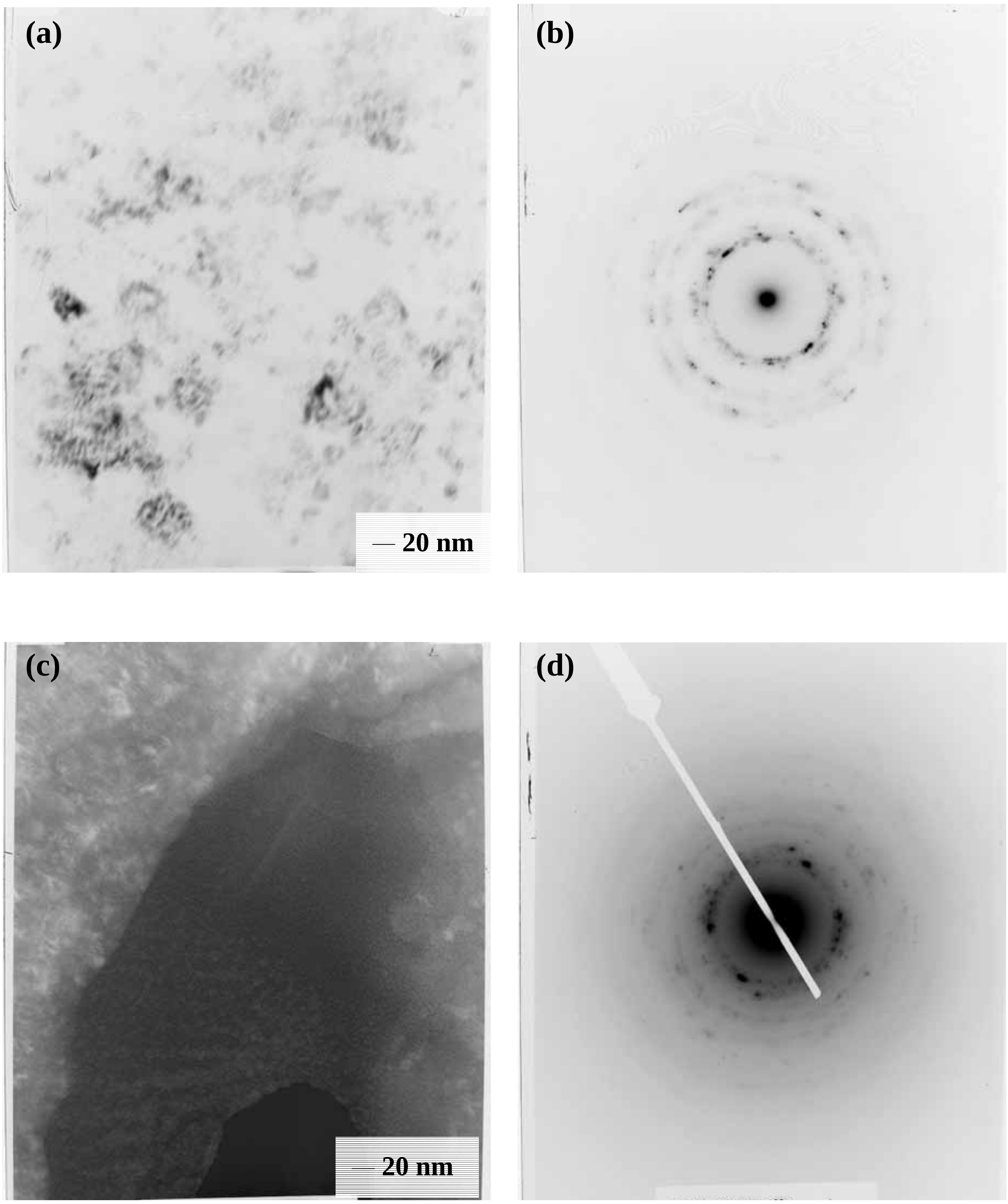

Figure 3.41 TEM bright field and dark field images and their associated diffraction patterns for the $Zr_{75}Ti_{25}$ alloy after 90 F&R cycles: (a)(b)(c)(d) showing the nanocrystalline region.

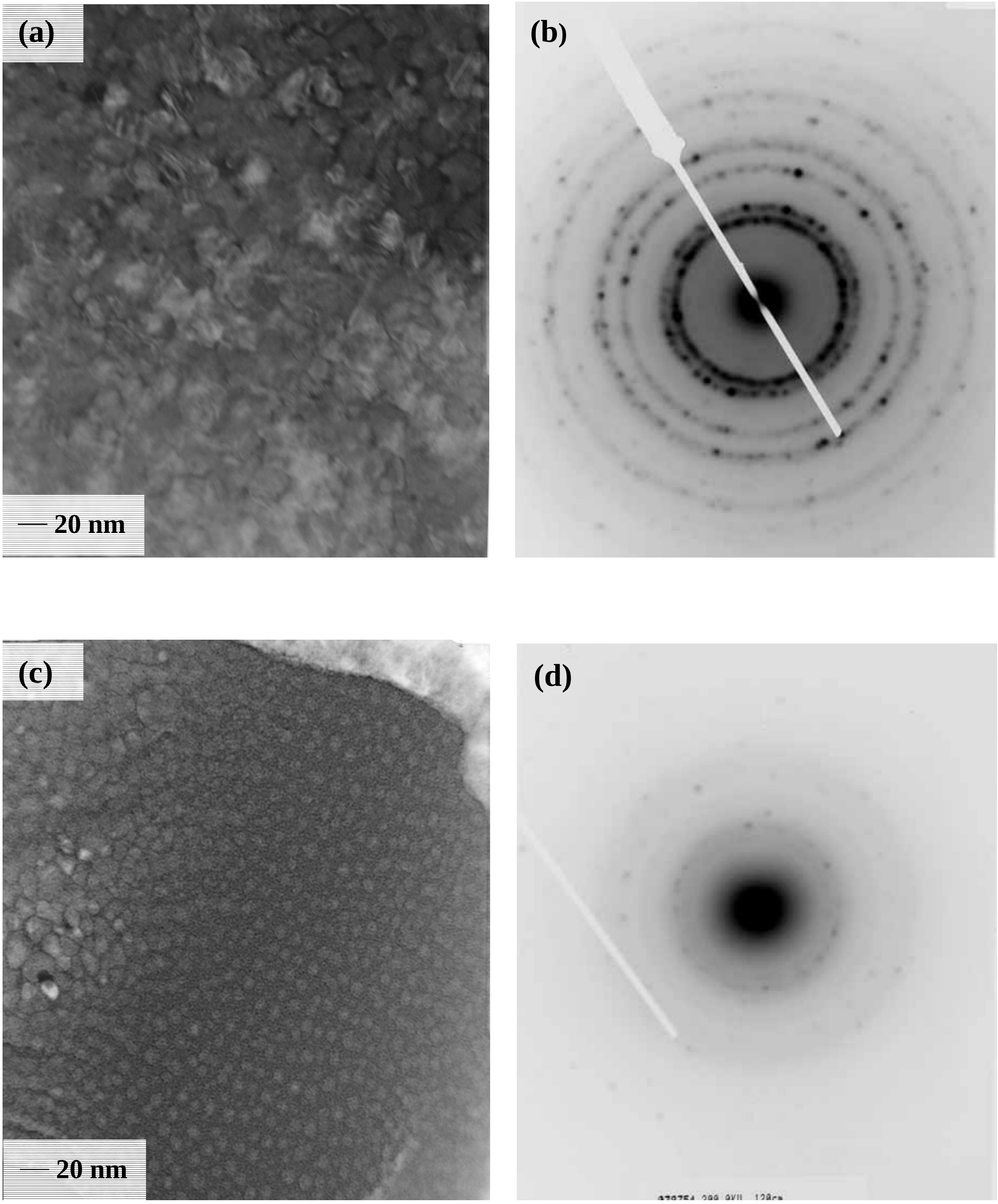

Figure 3.42 TEM bright field images and their associated diffraction patterns for the $Zr_{34}Ti_{33}Cu_{33}$ alloy after 100 F&R cycles: (a)(b) showing the nanocrystalline region, (c)(d) showing the nanocrystalline phases in the amorphous matrix, and (e)(f) showing the amorphous regime.

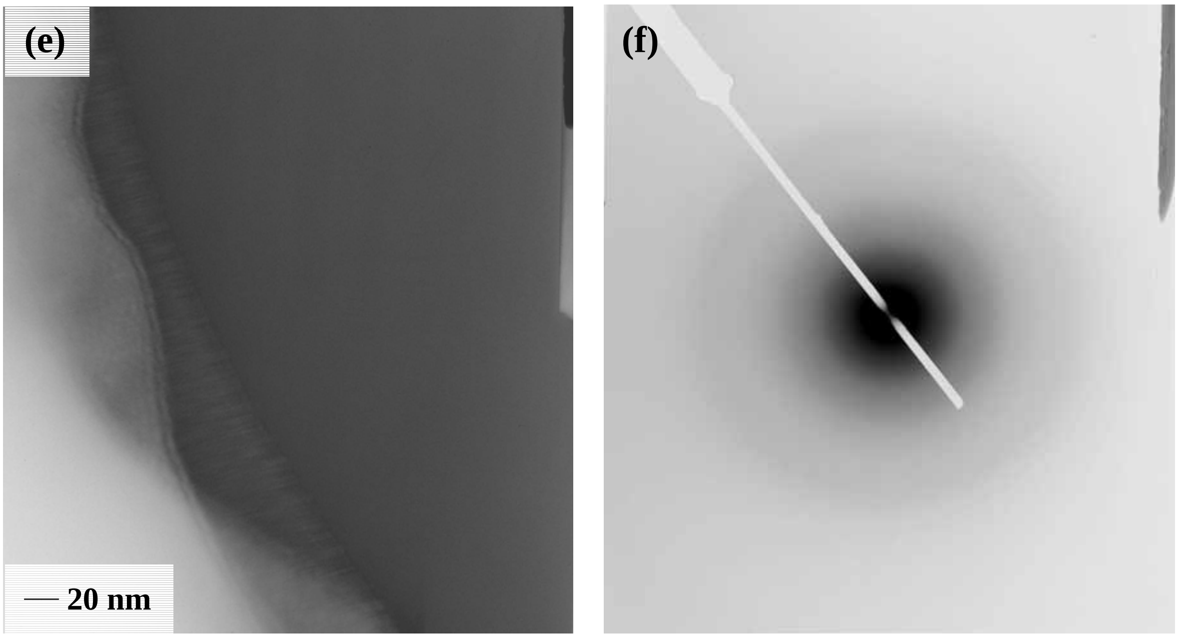
(e)
20 nm
(f)

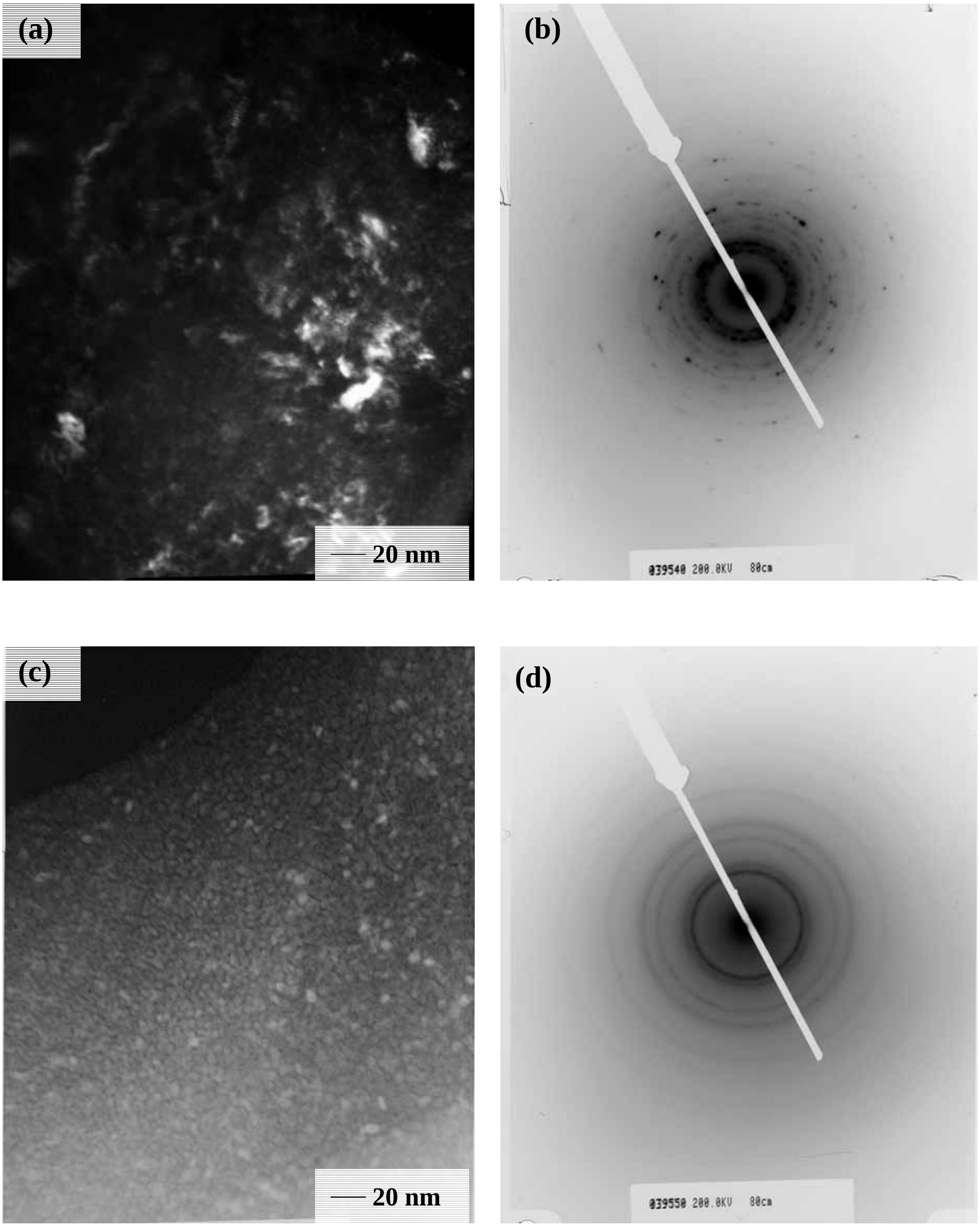

Figure 3.43 TEM bright field images and their associated diffraction patterns for the $Zr_{34}Ti_{33}Ni_{33}$ alloy after 100 F&R cycles: (a)(b) showing the nanocrystalline region, (c)(d) showing the nanocrystalline phases in the amorphous matrix, and (e)(f) showing the amorphous regime.

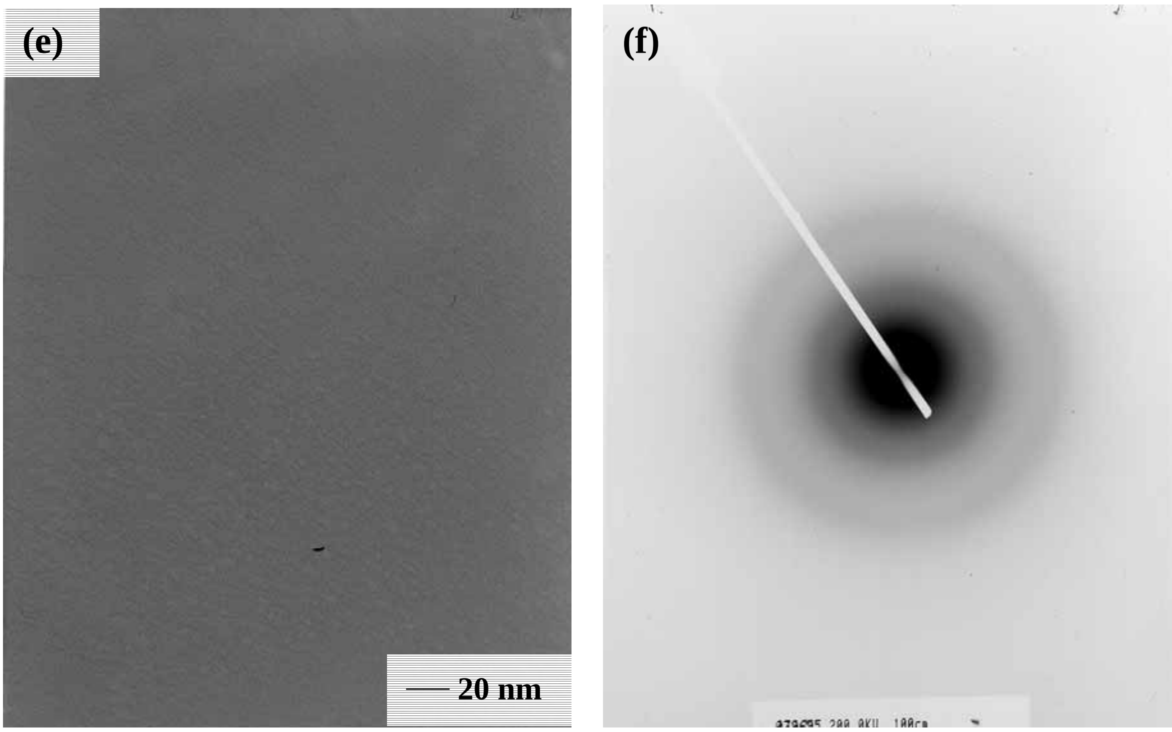
(e)
20 nm
(f)
079695 200.0KV 100cm

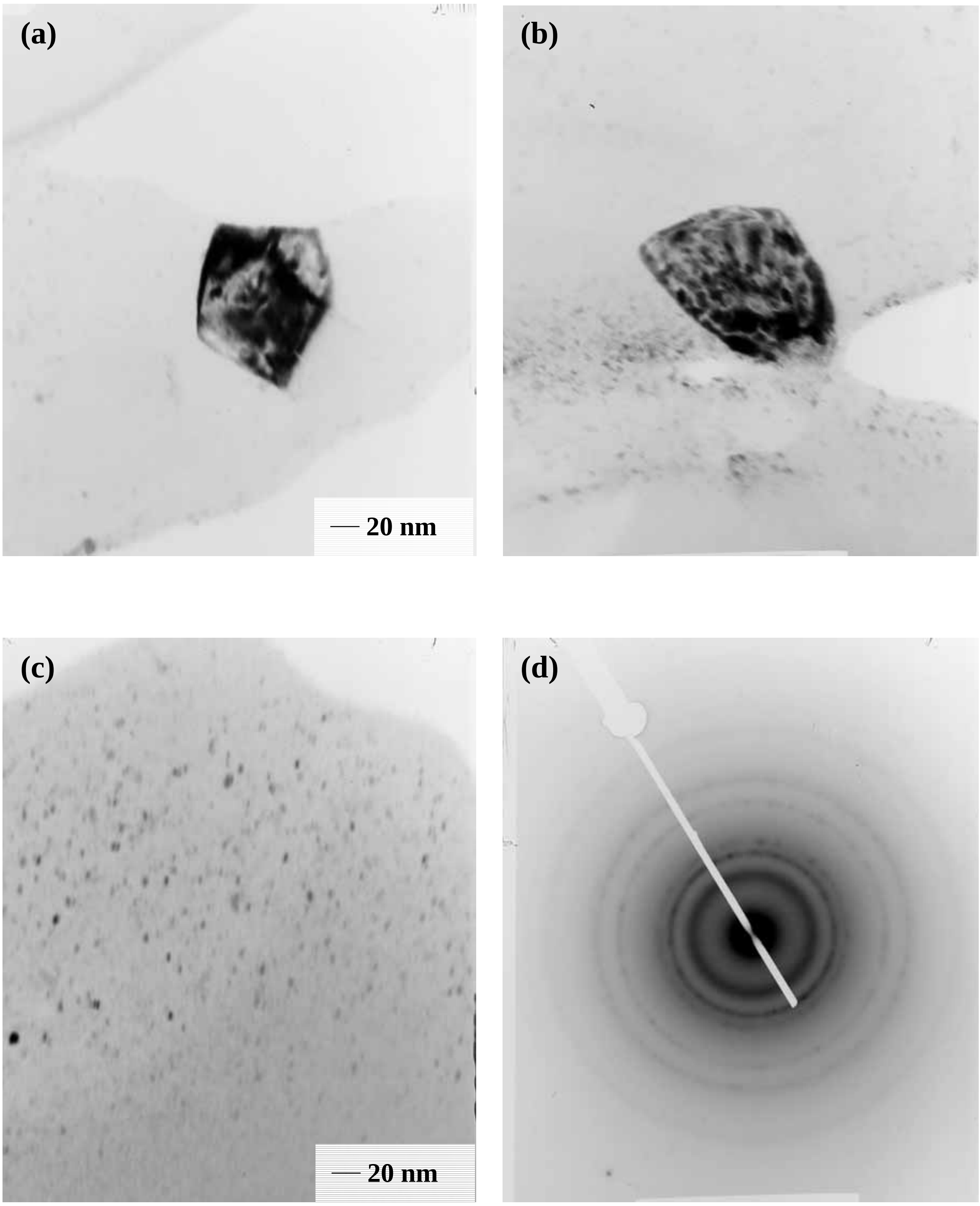

Figure 3.44 TEM bright field images and their associated diffraction patterns for the $Zr_{52}Ti_5Ni_{15}Cu_{18}Al_{10}$ alloy after 100 F&R cycles: (a)(b) showing the occasional large nanocrystalline phase, (c)(d) showing the nanocrystalline phases in the amorphous matrix, and (e)(f) showing the amorphous regime.

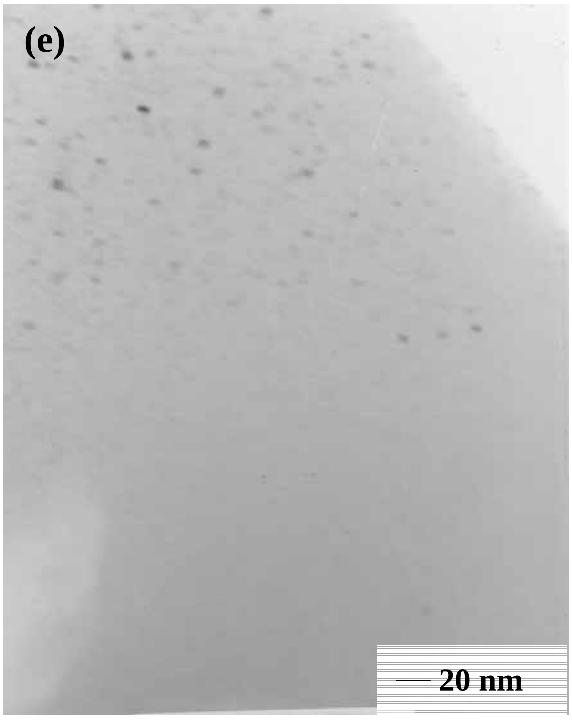
(e)
20 nm

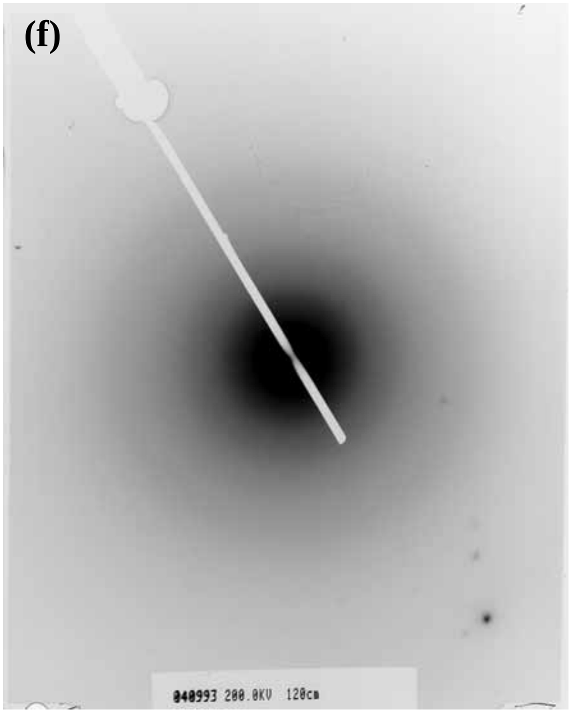
(f)
040993 200.0KV 120cm

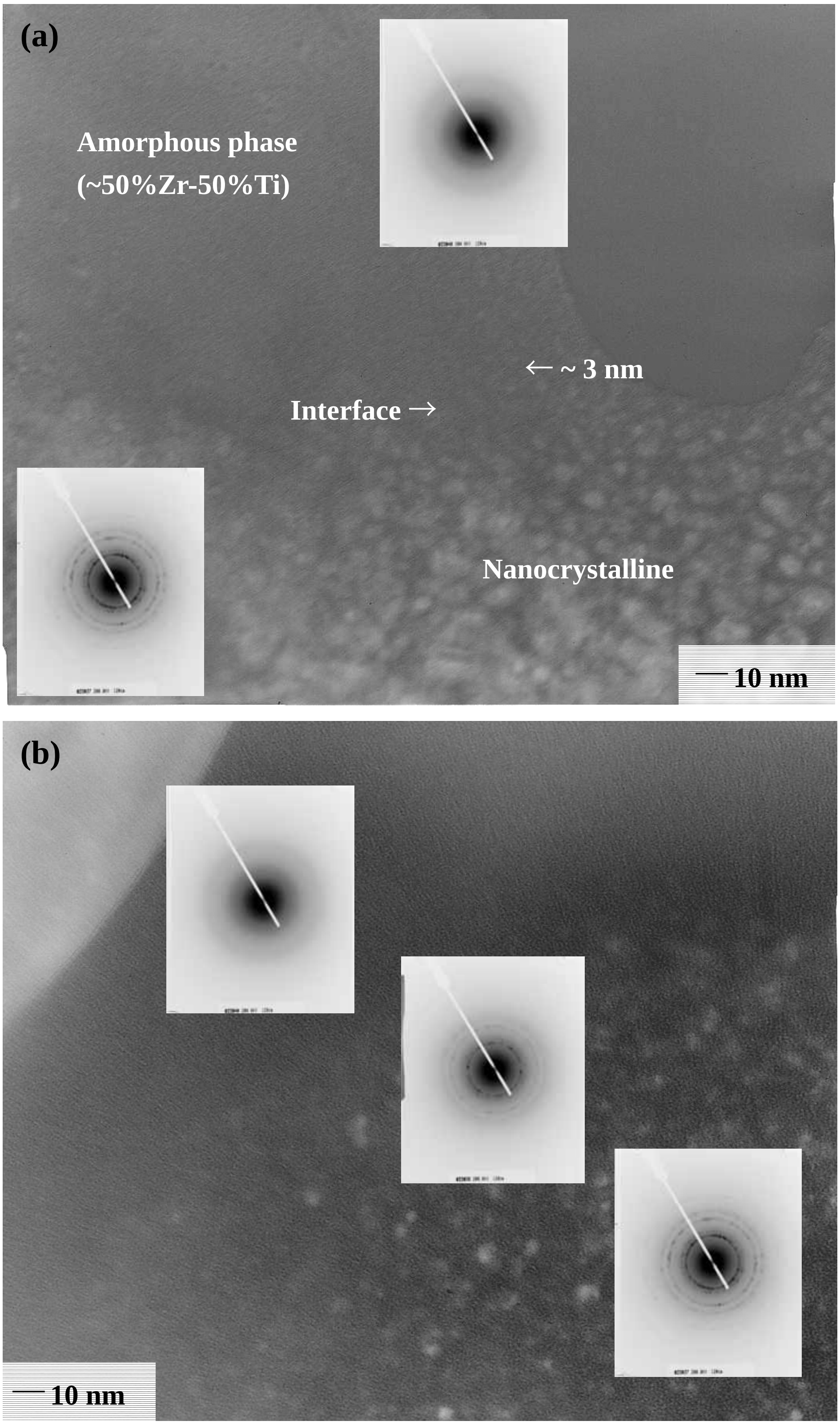

Figure 3.45 TEM bright field images of the interface region between the nanocrystalline and amorphous phases taken from the $Zr_{50}Ti_{50}$ alloys after (a) 60 and (b) 80 F&R cycles. The smallest nanocrystalline phase size near the interface is around 3 nm.

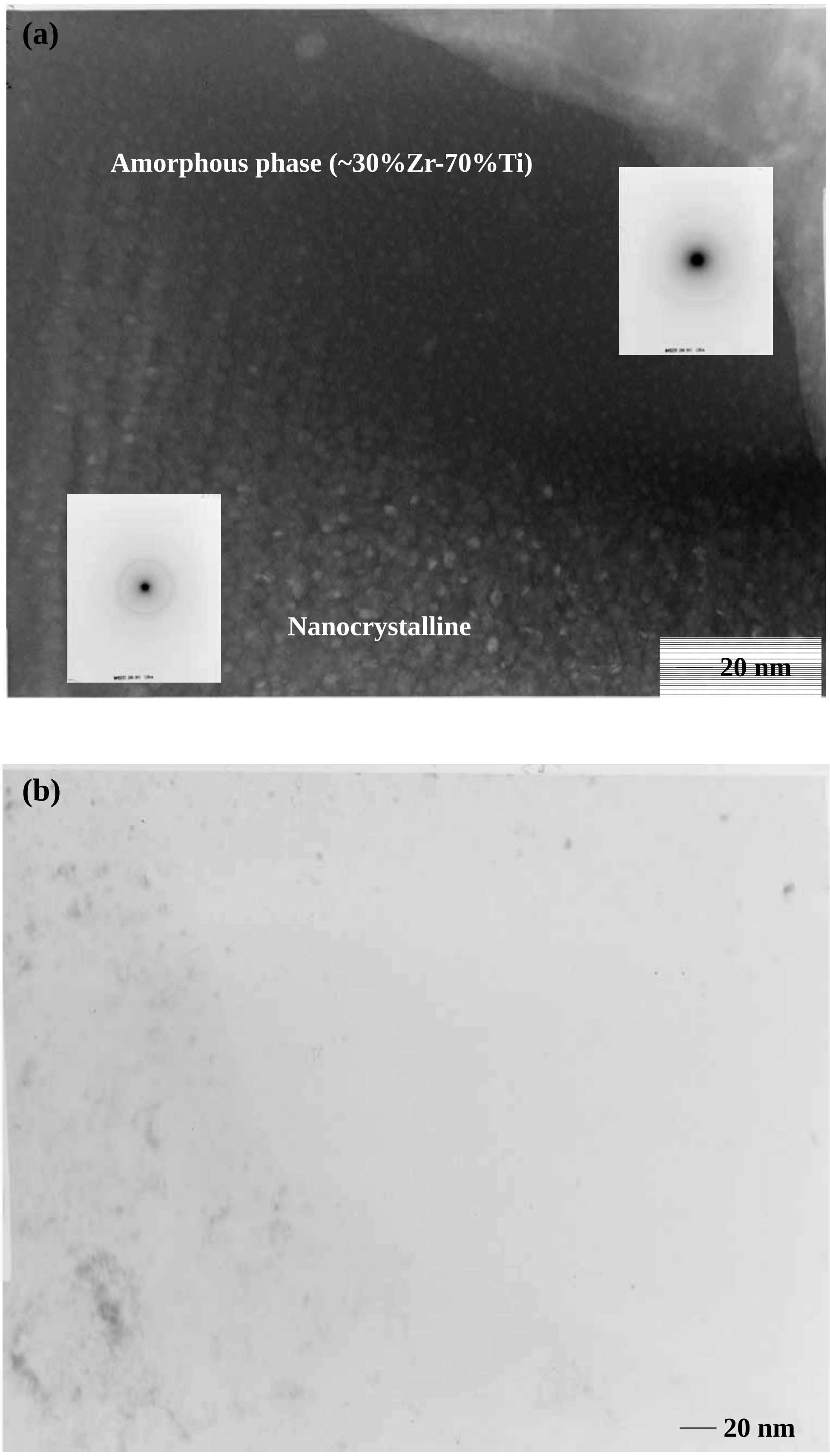

Figure 3.46 TEM (a) bright field and (b) dark field images of the interface region between the nanocrystalline and amorphous phases taken from the $Zr_{25}Ti_{75}$ alloys after 90 F&R cycles.

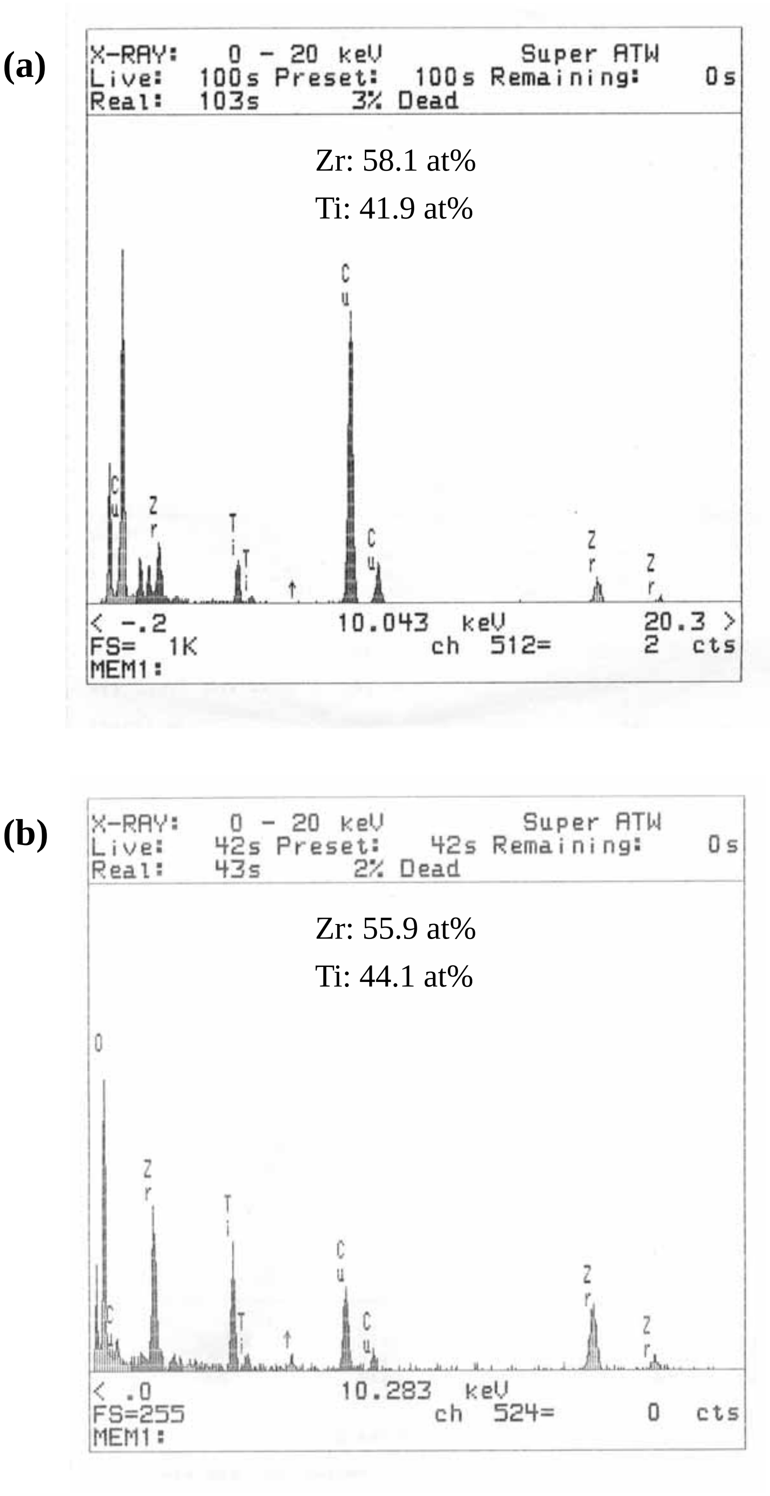

(a)

```
X-RAY:    0 - 20 keV           Super ATW
Live:   100s Preset:   100s Remaining:     0s
Real:   103s        3% Dead
```

Zr: 58.1 at%

Ti: 41.9 at%

```
< -.2             10.043  keV           20.3 >
FS=  1K                ch  512=          2  cts
MEM1:
```

(b)

```
X-RAY:    0 - 20 keV           Super ATW
Live:    42s Preset:    42s Remaining:     0s
Real:    43s        2% Dead
```

Zr: 55.9 at%

Ti: 44.1 at%

```
< .0              10.283  keV
FS=255                 ch  524=          0  cts
MEM1:
```

Figure 3.47 TEM/EDS results for (a) nanocrystalline (b) amorphous regimes of the $Zr_{50}Ti_{50}$ alloy after 60 F&R cycles (in Fig. 3.45(a)).

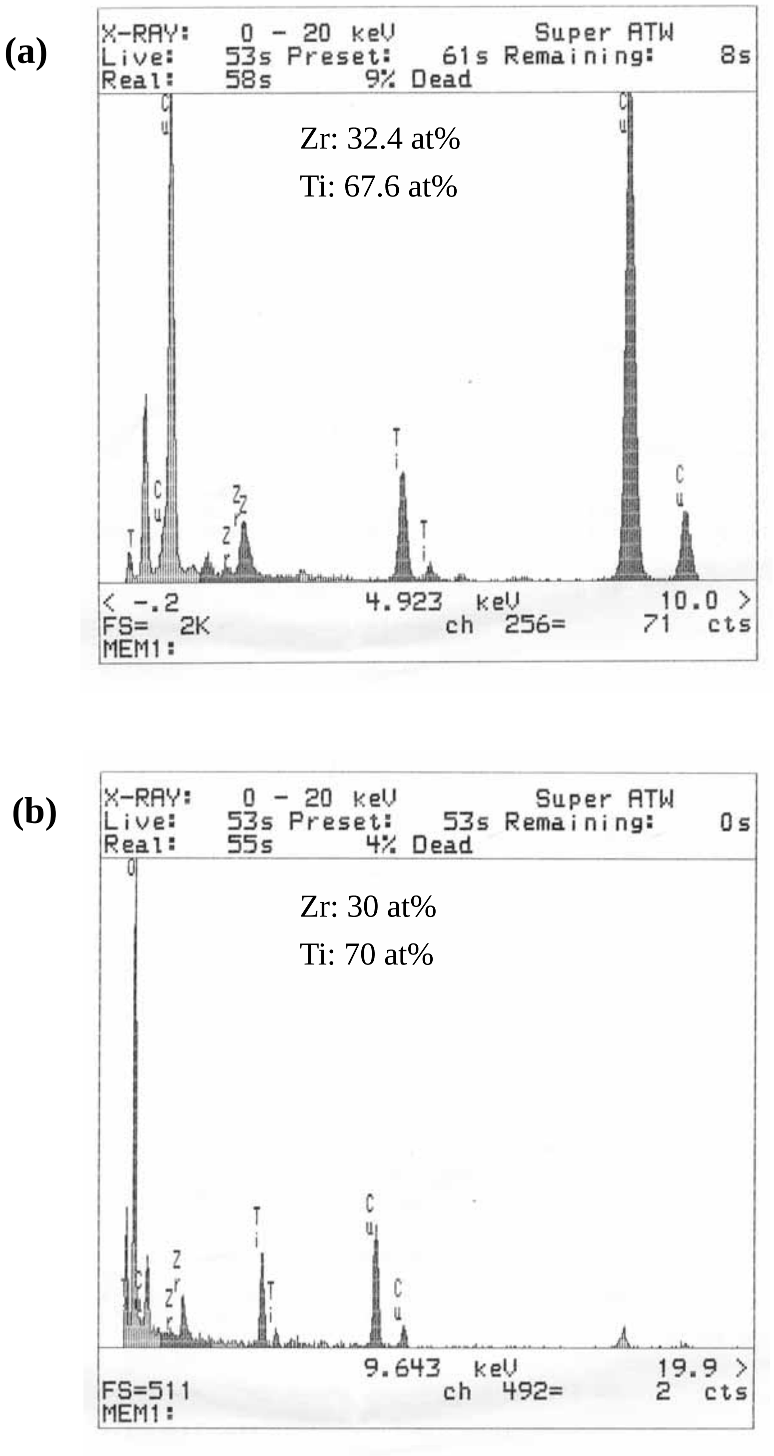

Figure 3.48 TEM/EDS results for (a) nanocrystalline (b) amorphous regimes of the $Zr_{25}Ti_{75}$ alloy after 90 F&R cycles (in Fig. 3.46(a)).

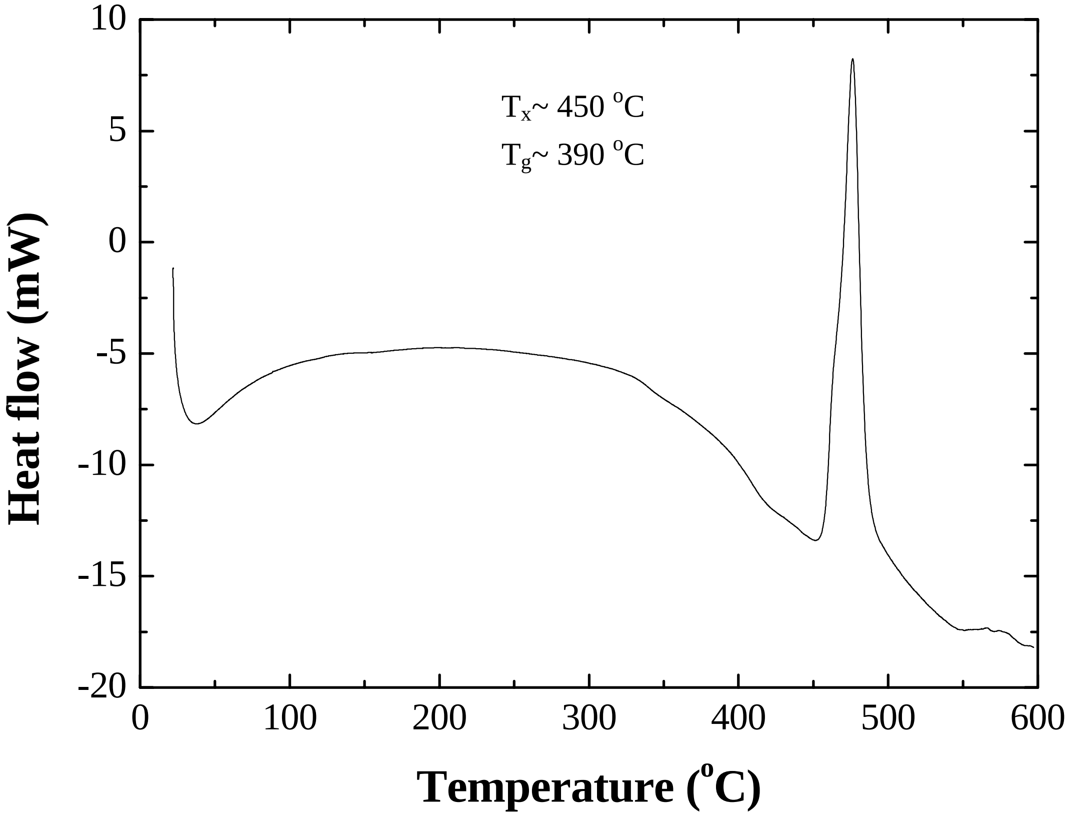

Figure 3.49 The DSC measurement of the nearly amorphous $Zr_{50}Ti_{50}$ alloy made by ARB route.

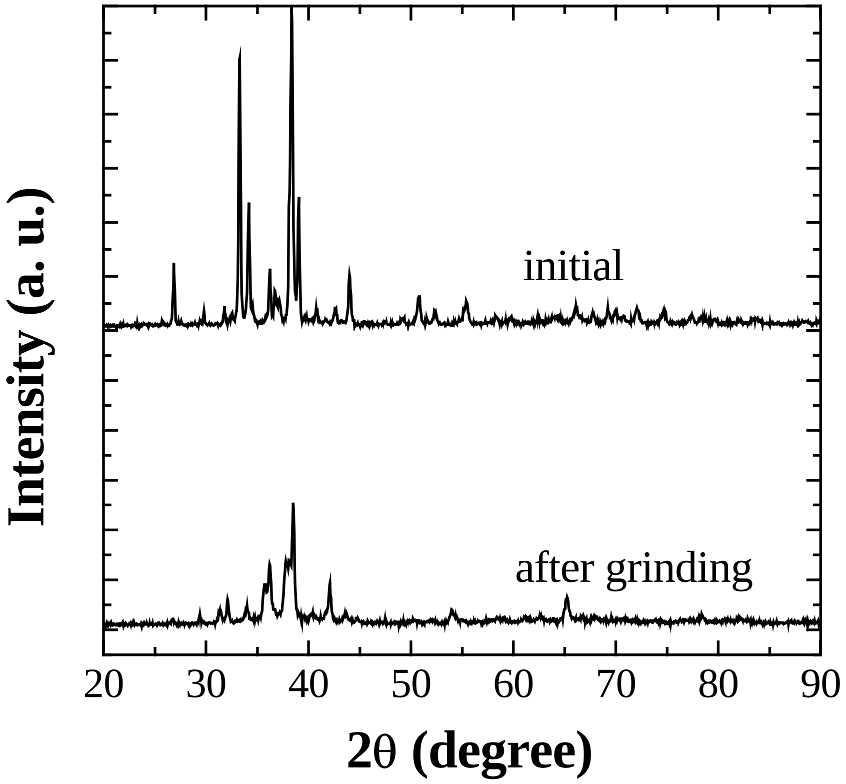

Figure 3.50 XRD patterns of the arc melted sample ($Zr_{52}Ti_5Ni_{15}Cu_{18}Al_{10}$).

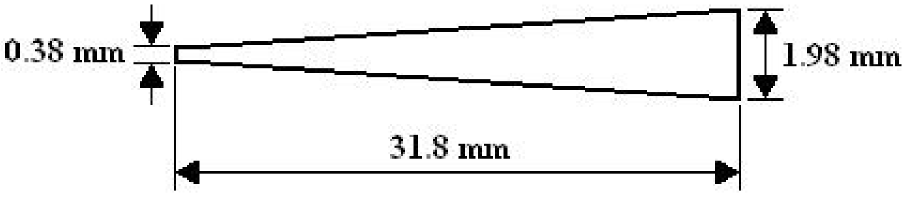

Figure 3.51 Schematic drawing of the size of wedge-shaped specimen made by drop casting method ($Zr_{52}Ti_5Ni_{15}Cu_{18}Al_{10}$).

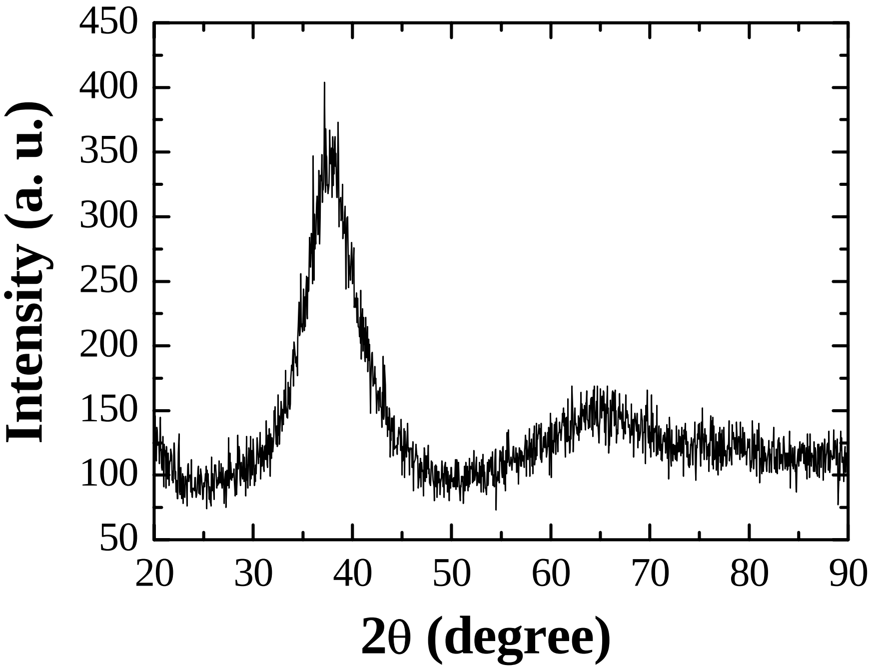

Figure 3.52 The XRD pattern of the melt spun sample ($Zr_{52}Ti_5Ni_{15}Cu_{18}Al_{10}$).

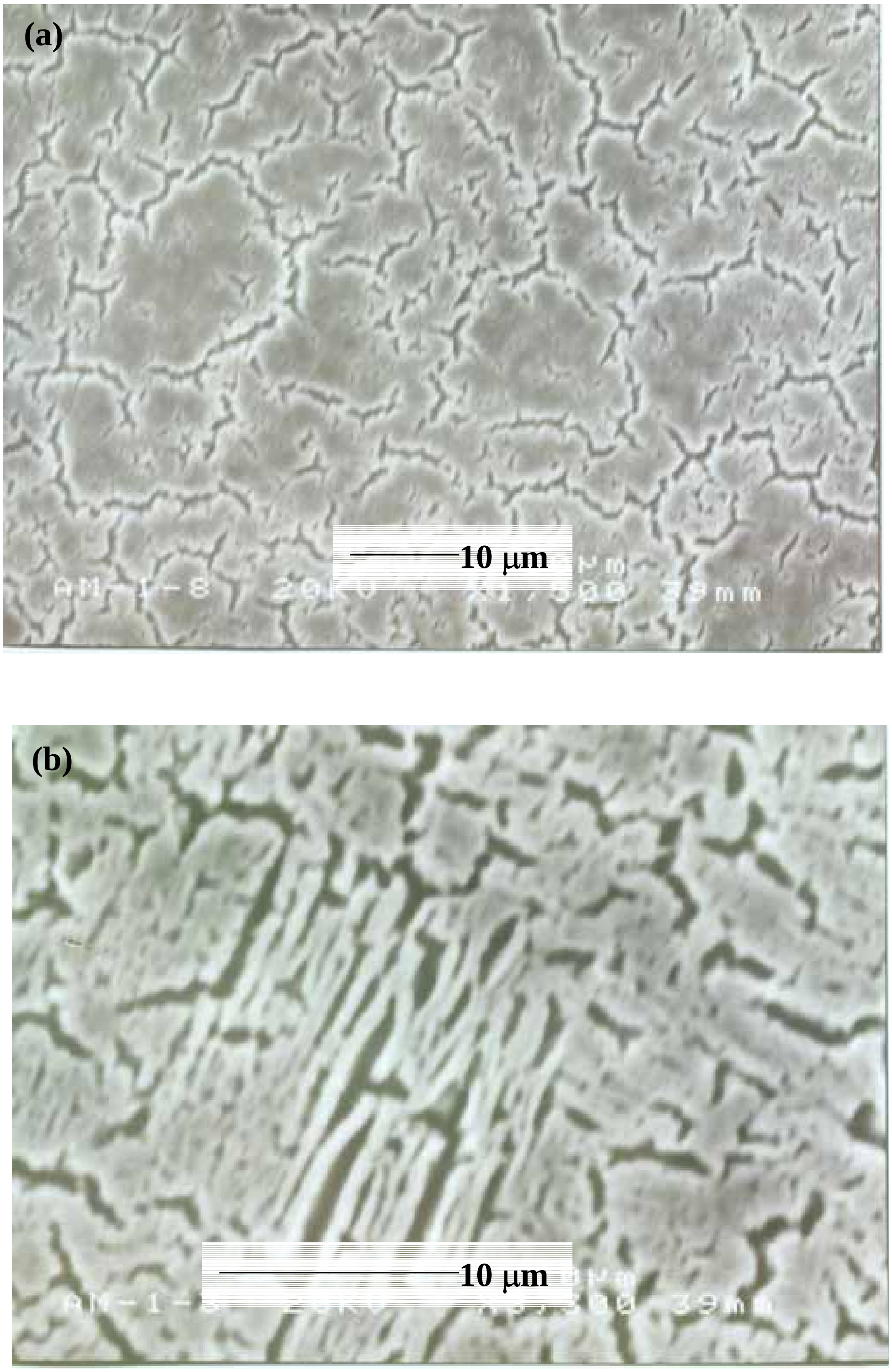

Figure 3.53 SEM/SEI of the arc melted sample, $Zr_{52}Ti_5Ni_{15}Cu_{18}Al_{10}$.

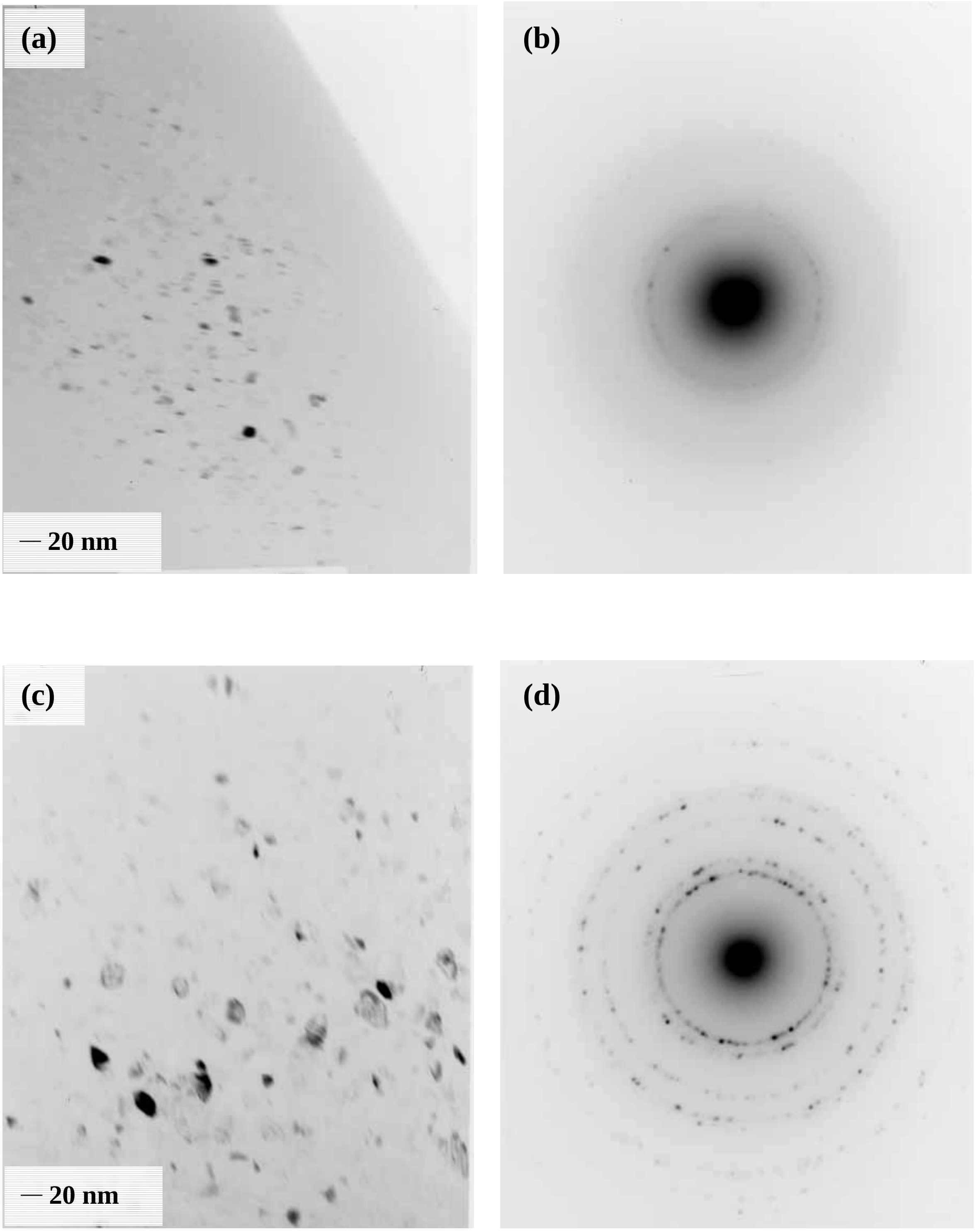

Figure 3.54 TEM dark field images and their associated diffraction patterns for the melt spun $Zr_{52}Ti_5Ni_{15}Cu_{18}Al_{10}$ alloy: (a)(b)(c)(d) showing the occasional larger nanocrystalline phase, and (e)(f) showing the fine nanocrystalline phases in the amorphous matrix.

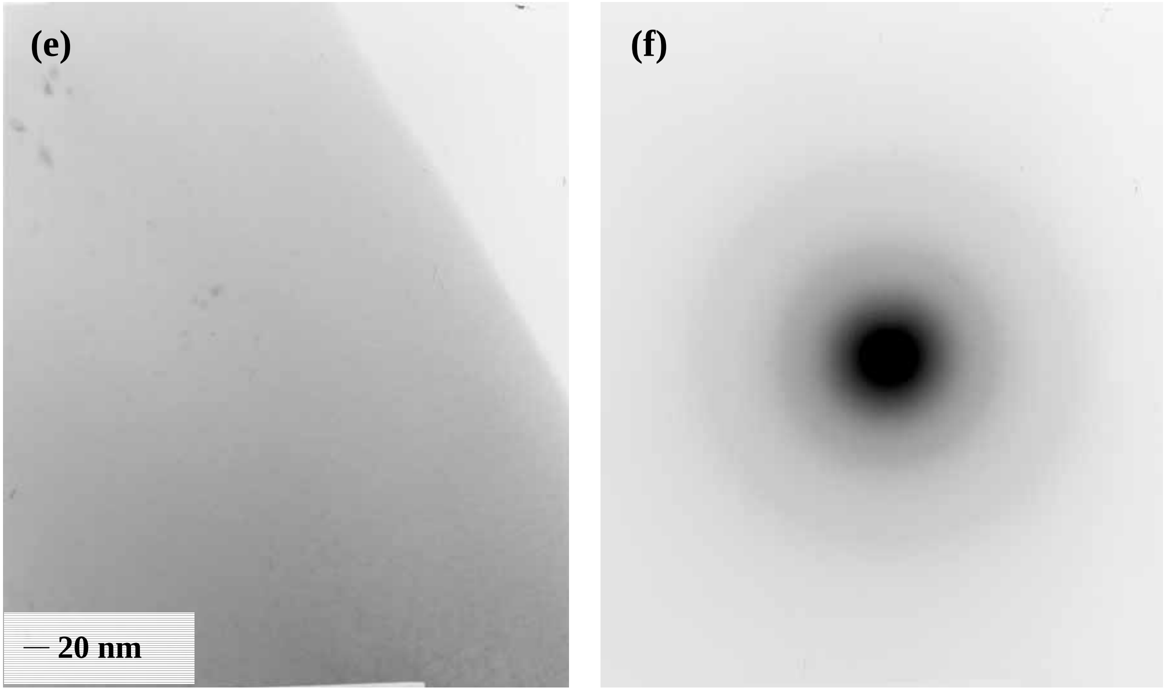
(e)
20 nm
(f)

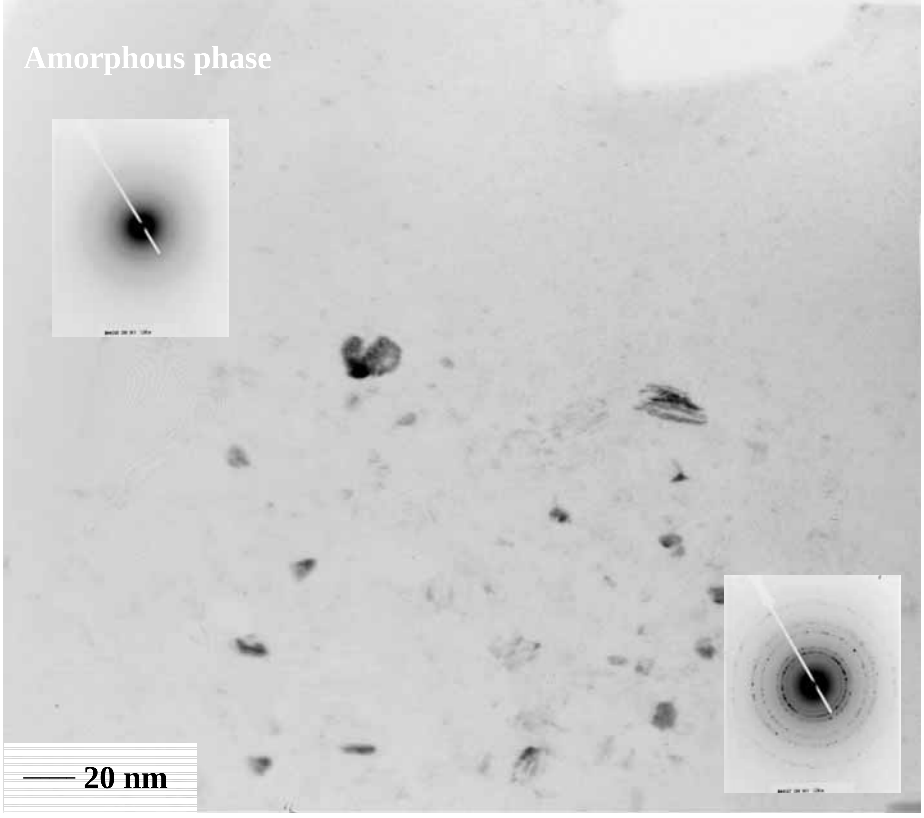

Figure 3.55 TEM dark field image of the interface region between the nanocrystalline and amorphous phases taken from the melt spun $Zr_{52}Ti_5Ni_{15}Cu_{18}Al_{10}$ alloy.

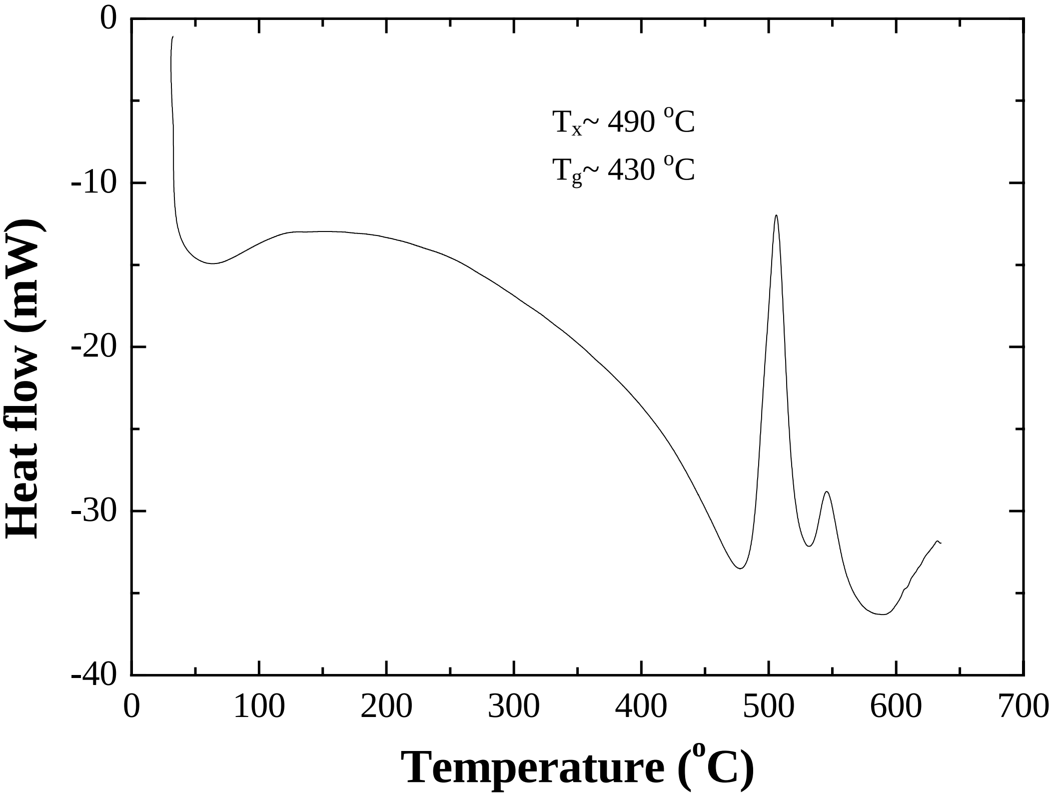

Figure 3.56 The DSC measurement of the melt spun $Zr_{52}Ti_5Ni_{15}Cu_{18}Al_{10}$ alloy.

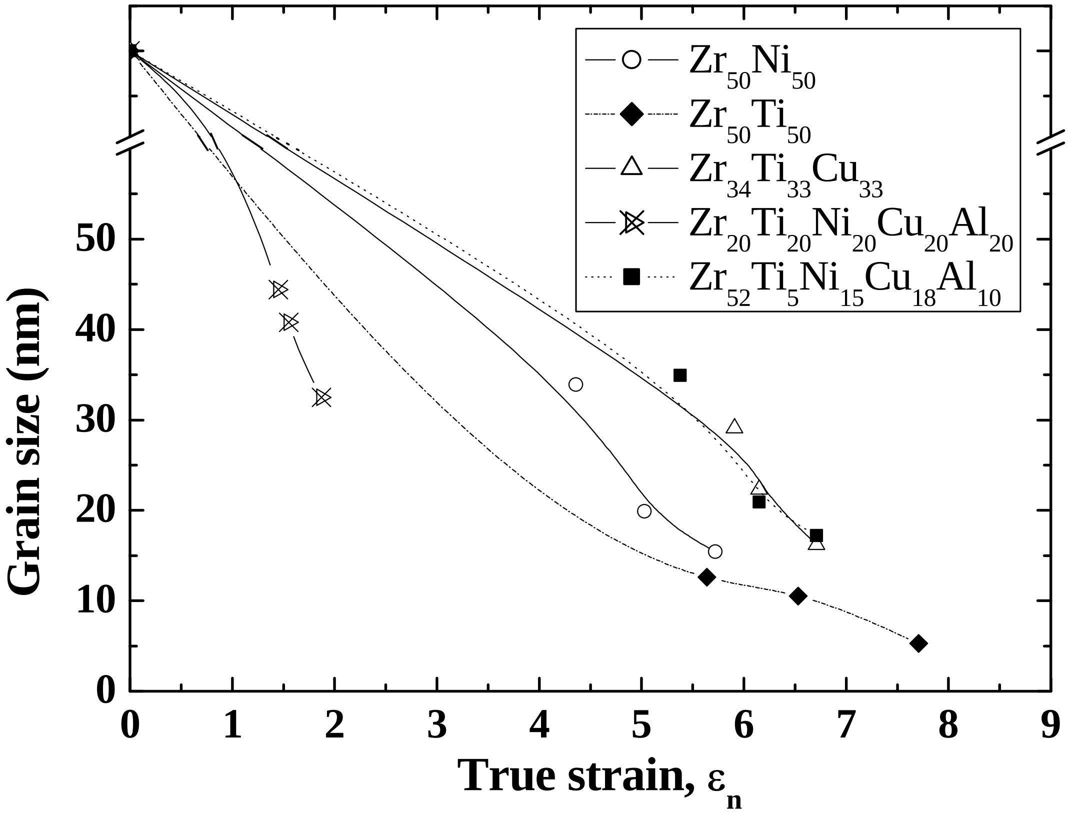

Figure 4.1 The estimated grain size variation of Zr as a function of accumulated true strain for various alloy systems, based on the XRD observations.

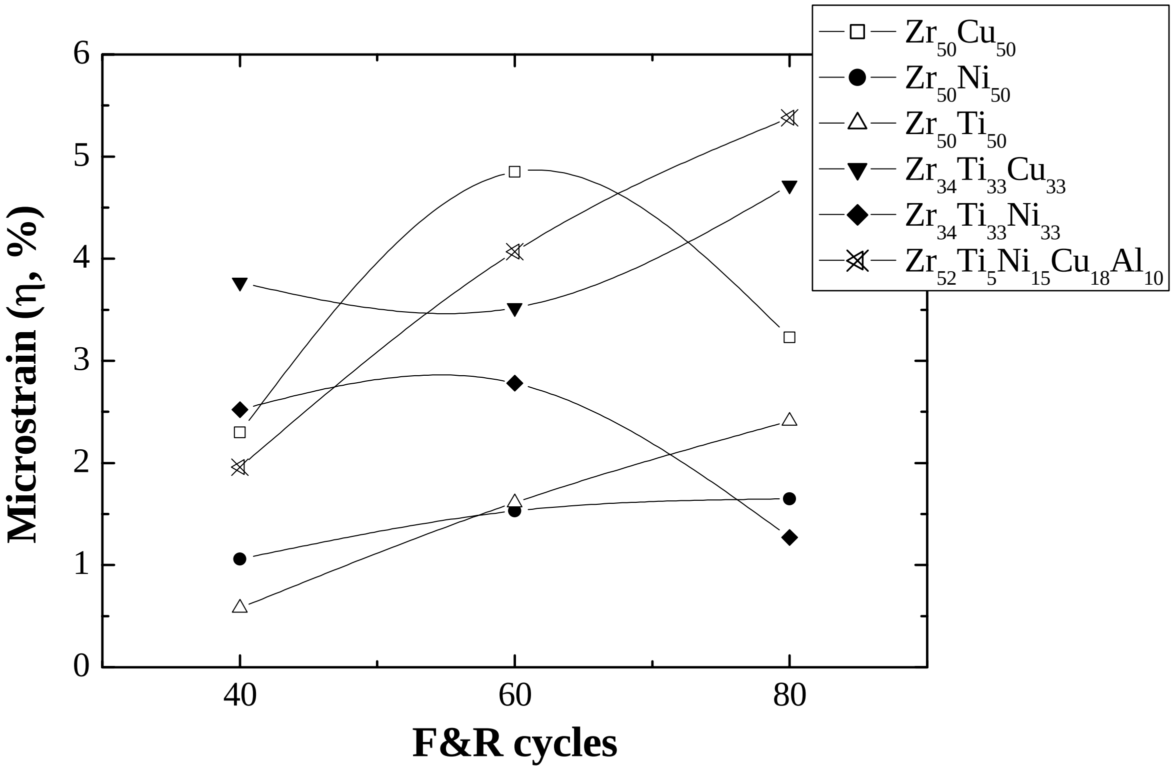

Figure 4.2 The variation of microstarin η values with different F&R cycles for various alloy systems.

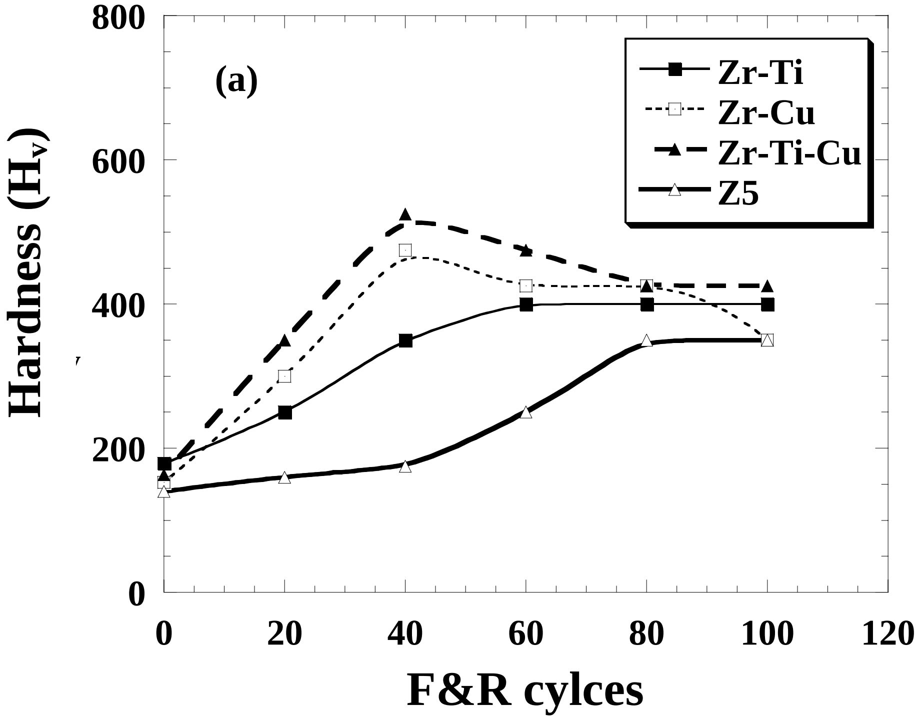

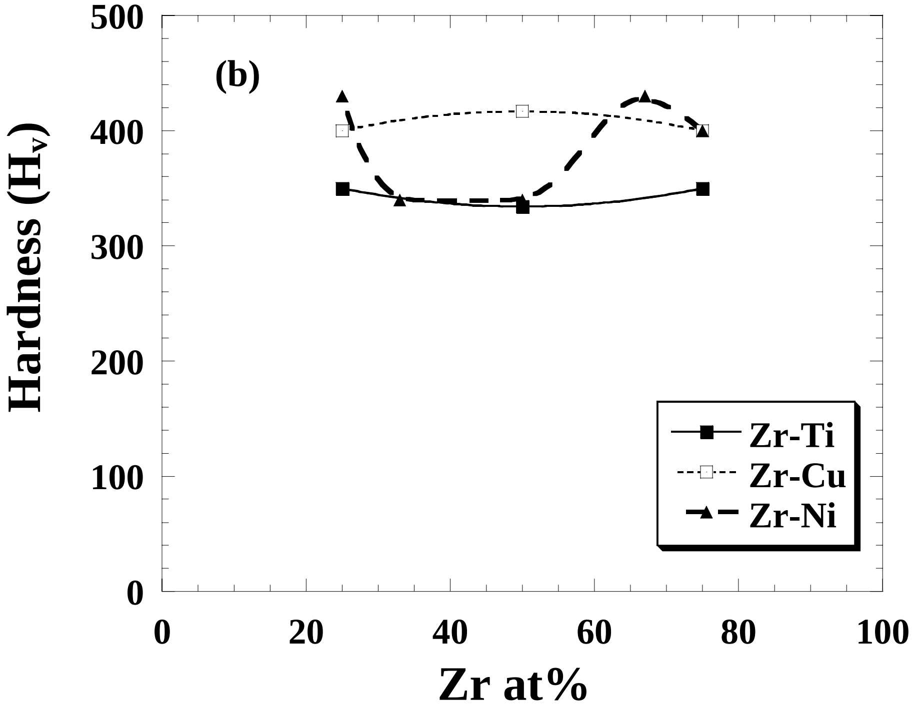

Figure 4.3 Variations of the H_v microhardness as a function of (a) F&R cycles, and (b) composition (Z5 represents the $Zr_{52}Ti_5Ni_{15}Al_{10}Cu_{18}$ alloy).

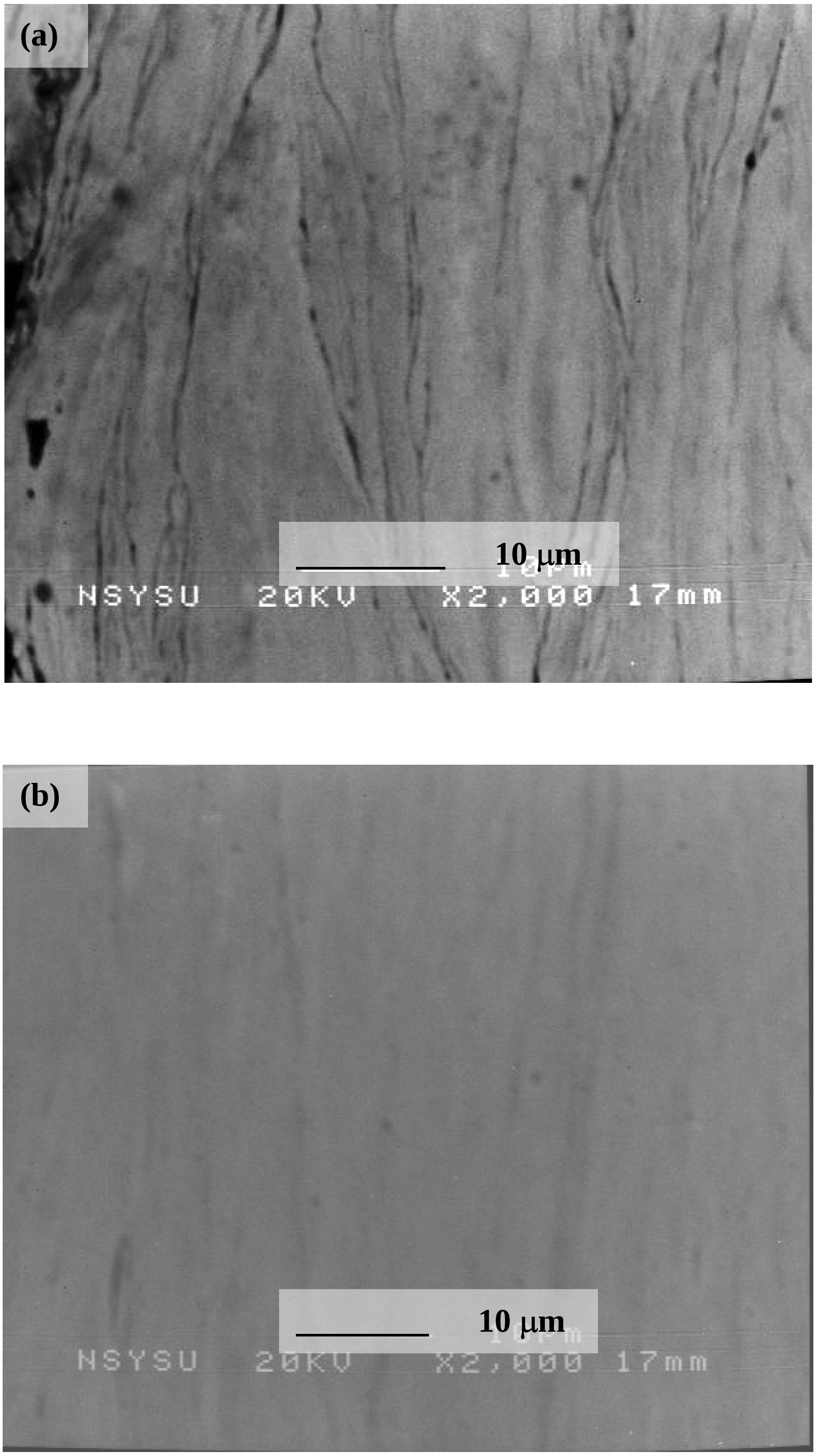

Figure 4.4 SEM/BEI side view of the $Zr_{50}Cu_{50}$ alloys after 40 F&R cycles: (a) without and (b) with the pre-hardening step of the Cu foils.

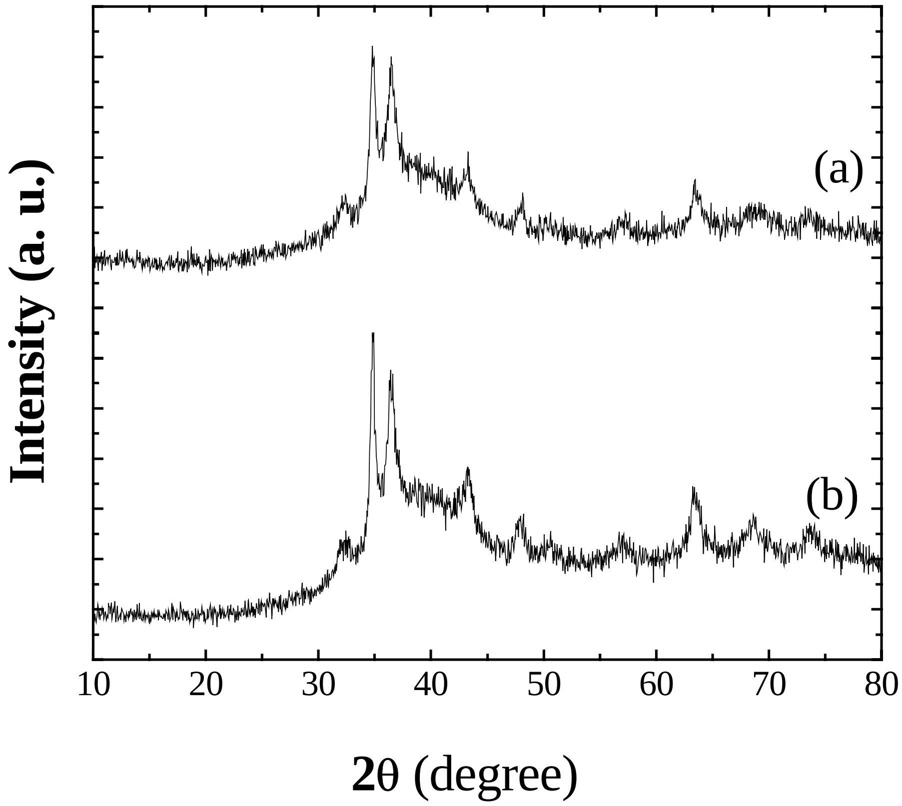

Figure 4.5 XRD patterns of the $Zr_{50}Cu_{50}$ alloys after 80 F&R cycles: (a) with and (b) without the pre-hardening step of Cu foils.

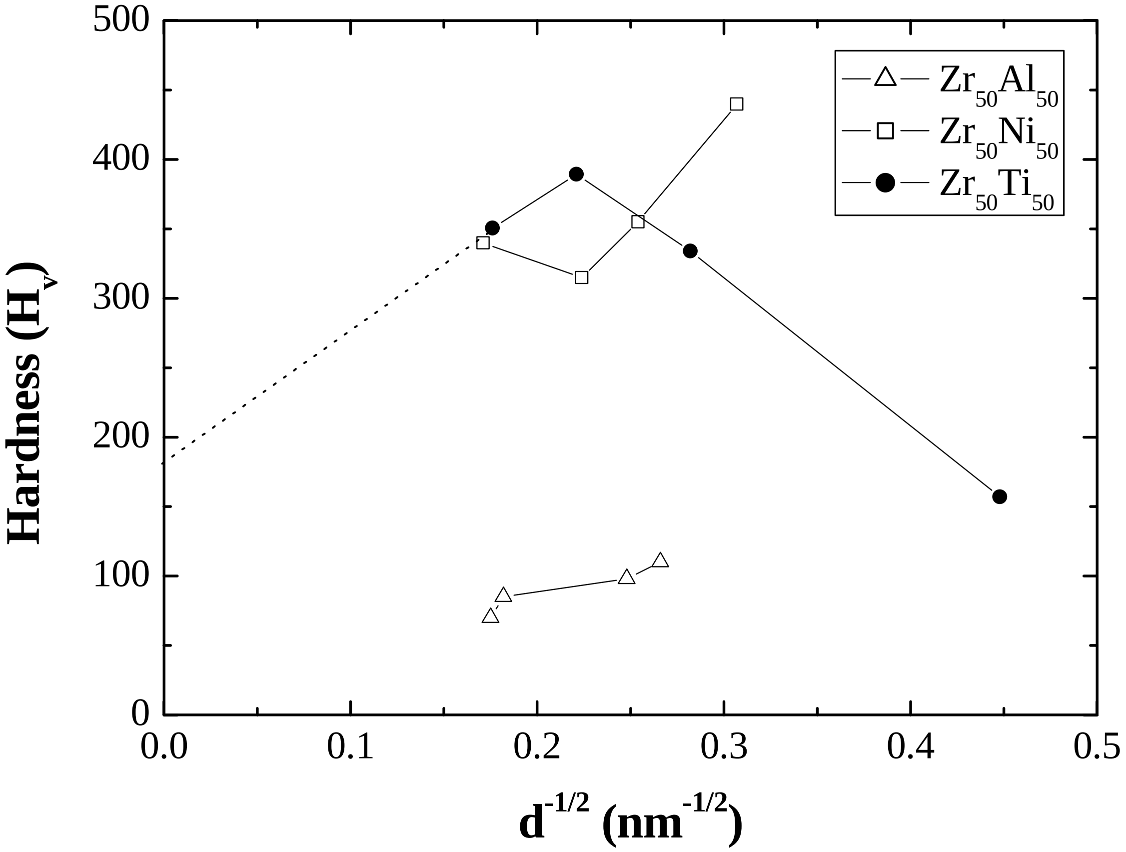

Figure 4.6 The plots of hardness and the inverse square-root of grain size for some binary alloys.

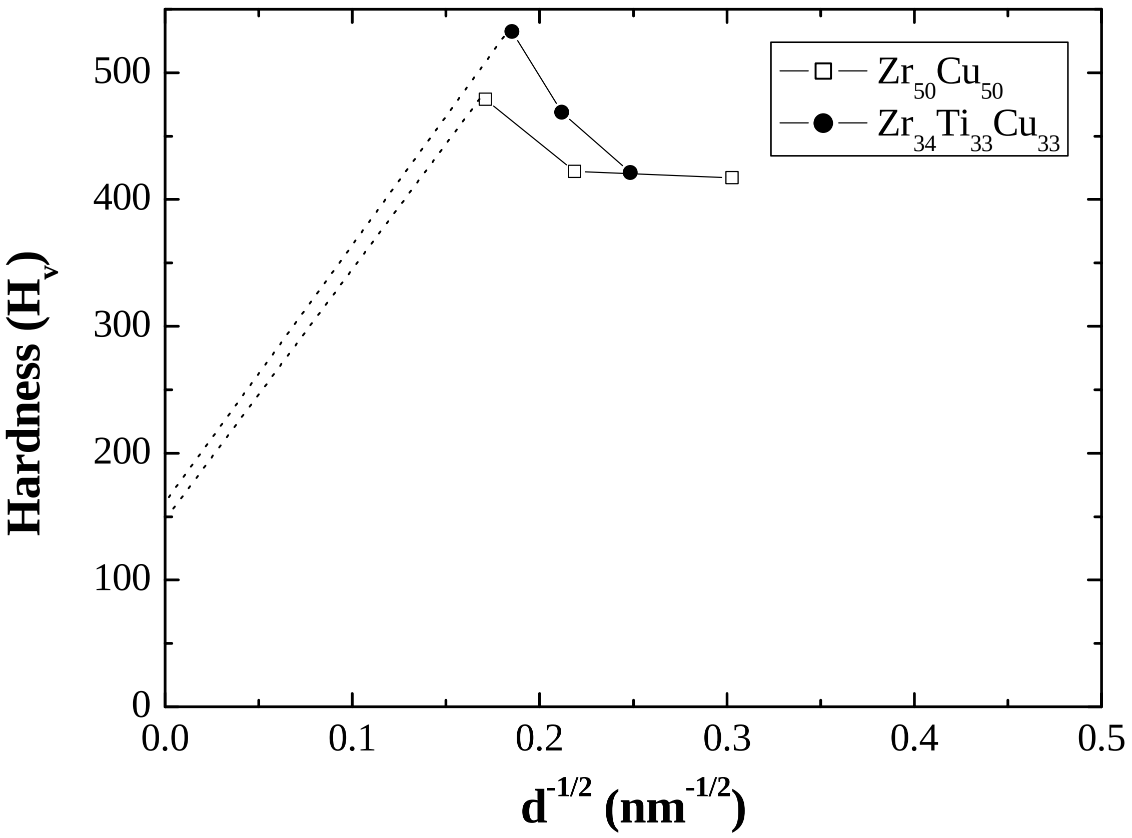

Figure 4.7 The plots of hardness and the inverse square-root of grain size for $Zr_{50}Cu_{50}$ and $Zr_{34}Ti_{33}Cu_{33}$ alloys.

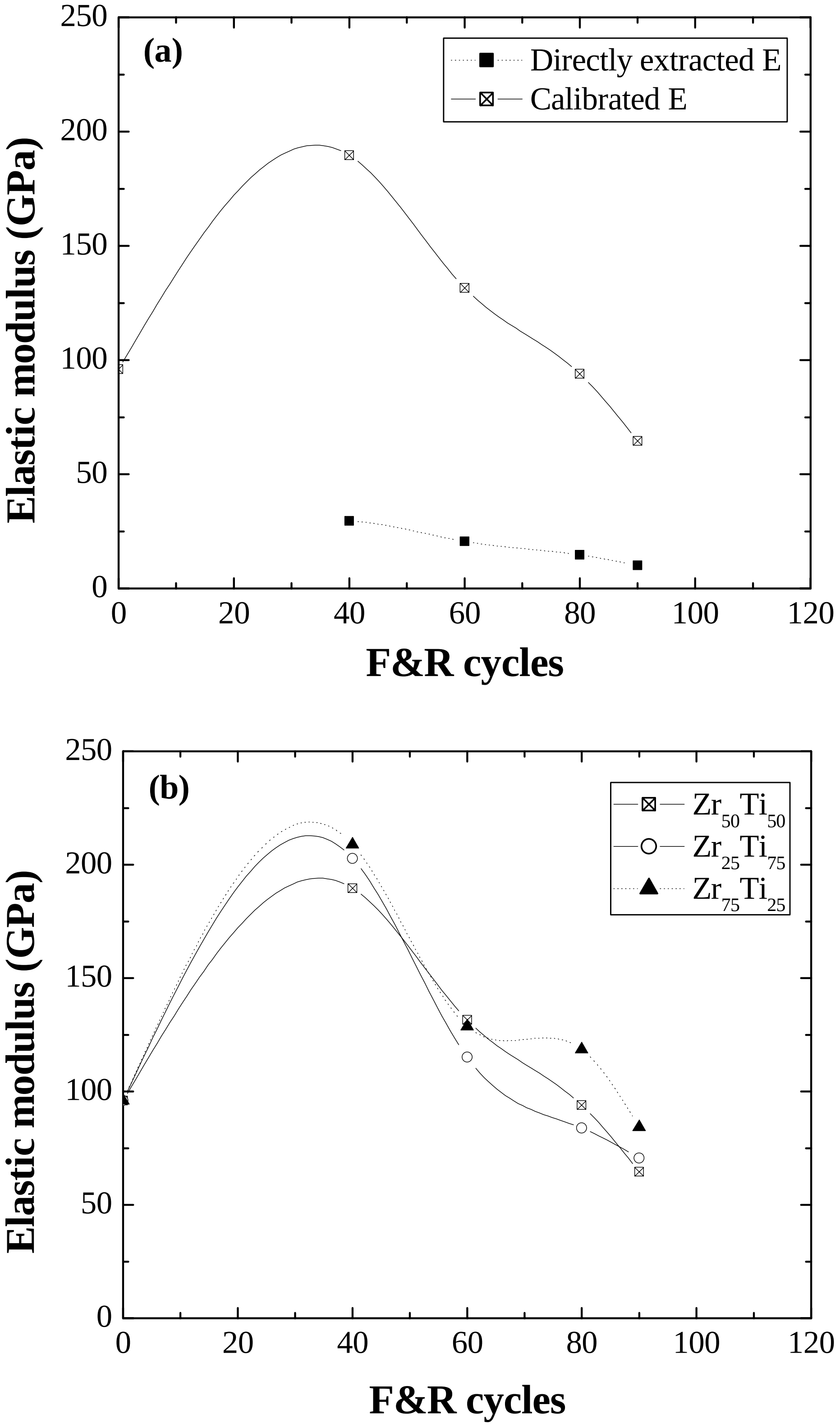

Figure 4.8 The (a) directly extracted and calibrated elastic modulus for $Zr_{50}Ti_{50}$, and (b) variations of the calibrated elastic modulus as a function of the F&R cycles for the Zr-Ti alloys.

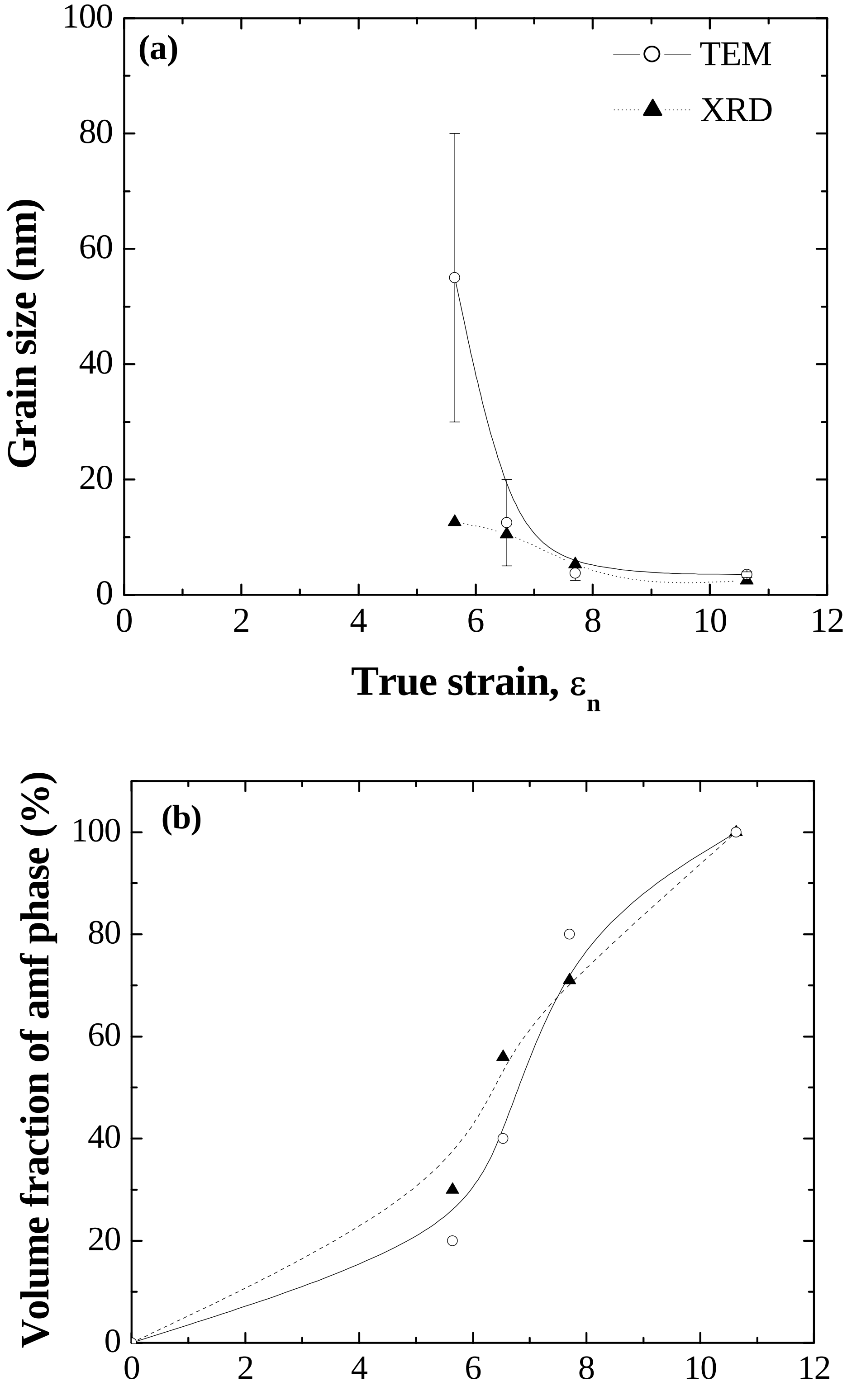

Figure 4.9 The estimated (a) grain size variation of Zr and (b) volume fraction of amorphous phase as a function of accumulated true strain, based on the XRD and TEM observations for the $Zr_{50}Ti_{50}$ alloys.

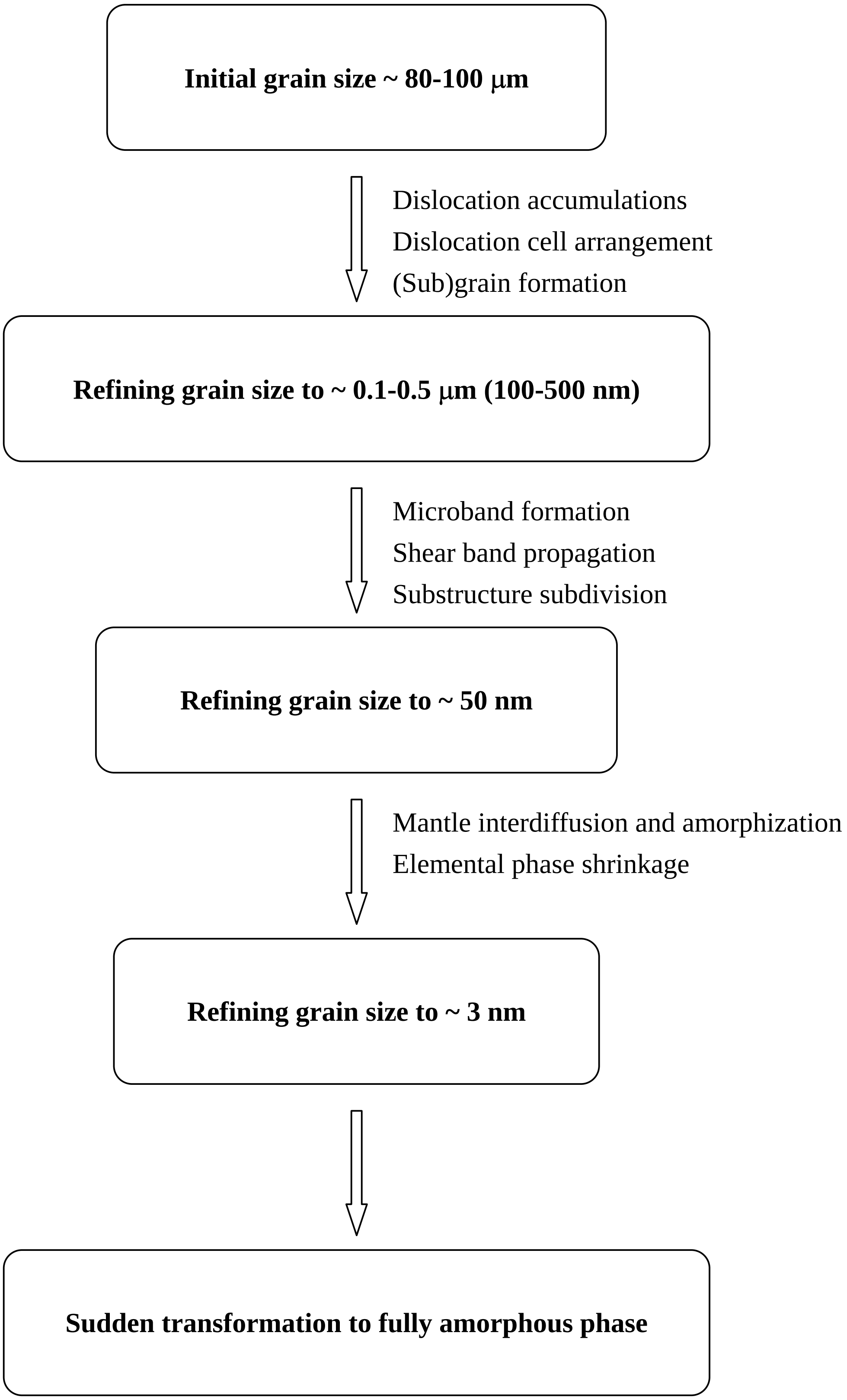

Figure 4.10 The evolution sequence and the major mechanism of nanocrystalline and amorphous transformation.

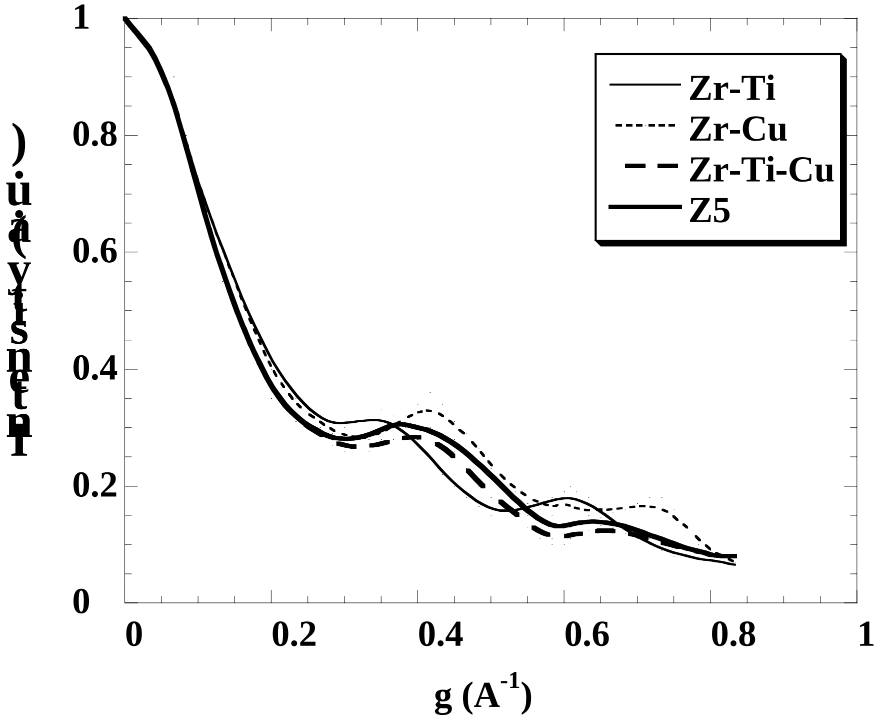

Figure 4.11 The intensity distribution as a function of the *g*-vector in the TEM diffraction patterns for the amorphous phase in the various Zr-X alloys (Z5 represents the $Zr_{52}Ti_5Ni_{15}Al_{10}Cu_{18}$ alloy).

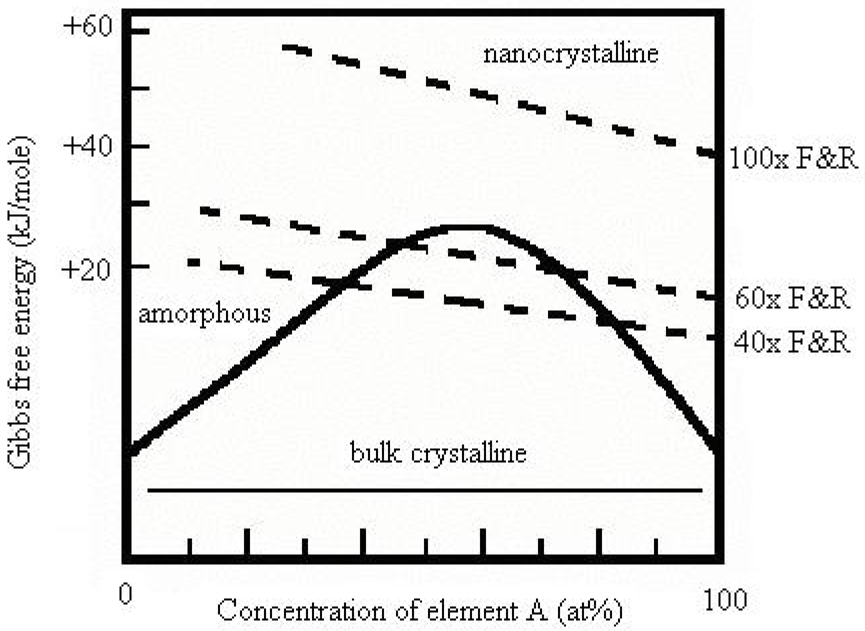

Figure 4.12 Schematic illustration of the evolution of the Gibbs free energy states for the amorphous (solid curved line), nanocrystalline (dotted lines), and bulk crystalline phases (solid straight line) in a binary alloy with increasing F&R cycles (or increasing interfacial energy terms).